

MULTIFUNCTIONAL NANOMATERIALS
DESIGNED FOR THE DETECTION
AND REMOVAL OF PRIORITY
CONTAMINANT SUBSTANCES FROM
WASTE AND DRINKING WATER

M S FROST

PhD 2015

MULTIFUNCTIONAL NANOMATERIALS
DESIGNED FOR THE DETECTION AND
REMOVAL OF PRIORITY CONTAMINANT
SUBSTANCES FROM WASTE AND
DRINKING WATER

MARK STUART FROST

A thesis submitted in partial fulfilment of the
requirements of the Manchester Metropolitan
University for the degree of Doctor of
Philosophy

*School of Science and the Environment
Division of Chemistry and Environmental
Science*

Manchester Metropolitan University

2015

Abstract

Heavy metal pollution in waste water and drinking water is a growing concern, with the European Commission producing the Water Framework Directive (**WFD**) and Drinking Water Directive (**DWD**) to set 'acceptable' levels for priority chemicals in water systems. Taking into account the innovative work being carried out in the area of nanosensors, this research has produced several methods for the quantitative analysis of some aqueous metal ions.

This study explored the use of citrate functionalised Au and Ag NPs and CuS nanoclusters. Citrate functionalised Au and Ag NPs were synthesised to develop for a localised surface plasmon absorption spectroscopy analysis technique, to determine the concentration of a Pb and Hg, respectively. This study concentrated on the molecular interactions of the surface-bound citrate molecules with the nanomaterial surface, and the metal ions in solution. Computational simulations into these interactions were also carried out as a comparison. The citrate speciation for the AuNPs and AgNPs was significantly different, showing single and double carboxylate coordinated molecules respectively. There were also differences in the heavy metal/citrate interaction. Notably, Pb^{2+} ions produced a rapid coagulation of the AuNPs, which was not observed when using AgNPs, demonstrating that the noble metal used for the fabrication of the nanomaterial has an effect on the nature of the metal/citrate bonding interactions. This coagulation produced a unique, very broad UV-Vis absorption spectrum, due to plasmon coupling. The Hg^{2+} /AgNP sample also produced localised surface plasmon absorption spectra that were unique when compared to all of the other metal ion/NP solutions.

The citrate functionalised AuNP were also incorporated into a SERS-based technique for the detection of Pb. This technique provided good results, with a low limit of detection ($\sim 25 \text{ ng/l}$) and a low relative standard deviation of 0.147%, over a wide range of practical concentrations ($\sim 25 \text{ ng/l}$ to 25000 ng/l). Although this method is non-selective, this technique would be highly useful for analysis of solutions after a Pb^{2+} ion-selective preconcentration step has been employed.

The most useful and impressive results, for any of the nanomaterial based chemical sensors produced in this study, were those obtained for the CuS cation-exchange nanosensor. The material was found to not only be sensitive to the concentration of Hg^{2+} ions in aqueous form, but also highly selective to Hg^{2+} ions in a solution containing several different metal ions commonly found in water samples (comparing the results from a solution containing just Hg^{2+} ions and the CuS nanoclusters, and the mixed metal solution containing the CuS nanoclusters produced a correlation coefficient of 0.9985). The data clearly shows that CuS cation-exchange nanosensor is extremely useful for the selective detection and accurate quantification of Hg^{2+} ions at low concentrations between 525 *ng/l* to 5250 *ng/l*. Therefore, this method is exceptionally suitable for the detection of Hg^{2+} ions at levels set by the DWD as 'acceptable'. Ultimately, this method entirely achieves the aims and objectives set for this research project, for the DWD.

Contents

Abstract.....	2
List of Figures	10
List of Tables.....	17
List of Equations	19
List of Abbreviations.....	20
Aims & Objectives of this Study	22
1 Introduction.....	24
1.1 Project Overview.....	24
1.2 The State of Chemical Pollution on a Global Scale	25
1.2.1 A contemporary look at atmospheric pollution.....	26
1.2.2 The chemical pollution of soil	29
1.2.3 An Introduction to the chemical pollution of aquatic systems	30
1.2.4 Mechanisms involved in the pollution of aquatic systems with heavy metals and their compounds.....	32
1.3 The Water Framework Directive and the Drinking Water Directive	33
1.4 Analytical Techniques for the Quantitative Determination of Metals in Aqueous Media	34
1.4.1 Analytical Procedures for the Determination of the Concentrations of Aqueous Metals	34
1.4.2 Potentiometric Analysis	36
1.4.3 Anodic Stripping Voltammetry	38
1.4.4 Atomic Spectrometry.....	40
1.4.5 Inductively Coupled Plasma Techniques.....	41
1.4.6 X-Ray Fluorescence and Total Reflection X-Ray Fluorescence.....	42
1.4.7 Neutron Activation Analysis.....	43

1.5	The Problems Associated with Current Methods of Heavy Metal Analysis	43
1.5.1	The Cost of Analysis and Limit of Detection	43
1.5.2	Time-Scale of Analysis	45
1.6	Summary of standard Analytical Techniques & Motivation for Nanosensors	45
1.7	The Structure of this Thesis	46
2	Nanosensors: A Literature Review	49
2.1	Introduction	49
2.2	Nanotechnology for the Detection of Metals	49
2.3	Localised Surface Plasmon Resonance and Noble Metal Nanoparticles	50
2.3.1	Introduction to Localised Surface Plasmon Resonance	50
2.4	The Response of the Localised Surface Plasmon Resonance Absorption Band to Local Refractive Index Changes and its use in the Detection of Metal Ions	53
2.5	The use of Surface Enhanced Raman Spectroscopy in the Detection of Metal ions	55
2.6	Utilising the Optical Characteristics of Semiconductor Nanomaterials for Sensing Applications	56
2.6.1	The electronic and optical properties of semiconductor nanoparticles	56
2.6.2	The use of Semiconductor Nanomaterials for the Chemical Sensing of Metal Ions	61
2.7	Summary and Concluding Remarks for the Current Nanosensor Technology	62
2.8	Background for the Nanomaterials used in this Study	63
2.8.1	Citrate Functionalised Gold and Silver Nanoparticles	63
2.8.2	CuS Nanoclusters	64
2.8.3	Predicted Optical Results for the CuS Ion-Exchange Nanosensor	70
2.9	Literature Review Summary	70

Nanosensors for the detection of aqueous metals	70
The nanosensors developed in this study	71
2.10 New Contributions to Knowledge Attained During this Study	71
3 Materials and Methods	73
3.1 Introduction	73
3.2 Materials	73
3.2.1 General Reagents & Solutions	73
3.2.2 General Instrumentation	75
3.2.3 Computational Simulations.....	76
3.2.4 Resources utilised for Data Analysis & Processing.....	76
3.3 Instrumental Analysis Techniques used in this Study	76
3.3.1 TEM and HRTEM.....	76
3.3.2 Uv-Vis Spectroscopy	77
3.3.3 Raman Spectroscopy	78
3.3.4 Photon Correlation Spectroscopy.....	79
3.3.5 Zeta-Potential.....	80
3.3.6 ATR-FTIR.....	81
3.3.7 XPS	82
3.4 Experimental Methodology	85
3.4.1 General Preparatory Methods for Glassware	85
3.4.2 Preparation of the Metal Ion Containing Stock and Control Solutions and Addition to the Nanosensor Solutions	85
3.4.3 Synthesis of the Citrate Functionalised Gold Nanoparticles and Citrate Functionalised Silver Nanoparticles	87
3.4.4 Synthesis of the Metal Sulfide Ion-Exchange Nanoclusters	88
3.5 Experimental Conditions for Sample Analysis and Characterisation	90
3.5.1 TEM and HRTEM Analysis.....	90
3.5.2 UV-Vis Absorption Spectroscopy	90

3.5.3	Measurements of the size and colloidal stability of the nanomaterials in solution using photon correlation spectroscopy	91
3.5.4	Measurement of Metal Ion Induced pH Changes	91
3.5.5	ATR-FTIR Spectroscopy	92
3.5.6	Computational IR Spectroscopy Calculations	92
3.5.7	Surface Enhanced Raman Spectroscopy.....	92
3.5.8	XPS	93
4	Results and Discussion (Part 1): The Response of Citrate Functionalised Gold and Silver Nanoparticle Solutions to the Addition of Heavy Metal Ions.....	94
4.1	Introduction	94
4.2	The response of the plasmon band absorption peak for citrate functionalised gold nanoparticle solutions upon the addition of heavy metal ions	94
4.3	Size characterisation with PCS and TEM imaging.....	100
4.4	Change in pH of Metal ion/AuNP Solutions after the Addition of the Metal Ion Precursor.....	107
4.4.1	Summary of Results and Discussion Part so far	111
4.5	Defining the Metal-Citrate Species formed at the Surface of the NPs by Applying ATR-FTIR Spectroscopy and Computational Predictions.....	112
4.5.1	ATR-FTIR Spectroscopy and Simulated Vibrational Transitions for the Surface-Bound Citrate Molecules on the Surfaces of the Gold and Silver Nanoparticles.....	112
4.5.2	Experimental ATR-FTIR Spectroscopy and Computational Studies into the Metal Ion/Surface Citrate Complexes Formed at the Surfaces of the Gold and Silver Nanoparticles and at Gold and Silver Surfaces.....	115
4.6	Using AuNP and AgNP Solutions to Detect Pb^{2+} , Cd^{2+} , Ni^{2+} , or Hg^{2+} Ions at Trace and Ultra-Trace Concentrations by Shifts to the Wavelength of the Plasmon Absorption Band in the UV-Vis Absorption Spectrum.....	120
4.6.1	Citrate Functionalised AuNPs as LSPR Based Nanosensors for Pb^{2+} ions	121

4.6.2	Citrate Functionalised AgNPs as LSPR Based Nanosensors for Hg ²⁺ Ions	122
4.7	Evaluating the usefulness of the Citrate Functionalised Gold and Silver Nanoparticles	122
4.8	Summary and conclusion	123
5	Results and Discussion (Part 2): Metal Ion Interaction with Citrate Functionalised Gold Nanoparticles and the Subsequent Raman Signal Enhancement for the Detection of Lead Ions	124
5.1	Characterisation of the Synthesised AuNPs and the Production of the SERS Substrates	125
5.2	Monitoring the Effects of Metal Ion Interaction with the Surface-Bound Citrate Molecules with Surface Enhanced Raman Spectroscopy	128
5.3	The Usefulness of AuNP SERS as a Nanosensor at Detecting Pb ²⁺ Concentrations at the WFD and DWD Acceptable levels	131
5.3.1	Detecting Pb ²⁺ ions in a Pb ²⁺ ion solution using SERS	132
5.3.2	Development of a Calibration Curve between 0 µg/l and 1.000 µg/l	134
5.3.3	Calibration Curve for 1.000 µg/l to 25.000 µg/l	137
5.3.4	Comparison of this SERS-based technique with standard techniques for the determination of the concentration of Pb in aqueous samples	141
5.4	Summary and Conclusion	142
6	Results and Discussion (Part 3): The Synthesis of a CuS Cluster for the Ultra-Sensitive and Selective Detection of Aqueous Hg ²⁺ ions using a Cation-Exchange Mechanism	144
6.1	Qualitative Analysis of the Synthesised Nanoclusters	144
6.1.1	Transmission electron microscopy analysis	144
6.1.2	UV-Vis absorption spectroscopy	146
6.1.3	X-ray photoelectron spectroscopy	150
6.2	Characterisation of the CuS Clusters with Increasing Hg Concentration	152

6.2.1	The determination of the bandgap energies of the doped nanoclusters and the widths of the band-edge localised states, using ‘Tauc plots’ and ‘Urbach’s rule’	153
6.3	Evaluating the CuS Ion-Exchange Sensor for the Selective Detection of Aqueous Hg ²⁺ Ions	163
6.4	Summary and Conclusion	165
7	Future Work	166
7.1	Preliminary Results for a ZnS Nanocluster Chromatography-Style Sensor	166
7.2	Justification for using Zinc Sulfide Clusters for the detection of Lead, Cadmium, Copper and Mercury Ions.....	166
7.3	The Production of a Chromatography-Style ZnS Cation-Exchange Sensor for the Quantitative determination of Several Metal Ions in a Mixture of Aqueous Metal Ions.....	171
7.3.1	Potential Designs for Further Nanosensor Technologies: Chromatography-Style LSPR based sensor for the detection of aqueous metals	173
8	Conclusion	176
8.1	Citrate Functionalised Gold and Silver Nanoparticle LSPR Absorption-Based sensor	176
8.2	AuNP SERS Sensing Method.....	177
8.3	Hg ²⁺ Selective Ion-Exchange CuS Nanocluster Sensor.....	178
9	References	181

List of Figures

<i>Figure 1-1 The major mechanisms which can lead to pollutants entering aquatic systems are from surface deposition via precipitation of atmospheric pollutants, surface run-off, leaching of chemicals from soils, and erosion</i>	<i>30</i>
<i>Figure 1-2 An example of a standard set-up for the potentiometric determination of a target ion</i>	<i>37</i>
<i>Figure 1-3 Four steps of ASV: (1) cleaning, (2) electroplating, and (3) stripping</i>	<i>39</i>
<i>Figure 1-4 A diagram of the applied potential vs Ag/Cl electrode over 5 minutes of a typical anodic stripping voltametry analysis procedure (adapated from²²).....</i>	<i>40</i>
<i>Figure 2-1 The excitation of surface plasmons on (a) bulk gold, where the increased length leads to an increased dampening factor and the plasmon oscillations cannot be sustained (b) a gold nanoparticle, where the reduced length of the material leads to a reduced dampening factor and a coherent oscillation of the surface plasmons</i>	<i>51</i>
<i>Figure 2-2 Plots showing the dependence of the position and shape of the plasmon absorption band, on the size and shape of the gold nanomaterials⁷³</i>	<i>52</i>
<i>Figure 2-3 The change in the LSPR absorption with a change in the local refractive index at the surface of the NP, due to the introduction of metal ions</i>	<i>54</i>
<i>Figure 2-4 The confinement of the exciton, created by reducing the dimensions of the material to below the Bohr exciton radius, leading to the increase in the bandgap energy and the opening of the electronic energy bands</i>	<i>57</i>
<i>Figure 2-5 The absorption spectra for ZnSe spheres with material dimensions relating to a bulk system (with crystallite diameters of >10 nm), medium crystal system (4 to 5 nm diameter), and a nanocluster (2 to 3 nm diameter)⁵¹</i>	<i>59</i>
<i>Figure 2-6 The processes involved in the excitation of an electron via an electron-photon interaction (1) an incoming photon excites an electron, promoting it into the conduction band (2) the non-radiative transition to the edge of the conduction band by the emission of a phonon (3) the recombination of the electron-hole pair, resulting in the emission of a photon with energy equal to approximately the bandgap energy of the material</i>	<i>60</i>

Figure 2-7 Electron charge transfer to a surface molecules, resulting in a reduction in fluorescence intensity.....	61
Figure 2-8 The absorption of a photon (1) leading to the promotion of an electron into the conduction band, the radiationless transition to the bottom of the conduction band involving the emission of a phonon (2), the radiationless transition from the bottom of the conduction band to a localised electronic energy level in the bandgap (3), and the final transition from the localised energy level to the valence band, resulting in the emission of a photon with an energy comparable to the energy gap between the localised state and the valence band.....	66
Figure 2-9 Illustrations demonstrating the ‘blurring’ of the bandgap edges as they extend into the bandgap due to the increased level of dopants and or disorder, and the subsequent broadening of the absorption spectra as electrons are promoted into the extended band states of the conduction band.....	67
Figure 2-10 The effects of lattice strain on the bandgap of the nanomaterial: (left) a CdSe substrate can change its bond lengths to find a more stable structure when a ZnS layer is grown on top of the nanostructure resulting in a change in the bandgap energy (right) where an increase in the bond length reduces the bandgap and the shortening of the bond length leads to a widening of the bandgap⁶³	68
Figure 2-11 Cation-exchange between the Zn²⁺ ions in a 1 nm ZnS nanocluster and the Pb²⁺ ions in solution to form a PbS nanocluster	69
Figure 3-1 A schematic of the electron beam path in a TEM (A) and HRTEM (B).....	77
Figure 3-2 Path of the light source used in a UV-Vis spectrometer⁹⁴	78
Figure 3-3 Scattering of light from small particles in a solution sample⁹⁷	79
Figure 3-4 changing intensities caused by moving nanoparticles⁹⁷	80
Figure 3-5 ATR-FTIR Crystal and the production of an evanescent wave	81
Figure 3-6 The XPS effect on a core level electron of an atom within a crystal structure.....	83
Figure 3-7 XPS spectra for different oxidation states for a Cu containing sample, taken for this study. (Top) The XPS spectrum for Cu²⁺ showing shake-up satellites, (Bottom) XPS spectrum for Cu¹⁺ showing an absence of shake-up peaks.....	84
Figure 3-8 Schematic for the synthesis steps for the production of the CuS NCs used here	89

Figure 4-1 UV-Vis absorption spectra for AuNP and metal ion/AuNP solutions, showing plasmon band absorbance maximums at a metal ion concentration of 1.905×10^{-4} M.....	95
Figure 4-2 UV-Vis absorption spectra for AgNP and metal ion/AgNP solutions showing plasmon band absorbance maximums at a metal ion concentration of 1.905×10^{-4} M.....	96
Figure 4-3 The absorption spectra for the Hg^{2+}/AgNP solution with a hg^{2+} ion concentration of 1.905×10^{-4} M.....	97
Figure 4-4 (Left to Right): AuNP and Ni^{2+}/AuNP, Cd^{2+}/AuNP, Hg^{2+}/AuNP and Pb^{2+}/AuNP solutions, with a 1.905×10^{-4} M metal ion precursor concentration, 24 hours after mixing	98
Figure 4-5 Diagram explaining the effect of a local refractive index change, compared to plasmon coupling caused by nanoparticles in close proximity, on the position of the plasmon band absorption peak in the UV-Vis absorption spectrum.....	98
Figure 4-6 Clear Pb^{2+}/AuNP solutions showing NP aggregates for AuNP radiuses of 16 nm, 47 nm, and 65 nm (left to right), at a Pb^{2+} ion precursor concentrations of 1.905×10^{-4} M.....	99
Figure 4-7 The solutions of (from left to right) AuNP, Hg^{2+}/AgNP, Cd^{2+}/AgNP, Ni^{2+}/AgNP and Pb^{2+}/AgNP with the metal ion/AgNP solutions showing slight sedimentation.....	100
Figure 4-8 TEM micrographs for the AuNP (left) and AgNP (right) solutions.....	101
Figure 4-9 Illustrations showing the discussed mechanisms for NP destabilisation: (a) metal ion interactions with the negatively charged carboxylate groups of the surface-bound citrate molecules, (b) build-up of positive charges around the surfaces of the NPs, provided by an increase in the concentration of protons in the solution, (c) re-protonation of the negative carboxylate groups of the surface-bound citrate molecules upon the decrease in the pH of the NP solution.....	106
Figure 4-10 Graph showing the particle sizes measured by PCS against the pH value of the corresponding AuNP solution, and metal ion/AuNP solutions with a metal ion concentration of 1.905×10^{-4} M	108
Figure 4-11 Solutions of AuNP at pH values of a) 6.3 b) 4.3 and c) 2.8.....	109
Figure 4-12 The decrease in pH over time after the addition of Pb^{2+} ions (1.905×10^{-4} M) to the AuNP solution	110

Figure 4-13 ATR-FTIR spectra for the surface citrate molecules for the AuNP and AgNP solutions.....	113
Figure 4-14 Simulated vibrational spectra for a surface-citrate molecule bound to a Au surface via a single carboxylate group (★) and for a surface-citrate molecule bound to a Ag surface via two carboxylate groups (■).....	114
Figure 4-15 ATR-FTIR spectra for the metal ion/AuNP solutions.....	116
Figure 4-16 ATR-FTIR spectra for the metal ion/AgNP solutions.....	116
Figure 4-17 Graphical representations of the computationally simulated metal ion/surface-citrate structures, on a Au surface, for the (A) Ni²⁺, (B) Cd²⁺, (C) Hg²⁺, and (D) Pb²⁺ metal ions [Note: that the 3 x 3 x 3 Au surface has been hidden for brevity].....	117
Figure 4-18 Graphical representations of the computationally simulated metal ion/surface-citrate structures, on a Ag surface, for the (A) Pb²⁺, (B) Ni²⁺, (C) Cd²⁺, and (D) Hg²⁺ metal ions [Note: that the 3 x 3 x 3 Ag surface has been hidden for brevity].....	118
Figure 4-19 The reduction of the O-H stretch band of the surface-bound citrate molecules, indicating the deprotonation of the hydroxyl group of the surface-citrates, upon the addition of Pb²⁺ ions to a solution of AuNPs.....	119
Figure 5-1 UV-Vis spectra for the AuNP and metal ion/AuNP SERS samples.....	126
Figure 5-2 The UV-Vis absorption spectra for the AuNP and metal ion/AuNP SERS samples. This was normalised at 400 nm to help demonstrate the relative red shifts for the Hg²⁺/AuNP, Cd²⁺/AuNP, and Ni²⁺/AuNP SERS samples, compared to the AuNP and Pb²⁺/AuNP samples.....	127
Figure 5-3 SERS spectrum for the AuNP sample showing the asymmetric stretching of the carboxylate groups ($\nu_{as}(\text{COO}^-)$), symmetric stretching carboxylate groups ($\nu_s(\text{COO}^-)$) and hydroxyl group stretches ($\nu(\text{C-OH})$) and ($\nu(\text{O-H})$).....	128
Figure 5-4 SERS spectra for the surface-bound citrate molecules of the AuNPs and for the mixture of Pb²⁺(0.19 mM) and AuNPs SERS sample.....	130
Figure 5-5 SERS spectra for the AuNP/metal ion SERS samples and a SERS sample produced from a AuNP solution containing all of the above metals at a concentration of 0.19 mM.....	131
Figure 5-6 The SERS spectral response to concentrations of Pb²⁺ ions within the range of 0 µg/l to 1.000 µg/l.....	132

Figure 5-7 A plot of the intensity ratio between the $\nu(\text{C-OH})$ band for the AuNP SERS sample over the $\nu(\text{C-OH})$ band for Pb^{2+} ion/AuNP SERS samples between the concentration range of 1.000 $\mu\text{g/l}$ to 0 $\mu\text{g/l}$. Error bars have been omitted as the error bar values were too small to be adequately displayed.....	133
Figure 5-8 A plot of the ratio of the concentration of Pb^{2+} ions over the intensities of the $\nu(\text{C-OH})$ band for the AuNP SERS sample and the Pb^{2+} /AuNP SERS samples, for concentrations between 0 ng/l and 1000 ng/l	135
Figure 5-9 The re-plotted calibration plot using the line of best fit obtained from the $n = 3$ polynomial equation from Figure 4.8 ratio of the concentration of Pb^{2+} ions over the intensities of the $\nu(\text{C-OH})$ band for the AuNP SERS sample and the Pb^{2+} /AuNP SERS samples	136
Figure 5-10 The plot of the optimised equation of best fit using the data obtained from plots Figure 4.8 and Figure 4.9	137
Figure 5-11 A plot of ratio of the intensities of the $\nu(\text{C-OH})$ band for the AuNP SERS sample and the Pb^{2+} /AuNP SERS samples for concentrations between 1 $\mu\text{g/l}$ and 25 $\mu\text{g/l}$	138
Figure 5-12 A plot of the ratio of the concentration of Pb^{2+} ions over the intensities of the $\nu(\text{C-OH})$ band for the AuNP SERS sample and the Pb^{2+} /AuNP SERS samples, for concentrations between 1×10^3 ng/l to 2.5×10^4 ng/l (1 $\mu\text{g/l}$ to 25 $\mu\text{g/l}$)	139
Figure 5-13 The re-plotted calibration plot using the line of best fit obtained from the $n = 3$ polynomial equation from Figure 4.14 versus ratio of the concentration of Pb^{2+} ions over the intensities of the $\nu(\text{C-OH})$ band for the AuNP SERS sample and the Pb^{2+} /AuNP SERS samples.....	140
Figure 5-14 A plot of the ratio of the concentration of Pb^{2+} ions over the intensities of the $\nu(\text{C-OH})$ band for the AuNP SERS sample and the Pb^{2+} /AuNP SERS samples, for concentrations between 1×10^3 ng/l to 2.5×10^4 ng/l (1 $\mu\text{g/l}$ to 25 $\mu\text{g/l}$)	141
Figure 6-1 TEM micrographs for the ZnS nanoclusters, showing cluster diameters of 3 to 5 nm	145
Figure 6-2 TEM micrographs for the CuS nanoclusters, showing cluster diameters of 3 to 5 nm	146
Figure 6-3 The UV-Vis absorption spectra for the ZnS (left) and Cu_xS (right) nanoclusters synthesised here. The insert for the CuS spectrum is the	

<p>peak corresponding to LSPR of the excess holes within the top of the valence band of the CuS nanoclusters 147</p>
<p>Figure 6-4 Reaction scheme for the 3 stage synthesis of the CuS nanoclusters ... 148</p>
<p>Figure 6-5 A Tauc plot of $(\alpha h\nu)^2$ against photon energy (eV), and the extrapolation of the straight portion of the curve to determine the optical direct-to-direct band transition across the bandgap for the CuS nanoclusters 149</p>
<p>Figure 6-6 A Tauc plot of $(\alpha h\nu)^{0.5}$ against photon energy (eV) and the evolution of the curve to $y = 0$, which determines the indirect optical band transition across the bandgap for the CuS nanoclusters..... 150</p>
<p>Figure 6-7 Deconvoluted XPS spectra for the CuS clusters, which displays shake-up peaks that represent the Cu(II) state (top), and Cu₂S clusters showing very low intensity shake-up peaks, representing a structure that is Cu_xS, where $x < 2$ and the majority of the Cu ions are in the Cu(I) state (bottom) 151</p>
<p>Figure 6-8 The UV-Vis absorption spectra for solutions of CuS nanoclusters, which contain different concentrations of Hg²⁺ ions ranging from 0.0000 µg/l to a 1:1 [Hg²⁺]:[Cu²⁺] ratio..... 153</p>
<p>Figure 6-9 A plot of the allowed direct and indirect bandgap energy, and the LSPR absorption band position, vs the concentration of Hg²⁺ ions in the CuS nanocluster solutions 155</p>
<p>Figure 6-10 TEM micrographs of the hollow core-shell morphology adopted by the CuS/Hg nanoclusters at an aqueous Hg²⁺ ion concentration of 0.5250 µg/l 156</p>
<p>Figure 6-11 A demonstration of the increase in the optical transition gap (here this is the allowed direct band transition) with an increase in holes in the valence band (the Moss-Burstein shift) 157</p>
<p>Figure 6-12 The transition energies for the LSPR absorption band and the allowed direct band transition for the CuS solutions containing different amounts of Hg²⁺ ions 158</p>
<p>Figure 6-13 At a Hg²⁺ ion concentration of 0.7875 µg/l, the hollow particles became whole with many different sizes ranging from 3 nm to 7 nm..... 159</p>
<p>Figure 6-14 TEM micrographs showing the morphology of the CuS/Hg nanoclusters at an aqueous Hg²⁺ ion concentration of 1.0500 µg/l 160</p>
<p>Figure 6-15 TEM micrograph of CuS/Hg nanoclusters at an aqueous Hg²⁺ ion concentration of 5.2500 µg/l..... 161</p>

Figure 6-16 XPS Spectra for a CuS solution containing a 1 : 1 ratio of CuS to Hg²⁺ ions, showing the presence of the Cu(I) oxidation state	162
Figure 6-17 A plot of the allowed direct band transition energy for different CuS/Hg²⁺ solutions and the corresponding test solutions containing the same amounts of Hg²⁺ ions in a mixed metal ion solution	164
Figure 7-1 The K_{sp} values for several metal sulfide materials (shown as 10ⁿ) containing metals commonly found in aquatic systems	167
Figure 7-2 ZnS cluster solutions after the addition of Pb²⁺, Cd²⁺, Cu²⁺, and Hg²⁺ ions metal ions, added to make a 1:1 concentration of Zn:M²⁺	167
Figure 7-3 The calculated bandgap values for β-HgS using the Brus equation.....	169
Figure 7-4 The Gibbs energy of formation for the cation-exchange reaction between ZnS and the respective divalent metal ions.....	170
Figure 7-5 The production of a chromatography-style absorbent paper.....	171
Figure 7-6 The chromatography-style ZnS cation-exchange sheets after the addition of different metal ion solutions.....	172
Figure 7-7 The ZnS cluster cation-exchange sheets after the addition of one drop of (left to right) Hg²⁺, Pb²⁺, Cu²⁺, and Hg²⁺ and Cu²⁺ solutions (each metal ion solution contains a respective equal concentration).....	172
Figure 7-8 A design for a waveguide sensor, for the detection of metals using the chromatography style principle.....	174

List of Tables

Table 1.1	<i>A list of examples for organic pollutants and potential sources of discharge into the environment.....</i>	<i>26</i>
Table 1.2	<i>A list of inorganic pollutants examples and potential sources of discharge into the environment.....</i>	<i>26</i>
Table 1.3	<i>World Health Organisation guideline values and health implications of common atmospheric pollutants^{2,4}</i>	<i>28</i>
Table 1.4	<i>Acceptable metal levels for a selected group of metals, which was set by the 2008/105/EC priority substance list¹⁷</i>	<i>33</i>
Table 1.5	<i>Acceptable heavy metal levels set by Directive 98/83/EC – the Drinking Water Directive¹⁹</i>	<i>34</i>
Table 1.6	<i>A table of specifications for commonly used analytical techniques for the detection of heavy metals (adapted from²¹)</i>	<i>36</i>
Table 1.7	<i>Table of standard limits of detection for elemental analysis of metals by inductively coupled plasma²⁴</i>	<i>42</i>
Table 1.8	<i>Acceptable concentrations set by the DWD and WFD, for the metals used in this study and the instrumental analysis needed to detect them</i>	<i>44</i>
Table 1.9	<i>Purchase and operating costs of standard heavy metal analysis instruments/equipment²⁶</i>	<i>44</i>
Table 1.10	<i>A list of some current instruments that can analyse water samples at the site and the metals that they can analyse which are included in this study.....</i>	<i>45</i>
Table 2.1	<i>A list of nanosensor examples for the detection of a target metal ion including the target ion, material and sensor type, and limit of detection</i>	<i>62</i>
Table 3.1	<i>A list of metal precursors which were used for control experiments and the concentration of the metal ion stock solutions.....</i>	<i>74</i>
Table 3.2	<i>The chemicals used to synthesise the nanomaterials used in this study.</i>	<i>74</i>
Table 3.3	<i>The components for the production of aqua regia, which was used for the cleaning of glassware</i>	<i>75</i>
Table 3.4	<i>Recipe for the production of the metal ion stock solutions</i>	<i>86</i>
Table 4.1	<i>Diameter estimation by PCS and TEM imaging for the AuNP and AgNP solutions in the presence of Ni²⁺, Cd²⁺, Hg²⁺, and Pb²⁺ ions (1.905 x 10⁻⁴ M).....</i>	<i>102</i>

Table 4.2 Zeta potential results for the AuNP and AgNP solutions in the presence of Ni^{2+}, Cd^{2+}, Hg^{2+}, and Pb^{2+} ions ($1.905 \times 10^{-4} M$) metal ion concentration, 24 hours after mixing	104
Table 4.3 Resultant pH values, 24 hours after the addition of metal ion precursors to solutions of AuNP solutions.....	107
Table 4.4 A list of the plasmon absorption band positions for the AuNP solutions with Pb^{2+} ion concentrations between 30.0 $\mu g/l$ and 0.0 $\mu g/l$ - here * represents the original experiment value noted in Section 3.1, as a comparison.....	121
Table 4.5 A table of the plasmon absorption band positions for the AgNP solutions with Hg^{2+} ion concentrations between 30.0 $\mu g/l$ and 0.0 $\mu g/l$ - here * represents the original experiment value noted in Section 3.1 as a comparison.....	122
Table 5.1 A table displaying the $\nu(C-OH)$ band intensity recorded for five measurements for Pb^{2+} ion concentrations between 0 $\mu g/l$ and 1 $\mu g/l$..	134
Table 5.2 Standard analytical techniques for the detection Pb	142
Table 6.1 Results from Tauc plots taken from UV-Vis absorptions data for solutions of CuS clusters which contain different concentrations of Hg^{2+} ion. The table contains energy values for the allowed direct bandgap transitions (E_d) and allowed indirect bandgap (E_i) transitions, the phonon energy (E_p) associated with the indirect transition ($E_i + E_p = E_g$), the Urbach energy (E_U) and the energy of the LSPR absorption band (E_{LSPR}).....	154
Table 7.1 Thermodynamic data for the cation-exchange for the reaction $ZnS + M_{ion} \rightarrow MS + Zn^{2+}$ using the formula $\Delta G^{\circ}_{TOTAL} = \sum \Delta G^{\circ}(\text{products}) - \sum \Delta G^{\circ}(\text{reagents})$.....	170
Table 7.2 The band widths for the coloured bands in Figure 7-7	173

List of Equations

<i>Equation 1.1 The Nernst equation²²</i>	<i>37</i>
<i>Equation 1.2 The altered Nernst equation²²</i>	<i>38</i>
<i>Equation 2.1 The wavelength response to the change in the local refractive index at the surface of a plasmonic material⁷⁶</i>	<i>52</i>
<i>Equation 2.2 The Urbach equation, used to measure the widths of the electronic states at the band edges, created by disorder and doping⁶²</i>	<i>67</i>

List of Abbreviations

AgNP(s)	<i>Silver Nanoparticle(s)</i>
AuNP(s)	<i>Gold nanoparticle(s)</i>
CB	<i>Conduction band</i>
Cd	<i>Cadmium</i>
Cu	<i>Copper</i>
Cu(I)	<i>Copper with a +1 oxidation state</i>
Cu(II)	<i>Copper with a +2 oxidation state</i>
CuS	<i>Copper sulfide nanoclusters</i>
DWD	<i>Drinking water directive</i>
e⁻	<i>Electron</i>
E_d	<i>Allowed direct bandgap transition</i>
E_g	<i>Bandgap</i>
E_i	<i>Allowed indirect bandgap transition</i>
E_p	<i>The energy of an absorbed or emitted phonon during an indirect transition</i>
Fe	<i>Iron</i>
h⁺	<i>Hole</i>
Hg	<i>Mercury</i>
LOD	<i>Limit of detection</i>
LSPR	<i>Localised surface plasmon resonance</i>
m[*]	<i>Effective mass</i>
NC	<i>Nanocluster</i>
Ni	<i>Nickel</i>
Pb	<i>Lead</i>
PCS	<i>Photon correlation spectroscopy</i>
QC	<i>Quantum Confinement</i>
R²	<i>Coefficient of determination (a measure of the linearity of a data set, quoted as a value between 0 and 1, where 1 indicates linearity)</i>
RSD	<i>Relative standard deviation</i>
SC	<i>Semiconductor</i>
SERS	<i>Surface enhanced Raman spectroscopy</i>
TEM	<i>Transmission electron microscopy</i>

UV-Vis	<i>The range of ultraviolet to the visible region of the electromagnetic spectrum</i>
VB	<i>Valence band</i>
WFD	<i>Water framework directive</i>
XPS	<i>X-ray photoelectron spectroscopy</i>

Aims & Objectives of this Study

The aims and objectives of this project are listed below:

Aims:

To develop a functional nanomaterials capable of detecting low level concentrations ($20 \mu\text{g/l}$ to $0.05 \mu\text{g/l}$) of a metal identified as a pollutant in the *Water Framework Directive (WFD)*, and the *Drinking water Directive (DWD)* (Pb, Cd, Hg, or Ni). The range of $20 \mu\text{g/l}$ to $0.05 \mu\text{g/l}$ was set as this incorporated the highest and lowest allowed concentrations of set across the WFD and DWD.

Objectives:

1. Fabrication of plasmonic Au nanoparticles (**AuNPs**) with citrate functionalised surfaces, suitable for localised surface plasmon resonance (**LSPR**) optical absorption based sensing, and as a surface enhanced Raman spectroscopy (**SERS**) substrate
2. Fabrication of Ag nanoparticles (**AgNPs**) with citrate functionalised surfaces, suitable for LSPR optical absorption based sensing
3. Characterise the AuNPs and AgNPs using: UV-Vis absorption spectroscopy to obtain LSPR absorption band values; transmission electron microscopy (**TEM**) and photon correlation spectroscopy (**PCS**) to evaluate the diameters of the NPs; zeta potential measurements to acquire data on the surface charges of the particles; attenuated total reflectance Fourier transform infrared spectroscopy (**ATR-FTIR**) to study the speciation of the surface citrate molecules on the surface of the NPs; computational predictions into the IR spectroscopy of the surface-bound citrate molecules to help and assign the different IR spectroscopic bands; additionally, the AuNPs will be characterised using Raman spectroscopy to obtain data to be used for SERS studies

4. Using AuNPs, detect at least one metal contaminant listed in the WFD and DWD (Pb, Cd, Hg, or Ni), down to 20 $\mu\text{g/l}$ to 0.05 $\mu\text{g/l}$ concentrations, via LSPR optical absorption shifts and SERS
5. Detect at least one metal contaminant listed in the WFD and DWD (Pb, Cd, Hg, or Ni) down to 20 $\mu\text{g/l}$ to 0.05 $\mu\text{g/l}$ concentrations, via LSPR optical absorption shifts, using AgNPs
6. Test the selectivity of the technique for that metal, in a system containing a mixture of aqueous metals, at concentrations commonly found in water samples tested by United Utilities Plc (**UU**)
7. Synthesise and optically characterise CuS nanoclusters (**NCs**), to be used for the selective detection of aqueous Hg in a mixed-metal sample, via an ion-exchange based method
8. Characterise the CuS NCs using: UV-Vis absorption spectroscopy to obtain optical absorption values for the optical band gap, indirect band gap, direct band gap and the Urbach energy of the NCs; high resolution transmission electron microscopy (**HRTEM**) to evaluate the diameters of the NPs; x-ray photoelectron spectroscopy (**XPS**) to characterise the oxidation state of the Cu^{n+} species of the CuS NCs
9. Detect Hg down to 20 $\mu\text{g/l}$ to 0.05 $\mu\text{g/l}$ concentrations by monitoring the changes in the optical absorption spectra of the NCs, which is related to the changes in the electronic structure of the NC, with an increasing contribution of the Hg^{2+} ions
10. Test nanosensor selectivity for Hg in a system containing a mixture of metals at concentrations commonly found in water samples, using metal concentration values provided by UU

1 Introduction

1.1 Project Overview

Nanomaterials are now widely integrated into the research areas of chemical sensing. The ultimate factor for the current success of nanomaterials for sensing applications is their highly controllable chemical and physical properties. Being able to tune and easily alter the properties of these materials has led to the production of many highly sensitive nanosensors with low limits of detection (**LOD**) – some being as low as $\mu\text{g/l}$ concentrations. This makes them excellent candidates for new commercial sensors, with the potential for integration into standard analytical practice. The focus of this research was to produce a novel nanosensor for the detection of an aqueous metal at concentrations within the ng/l to $\mu\text{g/l}$ regime: The concentration range of metals commonly within environmental and waste water samples.

The project was partially funded by *United Utilities PLC (UU)*, a company who manages the regulated water and waste water network in the north west of England. Their assigned target was the production of a nanosensor for the detection of any metal listed in the WFD and the DWD as ‘*priority substances*’ (see Section 1.3) – a legislation that sets the acceptable concentration limits for pollutants (‘priority substances’), notably the metals Pb, Cd, Ni and Hg. Therefore, UU have a great interest in meeting the criteria of these legislations for clean water; especially as the targets set in the WFD and the DWD will become requirements in 2016.

The research carried out here utilised three types of nanosensing techniques: citrate functionalised AuNPs and AgNPs for LSPR absorption spectroscopy; citrate functionalised AuNPs for a SERS-based sensing technique; and the development of an original CuS ion-exchange NC, for the selective detection of Hg within a mixed-metal solution.

Following this overview, there is a short introduction into global pollution, covering atmospheric pollution, soil, and water based pollution. They will contain lists of

common pollutants, sources and health effects, and examples of current analytical techniques to detect the listed pollutants. Continuing on from this will be an overview of water-based metal pollutants, leading into the background behind the WFD and the DWD. There will then be a discussion on the current standard analytical practices used for the quantitative detection of metals in aqueous media. Penultimately, the limitations of these techniques will be discussed leading to the motivation behind using nanosensors for the detection of metals. Finally, the remaining structure of the thesis will be described.

1.2 The State of Chemical Pollution on a Global Scale

With the increase in chemical use by industry and society, there is a growing awareness and subsequent concern about the chemicals released into the environment. The scientific community defines chemicals released into the environment as one of two terms: contaminants or pollutants.

- Contaminants are chemicals present in a sample, where there is no evidence that those chemicals will cause any harm.
- Pollutants are chemicals that are present in a sample, where there is evidence that those chemicals can cause harm.

As this study is set around chemical pollution, a more detailed definition can be included: Principally, pollution involves a change to an environmental system. In the public eye, the most recognizable origin of this change is chiefly attributed to chemical pollution by manufactured chemicals (pesticides, dyes, medical waste etc.); but in addition to manufactured chemical pollution, there are many naturally occurring pollutants e.g. leaching of toxic metals from natural clays and sediments, the release of metals from the natural erosion of soils etc.¹

Chemical pollutants can be categorised into two main groups: organic and inorganic chemical pollutants.

Table 1.1 lists some examples of organic pollutants, and Table 1.2 gives several examples of inorganic pollutants.

Table 1.1 A list of examples for organic pollutants and potential sources of discharge into the environment

Organic Pollutants	Sources
Detergents	The social used of detergents which are then discarded down domestic drains
Pesticides	Farmland runoff
Volatile organic compounds	Discarded industrial solvents
Drug pollution	Pharmaceutical drugs from hospitals or domestic sewerage

Table 1.2 A list of inorganic pollutants examples and potential sources of discharge into the environment

Inorganic Pollutants	Sources
Sulfur dioxide	Power plant emission
Phosphates and nitrates	Fertilisers used on farmland that can be introduced to waterways through runoff
Heavy metals	Motor vehicle discharge which can be introduced to aquatic systems by inner city drainage and runoff
	Erosion of lands by wind and water, or leaching from soils and sediments

1.2.1 A contemporary look at atmospheric pollution

Atmospheric pollution is a major environmental problem, in both developing and developed countries. Some of the health problems associated with atmospheric pollution are heart disease, increased risk of stroke, and lung cancer. In 2008, around 127 million people inhabited countries exceeding the acceptable levels of atmospheric pollutants.³ A 2013 report by the WHO estimates that in 2012 there were 3.7 million deaths related to atmospheric pollution.⁴ The World Health Organisation (**WHO**) has set standards for the acceptable levels of atmospheric chemical pollution (Table Table 1.3), to help combat chemical pollution and its related effects on the environment and health.² Major chemical pollutants found in

the atmosphere include particulate matter, volatile organic compounds (**VOCs**), ozone (O_3), nitrogen dioxide (NO_2), and sulfur dioxide (SO_2).²

Table 1.3 World Health Organisation guideline values and health implications of common atmospheric pollutants^{2,4}

Pollutant	Guideline Values	Examples of Sources	Health Implications
Particulate Matter			
PM_{2.5}	10 $\mu\text{g}/\text{m}^3$ (Annual Mean)	Household coal, agricultural waste incineration, forest fires	Cardiovascular and respiratory diseases including lung cancer
	25 $\mu\text{g}/\text{m}^3$ (24-Hour Mean)		
PM₁₀	20 $\mu\text{g}/\text{m}^3$ (Annual Mean)		
	50 $\mu\text{g}/\text{m}^3$ (24-Hour Mean)		
Ozone (O₃)			
	100 $\mu\text{g}/\text{m}^3$ (8-Hour Mean)	Formed from the photochemical reaction of pollutants such as: nitrogen oxides (NO _x) from vehicle and industry emissions and volatile organic compounds (VOCs) emitted by vehicles	Breathing problems, asthma, reduce lung function and lung diseases
Nitrogen dioxide (NO₂)			
	40 $\mu\text{g}/\text{m}^3$ (Annual Mean)	Power Stations, engines in vehicles, and nitrate aerosols in the presence of ultraviolet light and ozone	Bronchitis in asthmatic children, and reduced lung function
	200 $\mu\text{g}/\text{m}^3$ (1-Hour Mean)		
Sulfur dioxide (SO₂)			
	20 $\mu\text{g}/\text{m}^3$ (24-Hour Mean)	Burning of fossil fuels (coal and oil) and the smelting of sulfur containing mineral ores	Irritation of the eyes, inflammation of the respiratory tract, aggravation of asthma, chronic Bronchitis, infections of the respiratory system
	500 $\mu\text{g}/\text{m}^3$ (10-Minute Mean)		

Particulate matter, in the sense of chemical pollution, is classified as particles with a diameter of $\geq 10 \mu\text{m}$. It can be composed of chemicals such as minerals, sodium chloride, and black carbon from burning.² Inhalation of these particles can lead to chronic or acute health issues, especially lung cancer, which particulate pollution is most associated.⁴

Additionally, industrial and vehicle emissions are an obvious source of chemical pollution. These sources introduce volatile organic compounds into the atmosphere. These compounds, along with NO_2 , can react with sunlight, and aid in the production of O_3 .² Health problems arising due to O_3 exposure are still under debate, but the part that O_3 has to play in atmospheric mechanisms is well known. One issue is that O_3 catalyses the reaction between SO_2 and water in the atmosphere, producing sulphuric acid (H_2SO_4). This precipitates as acid rain. Acid rain is a persistent 'hot topic' within political, scientific, and public interests, with its formation and post-precipitation mechanisms contributing significant damage to the environment and human health.

1.2.2 *The chemical pollution of soil*

Chemical pollutants in soil can be in the form of either solid or liquid chemicals. Soils become contaminated by such mechanisms as the deposition of airborne pollutants (such as acid rain), public agriculture (toxic metals, pesticides and phosphorous), through chemical waste buried directly into the soil (breakdown of landfill components), migration and deposition of chemicals via groundwater and flowing water (agricultural waste, mining).^{5,6} In addition to these examples, soil can also contain naturally occurring chemical pollutants such as metals, such as arsenic, which can be absorbed by edible plants leading to the potential bioaccumulation of toxic chemicals in the food chain.

Ill-famed, naturally occurring heavy metals found in soils are arsenic, lead cadmium, nickel, mercury etc.^{7,8} Heavy metals are toxic to animals and humans. Some of its health issues include cancer, loss of hearing, gangrene, serious neurological conditions, memory loss, and death.⁷⁻¹⁰ Cadmium and arsenic are commonly found in tobacco plants, with smokers taking in, on average, 2 –10 *ppb*

of arsenic. Compost, sludge, lime and fertilisers are used by many countries to improve soil fertility and to maintain the production of crops. These inputs introduce such chemicals as heavy metals and phosphorous to soil systems.

Heavy metal pollutants in soils can also enter aquatic systems via mechanisms of leaching or sedimentation, whereby chemicals migrate from soil systems into aquatic systems or from overflow and run-off.¹¹

1.2.3 An Introduction to the chemical pollution of aquatic systems

Chemical pollutants can enter aquatic systems in many ways (Figure 1-1). Acid and other acid forming pollutants released from coal burning power stations and deposited on the surface of the earth by such mechanism as *acid rain* (Section 1.2.1) can change the chemical and physical properties of soil and aquatic systems. This can have destructive consequences.¹

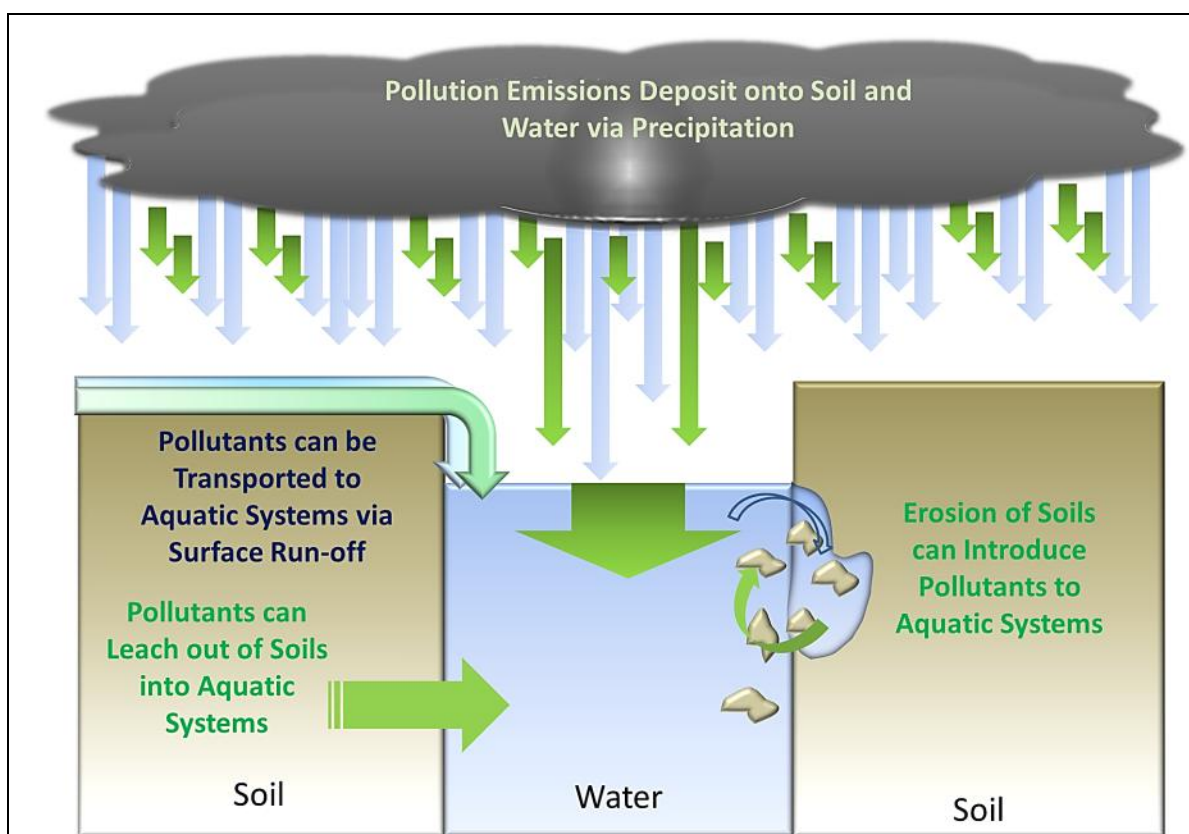


Figure 1-1 The major mechanisms which can lead to pollutants entering aquatic systems are from surface deposition via precipitation of atmospheric pollutants, surface run-off, leaching of chemicals from soils, and erosion

Sediment is one of the most common sources of water pollution. Every year water sources in the United States are polluted by over 1 million tons of sediment.¹² Sediment consists of mineral or organic solid matter that can be washed into water sources, or even carried from the land by erosion or natural materials by the wind. Some of the main sources of sediment pollutants originate from construction sites, agricultural and livestock, erosion, and city runoff. The heavy metals lead (Pb), zinc (Zn) and copper (Cu), are frequently found in roadside dust and soil because of the increase in vehicle use around the globe – especially in industrious areas, where there is a great need for transport of materials.^{6,11} Respectively, these toxic metals are commonly found in leaded petrol, tire treads and as a side product of the oxidation of lubricating oil that forms metal corrosive acids.⁶

Additionally, significant contributions to the chemical pollution of aquatic systems originate from the domestic use of chemicals. Household cleaners, dyes, paints and solvents are toxic and can build-up when they are disposed down drainage systems. Common household pesticides and herbicides can also leach into aquatic systems making it undrinkable *i.e.* one drop of 2,4-Dichlorophenoxyacetic acid (a common household herbicide) can make 10 million litres of water unfit for drinking.¹²

Water has the natural ability to clean itself of pollutants. Mechanisms such as sedimentation, chemical break-down of organic and organometallic chemicals, and dilution reduce the potential harmful effects of chemical pollutants. But these natural mechanisms are relatively slow, and large amounts of pollutants can go beyond the capacity of these natural cleaning mechanisms. Unless the chemicals are rapidly degradable they can remain present for weeks or even years. Subsequently, this can lead to a build-up of pollutants which can result in harm to the environment and the health of wildlife and humans.⁷⁻¹⁰ This is a persistent problem when it comes to heavy metal pollution as unlike the organic pollutants, metals cannot be degraded.

1.2.4 Mechanisms involved in the pollution of aquatic systems with heavy metals and their compounds

Unlike the organic pollutants, metals cannot be degraded. However, the mobility and toxicity of metals can be reduced by mechanisms such as adsorption and precipitation.

Infamous problems linked with long-term exposure to certain heavy metals range from adverse effects on the brain from lead and mercury; kidney and liver problems from metals such as cadmium; skin poisoning, kidney and central nervous system problems from arsenic.⁷⁻¹⁰ Heavy metal pollutants have been shown to have serious consequences: Low-dose exposure to mercury can cause severe and sometimes lifelong behavioural and cognitive problems.¹³ A study carried out in 2002, led by paediatrician *Philip J. Landrigan* at the Mount Sinai School of Medicine, found chemical pollution is responsible for all lead poisoning cases in the US.¹⁴ Research carried out in 2000 shows that lead can damage the infant brain at blood levels as low as 50 $\mu\text{g/l}$.¹⁰ These examples demonstrate the importance of heavy metal pollution control and detection with respect to human health issues.

When in soil, the metals cadmium, nickel, lead and mercury (Cd, Ni, Pb, and Hg) can be transformed to alternative oxidation states. This can reduce their mobility and toxicity. Immobilisations of metals by adsorption and precipitation mechanisms prevent leaching of the metals into ground water. Though, changes in soil system conditions such as:¹

- changes in pH
- changes in redox potential
- soil solution composition
- natural weathering processes

These may all increase metal mobility.¹⁵ Mobility of these heavy metal pollutants increases the concentrations of the heavy metals in aquatic systems.

The oxidation state of these heavy metals affects their toxicity thus affecting the potential for toxic effects to animals and humans. Also, heavy metal oxidation states affect mobilisation and thus the concentration of the metal in an aquatic system. Mobility of heavy metals can also be affected through binding with organic chemicals in aquatic/soil systems.¹ This production of organometallics can also reduce or increase their toxicity.¹⁶

1.3 The Water Framework Directive and the Drinking Water Directive

The European health commission has defined 'acceptable' concentration levels for many heavy metals commonly found in aquatic systems. The objectives of the Water Framework Directive (WFD) include the aim to achieve 'good chemical status' for surface water bodies by 2015.¹⁷ These objectives led to Article 16 of the WFD (2000/60/EC) which sets out a *Strategy against pollution of water*.¹⁷ This strategy is being implemented to reduce the level of hazardous substances in aquatic systems.

The first step was to establish a *First List of Priority Substances*: Directive 2008/105/EC of the European Parliament and the Council on Environmental Quality Standards in the field of water policy list 33 substances or group of substances to be included in this strategy.¹⁷ Within this list 11 substances have been identified as priority hazardous and a further 14 substances were identified as being subject to review - Hazardous substances typically include pesticides, solvents, hydrocarbons, and heavy metals.¹⁸

Table 1.4 Acceptable metal levels for a selected group of metals, which was set by the 2008/105/EC priority substance list¹⁷	
Monitored Metal	Acceptable Quality levels (µg/l)
Pb	7.2
Ni	20
Cd	0.2
Hg	0.05

As well as the WFD, there is another directive related to water pollution: the DWD. The DWD is a set of quality standards for microbiological, chemical and

organoleptic concentrations in drinking water – measured from the tap. The acceptable levels of microbiological, chemical and organoleptic concentrations in drinking water were set in *Council Directive 98/83/EC*.¹⁹ Of this list, cadmium, mercury, nickel, and lead are heavy metal substances which have defined acceptable limits in drinking water according to Directive 98/83/EC (Table 1.5 Acceptable heavy metal levels set by Directive 98/83/EC – the Drinking Water Directive).

Table 1.5 Acceptable heavy metal levels set by Directive 98/83/EC – the Drinking Water Directive¹⁹	
Chemical	Acceptable Limits ($\mu\text{g/l}$)
Pb	10
Ni	20
Cd	5
Hg	1

1.4 Analytical Techniques for the Quantitative Determination of Metals in Aqueous Media

In aquatic systems, metals can exist in organometallic and inorganic forms but they can also exist in an immobile state, trapped in a matrix. This means that a suitable analytical technique needs to be selected to determine the total concentration of the target metal in the acquired sample; but in addition to the final analysis step, there are several vital prerequisites pertaining to the storage, transport and separation of the metal forms in the aqueous sample.²⁰ This chapter covers some of the most common analytical techniques used for the quantitative determination of metals in aqueous samples.

1.4.1 Analytical Procedures for the Determination of the Concentrations of Aqueous Metals

After obtaining the aqueous sample, the first problem encountered is retaining the integrity of the sample to reduce errors in the final analytical results. A major consideration is sample storage. The material used for sample storage must be considered: materials that contain the target metal must, understandably, not be used; certain plastics can lead to the adsorption and absorption of some metals e.g. mercury can leach through some plastics.²⁰ It has been recommended that

the sample is collected in a polyethylene bottle, filtered through a 0.45 μm filter and stored at 4⁰C.²⁰

Due to the low concentrations of metals found in aquatic samples, a preconcentration procedure is often required. Of the available techniques, liquid-liquid extraction is reported to yield the best results with preconcentration factors of >100 being possible.²⁰ A further advantage of this technique is that it can remove most of the matrix found within the sample.²⁰

Liquid-liquid techniques are used for the extraction of organometallics and inorganic forms of a target metal. These procedures involve the extraction of the organometallics into a suitable organic solvent; whereas for the inorganic forms the selective complexation of the target metal is achieved and subsequent extraction of the formed complex is carried out using an appropriate solvent. The most widely used complexes employed to achieve complexation with the inorganic forms of the target metal are the dithiolcarbonates.²⁰

Liquid-solid extraction is also widely used for the preconcentration of metals. This method involves passing the sample through a column containing a solid material, suitable for the removal of the target metal. Such materials can be anion or cation exchange resins, adsorbate materials like alumina, silica gel or fine particle coated in organic molecules.²⁰

After the storage and preconcentration steps, the samples may be analysed. The most commonly used analytical techniques for the trace analysis of metals include potentiometry, voltammetry, atomic spectrometry, X-ray, and nuclear techniques.^{21,22} The most commonly available analytical methods all have comparable advantages and disadvantages. Table 1.6 is a summary of some of the properties of the most commonly used analytical methods for trace metal analysis.²¹

Table 1.6 A table of specifications for commonly used analytical techniques for the detection of heavy metals (adapted from²¹)

Technique	Directly Measurable Analytes			Detection limit
	Free Ions/Elements	Ions/Elements in Labile complexes	Total Elemental Concentration	
Potentiometry	✓	×	×	10 ng/l -10 µg/l
Voltammetry	✓	✓	×	1 ng/l -0.1 µg/l
Atomic Spectroscopy	✓	✓	✓	0.1 ng/l -0.1 µg/l
X-ray Techniques	×	×	✓	1 ng/l - 0.1 µg/l
Nuclear techniques	✓	✓	✓	1 pg/l - 1 ng/l

1.4.2 Potentiometric Analysis

Potentiometric analysis uses electrochemistry to determine the concentration of free ions and elements (Table 1.6). The technique is based upon the determination of the voltage difference between two electrodes, without the application of a current, placed in a sample solution (Figure 1-2). These two electrodes are referred to as the *external reference electrode* and the *working electrode* (here, this electrode is an *ion-selective electrode*, which will be used to determine the concentration of a pre-selected ion), respectively.²²

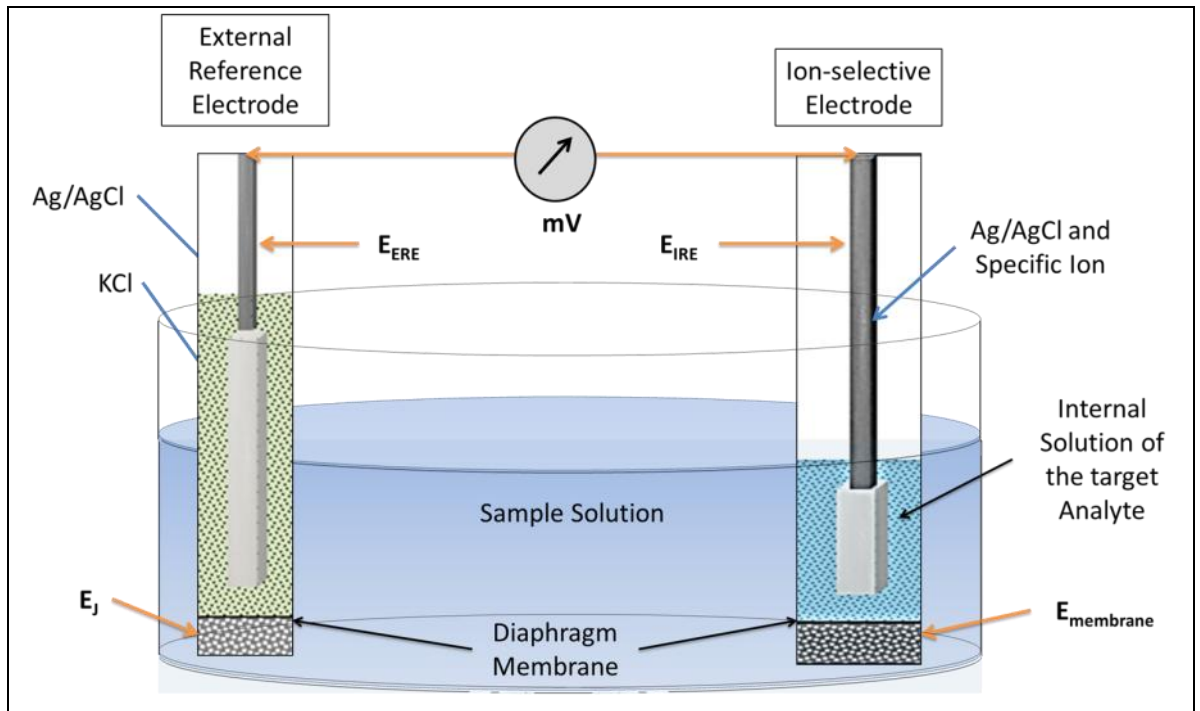


Figure 1-2 An example of a standard set-up for the potentiometric determination of a target ion

The potential of the reference electrode is independent of the concentration of ions within the solution; whereas the potential of the ion selective electrode is dependent upon the concentration of a particular ionic species.^{22,23} The ion selective electrode consists of an *internal reference electrode*, which is placed in a reference solution containing the target ion. This electrode is separated from the sample solution by an ion selective membrane *i.e.* only the target ion will pass through the membrane. In Figure 1-2, E_J represents a small potential junction, created as ions permeate through the membrane of the external reference electrode - this is usually minimised by using a saturated solution of potassium chloride (KCl); whereas $E_{membrane}$ represents the potential of the membrane of the ion-selective electrode, and is dependent on the activity of the target ion in the sample solution. This potential across the membrane is described by the *Nernst equation* (Equation 1.1).²³ Here R is the *ideal gas constant*, F is Faraday's constant, and z is the charge of the target ion whose activity is a .

$$E_{membrane} = 2.303 \frac{RT}{zF} \log \frac{a_{solution}}{a_{reference}}$$

Equation 1.1 The Nernst equation²²

The cell potential is then measured as $E_{cell} = E_{IRE} + E_{membrane} - E_{ERE} + E_j$. The terms E_{IRE} and E_{ERE} are independent of the concentration of the target ion and do not vary during the measurement and E_j is minimised by the saturated KCl solution, as stated above. As the activity of the target ion is constant inside the ion-selective electrode and the membrane is, hopefully, only permeable for the target ion, the cell potential is dependent on the activity of the target ion in the sample solution ($a_{solution}$). This leads to an altered Nernst equation (Equation 1.2).

$$E_{cell} = E' + 2.303 \frac{RT}{zF} \log a_{solution}$$

Equation 1.2 The altered Nernst equation²²

Here E' is the standard potential of the cell. The activity of the target ion is related to the concentration of the target ion by $a = \gamma C$, where γ is the activity coefficient. Variations in γ can be reduced by using an ionic strength adjustment buffer. This means that the potential of the cell now depends on the concentration of the target ion.²² The concentration of the target ion can now be realised with the use of calibration plots of standard solutions.

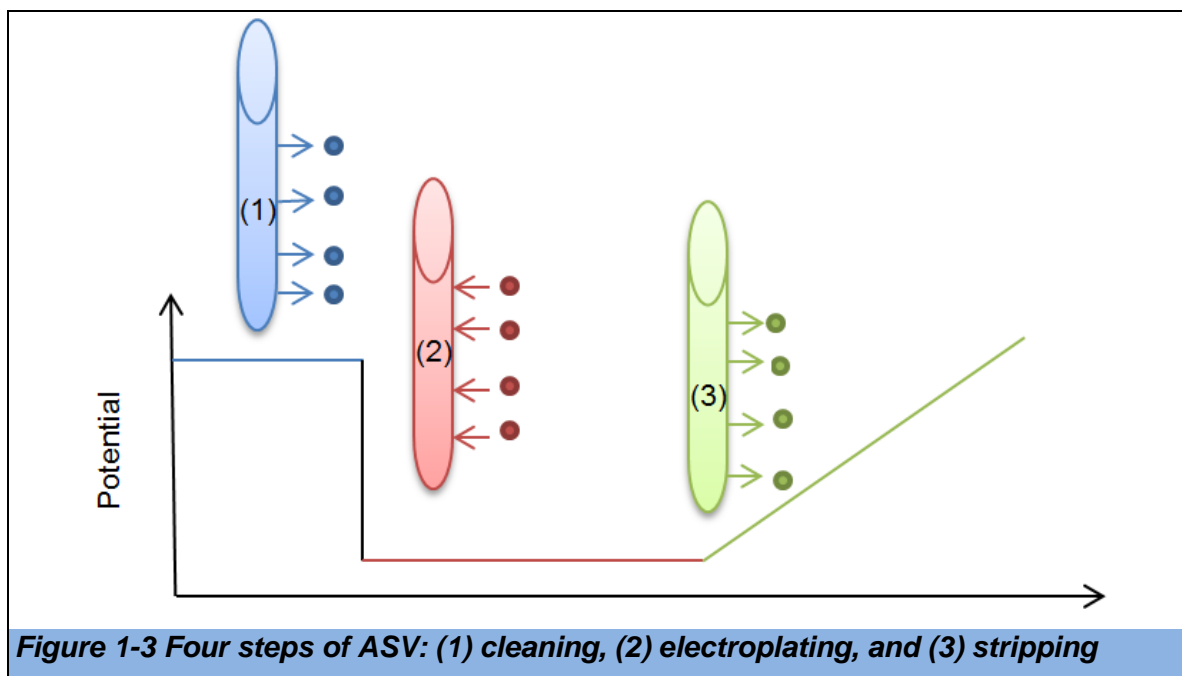
Potentiometric sensors have the advantage that it is low in cost. They also have the disadvantage of being able to detect only free ions and elements.²¹ This can be a benefit when one wants to detect free ion and elemental concentrations, but potentiometry cannot be used to determine concentrations of complexed ions – unlike anodic stripping voltammetry. Potentiometry also suffers interference from competing ions which can also reduce the accuracy of this technique.²¹

1.4.3 Anodic Stripping Voltammetry

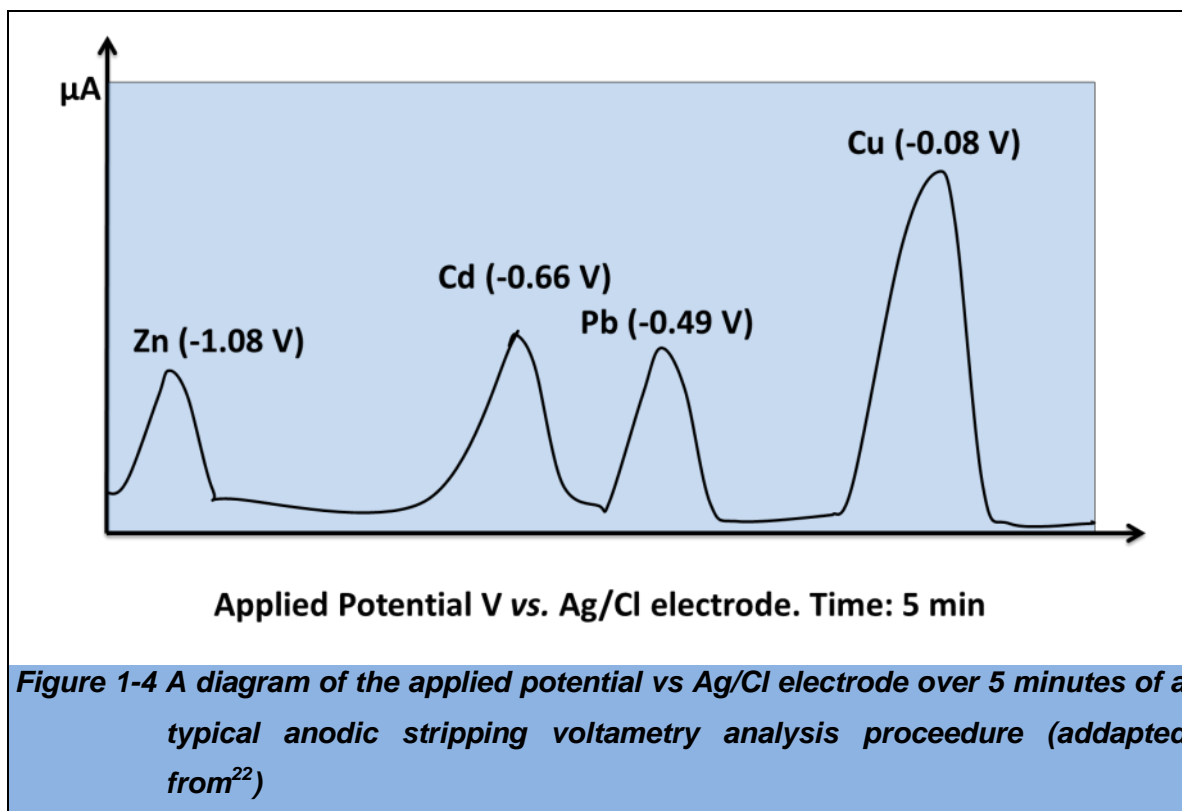
The well-established technique of anodic stripping voltammetry (**ASV**) has been used in trace element and ion detection. The sensitivity of voltammetry methods can be greatly increased by using a pre-concentration, or accumulation step which is fundamental to stripping voltammetry. In this step the element and or ion is accumulated at the electrode by either an attractive accumulation, or by natural

absorption onto the electrode's surface.^{21,22} The analytical signal is then generated by the subsequent voltammetric stripping step.

There are four steps to ASV; these include (1) cleaning, (2) electroplating, and (3) stripping (Figure 1-3).



The cleaning step uses a highly positive potential to clean the electrode. Because the potential is highly positive, the ions – in the case of metal ions, these are also positive – are stripped and the electrode becomes 'clean' of any analyte.²⁴ Electroplating is the process of building up a layer of analyte on the electrode by reducing the potential; the reduced potential will attract the analyte to the electrode's surface.²⁴ The stripping step can be described as desorption of the analyte which produces a change in the measured current relative to the amount of accumulated/absorbed element or ion.^{21,24}



Compared to potentiometric analysis, voltammetry can be more expensive but can provide a lower detection limit.²¹ This is advantageous for detecting lower concentrations of ions/elements. As voltammetry analysis uses a pre-concentration step, the technique has the advantage of being able to detect free ions and elements as well as complexed ions, whereas, potentiometric analysis cannot detect complexed ions.²¹ Although, using voltammetric analysis has the disadvantage of interferences from competing ions which can reduce the accuracy of the method.²¹

1.4.4 Atomic Spectrometry

Flame atomic absorption spectrometry (**FAAS**) uses a flame in which a liquid sample is introduced. The sample then dissociates to its constituent atoms (atomisation). UV/Vis electromagnetic radiation is focused through the flame and certain wavelengths are absorbed corresponding to the atoms present in the sample.²¹ FAAS is relatively inexpensive and simple to operate and suffers from little interference. However, some elements cannot be determined with good sensitivity as the flame temperatures used are often not hot enough to cause complete atomisation.²¹ Trace levels of B, W, Ta, Zr, As and Sn may not be determined by FAAS because of this reason.²¹

Graphite furnace atomic absorption spectrometry (**GFAAS**) is different from FAAS in that GFAAS uses a much higher atomisation temperature (up to 3000 K), and both solid and liquid samples may be analysed.^{21,22} It exhibits limits of detection (**LOD**) 10–100 times lower than those of FAAS.²¹ Despite this, some elements can still be difficult to analyse with acceptable precision.

Although, GFAAS produces better detection limits than FAAS and ICP-AES, a disadvantage is that it is only suitable to detect certain ions/elements (around >50), whereas, FAAS and ICP-AES can detect >63 and >73 ions/elements respectively.^{21,25} In addition, a major disadvantage is that GFAAS suffers from more interferences compared to FAAS and ICP-AES techniques.^{21,25}

1.4.5 Inductively Coupled Plasma Techniques

Inductively coupled plasma (**ICP**) techniques are one of the most widely used analytical techniques utilising atomic emission spectrometry for trace metal analysis.^{21,22,25,26} During these techniques liquid samples are ionised in argon plasma and then the products are detected by atomic emission spectroscopy (ICP-AES) or mass spectrometry (ICP-MS). Both techniques are reliable for detecting trace concentrations of elements, though mass spectroscopy has higher sensitivity (Table 1.7).²⁵

Table 1.7 Table of standard limits of detection for elemental analysis of metals by inductively coupled plasma²⁴

Metal	ICP-AES (Radial) (ppb, $\mu\text{g/l}$)	ICP-AES (Axial) (ppb, $\mu\text{g/l}$)	ICP-MS (Quadrupole) (ppt, ng/l)
Cd	1	0.1	0.01-0.1
Cr	2	0.4	0.1-1
Cu	2	0.3	0.1-1
Fe	1	0.3	0.1-1
Hg	9	1.2	1-10
Mg	0.1	0.03	0.1-1
Ni	6	0.4	0.1-10
Pb	14	1	0.01-0.1

Although the LODs are very low, a disadvantage of trace analysis using ICP techniques is that they are relatively more expensive to run than less sensitive methods.²¹

1.4.6 X-Ray Fluorescence and Total Reflection X-Ray Fluorescence

A commonly used technique in the area of elemental analysis is X-ray fluorescence (**XRF**). This technique can be used to analyse almost any element from Na to U.²¹ The sensitivity of XRF is dependent on the energy of the incident radiation, the geometry of the instrument used and efficiency of the detector.²¹ The achievable LOD depends on the sensitivity of the instrument and background level of the sample matrix.²¹ Samples often need to be in the form of a thin film for these techniques; this is useful as matrix effects do not usually play a significant role on affecting the sample signal which would create errors in the results.²¹ A calibration curve is established that is presumed to be valid for all matrices of the trace element being detected. When using state-of-the-art instrumentation for XRF, typical LODs of a few $\mu\text{g/cm}^2$ can be achieved.²¹ But unfortunately, compared to

the other trace analytical techniques, relatively large systematic errors can arise due to the calibration methods.²¹

In total-reflection X-ray fluorescence (**TXRF**), the incoming radiation is incident on the sample at an angle which is less than the *critical angle*. This produces totally reflected radiation. This greatly improves the LOD achievable: Where LODs down to as low as 2 $\mu\text{g}/\text{cm}^2$ may be detected.²¹ The improved LODs available are due to the low background levels that the used geometry produces which makes less intense peaks more visible.²¹

Both XRF and TXRF are relatively expensive compared to the other trace analysis methods discussed so far but they can detect lower amounts of trace elements in any matrix. This can be useful for environmental heavy metal analysis as heavy metals can be present in many organic matrix forms.

1.4.7 Neutron Activation Analysis

Neutron activation analysis (**NAA**) uses neutrons to irradiate the sample to be analysed.²¹ As a result of a nuclear reaction between the neutron and the element of interest, radioactive isotopes are formed. These isotopes emit radiation of varying energies that can be measured by a detector. The measured radiation energies can then be assigned to the elements in the sample; a signal of the element to be detected can be recognised as these isotopes have well-known characteristic signals.²¹ This technique has been shown to produce LODs from 10 - 100 $\mu\text{g}/\text{l}$; but in a monetary sense, this technique is very expensive.²¹

1.5 The Problems Associated with Current Methods of Heavy Metal Analysis

1.5.1 The Cost of Analysis and Limit of Detection

In section 1.2 it was shown that voltammetry, atomic spectroscopy and nuclear techniques can be seen to be the only standard techniques that can detect metal ions in the free and labile form; but unlike voltammetry, atomic spectroscopy and nuclear techniques have the advantage of being able to detect the total elemental concentration of a sample. A further advantage of atomic spectroscopy and nuclear techniques is their low LOD.

Metal concentrations in environmental systems can be on the order on *ng/l*. When looking at the acceptable concentration levels for metals, set by the DWD and WFD, it can be noted that these values are in the *ng/l* to $\mu\text{g/l}$ range. ICP-AES is suitable to detect concentrations within this range, except Hg which would require ICP-MS (Table 1.8).

Table 1.8 Acceptable concentrations set by the DWD and WFD, for the metals used in this study and the instrumental analysis needed to detect them				
Metal	ICP-AES (Radial) ($\mu\text{g/l}$)	ICP-AES (Axial) ($\mu\text{g/l}$)	ICP-MS (Quadrupole) (<i>ng/l</i>)	Lowest Acceptable Concentrations from the DWD and WFD ($\mu\text{g/l}$)
Cd	1	0.1	0.01-0.1	0.2
Hg	9	1.2	1-10	0.05
Ni	6	0.4	0.1-10	20
Pb	14	1	0.01-0.1	7.2

An economic downfall of the instrumental techniques needed to achieve such low limits of detection, within the *ng/l* to $\mu\text{g/l}$ range, is their expense. ICP-AES and ICP-MS techniques are relatively expensive, but the LODs achievable are perfect for the detection of metals within the *ng/l* to $\mu\text{g/l}$ range. Below is a table showing examples for the purchase and operating costs for ICP-AES and ICP-MS instruments.

Table 1.9 Purchase and operating costs of standard heavy metal analysis instruments/equipment²⁶		
Instrument/ Equipment	Purchase Price (Rounded to the nearest £1000)	Annual Operating Costs (Rounded to the nearest £1000)
ICP-AES	£32000– £64000	£4000
ICP-MS	£83000-£120000	£9000

Additional cost may be incurred, depending on the distance the sample must travel; this would add further costs such as fuel and vehicular maintenance, making the process even more expensive.

1.5.2 *Time-Scale of Analysis*

A further disadvantage of these techniques is due to the fact that water samples need to be transported to the place of the instrument, which could be time consuming. Further processing steps may be required, such as pre-concentration procedures. All of these factors are time consuming. This would be an issue if the sample was required urgently, possibly due to an ensuing environmental issue. To combat this, some instruments have been developed to test aqueous metal concentrations at the site where the water sample will be taken (Table 1.10).

Table 1.10 *A list of some current instruments that can analyse water samples at the site and the metals that they can analyse which are included in this study*

Instrument	Elements that can be Analysed from the WFD and DWD Priority Lists	Detection Specifications
Colorimeter II Test Kit²⁷	Pb	5 - 150 $\mu\text{g/l}$ (LOD)
	Ni	0.01 – 1 mg/l (LOD)
Portable PDV6000plus²⁸	Cd, Pb, Hg, Ni	10 $\mu\text{g/l}$ (Sensitivity)

The limits of detection for the Colorimeter II Test Kit is suitable for detect Pb and Ni in the range deemed 'acceptable' by both the DWD and WFD. The Portable PDV6000plus, on the other hand, will be able to measure Pb and Ni concentrations at the 'acceptable concentration' set by the WFD, but it fails to meet the levels set by the DWD for all of the other metals used in this study.

1.6 *Summary of standard Analytical Techniques & Motivation for Nanosensors*

To summarise:

- Though ICP-AES and ICP-MS analysis techniques provide adequate LOD ranges to detect metals in aquatic systems, at concentrations within the

acceptable limits set by the DWD and WFD, they are relatively expensive techniques.

- ICP-AES and ICP-MS analysis techniques also require sample transport from the site of the water to be tested, which can also lead to extra costs.
- From Table 1.10, the Colorimeter II Test Kit is the only instrument suitable to detect Pb at the levels set by the DWD and WFD.
- The Portable PDV6000plus is only suitable to detect Pb and Ni at the concentrations at levels set by the DWD and WFD

The above sections describe the downfalls of the standard analytical techniques currently used for the detection of the aqueous metals listed in the WFD and DWD. They highlight the motivation for the research and development of novel sensing techniques, to selectively detect aqueous metals, with LODs comparable to standard techniques, but, which are relatively cheaper, faster and with a lower limit of detection.

One of the most promising branches of research is the area of *nanosensors*, and the highlighted issues above are a constant driving force for their commercial development. Chapter 2 will cover the background theory behind the use of two of the main types of nanosensors used for the detection of metal ions in aqueous samples, and the materials used within this study: *localised surface plasmon resonance (LSPR)* and *surface enhanced Raman spectroscopy (SERS)*. A third branch of materials, semiconductor nanomaterials, will also be cover as a background to the development of the CuS ion-exchange technique developed within this study.

1.7 The Structure of this Thesis

This thesis is structured in the following way:

Chapter 1 is an introduction to water pollution and the WFD and DWD. It also describes the current standard analytical methods employed for the detection of metals in aqueous media. This chapter concludes with a critical analysis of the current procedures and proposes the usefulness of nanosensors for the detection of aqueous metals.

Chapter 2 comprises of a literature review on current nanosensor technology for the detection of metals. This chapter will concentrate mainly on LSPR and SERS based sensing, and an introduction to the current use of semiconductor nanomaterials for sensing purposes. There will then be a specific discussion on the materials chosen for this study, their design and expected results.

Chapter 3 consists of the experimental methodology and technique used in this study. It will describe the materials used, synthetic and preparatory procedures for the material samples, instrumental analysis methods, computational processes used, and data analysis approaches employed.

Chapter 4 is the first of 3 results and discussion chapters. It contains the experimental data for the study of citrate functionalised Au and Ag NPs for the detection of aqueous Pb and Hg, respectively. It will provide detailed information on the results and the leading physical and molecular mechanisms involved. This chapter will end with a critical analysis of the citrate functionalised NPs for sensing purposes.

Chapter 5 is a report on the SERS-based sensor which was developed in this study for the detection of Pb. There will be a detailed analysis of the results and the underlying mechanisms behind them, most notably the evolution of the SERS spectrum with the increased concentration of Pb. Mathematical models will be developed from the spectroscopic data to provide useful equations for the practical application of this sensor. The method will then be compared to standard analytical techniques.

Chapter 6 is dedicated to the results obtained for the new CuS ion-exchange nanosensor. A thorough analysis of the data will be performed and the spectroscopic progression, with the increase in Hg, will be evaluated.

Chapter 7 contains the preliminary results for the progression of the NC ion-exchange based sensor, using ZnS as the NC material, incorporated into an absorbent material. This idea involves the use of this absorbent material as a TLC-style sensor.

Finally, this thesis finishes with a conclusion of the work carried out for this project and an evaluation of the potential for furthering the work carried out here.

2 Nanosensors: A Literature Review

2.1 Introduction

This study focuses on the use of nanomaterials as sensors, for the detection of metals in aqueous media; specifically those listed in the WFD and DWD as 'priority substances'. The nanomaterials that were selected for this study can be separated into two groups: plasmonic nanoparticles and semiconductor nanoclusters (**NCs**). The plasmonic materials that are discussed in this research were used in two separate sensing techniques: *localised surface plasmon resonance (LSPR)* based sensing and *surface enhanced Raman spectroscopy (SERS)*. This literature review discusses the relevant theory needed to understand the results presented here. It also contains a review of some of the current plasmonic nanomaterial sensors that can be found within the literature, as means as a comparative discussion in the final conclusions of this thesis.

The idea for the use of the CuS NCs was adapted from ion-exchange synthetic techniques used in the production of custom semiconductor materials. The techniques used in the synthesis and utilisation of these NC sensors present a new nanosensor for the selective detection of metals in aqueous media. As this novel method uses adaptations from different sources and theories, it will be covered in detail in Section 2.8. A section in this literature review will be devoted to current semiconductor NP sensors for the detection of metals, as the use of NCs is not common within the literature for sensing purposes; although, the manipulation of optical properties of SC quantum dots is a well-studied area.

2.2 Nanotechnology for the Detection of Metals

Nanomaterials are now widely integrated into the research areas of chemical sensing.³⁰⁻³⁴

The ultimate factor for the current success of nanomaterials for sensing applications is their controllable chemical and physical properties. Varying the

chemical composition, size, and even the shape of nanomaterials control these properties, leading to fully customisable materials.³⁵ Novel effects can include:

- high surface area to volume ratios
- visible photon absorption
- conductivity
- magnetism
- visible photon emission

All of these have been applied to chemical sensing practices.^{30,31,33,36,37}

These properties are not always evident in the corresponding bulk material.^{30,35} Predominantly, the confinement of electrons at the nanometre scale is the cause of changes to material properties, when comparing bulk crystalline materials and their nanomaterial counterpart. Controlling the confinement of the electrons is achieved by controlling the chemical composition, size and shape of the nanomaterial.³⁵ Widely used nanoparticle materials include noble metals such as gold, silver and copper, and semiconductors such as ZnS, InP and CdSe.³⁸⁻⁴¹

Many noble metal nanoparticles famously exhibit the phenomenon LSPR. It has been shown to be useful for many sensing applications, including the analysis of metals, utilising such techniques as *LSPR absorption spectroscopy* and SERS (Sections 2.4 and 2.5).^{30,42,43} Additionally, many semiconductor nanomaterials are used in chemical sensing due to many possessing optical absorption and fluorescence properties that are highly sensitive to changes in the electronic structure of the nanomaterial.⁴⁴⁻⁴⁶

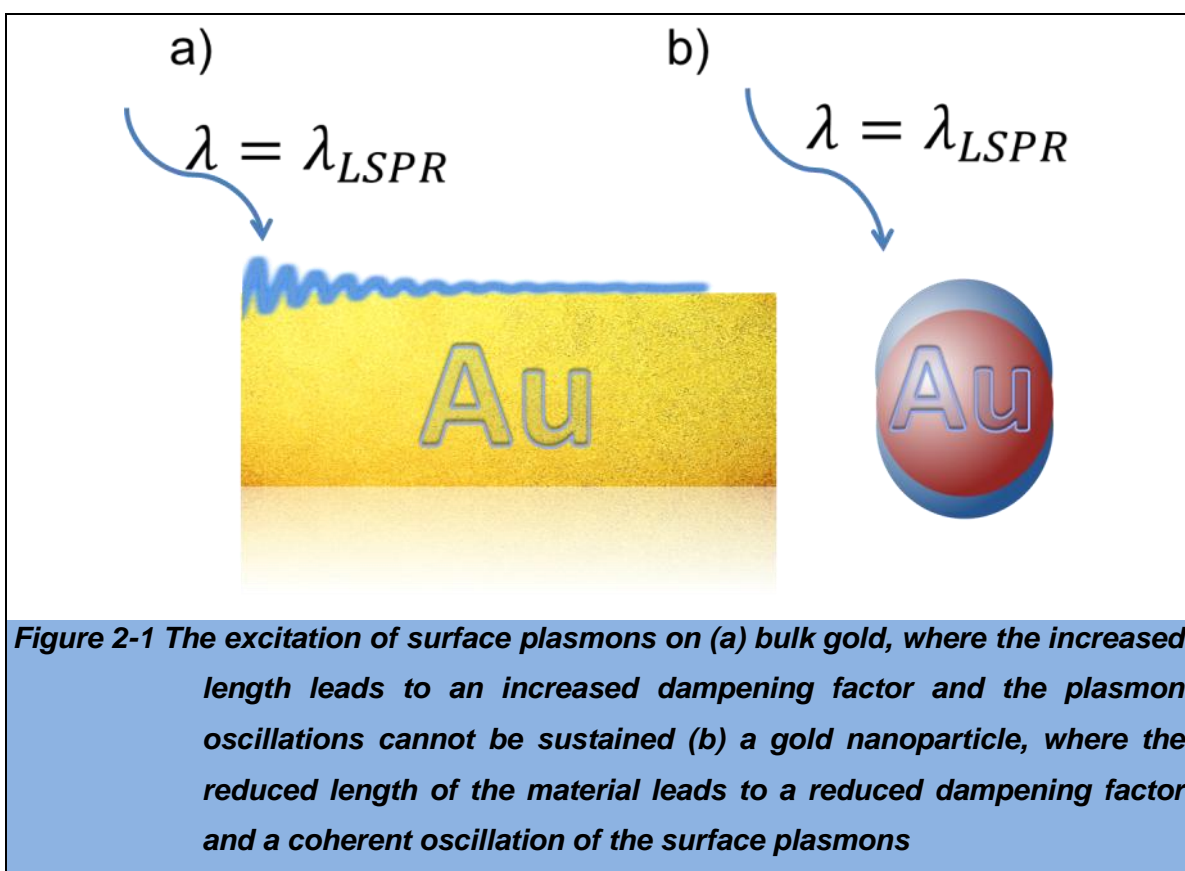
2.3 Localised Surface Plasmon Resonance and Noble Metal Nanoparticles

2.3.1 Introduction to Localised Surface Plasmon Resonance

Noble metal materials can demonstrate the phenomena *surface plasmon resonance* (**SPR**). SPR is observed as the oscillation of free-electrons (conduction band electrons), delocalised over the surface of the material. These oscillating free electrons are known as '*plasmons*'. This resonant oscillation can be induced using

electromagnetic radiation, with the characteristic plasmon resonance energy of the material noted as an absorption band in the optical spectra of the material.

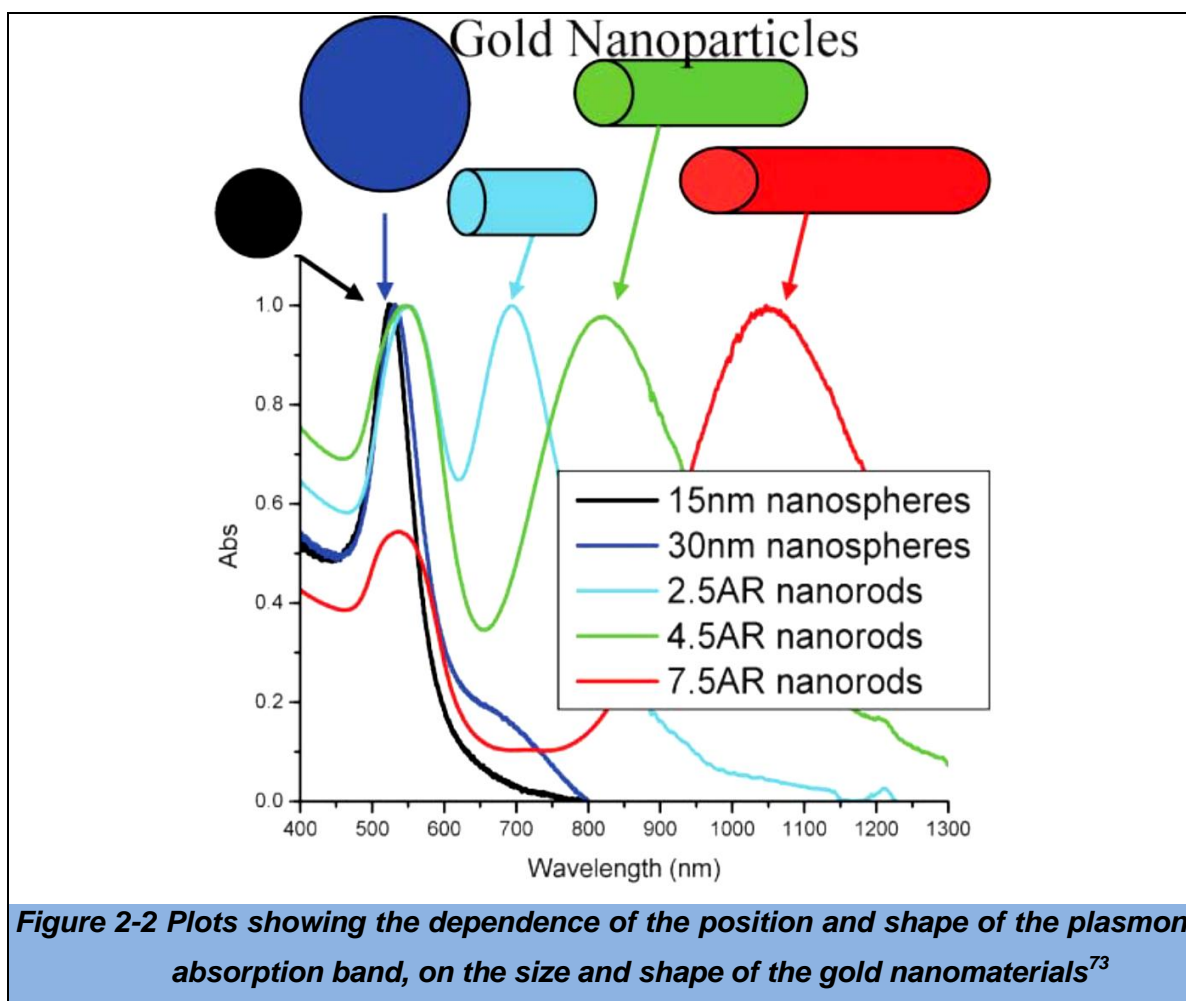
Mie theory has shown that SPR is present when the radius of a metal particle is large compared with the wavelength of light needed to produce plasmon resonance. In that case, the conduction band electronic oscillations are incoherent as they do not oscillate together as one (Figure 2-1(a)).⁴⁰ It is also shown that for a particle with a size comparable to the wavelength of the radiation being used to excite the plasmons, the conduction band electrons participate in coherent oscillation at the surface of the particle (Figure 2-1(b)).



This is termed LSPR and is a consequence of the plasmons being spatially confined on the surface of a material (in the case of this study, AuNPs and AgNPs).⁴⁰ Therefore, the plasmon absorption band wavelength is dependent on the size and shape of the material.

The optical absorption spectra of plasmonic NPs has a maximum absorbance at the plasmon resonant frequency.^{40,71} As the observed LSPR absorption band of the NP is dependent on the size, shape of the particles, allowing the plasmon

wavelength to be tuned by varying the size and shape of the particles (see Figure 2-2).⁴⁰



The LSPR absorption spectrum is also very sensitive to the surrounding environment, especially the chemical environment near the surface of the NP. Altering this chemical environment changes the *local refractive index* at the surface of the nanomaterial, resulting in a shift in the plasmon absorption spectrum. These are usually either a blue-shift or red-shift of the plasmon absorption band maximum,⁷² which is demonstrated in Equation 2.1.

$$\Delta\lambda = m(\Delta n)\exp(-2d/l)$$

Equation 2.1 The wavelength response to the change in the local refractive index at the surface of a plasmonic material⁷⁶

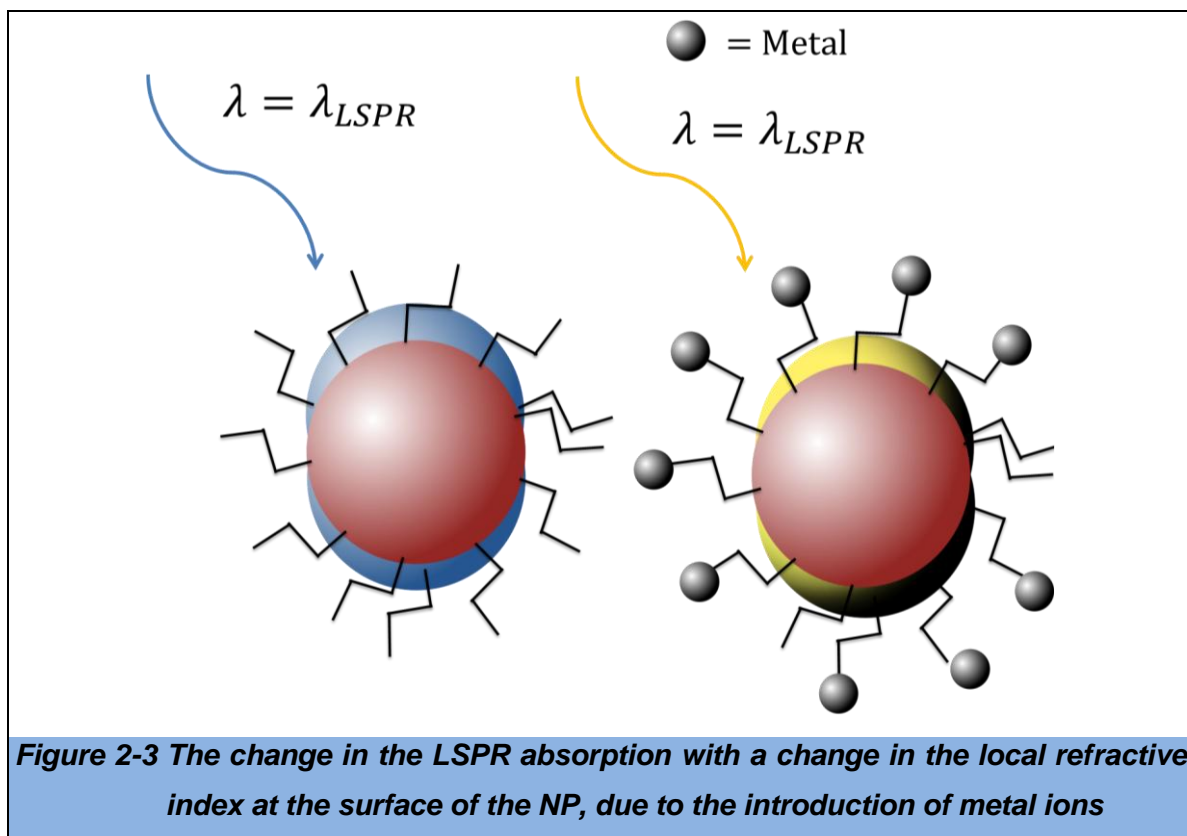
Where $\Delta\lambda$ is the change in the wavelength position of the plasmon absorption band, m is the 'response term' of the plasmonic material, Δn is the change in refractive index at the surface of the material, d is the thickness of the material at the surface of the plasmonic material, and l is the *decay length* of the plasmon wave *i.e.* the distance the plasmon wave can travel before it decays. To simplify, the shift in the wavelength position of the plasmon absorption band is proportional to the local refractive index change at the surface of the material; and it is this property that has been employed for chemical sensing purposes, including the detection of metal ions.

Another noticeable optical property arises when noble metal nanoparticles come into close range with each other. A phenomena known as *plasmon coupling* occurs. This is a result of the coupling of the electromagnetic fields surrounding the NPs. This coupling causes a large red shift in the LSPR absorption band maximum.⁷² In the case of solutions of AuNPs, plasmon coupling causes the solution to appear blue, due to the absorption of the yellow to red portion of the visible spectrum. This has also been used for sensing applications.⁷²

2.4 The Response of the Localised Surface Plasmon Resonance

Absorption Band to Local Refractive Index Changes and its use in the Detection of Metal Ions

For the detection of metal ions, using a LSPR absorption band method, the NPs are generally coated in *functional molecules*. These functional molecules are selected for their affinity for metal ions. This results in the build-up of the target metal ions at the surface of the material, leading to a change in the local refractive index and a resultant shift in the wavelength of the plasmon absorption band maximum (Figure 2-3).



Recently, a novel colorimetric assay was produced which incorporated the LSPR absorption peak of AgNPs for the detection of aqueous Ni^{2+} ions.⁷⁷ The surface-functional molecules were glutathione and l-cysteine, and were chosen as they displayed a high selectivity towards Ni^{2+} under specific conditions. Upon the addition of Ni^{2+} ions to the functionalised AgNP solution, a distinctive colour change was observed due to plasmon coupling. This was a result of the aggregation of the AgNPs, induced by the binding between Ni^{2+} and the surface-functional molecules. This method produced a detection limit of 120 nM.

AuNPs have been used recently for the selective detection of Hg^{2+} ions in aqueous media.⁷⁸ Carboxymethylagarose molecules were used as the functional molecules in this study. When these AuNPs were introduced to a Hg^{2+} ion solution, a blue shift in the LSPR absorption band was noted and a resultant colour change of the solution. This method was used to detect aqueous Hg^{2+} ions in the range of 0.01–100 ppm.

Au nanorods have also been used for their plasmonic characteristics. Lately, polyamine functionalised gold nanorods have been developed for a LSPR based nanosensors for the detection of aqueous Cu^{2+} ions.⁷⁹ The combination of

poly(sodium-4-styrenesulfonate) and polyethylenimine functional molecules provided positive charges to reduce the aggregation of the gold nanorods, and allowed the selective capture of Cu^{2+} ions for detection. This method produced a detection limit of 240 nM.

These examples illustrate some of the current capabilities of plasmonic nanomaterials, utilised for the detection of metal ions using a LSPR-based sensing method. These methods are reported to have a high selectivity towards the target metal ion and low LOD values, both of which are essential for producing a successful nanosensor-based technique.

2.5 The use of Surface Enhanced Raman Spectroscopy in the Detection of Metal ions

LSPR also has a profound effect on Raman scattering.⁷⁴ Chemicals can build up around the nanoparticles by attraction, and capture by molecules surrounding the nanoparticle. This leads to the improvement of chemical Raman signals by concentrating the chemicals on the surface of the NP; but, LSPR leads to the additional electromagnetic enhancement of the Raman signal, with enhancements up to $\sim 10^{14}$ times greater being achieved.⁷⁵ Using this technique even very weak Raman signals can be observed. The enhancement of the Raman scattering signal by LSPR is known as *surface enhanced Raman spectroscopy (SERS)*. One of the main practical design properties of a SERS substrate is that the wavelength of the Raman laser emission falls within the absorbance range of the plasmon absorption band. The closer the laser emission wavelength is to the plasmon band maximum wavelength position, the greater the enhancement factor for the Raman signal.

SERS has also been shown to have great potential as an analytical method.⁸⁰⁻⁸² SERS is a leading nanosensor-based method, producing impressive limits of detection - some of which are as low as *pg/l*.⁸³⁻⁸⁶ Using selected functional molecules can make the desired target metal ions build-up around the NPs, leading to the improvement of Raman signals by chemical enhancement, as well as the LSPR induced electromagnetic enhancement. Below are some examples of recent progress in the area of AuNPs for SERS based detection of metal ions.

Oligonucleotide-functionalized AuNPs with a silica shell have been produced for the sensitive detection of aqueous Hg^{2+} and Ag^+ ions, using a SERS-based technique.⁸⁷ This method exploits the affinity of the functional molecules towards Hg^{2+} and Ag^+ ions, allowing them to build up around the surfaces of the AuNPs. The linear detection range for the detection of Hg^{2+} ions was 0.1–1000 *nM*, and for Ag^+ ions the range was 10–1000 *nM*. Another Raman based sensor based on DNA-functionalised AuNPs was for the detection of Hg^{2+} ions, with a limit of detection of 0.45 *ng/l*.⁸⁸

These examples illustrate some of the current capabilities of SERS based techniques for the detection of metal ions, incorporating metal ion-selective functional molecules to help improve the chemical Raman signal, and utilising LSPR to further enhance the Raman signal. As a this method is much cheaper, faster and easy to carry out, with low limits of detection, SERS is a growing competitor for many standard analytical procedures, including ICP-MS.

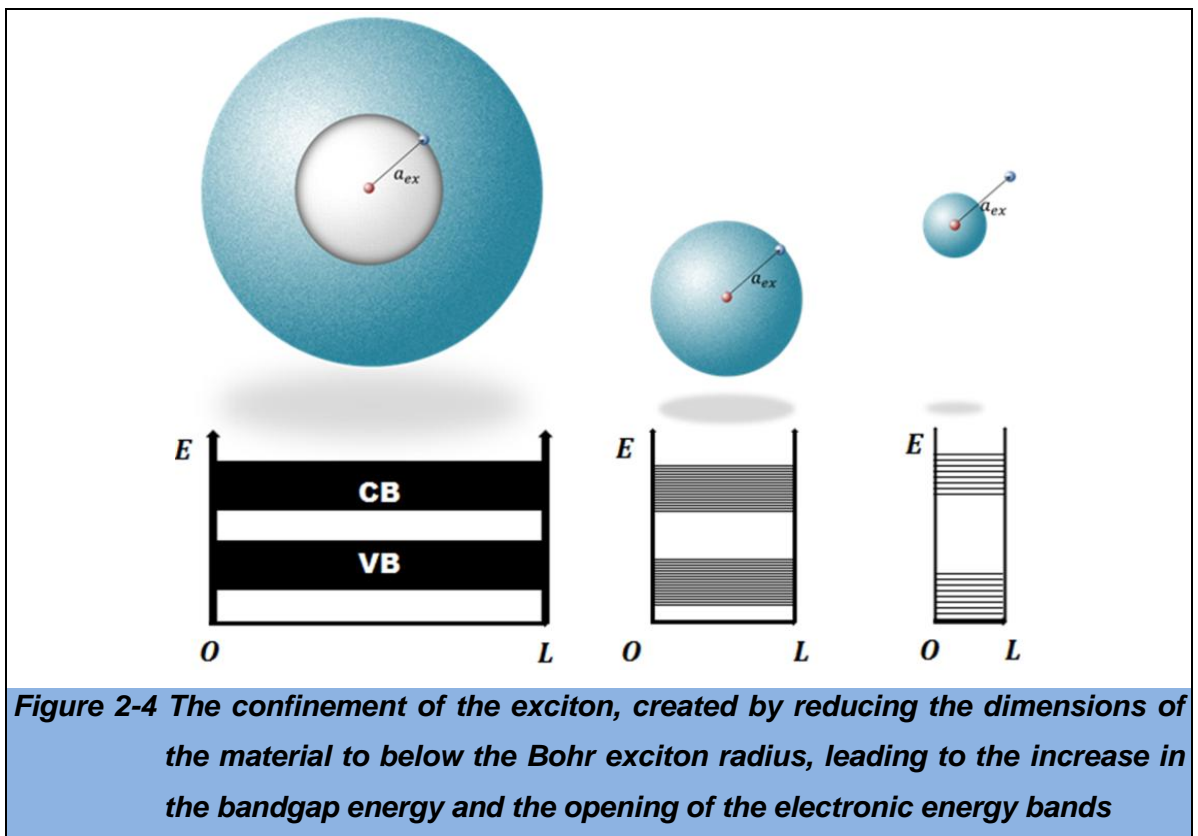
2.6 Utilising the Optical Characteristics of Semiconductor Nanomaterials for Sensing Applications

2.6.1 The electronic and optical properties of semiconductor nanoparticles

The electronic structure of solids consists of bands of allowed electronic energy levels, separated by disallowed gaps. The origin of this band structure can be explained using several different models, but here it is adequate to define its origins as the multiple addition of electronic energy levels to form molecular orbitals.^{47,49} The HOMO and LUMO bands are named the valence band and the conduction band respectively, with the energy gap between these bands being named the *band gap* E_g of the material.⁴⁷

The allowed and disallowed energies of the electronic bands for a material are dependent on the interatomic spacing, and the dimensions of the material. This is important as when the dimensions of the material become small enough, the electrons become confined, drastically altering the electronic properties of the material – this is known as *Quantum Confinement (QC)* and is the fundamental property of nanomaterials.⁴⁷

When comparing a bulk semiconductor material and its nanomaterial counterpart, it is found that the confinement of the excitons leads to an increase in the bandgap of the material (Figure 2-4). When the material is much smaller than the Bohr exciton radius, there is a strong QC effect and the electronic bands open up, creating a band structure that resembles molecular energy levels; at these small dimensions (on average, roughly smaller than $\sim 3 \text{ nm}$ to 5 nm) the materials are interchangeably referred to as clusters, quantum clusters or NCs.



Hence, even though nanomaterials can still possess an electronic band structure, the energy gaps between the electronic bands are larger than that of the corresponding bulk material e.g. the energy gaps between the electronic bands for ZnS nanomaterials are larger than that of bulk ZnS.^{47,49,52}

As the bandgap energy is dependent on the size of the nanomaterial, a size of a material can be chosen to obtain the desired bandgap energy. This has been used extensively in the optoelectronics industry to fabricate fluorescent materials which emit light of a desired wavelength. The fact that the emission wavelength can be tailored to a desired value has also found use in nanomaterial dyes and fluorescent nanosensors.⁵³

2.6.1.1 Quantum Confinement Related Absorption and Emission Processes for use in Nanosensors

For this project it is important to note that the promotion of an electron from the VB to the CB of a SC material produces a unique optical spectrum, which varies according to the material and its size. Additionally, the energy relaxation of the electron back to the VB can lead to the release of a photon making some SCs fluorescent. As the E_g is dependent on the material, different materials will absorb and emit photons of different energies.

The optical absorption spectrum of a SC material shows an absorbance onset related to the E_g of the material, which increases into the continuum states of the CB and vacuum states. Figure 2-5 is the absorption spectra for ZnSe at different dimensional sizes. It shows the spectra for a bulk system (with crystallite diameters of $>10\text{ nm}$), medium crystal system (a quantum dot of 4 to 5 nm diameter), and a nanocluster system (2 to 3 nm diameter). The bulk bandgap is the fundamental absorption and is shown at around $\sim 445\text{ nm}$. The QC effects is shown below, with the bandgap of the medium crystallite moving to around $\sim 400\text{ nm}$ (indicated by the shoulder in the absorption spectrum) and then the bandgap of the small crystallite, which has undergone the largest blue shift.

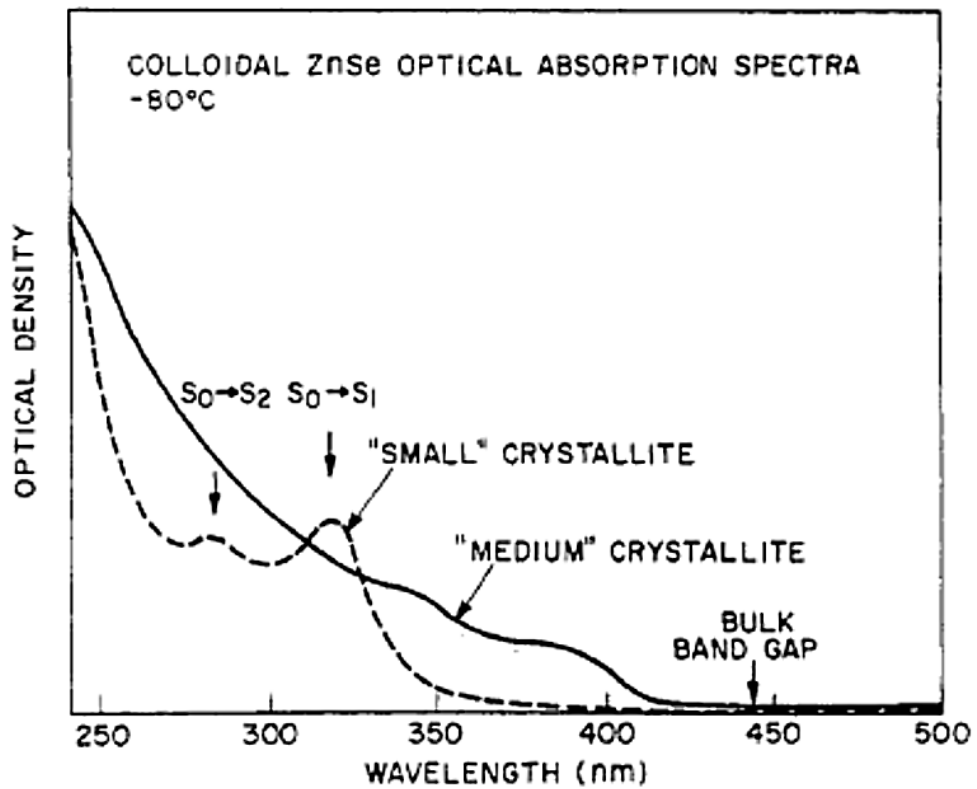
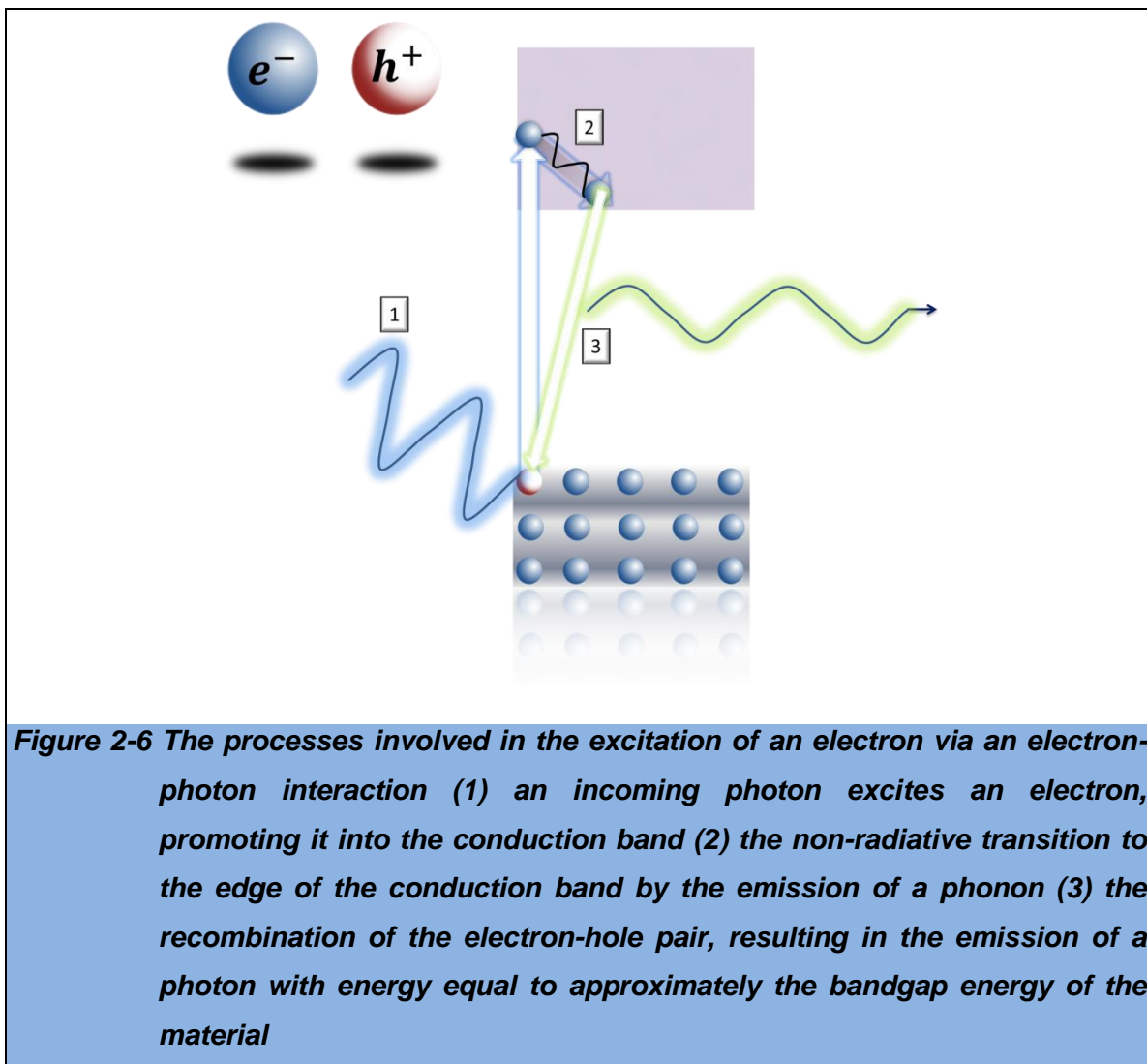


Figure 2-5 The absorption spectra for ZnSe spheres with material dimensions relating to a bulk system (with crystallite diameters of >10 nm), medium crystal system (4 to 5 nm diameter), and a nanocluster (2 to 3 nm diameter)⁵¹

The electron transition from the CB back to the VB, can result in the emission of photons (fluorescence), with energies comparable to the bandgap energy (Figure 2-6).

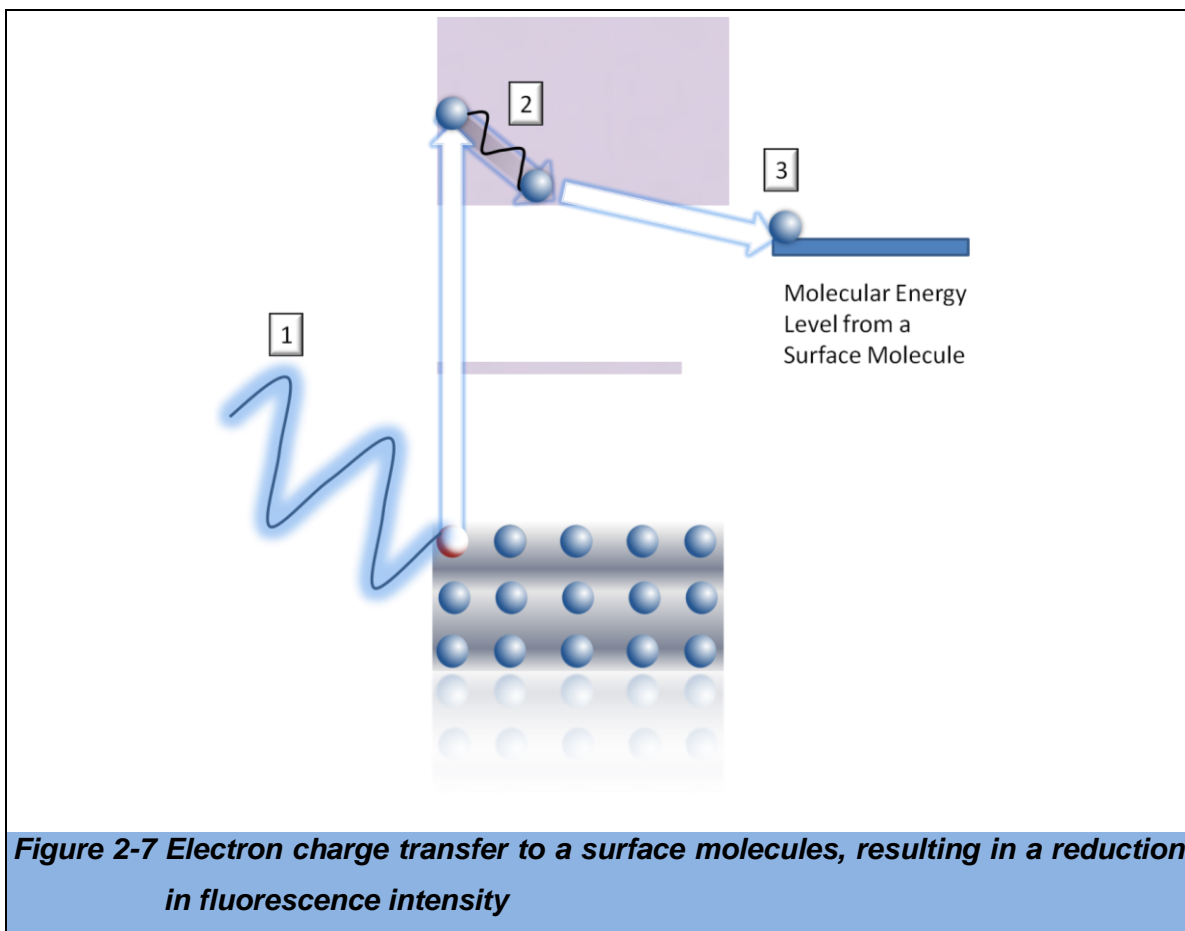


Therefore, on producing a nanomaterial of a required size, the desired energy of the emitted photons can be obtained. Figure 2-6 displays some of the fundamental processes that occur when an electron is promoted into the conduction band and the emission of a photon. (1) Shows the absorption of a photon of energy $>E_g$. (2) Represents the radiationless transition of the electron to the bottom of the conduction band. In (3) the electron returns to the valence band via the emission of a photon of an energy that is comparable to the bandgap of the material.

With the addition of functional molecules to the surface of the nanomaterial, a further mechanism can be introduced, *fluorescence quenching*. This is the most common technique in SC nanomaterial sensing.^{89,90}

Some sensors have been produced using surface-functional groups that will trap electrons from the SC via charge transfer when they are bound to target metals

(Figure 2-7); this inhibits emission, proportionally reducing the intensity of the fluorescence, relative to the concentration of the target metal ions in the sample.



2.6.2 The use of Semiconductor Nanomaterials for the Chemical Sensing of Metal Ions

Due to the fluorescent nature of SC NPs, most of the sensors based on these materials are centred on a fluorescence detection method, where the fluorescence intensity changes relative to the concentration of the target metal. Below are some examples.

ZnS NPs that were functionalised with L-cysteine have been synthesised for the detection of Cu^{2+} ions.⁸⁹ Upon interaction with the Cu^{2+} ions, the fluorescence of the NPs became quenched *i.e.* it decreased with an increase in the concentration of Cu^{2+} ions. This method provided a LOD of 7.1×10^{-6} M. Infrared-fluorescent N-acetyl-l-cysteine capped CdTe/CdS@ZnS-SiO₂ quantum dots have been synthesised for the selective detection of Hg^{2+} .⁹⁰ It was found that the metal ions quench the fluorescence of the particles. By using this method the concentration of

Hg²⁺ ions, ranging from $5.0 \times 10^{-9} M$ to $1.0 \times 10^{-6} M$ was determined, with a LOD of $1.0 \times 10^{-9} M$.⁹⁰

These examples display further progresses in the development of nanosensors, with low limits of detection for their respective target metals and ease-of-use. Although, disadvantages exist in the range of metals that these methods can detect – a major desire for practical use, especially in the context of industrial water analysis.

2.7 Summary and Concluding Remarks for the Current Nanosensor Technology

Below is a table showing some of the current LSPR and SC based nanosensors. The LOD values range from *mg/l* to *pg/l*.

Table 2.1 A list of nanosensor examples for the detection of a target metal ion including the target ion, material and sensor type, and limit of detection			
Target Metal Ion	Nanosensor Material & Technique	LOD	Ref
Ni²⁺	AgNP (LSPR Absorption)	7.4 $\mu\text{g/l}$	⁷⁷
Hg²⁺	AuNP (LSPR Absorption)	10 -100 x 10 ⁺³ $\mu\text{g/l}$	⁷⁸
Hg²⁺ and Ag⁺	AuNPs (SERS)	20 <i>ng/l</i> and 1.08 $\mu\text{g/l}$	⁸⁷
Hg²⁺	AuNPs (SERS)	0.45 <i>ng/l</i>	⁸⁸
Cu²⁺	ZnS (Fluorescence Quenching)	450 $\mu\text{g/l}$	⁸⁹
Hg²⁺	CdTe/CdS@ZnS–SiO ₂ (Fluorescence Quenching)	200 <i>ng/l</i>	⁹⁰

These values show that there is an increasing advancement in the limit of detection for nanosensors, especially for the metals Ni and Hg, named in the WFD and DWD as priority substances. The LOD for these detection methods for Ni and Hg, are already competitive with ICP-AES techniques, with reference 88 being competitive with ICP-MS.

Even though the results for the nanosensors discussed so far are impressive for a stand-alone analytical method, from an industrial point of view, a wider range of target metals is needed. This is required for the complete analysis of aqueous

samples that contain many different metals; especially when considering the list of metals named in the WFD and DWD and the introduction of their legislation. Therefore, this is a great motivation for the continued research and development of nanosensors, and the industrial driving force behind this project.

To summarise the general target gaps for the design of nanosensors for industrial purposes:

- More target metals need to be included into a particular nanosensor technique, if it is to become a contender for standard analytical methods
- The nanosensor must have a comparable or superior LOD, when compared to standard techniques
- Nanosensors capable of detecting metals rapidly, preferable at the sampling site, will increase the viability of the method as a contender for standard analytical methods, as this will add an additional benefit which methods such as ICP do not possess
- The development of standalone nanosensor-based detection devices. This will increase the portability of the method, reducing sampling costs

2.8 Background for the Nanomaterials used in this Study

This study incorporates three nanoparticle properties that have been discussed so far: LSPR absorption spectroscopy (Section 2.4), SERS (Section 2.5), and modification of the bandgap of semiconductor nanomaterials (Section 2.6). The materials used to utilise these respective properties are citrate functionalised AuNPs and AgNPs, and CuS clusters. This section gives a brief outline into the materials used and why they were chosen.

2.8.1 Citrate Functionalised Gold and Silver Nanoparticles

Firstly, citrate functional molecules for the Au and Ag NPs were chosen because of two properties:

1. They have a natural affinity towards metal ions, with many metal citrate molecules already synthesised^{91,92}

2. Sodium citrate is commonly used in the synthesis procedure for AuNPs and AgNPs, therefore no further preparation of the surfaces of the NPs needs to take place

It was predicted that the citrate molecules bound to the surfaces of the nanoparticles would also have a strong affinity for metals as this would lead to the production of metal-citrate complexes at the surface of the particles. A resultant shift in the LSPR absorption band, proportional to the concentration of the metal-citrate species at the surface, would follow. It was further predicted that the citrate-functionalised AuNPs could be used as a SERS substrate, as the LSPR absorption band is located near to the wavelength of the laser which would be used for Raman spectroscopy. This is integral for boosting the Raman spectroscopic signal.

Please note: When this work was proposed in 2010, it was unknown that there was a publication utilising citrate functionalised AuNPs for the detection of Pb;¹⁰⁰ This paper used the Pb-induced coagulation of the AuNPs at pH 11.3, to determine the concentration of Pb. They used an LSPR absorption method, as used here. Although this paper did show that this idea could be used for the selective detection of Pb at pH 11.3, the detection range (41.4 $\mu\text{g/l}$ to 3.1 mg/l) did not allow for the determination of Pb, at concentrations set by the WFD and DWD. Additionally, the method required the addition of 0.04 M KCl for the AuNPs to coagulate and produce a signal. The novelty of the idea set-out in this current study, did not use any additional pH changes or chemical additions, except the metal ion precursors already present in the solution.

2.8.2 CuS Nanoclusters

The CuS nanoclusters were prepared to selectively detect Hg^{2+} ions in a solution containing a mixture of different metal ions. This method uses cation-exchange processes to dope the CuS nanoclusters with Hg^{2+} ions in exchange for Cu^{2+} ions; this was further hypothesised to ultimately change the bandgap value of the NC proportionally to the concentration of the Hg^{2+} ions in solution.

Ions will exchange in solution when the *solubility product constant*, k_{sp} , of a potential product is much lower than the material that is present in the solution *i.e.* in this case, the k_{sp} value for HgS is much less than the value for CuS. This led to the idea that Hg^{2+} ions would exchange with the Cu^{2+} ions, resulting in a shift in the bandgap of the NC, relative to the concentration of the Hg^{2+} ions in the NC solution.

To explain the predicted analytical outcome of this system, key concepts in bandgap engineering will be explained.

2.8.2.1 The effects of dopants on the absorption characteristics of semiconductors

The incorporation of defects or dopants into the nanocrystal structure has a profound effect on the electronic properties of the material (Figure 2-8). The defects or dopants lead to extra electronic energy levels appearing in the bandgap of the material (*localised* energy levels). These levels can accept the electrons as they return to the valence band, reducing the energy of the emitted photon.

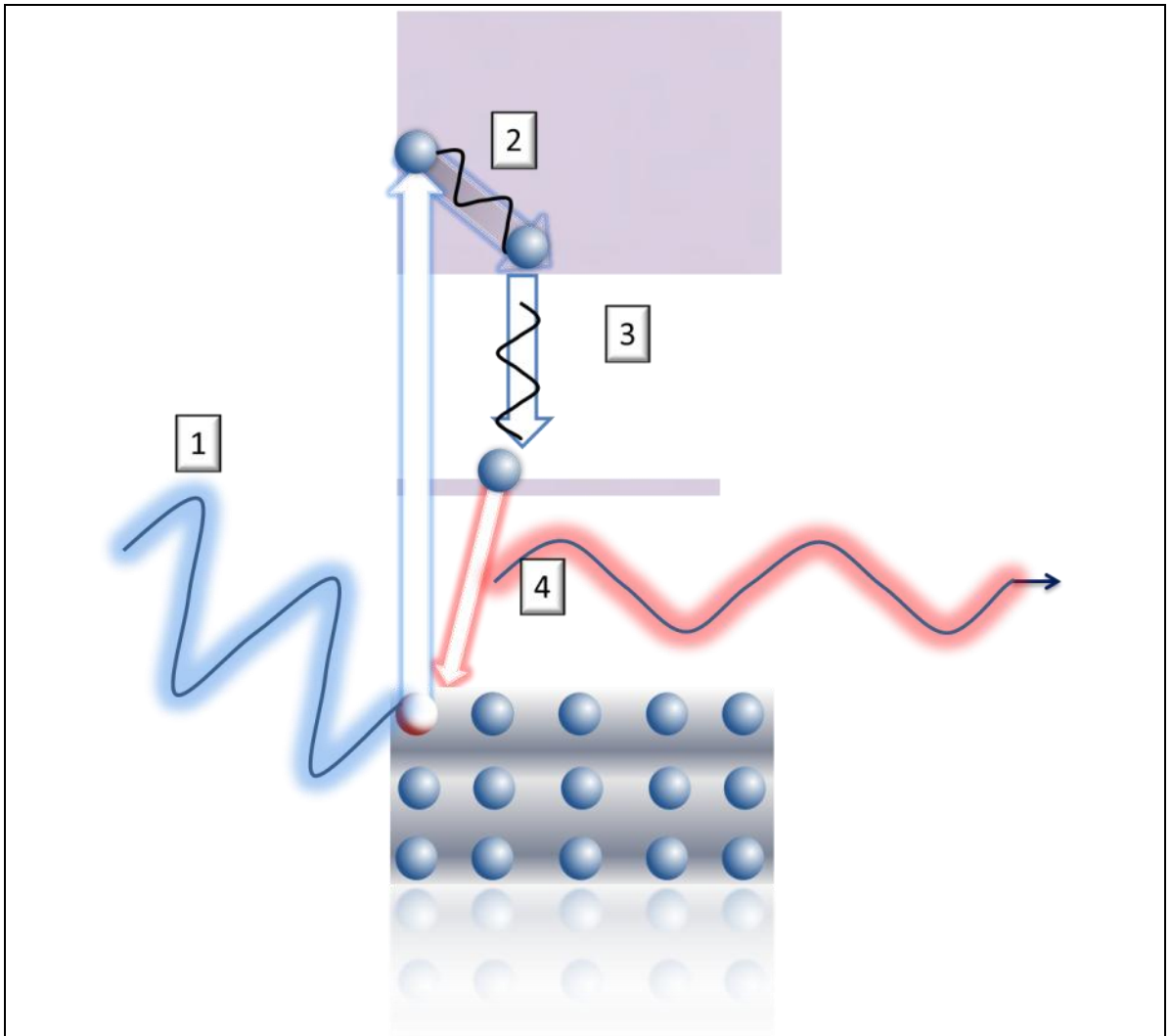
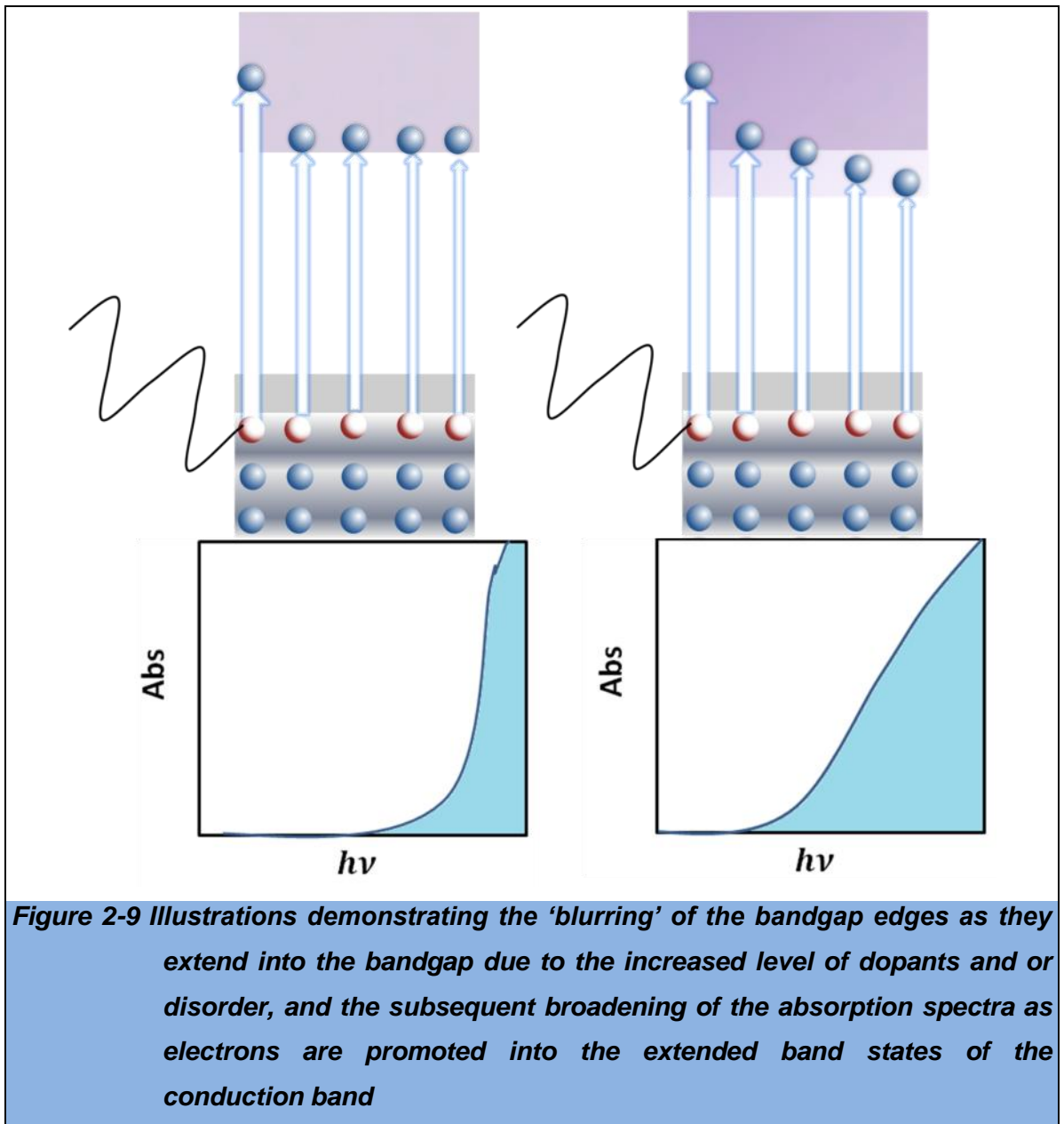


Figure 2-8 The absorption of a photon (1) leading to the promotion of an electron into the conduction band, the radiationless transition to the bottom of the conduction band involving the emission of a phonon (2), the radiationless transition from the bottom of the conduction band to a localised electronic energy level in the bandgap (3), and the final transition from the localised energy level to the valence band, resulting in the emission of a photon with an energy comparable to the energy gap between the localised state and the valence band

The continued addition of dopants or defects will start to have a profound effect on the electronic structure of the nanomaterials: (1) this further addition leads to a 'blurring' of the edges of the valence and conduction bands - as the dopants and defects become incorporated over the entire crystal structure, the electronic levels become *delocalised* and begin to overlap with the band edges (Figure 2-9).



This form of bandgap modulation can be measured using the *Urbach equation*, which is a measure of the widths of the states at the band edges (Equation 2.2).⁶²

$$\alpha = \alpha_0 \exp \left[1 - \frac{E - E_g}{\Delta(n, T)} \right]$$

Equation 2.2 The Urbach equation, used to measure the widths of the electronic states at the band edges, created by disorder and doping⁶²

Where, E_g is the bandgap energy, Δ is the Urbach parameter and E is the energy width of the states extending into the bandgap. Plotting $\ln a$, where a is the absorption coefficient, against the energy of the incident photons will yield a spectra. The gradient of this plot will be equal to the widths of the states extending into the bandgap from the band edges.

Another common situation encountered in bandgap engineering, is the increase or decrease in the bandgap energy because of induced strain on the crystal structure.⁶³ This is shown in Figure 2-10, where the bandgap of the substrate material will reduce upon the reduction of the bond lengths within the crystal lattice, or widen with the lengthening of the bond lengths within the crystal lattice.

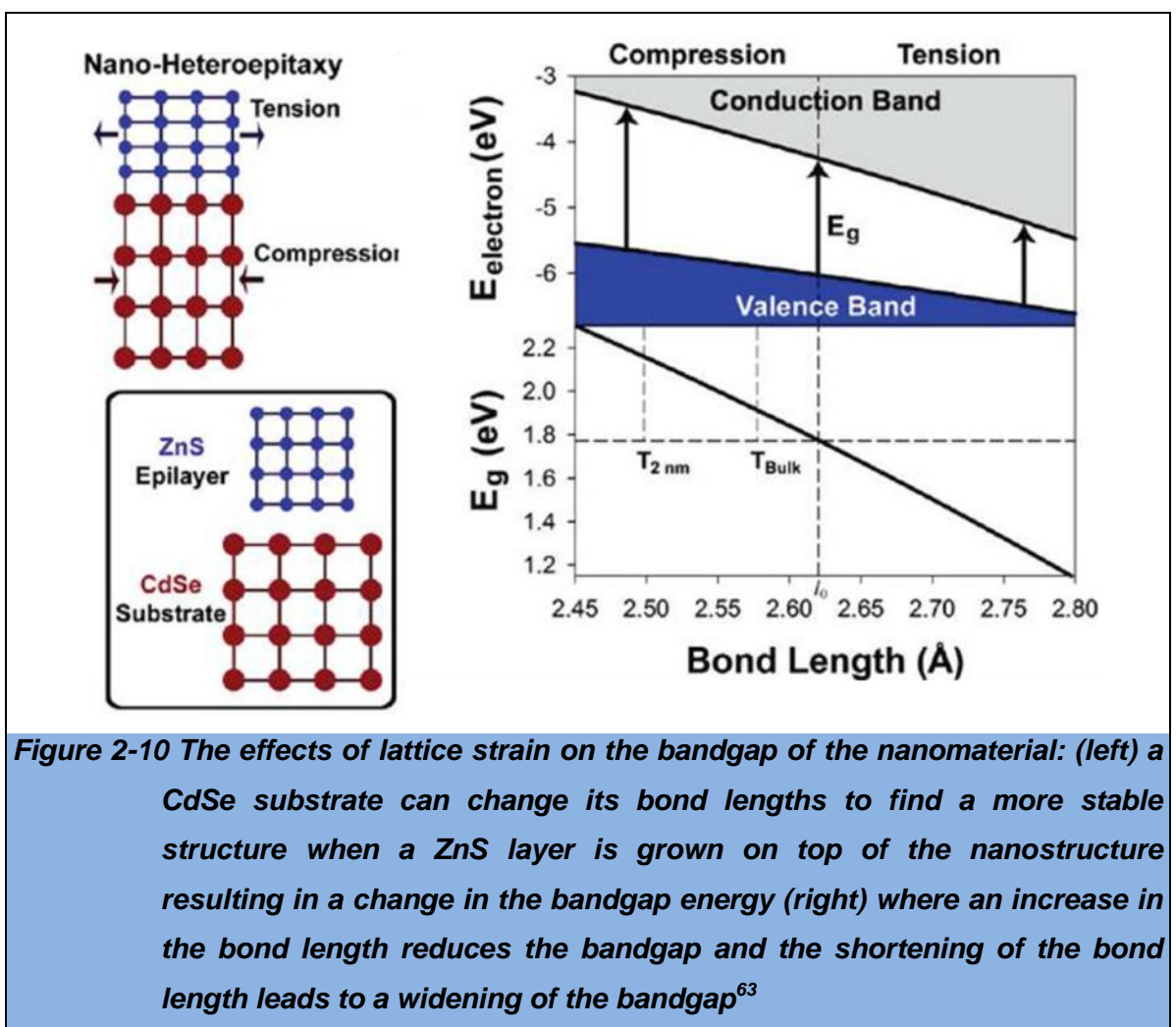
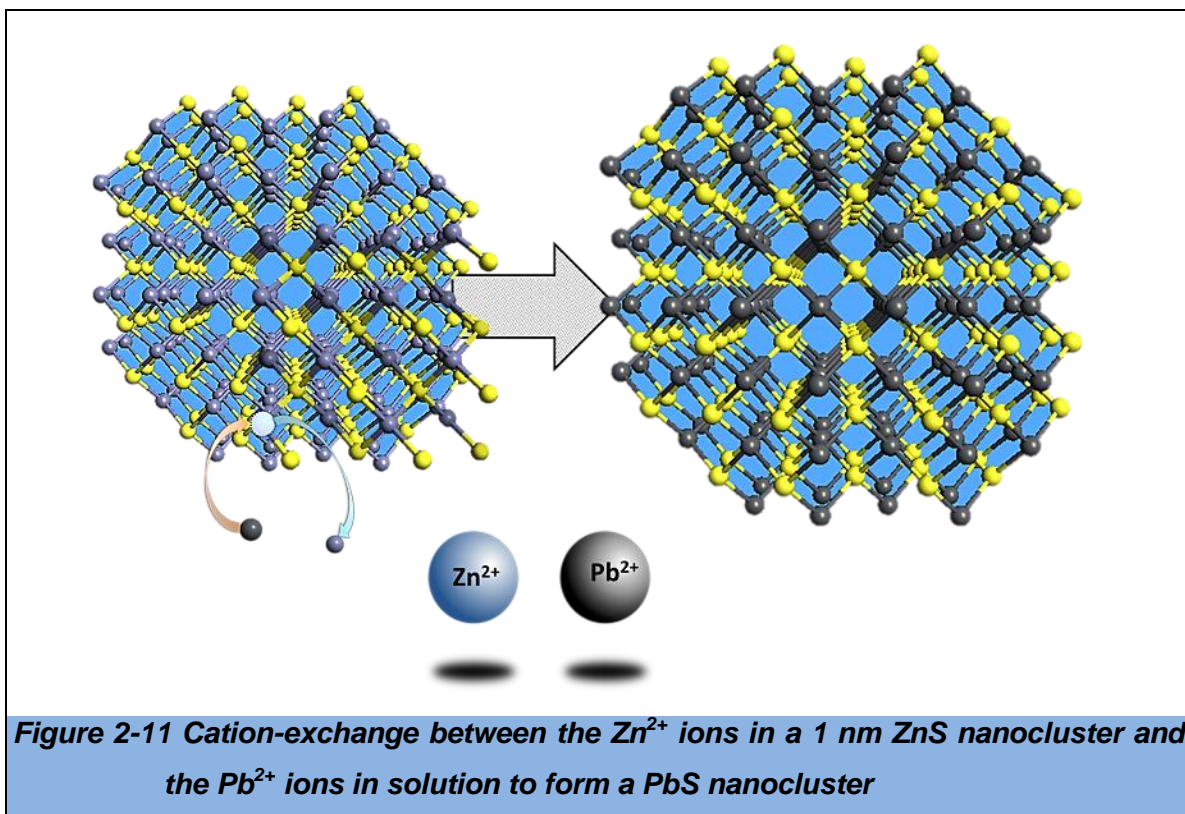


Figure 2-10 The effects of lattice strain on the bandgap of the nanomaterial: (left) a CdSe substrate can change its bond lengths to find a more stable structure when a ZnS layer is grown on top of the nanostructure resulting in a change in the bandgap energy (right) where an increase in the bond length reduces the bandgap and the shortening of the bond length leads to a widening of the bandgap⁶³

2.8.2.2 Using cation-exchange processes to change the electronic structure of the nanomaterial

A method that has been used extensively for the synthesis and modification of nanomaterials is ion-exchange reactions.^{64,65} Cation-exchange is commonly used to add metal ion impurities to materials or even to exchange all of the cations in the starting material, to convert it to another material (Figure 2-11).⁶⁶



Stopping the cation-exchange reaction reaching a full conversion can even be used to create a core-shell nanoparticle structure.⁶⁷

When the nanoparticles have a larger radius than $> \sim 5 \text{ nm}$, the crystal retains its crystal structure, with respect to its anionic positions, after the cations have been exchanged.⁶⁸ When the radius of the nanomaterial is $< \sim 5 \text{ nm}$, the crystal structure will change its shape and sometimes its crystal geometry, to create a more stable crystal structure.⁶⁸

These ideas have all been incorporated in the design of the CuS nanosensor.

2.8.3 Predicted Optical Results for the CuS Ion-Exchange Nanosensor

Using the theory presented above, several predictions can be made about the evolution of the optical spectra for the CuS NCs and their interaction with the aqueous Hg^{2+} ions:

- As the k_{sp} value for HgS is much lower than that of CuS, it is expected that the CuS NC will start to exchange the aqueous Hg^{2+} ions for Cu^{2+} ions in the NC
- As the bandgap values for CuS and HgS are different, a shift in the UV-Vis absorption spectrum is predicted with an increase in Hg^{2+} ions
- As Hg^{2+} ions are much larger than Cu^{2+} , it is also expected that the absorption spectra will start to show an increased Urbach tail, due to the internal strain within the NC

2.9 Literature Review Summary

The work carried out here on LSPR and SERS continues with the ideas of selective functional molecules and achieving a low limit of detection. Below is a summary of the points covered in this chapter:

Nanosensors for the detection of aqueous metals

- Nanomaterials are now widely integrated into the research areas of chemical sensing, utilising such techniques as LSPR absorption spectroscopy, SERS (Sections 2.4 and 2.5), and fluorescent semiconductor nanomaterials
- there is an increasing advancement in the limit of detection for nanosensors, with some already being competitive with ICP-MS
- The nanosensor must have a comparable or superior LOD, when compared to standard techniques
- More target metals need to be included into a particular nanosensor technique if it is to become a contender for standard analytical methods
- Nanosensors capable of detecting metals rapidly, preferable at the sampling site, will increase the viability of the method as a contender for

standard analytical methods, as this will add an additional benefit which methods such as ICP do not possess

- The development of standalone nanosensor-based detection devices to increase the portability of the method, reducing sampling costs
- This study planned to use LSPR absorption spectroscopy, SERS and ion-exchange nanosensors for the detection of the metals named in the WFD and DWD as priority substances

The nanosensors developed in this study

- Citrate functional molecules were chosen for the Au and Ag NPs, for use with a LSPR absorption spectroscopy method, due to their affinity towards aqueous divalent metals
- The use of citrate functionalised AgNPs for the detection of metals had not been used previously
- Even though citrate functionalised AuNPs had been used for the detection of Pb, the detection range was too high to be practical for the determination of Pb at concentrations set by the WFD and DWD. A KCl additive was also required during this process
- In this study, the citrate functionalised AuNPs would be used 'as prepared', with no further additives being added to the solutions
- SERS substrates will also be produced using the AuNPs, due to the matching of the Raman laser wavelength with the LSPR absorption band of the NPs, which will enhance the Raman signal
- CuS NCs are to be used for the selective determination of Hg²⁺ in a solution of mixed aqueous metal ions

2.10 New Contributions to Knowledge Attained During this Study

During this study, there were several notable contributions to knowledge:

- Computational studies were carried out on the potential citrate-NP and metal-citrate-NP complexes, for the AuNP and AgNP-bound functional

molecules in metal ion solutions. This had never before been published using these materials.

- The determination of the concentration of Pb in solution via a SERS based technique provided a new contribution to knowledge via a new SERS material. This was subsequently published
- A new synthetic route to was designed and utilised for the synthesis of CuS NCs
- A new Hg selective ion-exchange sensor was created using the CuS NCs

The next chapter presents the materials and methodology used within this study.

3 Materials and Methods

3.1 Introduction

In order to evaluate the performance of the fabricated nanosensors, it was necessary to study the sensitivity and the selectivity towards a target metal, within the practical working range of ng/l - $\mu g/l$. This chapter discloses the different techniques used in manufacturing and characterisation of these nanosensors. The Materials section (Section 3.2) provides a list of all of the chemicals used in this study. This is followed by a practical description of the analytical techniques employed. Section 3.4 provides detailed descriptions of the synthesis of the sensors; whilst Section 3.5 discloses detailed preparatory steps for samples, characterisation set-ups and the data analysis techniques used in this study.

3.2 Materials

3.2.1 General Reagents & Solutions

All of the chemicals listed in Table 3.1 and Table 3.2 were purchased from Sigma-Aldrich (UK). All solutions used within this study were made using deionised water, and prepared in glassware that had been cleaned in *aqua regia* (Table 3.3). Table 3.1 displays the metal ion sources used to produce the metal ion stock solutions. These stock solutions were later employed for characterisation and control experiments.

Table 3.1 A list of metal precursors which were used for control experiments and the concentration of the metal ion stock solutions

Metal Ion	Metal Ion Source	Grade of Product	Concentration of Metal Ion in Stock Solution
Pb²⁺	Pb(NO ₃) ₂	ASC >99.0%	3.81 x 10 ⁻⁴ M (79.00 mg/l)
Cd²⁺	CdCl ₂	ASC >99.0%	3.81 x 10 ⁻⁴ M (42.85 mg/l)
Ni²⁺	NiCl ₂	ASC >99.0%	3.81 x 10 ⁻⁴ M (22.38 mg/l)
Hg²⁺	HgCl ₂	99.5%	3.81 x 10 ⁻⁴ M (76.47 mg/l)
Fe²⁺	FeSO ₄ ·7H ₂ O	ASC >99.0%	3.81 x 10 ⁻⁴ M (21.29 mg/l)

Table 3.2 lists the reagents that were employed in the synthesis of the nanomaterials.

Table 3.2 The chemicals used to synthesise the nanomaterials used in this study

Citrate Functionalised Gold & Silver Nanoparticles		
Chemical	Linear Formula	Grade of Product
Gold(III) chloride trihydrate	HAuCl ₄ ·3H ₂ O	99.999% trace metals basis
Silver nitrate	AgNO ₃	99.999% trace metals basis
Trisodium citrate dihydrate	HOC(COONa)(CH ₂ COONa) ₂ ·2H ₂ O	Meets USP testing specifications
Zinc Sulfide & Copper Sulfide Clusters		
Chemical	Linear Formula	Grade of Product
Zinc acetate	Zn(CH ₃ COO) ₂ ·2H ₂ O	99.999% trace metals basis
Sodium sulfite	NaS ₂	Meets USP testing specifications
Copper chloride	CuCl ₂	99.999% trace metals basis

Table 3.3 The components for the production of aqua regia, which was used for the cleaning of glassware
Recipe for Aqua Regia* (10 ml)
2.5 ml Nitric acid (Concentrated)
7.5 ml Hydrochloric acid (Concentrated)

Please note, the majority of the materials listed in Table 3.1 are highly toxic and must be handled with care. Additionally, extreme care must be taken when using aqua regia as it is highly corrosive.

3.2.2 General Instrumentation

Uv-Vis absorption spectroscopy, for all of the studied nanomaterials, was carried out using a *Perkin Elmer Lambda 40 UV-Vis Spectrometer*.

Transmission electron microscopy (**TEM**) analysis of the AuNP and AgNP samples was carried out using a *JEOL JEM-200*. Additionally, high resolution TEM (**HRTEM**) micrographs of the ZnS, Cu₂S, CuS, Cu_xSHg_y and HgS clusters were obtained using a *Philips CM200 FEG TEM*. X-ray photoelectron spectroscopy (**XPS**) measurements were carried out using a *Thermo Scientific K-alpha spectrometer* with a monochromated Al K α radiation source. HRTEM micrographs, and XPS data were obtained with help from Joseph C. Bear at University College London.

Photon correlation spectroscopy (**PCS**) measurements were obtained using a *Malvern Zetasizer nano ZS* (633 nm He-Ne laser, maximum power 5 mW), which estimates the particle diameters by *dynamic light scattering*. Zeta potential measurements were also made using the *Malvern Zetasizer nano ZS* instrument employing a zeta potential cell.

Monitoring the pH of the metal ion/AuNP and metal ion/AgNP solutions was achieved using a *Hanna Instruments pH 209* pH meter employing a standard pH electrode.

Attenuated total reflectance Fourier transform infrared spectroscopy (ATR-FTIR) spectra were recorded for the metal ion/AuNP and metal ion/AgNP samples using a *ThermoScientific Nicolet iS5 FTIR iD5 ATR*.

Raman and Surface Enhanced Raman Spectroscopy (**SERS**) spectra were obtained using the *Renishaw inVia Raman Microscope* with a *514 nm argon laser* (50 mW).

3.2.3 Computational Simulations

Simulated infrared (**IR**) spectra of the surface-citrate molecules, the metal ion-surface-citrate molecules, were achieved using a semiempirical *PM6* method by using *MO-G* for the *SCIGRESS* program.^{101,102} Before IR spectral predictions were calculated all of the chemical structures were geometrically optimised by a molecular mechanics method (*MM2*).

3.2.4 Resources utilised for Data Analysis & Processing

Analysis of spectral data and the production of all data plots were carried out using a combination of *Microsoft Excel* and *Origin 6.0*. Statistical analysis and numerical calculations were performed exclusively with *Microsoft Excel*, and any peak fitting procedures were achieved using *Origin 6.0*. The *Gatan 3.0.1* program was used for the post-processing and analysis of the HRTEM micrographs and.

3.3 Instrumental Analysis Techniques used in this Study

3.3.1 TEM and HRTEM

In this study, TEM and HRTEM micrographs were obtained to measure the size of the nanomaterials. HRTEM micrographs were used exclusively for the CuS/Hg NCs; where HRTEM provided details on the effects of Hg²⁺ doping at an atomic resolution.

TEM is a microscope technique that solves the problem of viewing objects that possess dimensions much smaller than the wavelength of light, by using electrons as its source of radiation.⁹³ Materials with dimensions much smaller than the wavelength of light, such as NPs, cannot be seen with a conventional light-based microscope. This is due to the wavelength being much larger than the object itself

i.e. the object cannot be seen. Electrons can possess wavelengths much smaller than the wavelength of light, and can be used to view objects with nanodimensions; and when using HRTEM, even the atoms of the material.

In a TEM electrons are directed towards a specimen. These electrons will pass through the sample material, through an objective lens and aperture, and arrive at the image plane, where they will be detected by an electronic imaging device (Figure 3-1 A schematic of the electron beam path in a TEM (A) and HRTEM (B) Figure 3-1).⁹³ A HRTEM works in the same way except that the objective aperture allows more of the electron beam to pass through. This is important as this allows more of the electron wave information to be detected: This information contains the values of the phases and amplitudes of the electron waves in the beam. This results in a more detailed image, showing changes in the contrast due to the atomic structure of the material, material thickness, and high electron density elements.

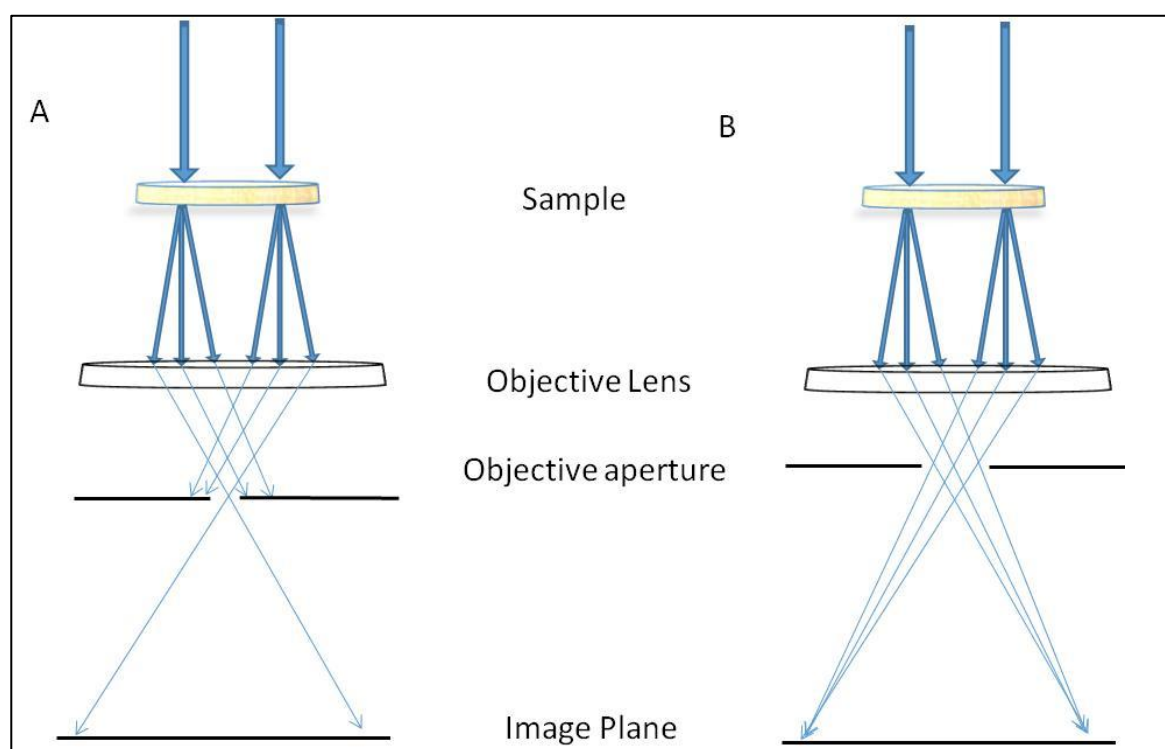


Figure 3-1 A schematic of the electron beam path in a TEM (A) and HRTEM (B)

3.3.2 Uv-Vis Spectroscopy

Uv-Vis spectrometers use ultraviolet and visible light to measure the absorbance, reflectance and transmission of ultraviolet and visible light by a sample. In the case of Au and Ag NPs, the absorption of ultraviolet and visible light is measured

to give information about LSPR absorption; and for the semiconductor NCs, the UV-Vis spectrum was used to calculate the electronic properties of the material with an increasing concentration of Hg *i.e.* changes to the direct and indirect band gap values, and Urbach energies.

The ultraviolet light is produced by the electrical excitation of deuterium or hydrogen, which at low pressures produces a continuous ultraviolet photon spectrum with wavelengths between 160 – 375 nm.⁹⁴ Tungsten filament lamps are used as a source of visible light producing photon wavelengths between 350 - 2500 nm.⁹⁴ The two sources of radiation illuminate the '*concave grating*' (Figure 3-2) which separates the radiation into its different wavelength components;⁹⁴ these wavelengths are then selected by the *selecting mirror*, and passed through the sample and a reference (or '*blank*') sample, which is usually the solution solvent being used in the sample. The *photomultiplier* enhances the signal which it receives. This is then converted to data.

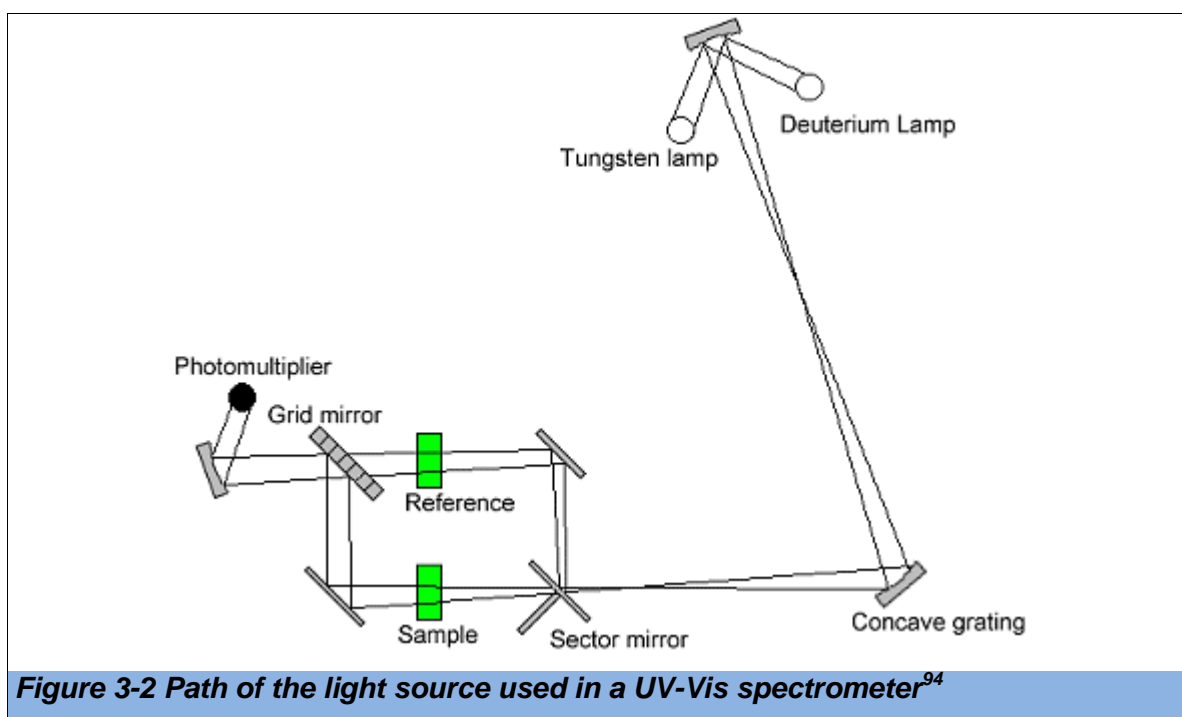


Figure 3-2 Path of the light source used in a UV-Vis spectrometer⁹⁴

3.3.3 Raman Spectroscopy

Raman spectroscopy is a spectroscopic technique which utilises inelastic scattering of monochromatic light, that is light of a single wavelength, from a laser source.⁹⁵ During inelastic scattering, the wavelength of the incident photons changes upon the interaction with the sample. Photons of the monochromatic light are absorbed by the sample and then reemitted with increased or decreased

wavelengths; this is called the *Raman Effect*.⁹⁵ This change in wavelength of the emitted photons provides information about vibrational, rotational and other transitions in molecules. Raman spectroscopy can be used to study solid, liquid and gaseous samples.⁹⁵ A major advantage of Raman spectroscopy is its capability to provide a vast amount of information about the molecular structure of a sample, even for complex molecules such as biological materials.⁹⁶ In this study it is utilised to characterise the carboxylate and hydroxyl bands of the surface-bound citrate molecules on the surfaces of the AuNPs, and monitor the effects of metal ions introduced to the NP samples.

3.3.4 Photon Correlation Spectroscopy

Here, photon correlation spectroscopy (**PCS**) was used to estimate the size of the Au and Ag NPs, and monitor any changes in particle size due to metal-ion induced aggregation, as the positive metal ions collect around the surfaces of the NPs.

PCS works on the principle that the NPs in a liquid move about randomly.⁹⁷ This is known as *Brownian motion*. Brownian motion is defined as ‘*The random movement of particles in a liquid due to the bombardment by the molecules that surround them*’.⁹⁷ The speed of this random movement by the NP is related to its size: Small particles move quickly in a liquid and large particles move more slowly. Therefore, the size of the particles can be estimated by measuring this motion, and applying theoretical models.⁹⁷

Measurements are carried out by illuminating the particles with laser light and recording the changes in intensity in the scattered light (Figure 3-3).⁹⁷

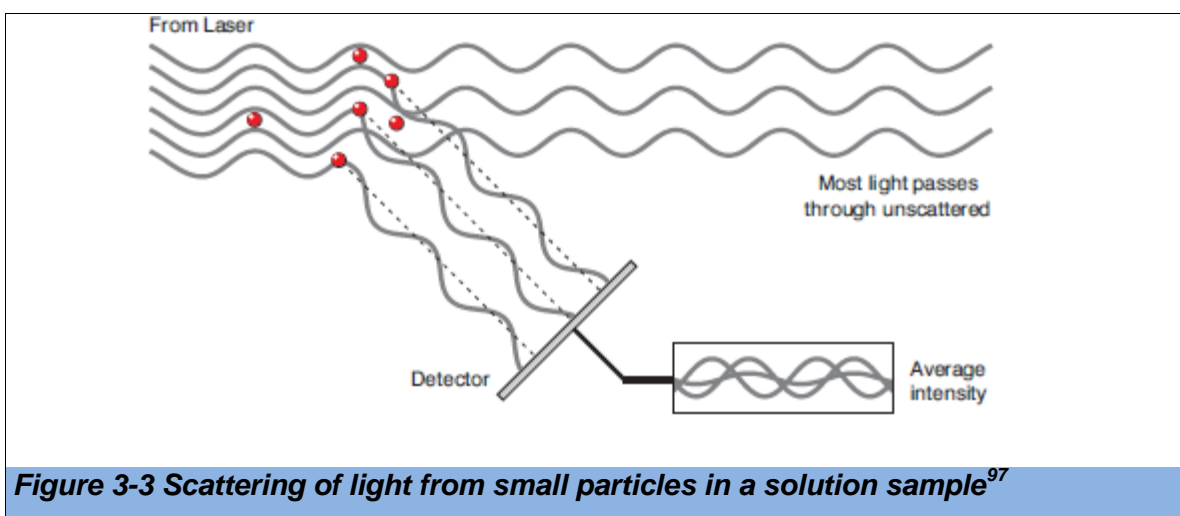
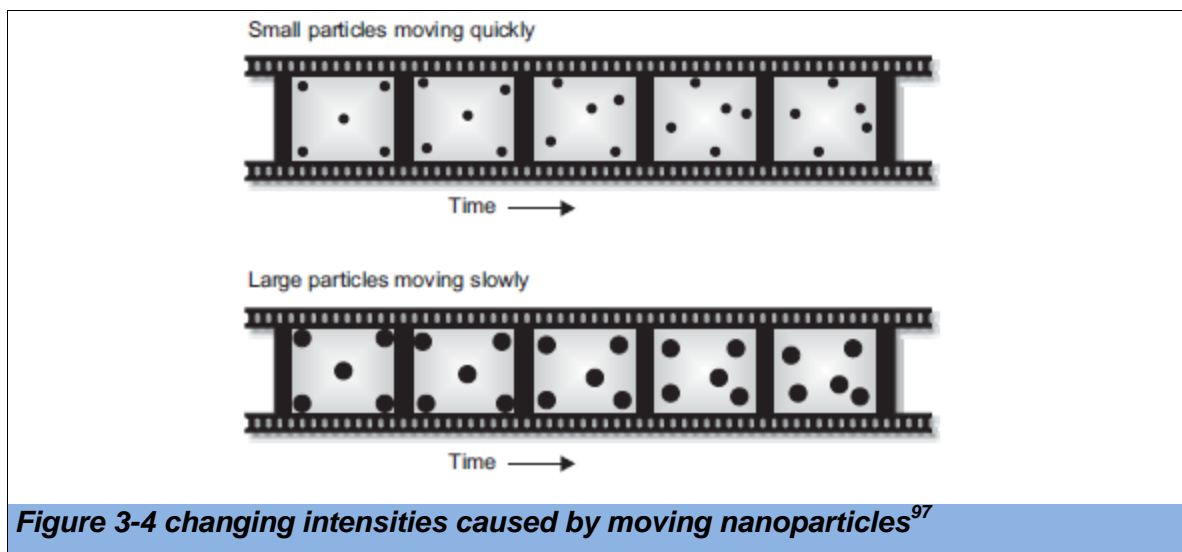


Figure 3-3 Scattering of light from small particles in a solution sample⁹⁷

As the particles are constantly in motion, the intensity of scattered light detected will also appear to move *i.e.* the intensity fluctuates. Using PCS, an analysing system measures the rate of these intensity fluctuations and then uses this to calculate the size of the particles.⁹⁷



3.3.5 Zeta-Potential

The zeta-potential of a particle is directly related to the surface charges of the NP and thus the NP-NP repulsion in a NP solution *i.e.* the stability of the NPs. A stable NP surface charge is defined by DLVO theory as ± 40 mV.

Zeta-potential measurements are achieved by running a current through a NP solution. The movement of the NPs under this current is monitored using the same technique as with PCS, employing a laser to measure the movement of the particles which is relative to the surface charges of the NPs.

Zeta-potential measurements were important for this study as the surface charge and stability of the NPs was expected to change with the addition of the positively charged metal ions, to the negatively charged surfaces of the NPs. This change was found to be extremely important for the combination of the AuNPs and Pb^{2+} ions. Furthermore, with the combination of data obtained from ATR-FTIR studies, zeta-potential measurements were used to determine the bonding modes of the surface-bound citrate molecules of the NPs.

3.3.6 ATR-FTIR

ATR-FTIR is the most used FTIR spectroscopy technique. (REF) Its most attractive features include: Sample preparation is not required, it has a very thin sampling pathlength and depth into the sample meaning very thick samples can be easily studied using this method. In contrast, for standard FTIR the sample must be diluted with IR transparent material and pressed into a pellet or thin film to limit spectral saturation in transmission mode.

For ATR-FTIR spectroscopy the sample is pressed against a high-refractive index crystal, the ATR crystal (Figure 3-5). An IR beam is directed into this crystal where it will undergo internal reflection creating an *evanescent* wave. As the wave travels through the crystal, part of the IR beam is absorbed and reflected by the sample in contact with the surface of the crystal. This beam is then returned to the detector.

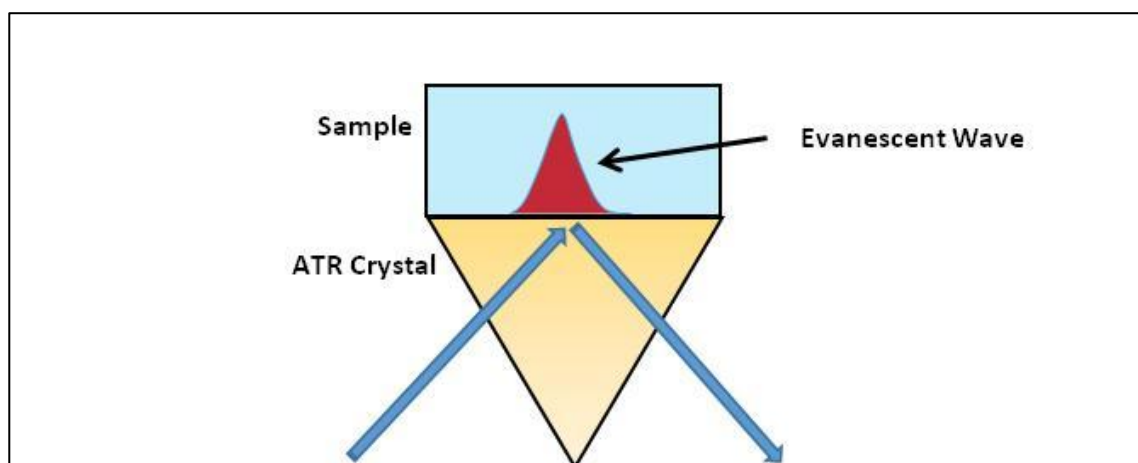


Figure 3-5 ATR-FTIR Crystal and the production of an evanescent wave

This technique was used for the analysis of the citrate functionalised Au and Ag NPs. The dried samples were dried onto glass slides that were then pressed against the ATR crystal. More specifically, ATR-FTIR to obtain IR spectra for the surface-bound citrate molecules on the surfaces of the NPs. The IR spectroscopy of citrate molecules is an important tool for the evaluation of citrate-surface bonding modes and the protonation states of the carboxylate and hydroxyl groups of the molecule. The presence or absence of certain carboxylate peaks is an indication of surface bonding via single or double carboxylate groups. With the remaining carboxylate groups providing a negative charge to the surface of the NPs, this has many implications on the stability of the NPs in relation to NP-NP

repulsion *i.e.* the more negative the surface of the NP, the more repulsion it feels between the other NPs.

3.3.7 XPS

To explain the processes that take place during the acquisition of an XPS spectrum, the band structure will have to include definitions of several additional properties. Above the conduction band are the vacuum states; excitation of an electron to these states corresponds to the ionisation of the material and the ejection of the electron from the surface of the material. The boundary between the conduction band and the vacuum states is known as the vacuum level (E_{vac}); once again, E_f is the Fermi level. ϕ_A is the *work function*, and is the energy between the vacuum level and the Fermi level; and the energy required to achieve an electronic transition into the vacuum is known as the binding energy, E_b . X-rays are energetic enough to excite core electrons into the vacuum states and XPS measures the kinetic energy of these ejected electrons via an electron energy analyser.

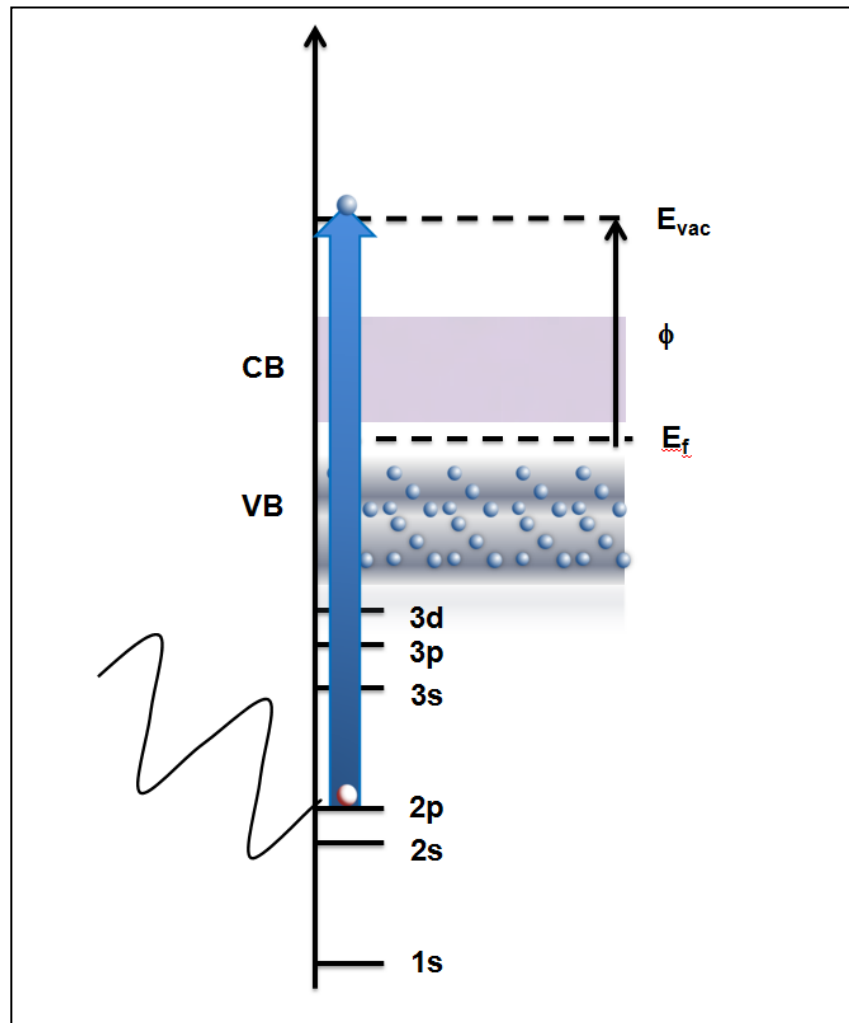


Figure 3-6 The XPS effect on a core level electron of an atom within a crystal structure

The binding energies of these core electrons can then be calculated with the following equation, where E_k is the kinetic energy of the electron:

$$E_b = h\nu - E_k - \phi$$

Here, XPS will be carried out to determine the oxidation state of Cu in the CuS NCs. To understand the XPS spectra for the Cu core electron in the 2 p shell, two important factors must be considered: Firstly, XPS spectra clearly displays spin-orbit splitting. This results in the Cu 2p shell being split into the $2p_{1/2}$ and $2p_{3/2}$ electronic energy levels, with the $2p_{3/2}$ peak appearing twice as intense in the XPS spectrum for Cu. Secondly, Cu^{2+} famously exhibits what are known as 'shake-up satellites' within its XPS spectra (Figure 3-7 **Error! Reference source not found.**).

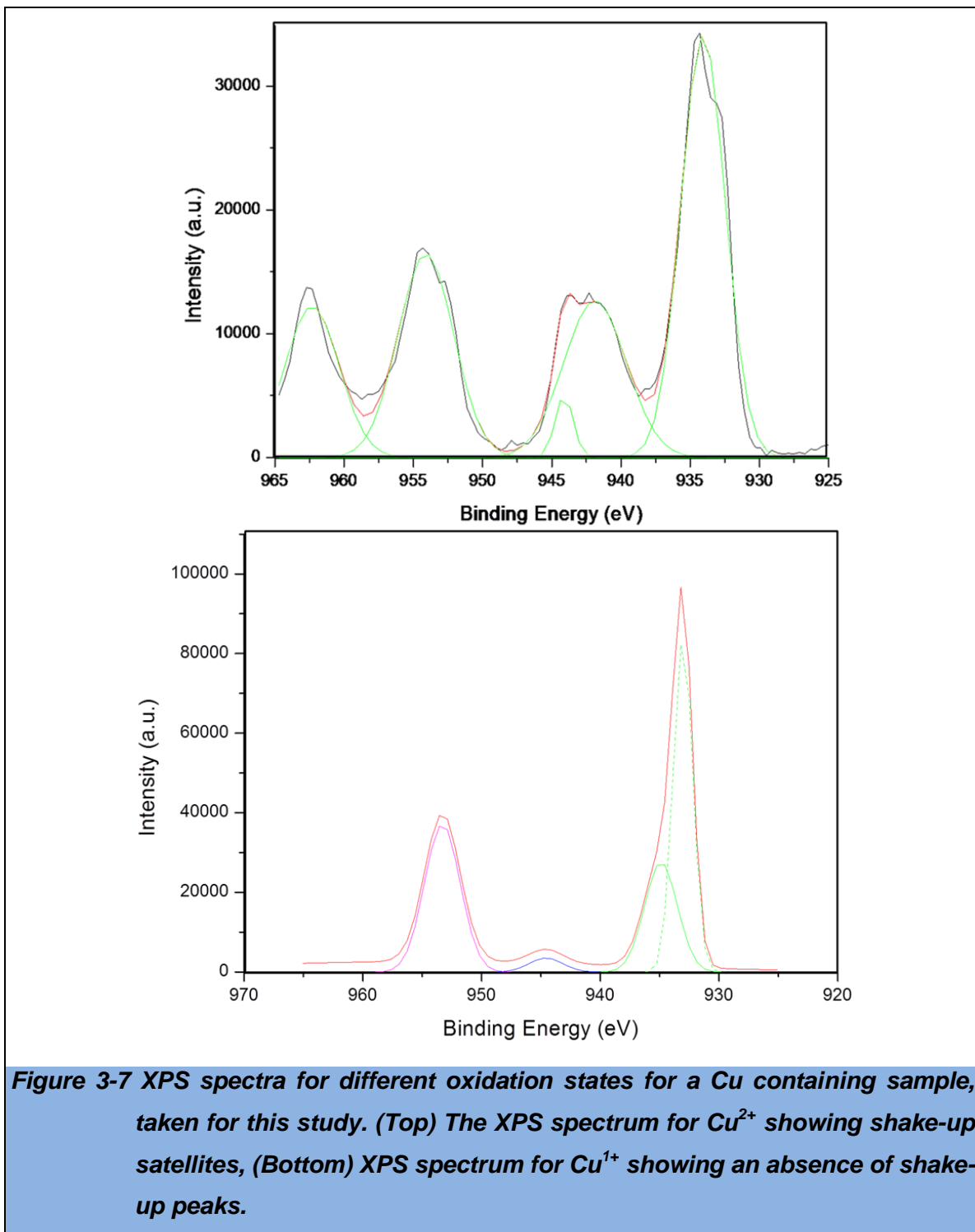


Figure 3-7 XPS spectra for different oxidation states for a Cu containing sample, taken for this study. (Top) The XPS spectrum for Cu²⁺ showing shake-up satellites, (Bottom) XPS spectrum for Cu¹⁺ showing an absence of shake-up peaks.

These occur when the excitation energy of the ejected electron is used to excite an ion to a higher energy level – typically a few eV above its ground state. This results in the ejected electron having a reduced kinetic energy, leading to secondary peaks appearing at higher E_b values. This is seen with the Cu²⁺ oxidation state but not for the Cu¹⁺ or Co⁰ oxidation states. This means XPS is a useful tool in the identification of the oxidation state of Cu in a material and will be used here to show the Cu²⁺ oxidation state of the CuS NC.

3.4 Experimental Methodology

3.4.1 General Preparatory Methods for Glassware

All of the glassware used in this study was first cleaned by washing with copious amounts of deionised water to help remove any potential contaminants. Acetone was further employed to remove any potential organic components that could still be present. Additional cleaning was carried out by the drop-wise addition of *aqua regia* to the inside walls and base of the glassware (approximately 10 ml) – a glass pipette is essential for this process as *aqua regia* is known to react violently with some organic materials. This was followed by gently tipping the glassware to ensure the entire inside surface of the container was washed with the solution. The *aqua regia* used for this preparation method was made from a 1:3 molar ratio of nitric acid and hydrochloric acid, respectively.

Aqua regia was employed to ensure the glassware was free from any inorganic contaminants, especially those embedded on the inside surface of the glassware. For analytical purposes, this was an important step: As the nanosensors were highly sensitive, any remaining contaminants could potentially provide false data from interfering ions. The solution was then disposed of over a large quantity of ice and neutralised with concentrated NaOH. The glassware was then washed with copious amounts of deionised water to remove and neutralise the acid, and sealed until it was required.

3.4.2 Preparation of the Metal Ion Containing Stock and Control Solutions and Addition to the Nanosensor Solutions

The aim of this project was to produce a nanosensors-based technique to detect at-least one type of metal ion that is present on the priority list of the Water Framework Directive and Drinking Water Directive. With the exception of $\text{FeSO}_4 \cdot 7\text{H}_2\text{O}$, the specific metal ion sources that are shown in Table 3.1 were selected to produce metal ion solutions of those metals found in Table 1.4 and Table 1.5, the priority substances quoted by the WFD and DWD (Section 0) - $\text{FeSO}_4 \cdot 7\text{H}_2\text{O}$ was added to the list of control solutions at the request of *United Utilities plc*, as it was predicted that iron may become a 'priority substance' in the near future. These particular sources were found to be standard sources for the required metal ions.

As all of the above ions can be present in aqueous systems the metal ion solutions were used as control tests to look for selective and interfering interactions between the ions and the nanomaterials. This is of fundamental importance for selective metal sensors, especially as the highly sensitive nature of the nanosensors meant that they could be liable to give false results, even under minor interferences.

All metal ion solutions were prepared on the day of use, by dissolving each metal ion source in deionised water to make up the desired concentration (Table 3.1). $\text{FeSO}_4 \cdot 7\text{H}_2\text{O}$ was prepared using deionised water that had been degassed with nitrogen to remove dissolved oxygen that readily oxidises Fe^{2+} ions to Fe^{3+} . This involved bubbling nitrogen gas through the deionised water for two hours. The solution was then prepared as described below and sealed with a nitrogen atmosphere. An additional method is sometimes employed within the literature, using sulphuric acid to delay the oxidation process. This alternative was deemed unfit for this study as the reduced pH value of the ion solution would affect the speciation state of the surface-bound citrate molecules, interfering with the comparative study between the NPs and the different divalent ions.

The respective powders were weighed out in a tarred weighing boat (Table 3.4).

Table 3.4 Recipe for the production of the metal ion stock solutions			
Required Aqueous Metal Ion	Metal Ion Source	Amount of Metal Ion Source Added to 1000 ml	Concentration of Metal Ion in Stock Solution
Pb²⁺	$\text{Pb}(\text{NO}_3)_2$	0.1262 g	$3.81 \times 10^{-4} \text{ M}$ ($79.00 \times 10^3 \mu\text{g/l}$)
Cd²⁺	CdCl_2	0.0698 g	$3.81 \times 10^{-4} \text{ M}$ ($42.85 \times 10^3 \mu\text{g/l}$)
Ni²⁺	NiCl_2	0.0494 g	$3.81 \times 10^{-4} \text{ M}$ ($22.38 \times 10^3 \mu\text{g/l}$)
Hg²⁺	HgCl_2	0.1034 g	$3.81 \times 10^{-4} \text{ M}$ ($76.47 \times 10^3 \mu\text{g/l}$)
Fe²⁺	$\text{FeSO}_4 \cdot 7\text{H}_2\text{O}$	0.1059 g	$3.81 \times 10^{-4} \text{ M}$ ($21.29 \times 10^3 \mu\text{g/l}$)

The powders were then added to individual 1000 ml volumetric flasks. A small amount of deionised water was initially added to each weighing boat, via a Pasteur pipette, to wash off any visible solid, which was then poured into the flask. The dry

weighing boat was returned to the balance to ensure there was no measurable residue remaining. This ensured that all of the powder had been transferred into the flasks ensuring accurate concentrations could be established. After the solutions were made up to the 1000 ml volumetric level, magnetic stirrer bars were added. These were rotated to disperse the solid within the solution. The solutions were left stirring for three hours to ensure that the solid had dissolved.

The limits of detection of metal ions for the majority of nanosensor-based analytical techniques are usually within the *ng/l* or *µg/l* concentration range - with a smaller portion having detection levels lower than *ng/l*. A further objective of this project was to produce a nanosensor-based technique that is competitive with both standard analytical methods and current nanosensors-based techniques. Because of this, the metal ion stock solutions needed to be diluted down to within the *ng/l* to *µg/l* concentration range. This was achieved by a sequence of standard serial dilutions.

All of the metal ion solutions were mixed with the AuNP, AgNP and CuS nanocluster solutions as a one to one, volume to volume ratio.

3.4.3 *Synthesis of the Citrate Functionalised Gold Nanoparticles and Citrate Functionalised Silver Nanoparticles*

The citrate functionalised AuNP and AgNPs were synthesised for use as LSPR-shift based nanosensors for the detection of one of the above metal ions, with the AuNPs additionally being produced for a SERS-based technique. The citrate molecules were chosen for their affinity for divalent metal ions.

The AuNPs and AgNPs were synthesised through a standard reduction method, utilising trisodium citrate dihydrate to reduce gold chloride and silver nitrate, respectively.^{98,99} These methods were selected due to their simplicity and reliability for creating uniformed monodispersed nanoparticles. These techniques are also highly reproducible, making it easy to recreate nanoparticles with the same diameters for repeated experiments. Being able to create uniformed NPs was important for the sensitivity of the LSPR-based analysis in two major ways (see Section 2.4): For relatively smaller particles, a larger shift in the local refractive index can be expected due to the ratio of metal ions to surface area increasing;

additionally, a mixture of particle sizes would lead to a range of LSPR values, showing as broad and potentially asymmetrical absorbance peaks, making it difficult to accurately calculate the concentration of the aqueous metal ions.

To synthesise the AuNPs used in this study: 105 *ml* of deionised water was heated to boiling in a 250 *ml* conical flask. The water was removed from the heat and trisodium citrate dihydrate (61.7 *mg*) was added under stirring. A 1 *ml* aqueous solution containing gold chloride trihydrate (HAuCl₄.3H₂O) (9.9 *mg*) was added to the hot citrate solution and left for 15 minutes. The solution became increasingly red, indicating the synthesis of gold nanoparticles.

For the synthesis of the AgNPs: Firstly, a 50 *ml* of an aqueous AgNO₃ solution (1 x 10⁻³ *M*) was heated to boiling. To this solution, a 5 *ml* aqueous solution of trisodium citrate dihydrate (58.7 *mg*) was added drop-wise using a Pasteur pipette whilst vigorous stirring the solution with a magnetic stirrer. When the solution became pale yellow it was removed from the heat source. Stirring was continued until the solution had cooled to room temperature. The solution was then made up to 105.7 *ml* to keep the citrate concentration equal in both the AuNP and AgNP solutions. This was important for quantitatively comparing the interactions between the metal ions and the surface-bound citrate molecules on the AuNPs and AgNPs.

3.4.4 *Synthesis of the Metal Sulfide Ion-Exchange Nanoclusters*

Clusters with diameters of < 5 *nm* were employed for two main functions. Firstly, the addition of exchangeable cations leads to a complete rearrangement of the crystal structure to a more favourable geometry. When the ionic radii of the exchangeable cations are comparable, the new cluster retains a diameter comparable to that of the sacrificial cluster (Section 2.8.2.2). This allows the production of clusters via an easier route, if the normal synthetic route is lengthy or difficult. Secondly, clusters have very high surface to volume ratios, relative to their nanoparticle and bulk counterparts. Any exchanged cation at the surface of a cluster will provide a relatively higher contribution to the electronic structure compared to an exchanged cation at the surface of a nanoparticle. This translates as: clusters should provide a more sensitive optical detection system as small concentrations of target ions will have a large effect on the properties of the

cluster, meaning it would take a smaller concentration of metals to cause a detectable change in the spectra of the NCs.

The synthesis of the CuS nanoclusters used a 3-step-synthesis route: The initial step was to synthesise a solution of ZnS nanoclusters, to be used as sacrificial templates for the production of CuS. The production of CuS nanoclusters then followed via the intermediate cluster material Cu_2S .

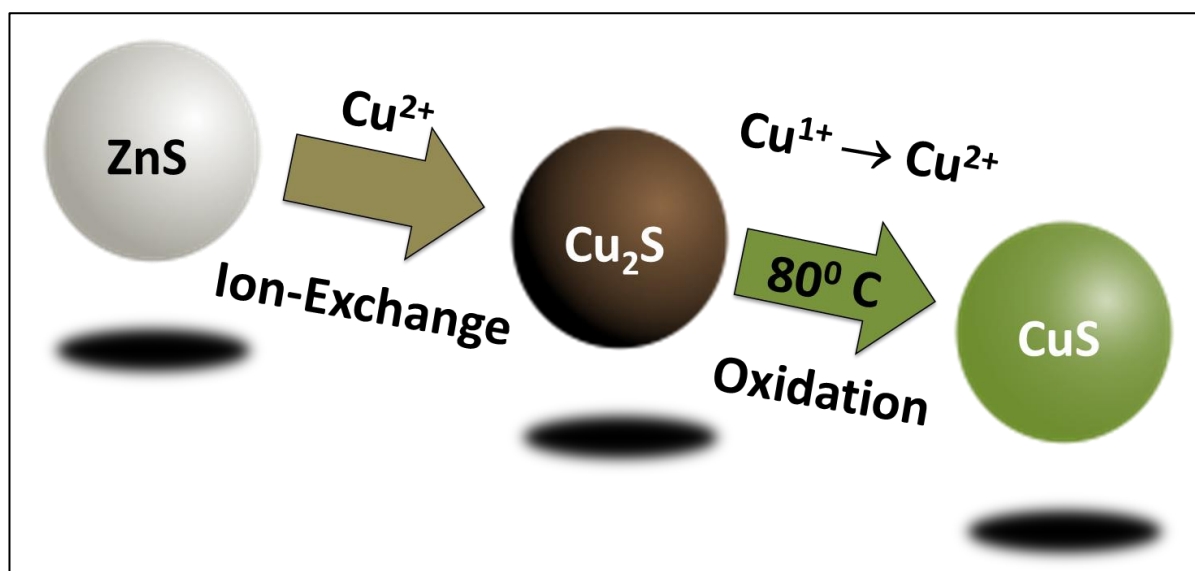


Figure 3-8 Schematic for the synthesis steps for the production of the CuS NCs used here

As CuS clusters are usually synthesised by much lengthier routes, ZnS clusters were selected as sacrificial templates: This selection was made due to the higher solubility product constant of ZnS, and the rapid room temperature synthesis route utilised to produce uniform sized clusters. This provides an easier, alternative, synthetic route for the synthesis of the CuS clusters.

Due to Cu_2S having a lower k_{sp} value than CuS, the addition of Cu^{2+} ions to the solution of ZnS clusters will result in the production of Cu_2S . A further step is then required to convert the Cu^{+1} oxidation state of Cu_2S to the Cu^{2+} oxidation state of CuS. An oxidation reaction is instigated via the heating of the Cu_2S cluster solution, finally resulting in the desired CuS cluster solution.

3.4.4.1 The Three-Step Synthesis of the CuS Nanoclusters

ZnS nanoclusters, between the sizes of 2-3 nm, were synthesised using the method described by Iqbal *et al.*¹⁰¹ Whilst the solution was being stirred, 50 ml of Na₂S·9H₂O (20 mM) was added drop-wise to a 250 ml conical flask containing 50 ml of Zn(CH₃COO)₂·2H₂O (20 mM). This was carried out with constant stirring over a period of 20 minutes at room temperature. During this time the solution changes from clear to white, indicating the production of the ZnS cluster solution.

The secondary step involves the addition of Cu²⁺ ions to the ZnS nanocluster solution. This step leads to a cation-exchange process between the Zn²⁺ ions within the ZnS structures and the free Cu²⁺ ions in the solution, rapidly producing Cu₂S nanoclusters – due to the lower solubility product constant of Cu₂S this is the preferred stoichiometry for the cluster (2×10^{-47} , compared to ZnS (4×10^{-24}) and CuS (4×10^{-38})).

The final step to this procedure is the oxidation of the Cu₂S nanoclusters. This is carried out to obtain the CuS clusters. This is achieved by refluxing the solution of Cu₂S clusters to *c.a.* 80°C for 1 hour. The solution will change from brown to green, displaying the presence of the CuS nanoclusters.

3.5 Experimental Conditions for Sample Analysis and Characterisation

3.5.1 TEM and HRTEM Analysis

For TEM and HRTEM analysis, nanomaterial samples were prepared by drying 5 x 20 µl drops of the sample solution onto a carbon mesh TEM grid. This disk was then allowed to dry in air at room temperature.

3.5.2 UV-Vis Absorption Spectroscopy

For UV-Vis analysis, the AuNP, AgNP, and CuS NC solutions were placed in a 1 x 1 x 5 cm quartz cuvette. The entrance and exit slit widths were set as 2 nm each and the spectral region of 200 nm to 1100 nm was scanned for each sample. Deionised water was used as a blank sample for each measurement.

UV-Vis spectra for the SERS samples was obtained by using a clean microscope slide as a blank and attaching the SERS sample to the inside of the spectrometer, ensuring that the sample was in line with the spectrometer beam and detector.

3.5.3 Measurements of the size and colloidal stability of the nanomaterials in solution using photon correlation spectroscopy

PCS measurements were obtained by adding the sample solutions to a 1 x 1 x 5 *cm* plastic cuvette. The plastic cuvette was then placed within a Zetasizer nano ZS. The detector was set up in Optimisation mode, which selects the best setup for the detector – this was 13⁰ forward scattering mode with a range of between 18 - 25 repeated measurements.

Note: The top of the liquid sample was filled into the cuvette so that the height of the solution was no more than 1 *cm*. This is partly due to the height of the laser, 8.5 *mm*, and additionally, too much liquid in the cell also increases the time the liquid needs to reach a thermal equilibrium. This is important, as the estimated size of the NP diameter is based on Brownian motion, and the speed at which the particle moves; a warmer solution will cause the NPs to move more rapidly, providing a false estimate - using the thermal cap (the plastic cell stop cap) helps maintain thermal stability.

3.5.4 Measurement of Metal Ion Induced pH Changes

This system was calibrated using two separate buffer solutions of pH 7 and pH 4. The electrode was always washed with deionised water before and after the emersion of the probe into the buffer and sample solutions. This was to ensure that there was no cross contamination of the sample, or the buffers, that may provide false readings. The electrode was placed within a solution which was being stirred via a magnetic stirrer. This was to help the probe reach a stable pH reading. For the timed study carried out in section 4.4, the electrode was left submerged for the duration of the experiment.

3.5.5 ATR-FTIR Spectroscopy

Attenuated total reflectance Fourier transform infrared spectroscopy (ATR-FTIR) was used to obtain the vibrational spectra of the surface-citrate and metal-citrate species present on the surfaces of the AuNPs and AgNPs. Solutions were added as a single 20 μl drop onto a glass slide and allowed to dry in air. A blank ATR-FTIR sample spectrum was obtained for a clean glass slide and then the spectra were recorded by placing the sample face down onto the ATR crystal. The spectra were taken for the range of 3650 cm^{-1} to 650 cm^{-1} in transmission mode.

3.5.6 Computational IR Spectroscopy Calculations

Calculated IR spectra for the surface-citrate molecules, and for the heavy metal ions bound to the surface-citrate molecules, were studied using a semiempirical *PM6* method by using *MO-G* for the *SCIGRESS* program.^{101,102} To simulate the surface of the Au and Ag NPs a 3 x 3 x 3 sheet consisting of the respective NP atoms was created. These atoms were then fixed at their geometrical coordinates so that the sheet would not deform during geometrical optimization. Citrate molecules were then added to the surface by one or two of the carboxylate groups. Before IR spectral predictions were calculated, all of the chemical structures were geometrically optimized by a molecular mechanics method (*MM2*). This process was then repeated with one of the heavy metal ions situated in close proximity to the surface bound-citrate molecule, to give a geometrically stabilised metal-citrate complex at the surface of the sheet.

3.5.7 Surface Enhanced Raman Spectroscopy

SERS spectroscopy was used to obtain vibrational spectra of the citrate functional molecules on the AuNPs surfaces, before and after the addition of different concentrations of metal ions. The SERS samples were prepared by dropping 3 x 20 μl of the solution of AuNPs, or metal ion/AuNP mixtures, onto glass slides. After the addition of each drop the glass slides were dried at room temperature. The repeated addition of the small volume of AuNP or metal ion/AuNP solutions glass slides was carried out to create a closely packed AuNP array to increase the Raman signal.

The Raman spectrometer was calibrated using the spectrum of a Si wafer to a Raman shift value of 520 cm^{-1} .

The Raman spectra were obtained using a confocal objective with a $20\ \mu\text{m}$ slit width. A total of 5 measurements were taken for each sample, each with a 15 s exposure. Background removal was done by applying a polynomial baseline of around $n = 4 - 5$.

3.5.8 XPS

CuS NC samples were prepared for XPS analysis by drying $5 \times 20\ \mu\text{l}$ drops of the NC solutions onto glass slides. These slides were then allowed to air dry. For analysis, the sample slides were cut into smaller segments and placed on the conductive sample holder of the XPS spectrometer - this reduces charging effects which would alter the electronic structure of the sample and provide inaccurate data. The instrument was set up using a dual beam charge compensation system and an x-ray beam spot size of $400\ \mu\text{m}$, focused onto the sample material. The x-ray energy was $1486.68\ \text{eV}$, provided by an $\text{Al-K}\alpha$ source. High resolution scans were obtained with a data point frequency of $0.4\ \text{eV}$, for a multiple of 4 scans, for the Cu $2\text{p}_{1/2}$ and $2\text{p}_{3/2}$ peaks. The data was plotted using the Origin 6.0 software. A spectrum of the C (1s) peak is usually taken to serve as a reference peak, which the entire spectra will be off-set to align the C 1s peak with a binding energy of $284.8\ \text{eV}$; but as the Cu XPS spectra are only been shown for qualitative purposes, this spectra has not been included.

4 Results and Discussion (Part 1): The Response of Citrate Functionalised Gold and Silver Nanoparticle Solutions to the Addition of Heavy Metal Ions

4.1 Introduction

The aim of this project was to produce a functional nanomaterial that can be used to detect a heavy metal (Pb, Cd, Ni, or Hg) in an aqueous sample, at concentrations between 30 $\mu\text{g/l}$ to 0 ng/l . This 'practical' concentration range was decided on as the 'acceptable' concentrations set by the WFD and DWD fall within this regime (Section 1.3).

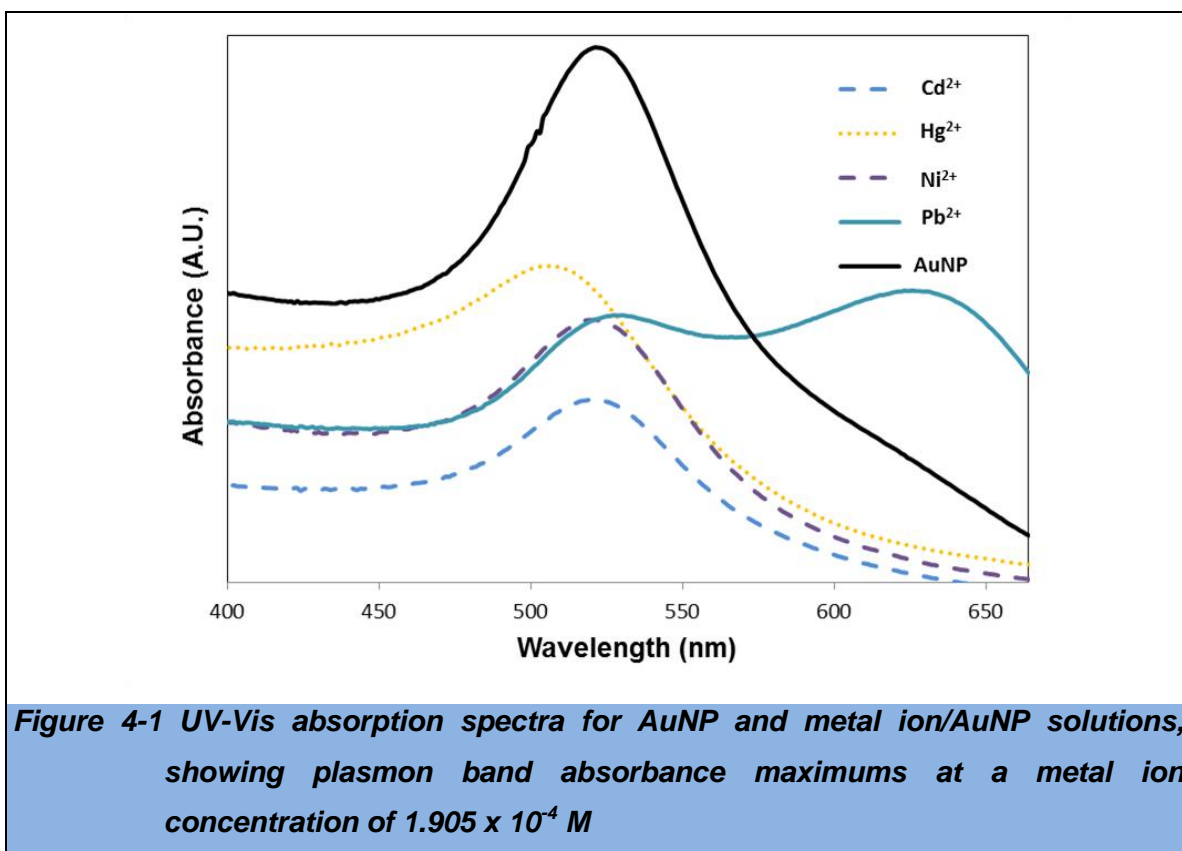
The current chapter presents experimental data pertaining to the response of the citrate functionalised AuNPs and AgNPs synthesised here, to the addition of different metal ions (Pb^{2+} , Cd^{2+} , Ni^{2+} , and Hg^{2+}). Characterisation of these NP/metal ion solutions was carried out using TEM, UV-Vis LSPR absorption spectroscopy, PCS, pH measurements, and ATR-FTIR. Additionally, to help explain these results, this data were compared with computational simulations of the surface-citrate and metal-surface-citrate species on the surfaces of the NPs. This collection of data was then utilised to study whether the nanomaterials could be used as nanosensors within the 'practical' concentration regime, and therefore be suitable for industrial use.

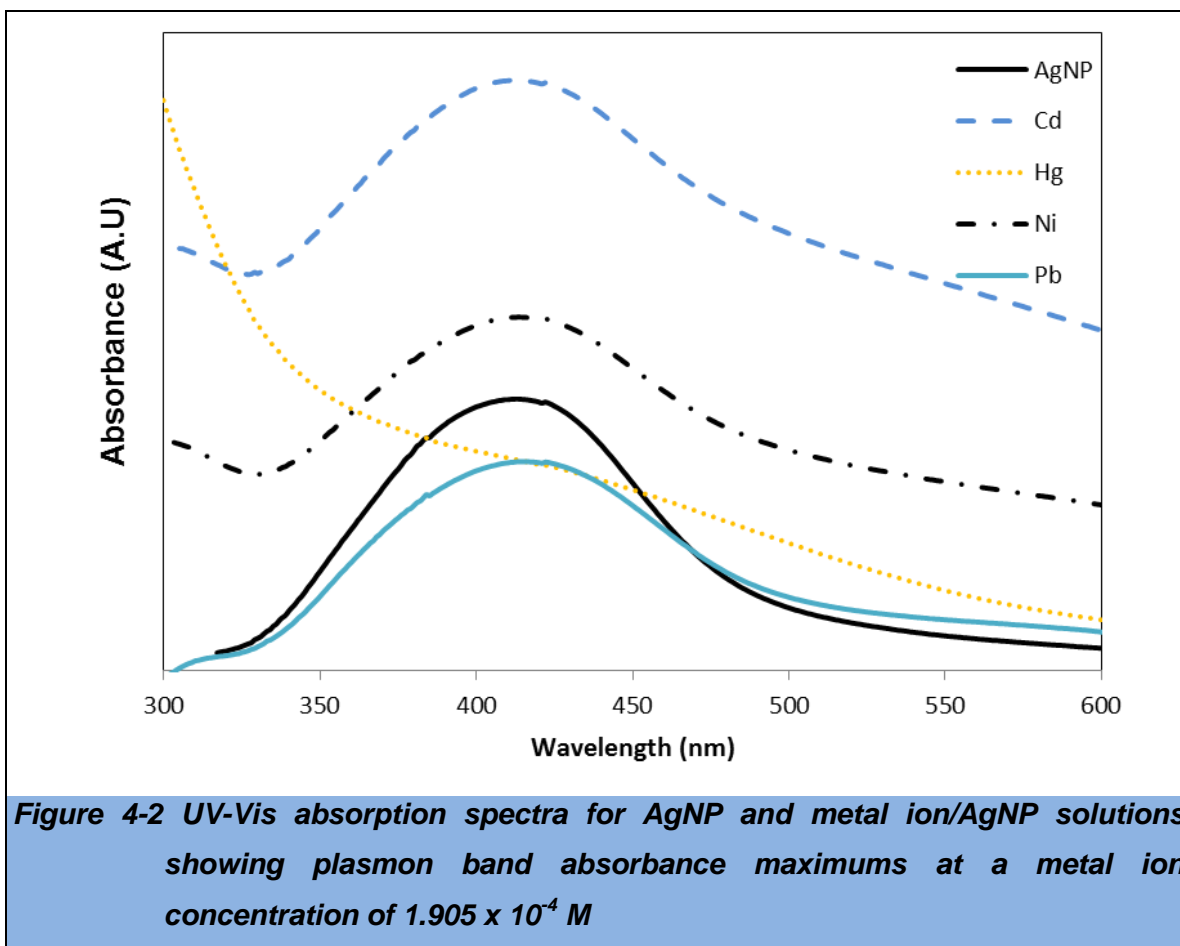
4.2 *The response of the plasmon band absorption peak for citrate functionalised gold nanoparticle solutions upon the addition of heavy metal ions*

Following the procedure described in Section 3.5.2, a UV-Vis absorption spectrum for each solution of freshly prepared AuNPs and AgNPs was taken. This technique was used to show the characteristic plasmon band absorption peak of the NPs.

This is a fundamental characterisation technique for plasmonic NPs and is the foundation for this type of sensing technology (see Section 2.4). AuNP and AgNP solutions, containing both the plasmonic NPs and a metal ion (Ni^{2+} , Cd^{2+} , Hg^{2+} , or Pb^{2+}), were then prepared by the method described in Section 3.4.2. Following this, the corresponding UV-Vis absorption spectra were taken to compare the plasmon band absorption peak positions, relative to the as-prepared AuNP and AgNP solutions (Figures 3.1 and Figure 4-2).

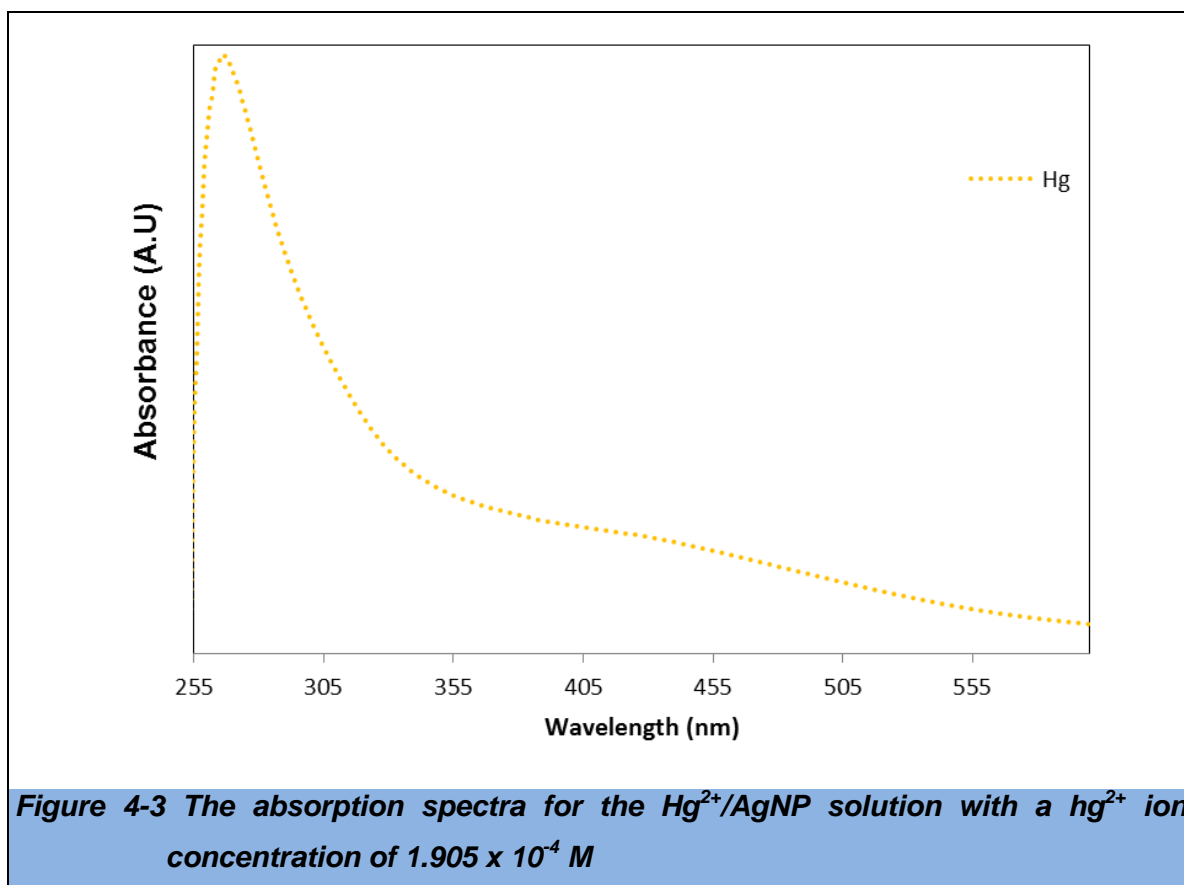
The AuNP solution prepared by the citrate reduction route was characteristically red, displaying an optical absorption spectrum with a distinctive plasmon band absorbance maximum at 525 nm (Figure 4-1). The AgNP solution, also prepared via the citrate reduction route, displayed a characteristic yellow, with a plasmon band absorbance maximum at 415 nm (Figure 4-2). Figure 4-1 and Figure 4-2 also show that metal ion/AuNP and metal ion/AgNP solutions, containing Ni^{2+} , Cd^{2+} , Hg^{2+} , or Pb^{2+} ions at concentrations of $1.905 \times 10^{-4} \text{ M}$, resulted in a shift in the wavelength of the plasmon band absorbance maximum.





The solutions $Ni^{2+}/AuNP$ and $Cd^{2+}/AuNP$ exhibited a shift of $-2 nm$ in the plasmon band absorption peak, whilst the $Hg^{2+}/AuNP$ solution produced shift of $-18 nm$. In contrast, the solutions $Ni^{2+}/AgNP$, $Cd^{2+}/AgNP$ and $Pb^{2+}/AgNP$ exhibited a shift in the plasmon band absorption peak of $+1 nm$, $-1 nm$ and $+3 nm$ respectively. These relatively minor shifts, on the order of $1 nm$ to $18 nm$, are due to the relationship between the absorption spectra and the local refractive index at the surface of the NPs – the basis for this sensing technology (Section 2.4). This relationship indicates that the metal ions were interacting with the surface of the NPs. A further assumption can be made that the metal ions are interacting with the surface-citrate molecules due to their high affinity for divalent metal ions. Interestingly, the position of the plasmon band absorbance maximum for the $Hg^{2+}/AgNP$ solution is dominated by a broad absorption that partially masks the plasmon band absorption. Because of this it is difficult to produce a value for the exact position of the plasmon band maximum absorbance. This broad absorption is not typical of absorption spectra of plasmonic NPs, which generally show well resolved absorption peaks - as can be seen from the absorption spectra of $Ni^{2+}/AuNP$ and

$\text{Cd}^{2+}/\text{AuNP}$, $\text{Hg}^{2+}/\text{AuNP}$, $\text{Ni}^{2+}/\text{AgNP}$, $\text{Cd}^{2+}/\text{AgNP}$ and $\text{Pb}^{2+}/\text{AgNP}$ (Figures 3.1 and 3.2). The literature suggests that this peak is due to the formation of an Ag/Hg amalgam.^{103,104} This has been seen to cause a blue-shift in the AgNP absorption spectrum, creating a new plasmon absorption band $\sim 268 \text{ nm}$. This is shown by the intense peak positioned at 266 nm (Figure 4-3).



Notably, the $\text{Pb}^{2+}/\text{AuNP}$ solution was the only sample at a metal ion concentration of $1.905 \times 10^{-4} \text{ M}$ to display two absorbance maxima associated with plasmon band absorption. This sample produced shifts to the plasmon band peak of $+6 \text{ nm}$ and $+108 \text{ nm}$. The relatively large shift is due to plasmon-coupling effects, typically caused by the aggregation of AuNPs (Section 2.3). This is further backed by the observation that, whilst all of the other metal ion/AuNP solutions remained red, the $\text{Pb}^{2+}/\text{AuNP}$ solution turned blue before becoming colourless (Figure 4-4): As stated in Section 2.4, a blue AuNP solution is characteristic of aggregation and plasmon coupling occurring due to the appearance of a broad plasmon band from around $\sim 500 \text{ nm}$ to $\sim 700 \text{ nm}$, causing blue light to be scattered.



Figure 4-4 (Left to Right): AuNP and Ni²⁺/AuNP, Cd²⁺/AuNP, Hg²⁺/AuNP and Pb²⁺/AuNP solutions, with a 1.905 x 10⁻⁴ M metal ion precursor concentration, 24 hours after mixing

As with the other metal ion/AuNP solutions, the small shift of +6 nm suggests that this shift is a result of the interaction between the Pb²⁺ ions and the surface citrate molecules. As all of the other metal ion/AuNP solutions remained red, this shows there is a lack of AuNP aggregation in these solutions. This is summarised in Figure 4-5.

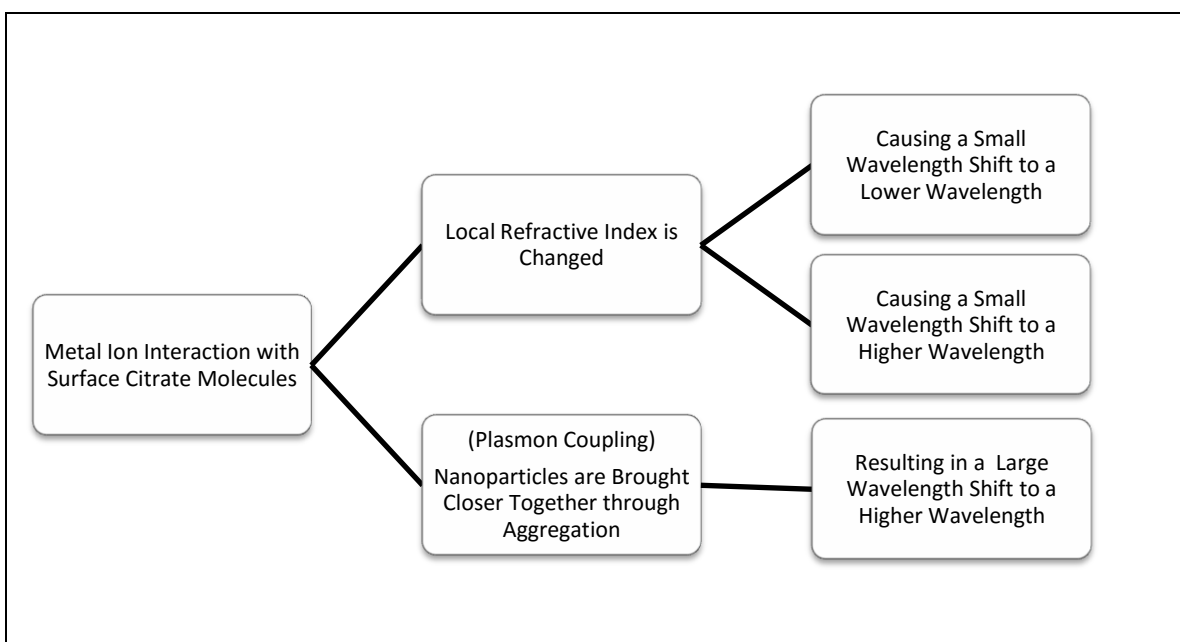
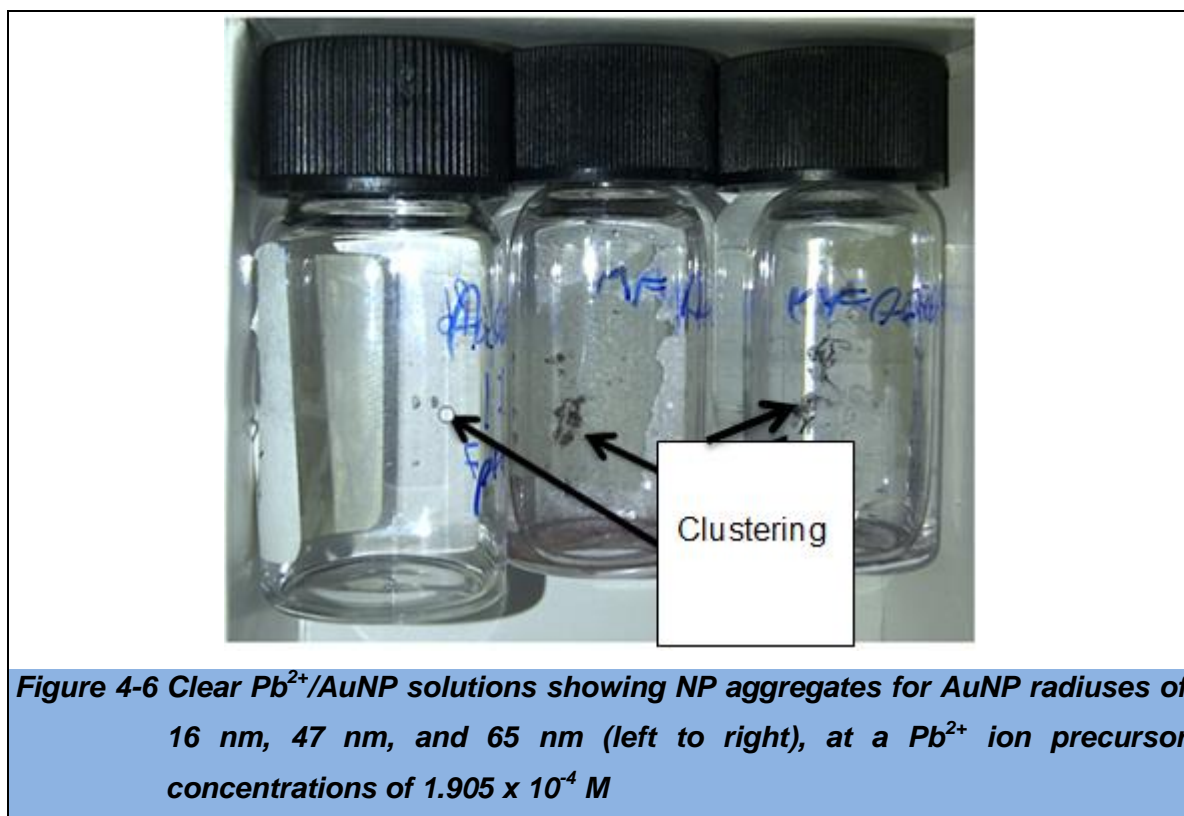


Figure 4-5 Diagram explaining the effect of a local refractive index change, compared to plasmon coupling caused by nanoparticles in close proximity, on the position of the plasmon band absorption peak in the UV-Vis absorption spectrum.

The exhibited colour change from red to blue, for the Pb²⁺/AuNP solution, has been shown to be a result of plasmon coupling; but the colour change from blue to colourless is not an attribute of plasmon coupling. A hint at the reason behind this colour change was seen when repeating the Pb²⁺/AuNP mixture with larger

AuNPs with radii of 65 nm, 47 nm, and 16 nm: Pb^{2+} /AuNP solutions, produced from these larger AuNPs also became clear at a Pb^{2+} ion concentration of $1.905 \times 10^{-4} M$; but in these solutions, a precipitate of AuNPs could clearly be seen (Figure 4-6).



This aggregation behaviour accounts for the blue colour that is observed, as plasmon coupling is attributed to plasmonic NPs being in close proximity. The solution then becomes colourless because of a reduction in the scattering of light by the NPs, as the aggregated AuNPs reach a critical mass and precipitate out of solution. PCS and TEM imaging was employed to further support this hypothesis.

In contrast, the Pb^{2+} /AgNP solution did not show any plasmon coupling effects. This shows a great difference in response with the only variable being the nanomaterial used i.e. Au or Ag NPs. Intriguingly, all of the metal ion/AgNP solutions showed slight shifts in the plasmon band maximum. Although, after 24 hours all of the metal ion/AgNP solutions showed a band of colour, which had formed in the lower half of the sample vial (Figure 4-7), implying slight sedimentation of the AgNPs. However, no plasmon coupling effects were observed in the UV-Vis absorption spectra. This suggests a slight destabilising of

the AgNPs in solution but this is not significant enough to cause plasmon coupling, as in the $\text{Pb}^{2+}/\text{AuNP}$ solution.



Figure 4-7 The solutions of (from left to right) AuNP, $\text{Hg}^{2+}/\text{AgNP}$, $\text{Cd}^{2+}/\text{AgNP}$, $\text{Ni}^{2+}/\text{AgNP}$ and $\text{Pb}^{2+}/\text{AgNP}$ with the metal ion/AgNP solutions showing slight sedimentation

4.3 Size characterisation with PCS and TEM imaging

TEM micrographs were obtained to obtain a physical image of the NPs to characterise them on size, spherical appearance and aggregation. PCS was performed using the procedure described in section 3.3.4. This analysis technique was employed to measure the size of the as-prepared AuNP, AgNP solutions, and the NPs in the metal ion/AuNP mixtures.

When comparing data obtained from PCS analysis for the AuNPs and AgNPs, the diameters estimated are comparable to those seen in the TEM micrographs acquired here. PSC data provided an estimated diameter of 6 nm for the as-prepared AuNPs and 4 nm for the as-prepared AgNPs. These estimations were verified with TEM imaging (Figure 4-8 and Table 4.1). All of the metal ion/NP solutions were estimated to have particle size increases compared to the AuNP and AgNP solutions.

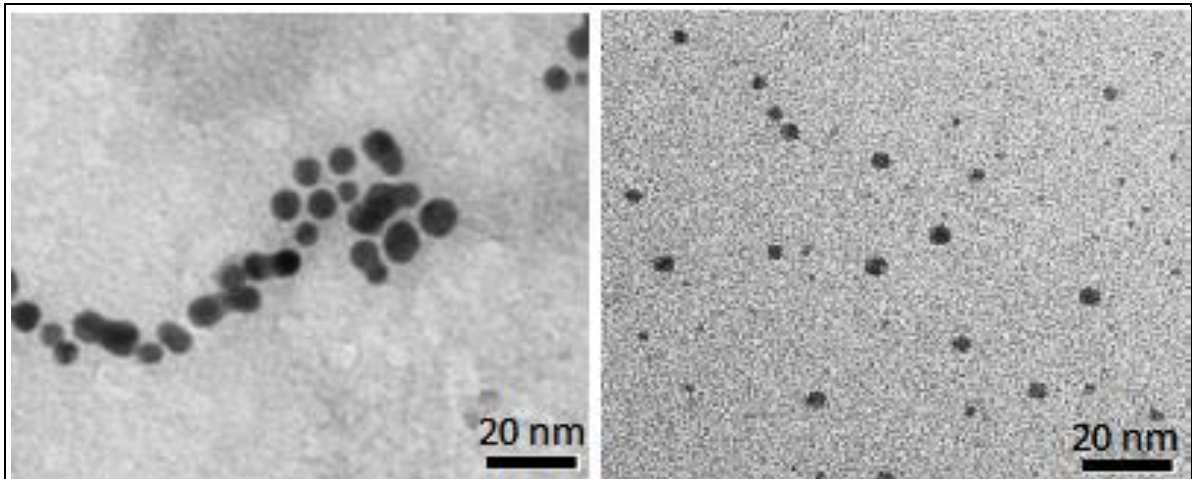


Figure 4-8 TEM micrographs for the AuNP (left) and AgNP (right) solutions

Further PCS results indicated the presence of large particles in the $\text{Pb}^{2+}/\text{AuNP}$ sample ($>200 \text{ nm}$), which are assigned to large aggregates composed of the 6 nm AuNPs. Additionally, all of the other metal ion/AuNP solutions, at the same concentration of metal ions, displayed a diameter increase, although this was not on the magnitude of the $\text{Pb}^{2+}/\text{AuNP}$ solution: The other metal ion/AuNP showed relatively similar size increases of between 10 nm and 12 nm , which can also be assigned to aggregates composed of the 6 nm AuNPs (Table 4.1). Results for the metal ion/AgNP solutions gave an estimated size increase within the range of 5 nm to 17 nm . Unlike the $\text{Pb}^{2+}/\text{AuNP}$ solution, none of the metal ion/AgNP solutions showed the presence of large aggregates.

Table 4.1 Diameter estimation by PCS and TEM imaging for the AuNP and AgNP solutions in the presence of Ni²⁺, Cd²⁺, Hg²⁺, and Pb²⁺ ions (1.905 x 10⁻⁴ M)

Sample	Metal ion	Metal Ion Concentration (M)	Average Particle Diameter Obtained via PCS (nm)	Average Particle Diameter Obtained via TEM (nm)
AuNP	-	-	6	6 - 10
Pb ²⁺ /AuNP	Pb ²⁺	1.905 x 10 ⁻⁴	>200	
Cd ²⁺ /AuNP	Cd ²⁺	1.905 x 10 ⁻⁴	16	
Ni ²⁺ /AuNP	Ni ²⁺	1.905 x 10 ⁻⁴	18	
Hg ²⁺ /AuNP	Hg ²⁺	1.905 x 10 ⁻⁴	18	
AgNPs	-	-	4	4 - 5
Pb ²⁺ /AgNP	Pb ²⁺	1.905 x 10 ⁻⁴	16	
Cd ²⁺ /AgNP	Cd ²⁺	1.905 x 10 ⁻⁴	15	
Ni ²⁺ /AgNP	Ni ²⁺	1.905 x 10 ⁻⁴	20	
Hg ²⁺ /AgNP	Hg ²⁺	1.905 x 10 ⁻⁴	8	

This shows that compared to all of the other metal ion/AuNP solutions characterised here, Pb²⁺ ions have a unique interaction with the citrate molecules on the surface of the AuNPs. This unique interaction led to the destabilisation and aggregation of the AuNPs, and a resulting change in the optical properties of the NPs (via plasmon coupling).

Commonly, NPs are found to aggregate when the surface charges of the particles are not sufficient to produce adequate particle-particle repulsion. This principle has been explained by Derjaguin, Lindau, Verwey and Overbeek (DLVO) theory. DLVO theory states that the stability of a colloidal system is dependent on the sum of the van der Waals attractive forces and the repulsive electrical double layer forces present between the NPs.¹⁰⁵ Theoretically a stable surface charge is defined as either ± 40 mV, which provides enough particle-particle repulsion to prevent aggregation.

To study the surface charge, and thus the stability, of the AuNP solution and the metal ion/AuNP solutions, zeta-potential measurements were carried out. The negatively charged deprotonated carboxylic groups of the surface-citrate molecules of the AuNPs were found to possess a surface charge of -44.30 mV . As predicted by DLVO theory, this provided enough particle-particle repulsion to stop the AuNPs from aggregating instantly. When comparing the surface charge values for the AuNP and AgNP solutions, the AuNP solution was found to be more than twice as negative. This shows that the AgNP solution was less stable, with respect to surface charge, than that of the AuNP solution. This would explain the appearance of a coloured band in the metal ion/AgNP and AgNP solutions as there was less particle-particle repulsion, bringing the NPs closer together resulting in slight sedimentation (Table 4.2). A reason for this difference is likely due to different citrate species being present on the surfaces of the AuNPs, with respect to the AgNPs: Assuming that all of the surface-citrate carboxylate groups are deprotonated, different binding modes of the surface-citrates will result in different numbers of carboxylate groups pointing away from the surface of the NP *i.e.* the more carboxylate groups pointing away from the surface of the NP, the greater the negative surface charge of the NP. This translates to the greater negative charge at the surfaces of the AuNPs, is due to a different surface-citrate binding mode, relative to the surface-citrate molecules on the surfaces of the AgNPs.

Table 4.2 Zeta potential results for the AuNP and AgNP solutions in the presence of Ni²⁺, Cd²⁺, Hg²⁺, and Pb²⁺ ions (1.905 x 10⁻⁴ M) metal ion concentration, 24 hours after mixing

Sample	Metal Ion Precursor Concentration in the NP Solution (M)	Zeta Potential (mV)
As-Prepared AuNP	-	- 44.30
Pb ²⁺ /AuNP	1.905 x 10 ⁻⁴	-1.11
Pb ²⁺ /AuNP	5 x 10 ⁻⁵	- 19.20
Cd ²⁺ /AuNP	1.905 x 10 ⁻⁴	~ (- 40)
Ni ²⁺ /AuNP	1.905 x 10 ⁻⁴	~ (- 40)
Hg ²⁺ /AuNP	1.905 x 10 ⁻⁴	~ (- 40)
As-Prepared Ag/NP	-	-16.6
Pb ²⁺ /AgNP	1.905 x 10 ⁻⁴	- 15.7
Cd ²⁺ /AgNP	1.905 x 10 ⁻⁴	- 13.5
Ni ²⁺ /AgNP	1.905 x 10 ⁻⁴	-16.3
Hg ²⁺ /AgNP	1.905 x 10 ⁻⁴	-17.5

Relative to the AuNP solution, the Ni²⁺, Cd²⁺, or Hg²⁺ metal ion/AuNP solutions showed a similar reduction in surface charge (~ +4.30 mV). Compared to any of the other metal ion/NP solutions the Pb²⁺/AuNP solution underwent a much larger reduction in the surface charge of the NPs (+43.2 mV). This significantly reduced the particle-particle repulsion, creating a more destabilized NP solution. For the metal ion/AgNP solutions, the introduction of Pb²⁺, Cd²⁺, or Ni²⁺ ions resulted in a reduction in the surface charge of between +0.3 to +2.9 mV. In contrast, Hg²⁺ ions were the only metal ions to cause an increase in the surface charge (-0.9 mV) but the mechanisms behind this are uncertain.

In solution, divalent metal ions can bind with free citrate molecules via the carboxylate groups and the protonated alcohol group. If Ni²⁺, Cd²⁺, Hg²⁺, or Pb²⁺ ions were to bind with the carboxylate groups of the surface bound citrate molecules there would be a reduction in the surface charge. This would then

reduce the particle-particle repulsion between the NPs and increase the potential for aggregation. With this in mind, it can be expected that the surface charge of the NPs became more positive upon the addition of Ni^{2+} , Cd^{2+} , Hg^{2+} , or Pb^{2+} ions (except in the case of $\text{Hg}^{2+}/\text{AgNP}$). This mechanism for the reduction in surface charge explains the reason for the observed aggregation, but further mechanisms for this reduction can be more numerous (Figure 4-9). Such routes may involve negative pH changes, which cause the build-up of positively charged protons around the NPs, reducing the overall negative charge surrounding the particle (Figure 4-9b); a negative change to the pH of the solution can additionally re-protonate the carboxylate groups of the surface citrate molecules (Figure 4-9c); a further reduction of the surface charge, due to the re-protonation of the carboxylate groups, can also occur during the interaction with the metal ions in solution, as part as a reaction mechanism. These will be discussed in the following sections (Section 3.1 - 3.3).

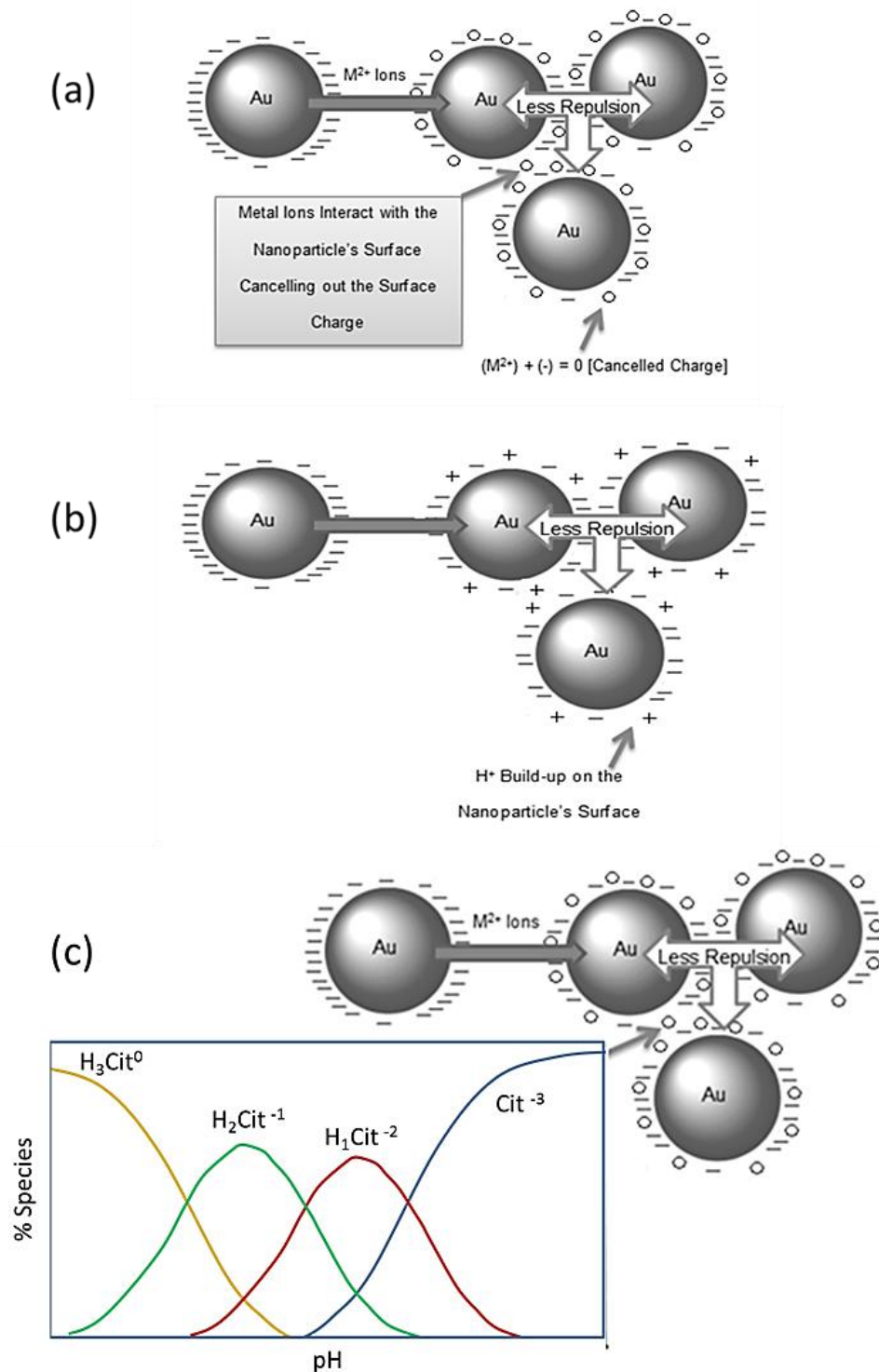


Figure 4-9 Illustrations showing the discussed mechanisms for NP destabilisation: (a) metal ion interactions with the negatively charged carboxylate groups of the surface-bound citrate molecules, (b) build-up of positive charges around the surfaces of the NPs, provided by an increase in the concentration of protons in the solution, (c) re-protonation of the negative carboxylate groups of the surface-bound citrate molecules upon the decrease in the pH of the NP solution

4.4 Change in pH of Metal ion/AuNP Solutions after the Addition of the Metal Ion Precursor

Due to the importance of the *pH* of the solution to the surface charge of the NPs, and the resulting particle-particle repulsion, the *pH* of the AuNP solution and metal ion/AuNP solutions was measured.

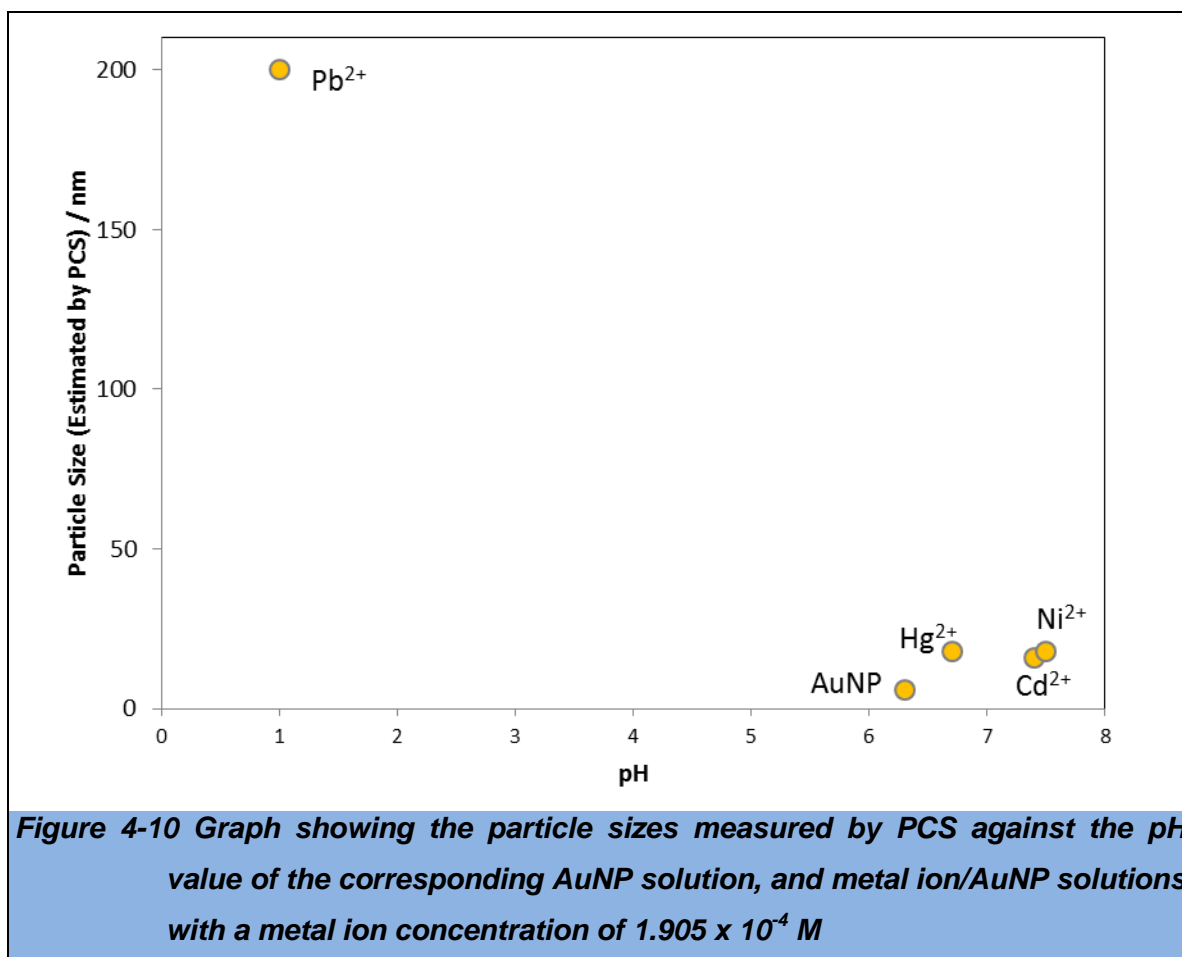
In addition to a relatively large reduction in the surface charge of the AuNPs, the Pb²⁺/AuNP solution, with a metal ion concentration of $1.905 \times 10^{-4} M$, displayed a relatively large reduction in the *pH* of the solution by -5.3 units. All of the other metal ion/AuNP solutions showed a change in the *pH* in the range of 0.4 to 1.3 units (Table 4.3).

Au Sample	Metal ion	Metal Precursor Concentration in AuNP Solution (M)	pH of Prepared Solutions after 24 hours
AuNP	-	-	6.3
Pb²⁺/AuNP	Pb ²⁺	1.905×10^{-4}	1.0
Cd²⁺/AuNP	Cd ²⁺	1.905×10^{-4}	7.4
Ni²⁺/AuNP	Ni ²⁺	1.905×10^{-4}	7.5
Hg²⁺/AuNP	Hg ²⁺	1.905×10^{-4}	6.7

Uniquely, the Pb²⁺/AuNP solution was the most acidic solution analysed. When the ion concentration was reduced by half, the *pH* of the solution had only decreased to a value of 4.58, leaving a blue/purple solution.

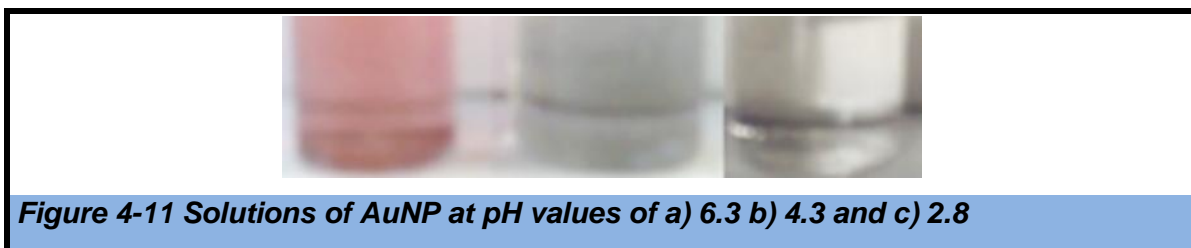
The large decrease in *pH* for the Pb²⁺/AuNP solution is an important find as the *pH* value of the AuNP solution affects the aggregation properties of NPs.¹⁰⁷ At lower *pH* values the positively charged protons in the solution will start to gather around the negatively charged surfaces of the NPs. This in turn reduces the surface charges and destabilises the NP solution. At a low enough *pH*, the protons will effectively cancel out the surface charge causing mass aggregation of the AuNPs

as the particle-particle repulsion diminishes. Therefore it cannot be said, that the aggregation of the AuNPs was solely due to the positively charged Pb^{2+} ions interacting with the negatively charged carboxylate groups of the surface-bound citrate molecules. PCS data further demonstrates this by showing the relationship between the average particle diameters of the NPs in the metal ion/NP solutions, relative to the pH of the solution (Figure 4-10).

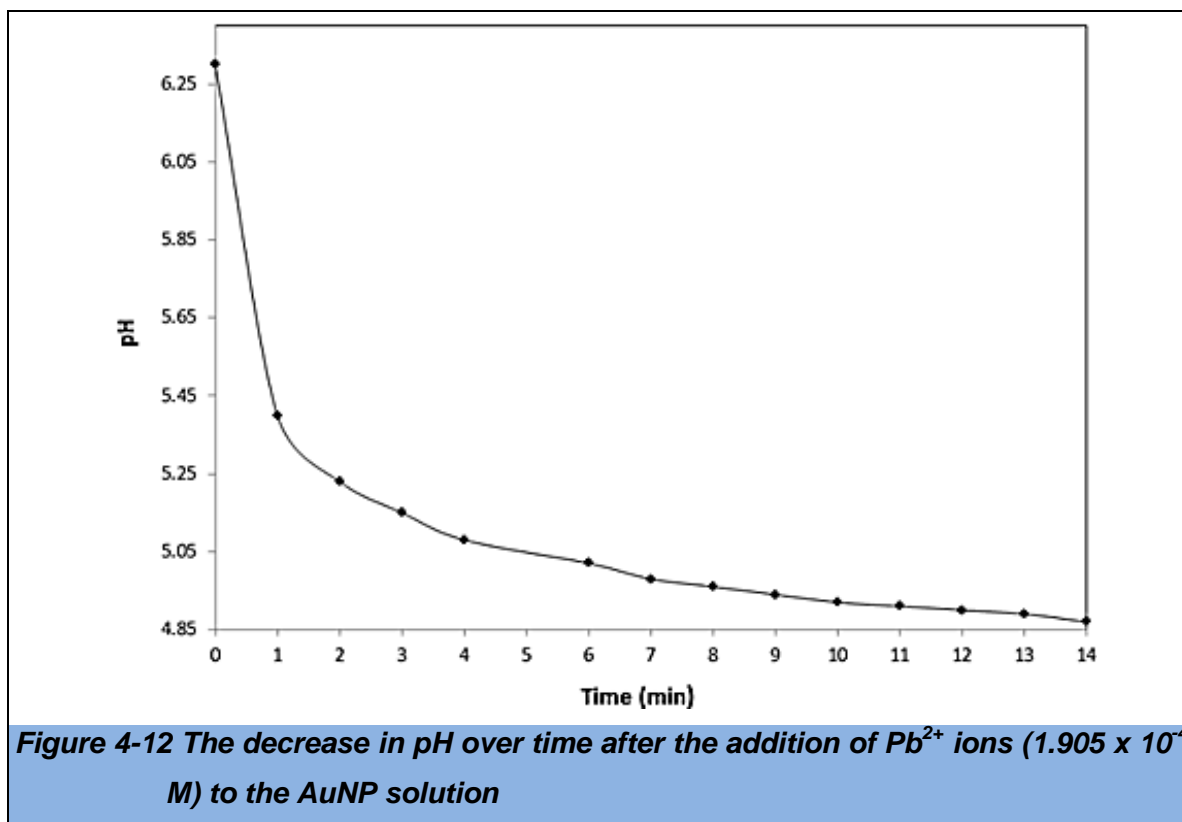


Between the pH range of 6.7 and 7.5 the particles within the solution were at similar sizes. At a pH value of 7.6 the particle diameter was larger than that of the metal ion/AuNP solutions within the range of 6.7 to 7.5, and for the Pb^{2+} /AuNP solution the particle size had increased dramatically at a pH of 1. This could be due to a re-protonation process, as at lower pH values ($pH < 3$) the carboxylate groups of the free citrate molecules in solution become fully protonated due to their pK_a values. This would also be a cause for NP aggregation. Contrastingly, there is evidence to suggest that this may not occur for surface-bound citrate molecules. Mudunkotuwa *et.al* has shown that the carboxylate groups of the

surface-bound citrate molecules of TiO₂ NPs (4 nm diameter) do not become protonated at low *pH*.¹⁰⁷ Assuming that this is also true for AuNP solutions, the reduction in the surface charge contributed by the negatively charged carboxylate groups can likely be due to Pb²⁺ binding alone: As the increased concentration of protons, due to a low *pH*, would not protonate the carboxylate groups of the surface bound citrates and therefore the negative surface charges would remain. Although, the dramatic decrease in *pH* would destabilise the AuNP solutions by the collection of the protons around the surface of the NPs. This was demonstrated by inducing AuNP aggregation, by lowering the *pH* of the AuNP solution. It was found that the solution became blue at *pH* ~4 due to aggregation and subsequently plasmon coupling effects. The solution then became clear at *pH* ~2, due to the sedimentation of the NPs (Figure 4-11). This colour change clearly matches the observed colour change of the Pb²⁺/AuNP solution at a Pb²⁺ concentration of 1.905 x 10⁻⁴ M; showing that the metal ion interactions with the negative charges of the surface-bound citrate molecules, is not the only factor to consider when examining the causes of AuNP aggregation; although, the change in *pH*, surface charge, and the subsequent effects of plasmon coupling were observed to be dependent on the Pb²⁺ ion concentration: On reducing the concentration of Pb²⁺ ions by half the *pH* decreased to 4.8 and plasmon coupling effects were not observed. These *pH* changes, on the addition of metal ions to citrate functionalised NPs has not been reported within the literature.



A timed study was carried out into the *pH* decrease of a Pb²⁺/AuNP solution (1.905 x 10⁻⁴ M) to explore the different transitional steps taken during the interaction process, as a comparison to the literature on free citrate-metal ion complexes (Figure 4-12).



During the first minute there was a relatively sharp decrease in pH (-0.9 units). Over a 14 minute period the solution pH continued to decrease to a pH of 4.87. The pH of the solution remained at 4.87 for a further 30 minutes. After a 24 hour period the solution pH had decreased further to 4.58. A graph of $(1/pH)$ versus time produced a linear plot ($R^2 = 0.98$) from 4 to 15 minutes, signifying a second order reaction rate. In addition, when the Pb^{2+} ion concentration was doubled, the rate of the reaction quadrupled, which is also characteristic of a second order reaction. The data between 0 - 4 minutes and for >30 minutes was nonlinear when plotting a graph of $(1/pH)$ versus time. This data indicates the existence of at least three transitional reactions taking place; resulting in the formation of intermediate species between the Pb^{2+} ions and the surface bound citrate molecules. A similar three-step reaction path has been noted for the interaction of Cu^{2+} ions with unbound citrate molecules in solution.¹⁰⁸ This shows an interesting parallel between the reaction of Pb^{2+} ions with the surface-bound citrate molecules of the AuNPs and the reaction between Cu^{2+} ions and unbound citrate molecules in solution; although, no record has been found in the literature that shows that Pb^{2+} ions react with unbound citrate molecules in this way.

Considering the increase in the pH of the metal ion/AuNP solution upon the addition of the Cd^{2+} , Ni^{2+} , or Hg^{2+} ions, compared to the pH of the AuNP solution, we cannot say that the pH change has resulted in a slight aggregation of the NPs. This is because a more basic solution preserves the deprotonated state of the negative carboxylate groups *i.e.* particle-particle repulsion is conserved and thus no aggregation occurs. Therefore, the reduced surface charge of the NPs can only be due to the interaction of the positive metal ions, with the negative carboxylate groups of the surface-bound citrate molecules.

In contrast, the pH of the Pb^{2+} /AuNP solutions decreases with a metal ion precursor concentration of $1.905 \times 10^{-4} M$ and $9.525 \times 10^{-5} M$, and the surface charge of the NPs is reduced. Consequently, the assumption that the decrease in the surface charge of the NPs is exclusively an attribute of the bonding between the positive metal ions and the negative carboxylate groups, cannot be made. This assumption cannot be made because, not only does the metal ion interaction with the carboxylate groups reduce the surface charge of the NP but the reduction in the pH of the solution, which reduces the surface charge of the NP. As discussed, this can be done by a build-up of positively charged protons around the surface of the NP, or by the protonation of the negative carboxylic groups.

4.4.1 Summary of Results and Discussion Part so far

To summarise the findings up to this point, within this report: The evidence presented here strongly suggests that when using a Pb^{2+} ion precursor, the resultant pH decrease was a major driving force for the observed aggregation of the NPs. This leads to the large red shift in the wavelength of the plasmon band absorbance maximum. The evidence also shows that this was unique to Pb^{2+} ions, with respect to the other metal ion/AuNP solutions studied here. These results can then be seen as important for the further understanding of aggregation of citrate functionalised nanoparticles in the presence of metal ions – especially as these observations have not been found within the literature; but these findings now beg the questions: What metal-citrate species are formed at the surface of the citrate functionalised NPs? Also, how does this affect the surface charge of the NP and the pH of the metal ion/NP solution? These questions are addressed in the

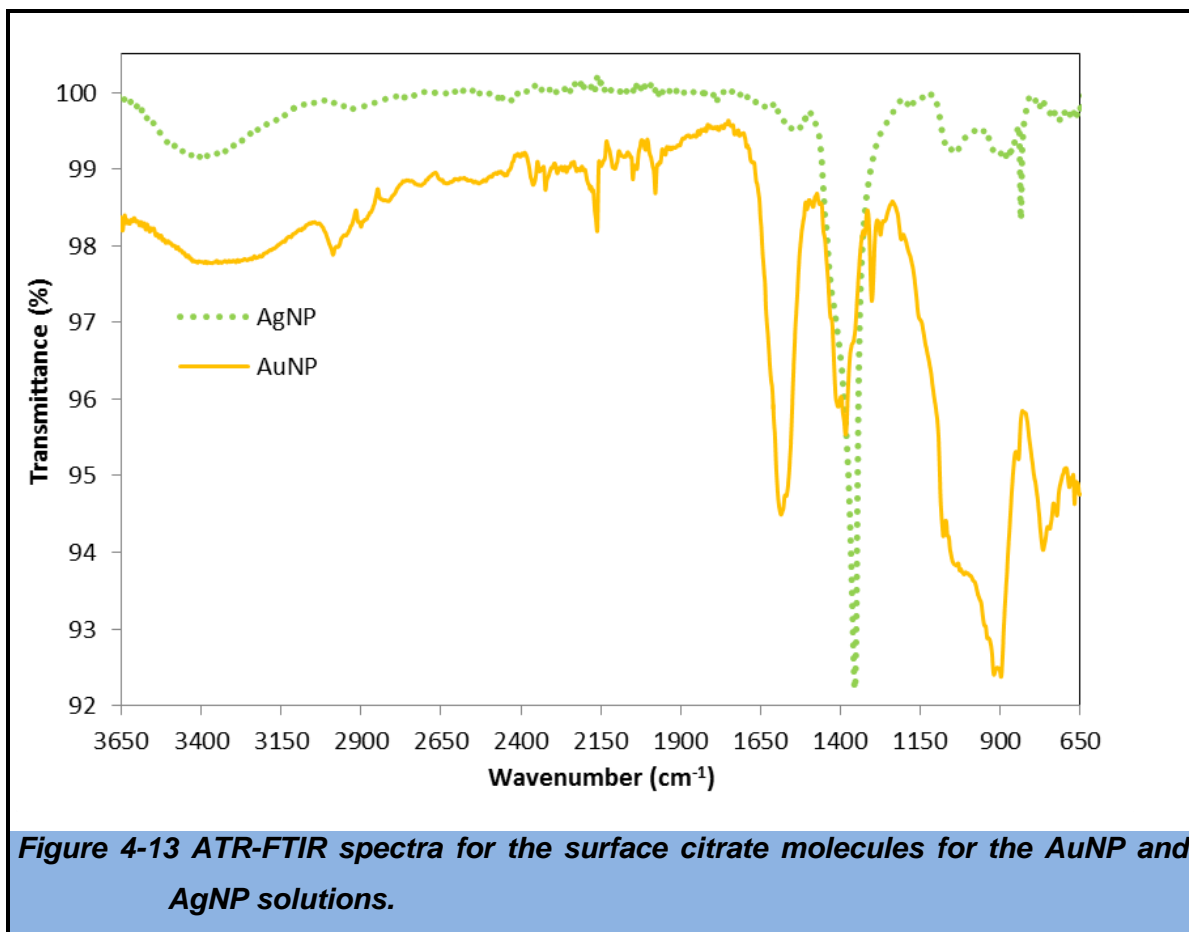
following section with the aid of ATR-FTIR spectroscopy and computational predictions.

4.5 Defining the Metal-Citrate Species formed at the Surface of the NPs by Applying ATR-FTIR Spectroscopy and Computational Predictions

In solution, divalent metal ions can bind with free citrate molecules via the carboxylate groups and the protonated alcohol group. Metal ions can bind to the citrate molecule via the hydroxyl group of the citrate. This can occur either leaving the hydroxyl group protonated or deprotonating the hydroxyl group to release a proton into the solution. The work presented in here was carried out to try to understand the mechanisms involved in the metal ion-citrate binding at the surface of the AuNPs and AgNPs.

4.5.1 ATR-FTIR Spectroscopy and Simulated Vibrational Transitions for the Surface-Bound Citrate Molecules on the Surfaces of the Gold and Silver Nanoparticles

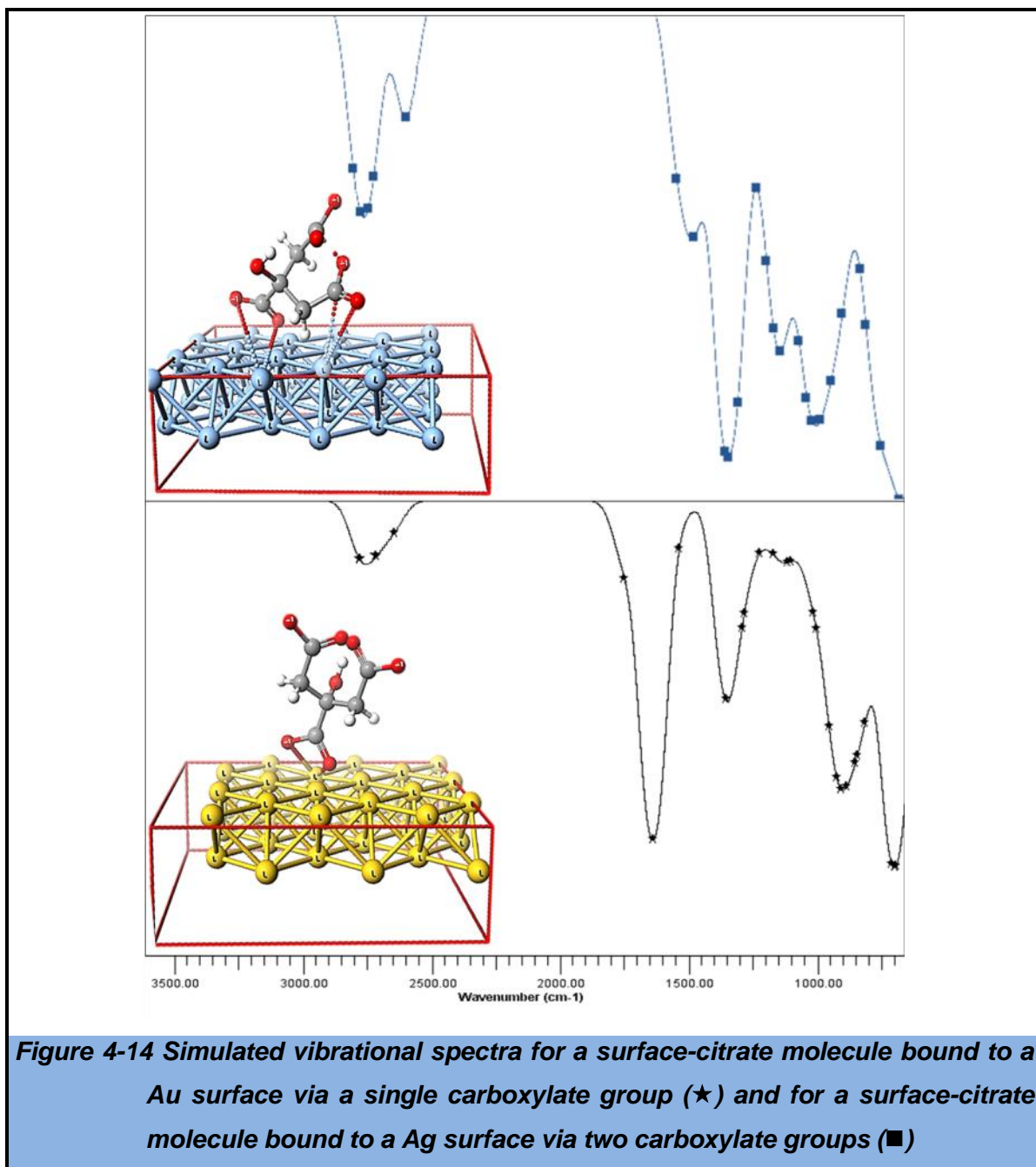
ATR-FTIR spectra of the AuNP and AgNP solutions displayed an intense band positioned at 1393 cm^{-1} and 1353 cm^{-1} respectively. This band results from the symmetric stretching of the carboxylate groups (Figure 4-13). The band positions are different than that of the literature value for unbound citrate molecules (1417 cm^{-1}), indicating that the citrate molecules are bound to the surface of the Au and Ag NPs.



The ATR-FTIR spectra for the Au and Ag NP samples display the O-H stretch mode of the hydroxyl group of the surface bound citrate molecules. This is displayed by a broad peak centred at 3310 cm^{-1} and 3382 cm^{-1} respectively. The respective wavenumber values for the O-H stretch show that the O-H bond for the surface citrate molecule on the AgNP surface is stronger than that of the surface citrate molecules of the AuNPs. In addition, the surface citrate molecules on the AuNPs show a weak peak centred at 1298 cm^{-1} , corresponding to rotation of the unbound hydroxyl group of the citrate.¹⁰⁹ As this band is absent from the AR-FTIR spectra for the AgNP solution, this could indicate that the hydroxyl group of the surface citrate molecules is bound to the NP surface. The most notable difference in the ATR-FTIR spectra is that the intense band of the asymmetric carboxylate stretch ($\sim 1580\text{ cm}^{-1}$) is absent from the AgNP sample. This is due to the asymmetric carboxylate stretch being parallel to the surface of the AgNPs, causing the transition to be infrared inactive.¹¹⁰ This indicates that multiple carboxylate groups of the surface-bound citrate molecules are attached to the surface of the AgNPs. The ATR-FTIR spectrum for the AuNP sample does show an intense band attributed to the asymmetric carboxylate stretch, suggesting that the citrate

molecules are bound by a single carboxylate group. These observations are complimented by computational simulations for the structure of the surface-bound citrate molecules on Au and Ag surfaces and the resultant IR spectra.

Simulated IR spectra for surface bound citrate molecules bound by a single carboxylate group and by two carboxylate groups are shown in Figure 4-14. The calculated spectra closely match the experimental ATR-FTIR spectra for the Au and Ag NP solutions.



The simulated spectrum for the surface citrate molecule bound by a single carboxylate group has two intense bands which are attributed to the symmetric and asymmetric carboxylate stretches; which matches the experimental ATR-FTIR spectrum for the AuNP sample. Additionally, the calculated spectrum for the surface citrate molecule bound by two carboxylate groups only contains the band associated with the asymmetric carboxylate stretch; which matches the experimental spectrum for the AgNP sample. These proposed citrate conformations can explain the experimental data obtained for the surface charge of the NPs: As two carboxylate groups of each surface-bound citrate molecule are bound to the surface of the AgNP, only one unbound carboxylate group from each molecule will be able to contribute to the negative surface charge; In contrast, as one carboxylate group of each surface-bound citrate molecule is bound to the surface of the AuNP, two unbound carboxylate groups from each molecule can contribute to the negative surface charge. Therefore, the AuNPs would have a more negatively charged surface than the AgNPs due to a larger contribution of negative charges from the carboxylate groups of the surface-bound citrate molecules.

4.5.2 *Experimental ATR-FTIR Spectroscopy and Computational Studies into the Metal Ion/Surface Citrate Complexes Formed at the Surfaces of the Gold and Silver Nanoparticles and at Gold and Silver Surfaces*

ATR-FTIR spectra for the metal ion/AuNP and metal ion/AgNP solutions demonstrate the differences in the metal-citrate speciation by the peaks present for the carboxylate groups (Figure 4-15 and Figure 4-16). Please note that the >100 % transmittance is most likely caused by discrepancies in the rough surface of the samples, produced by the particles, when compared to the smooth surface of the blank sample *i.e.* the value of >100 % here, has no real physical meaning.

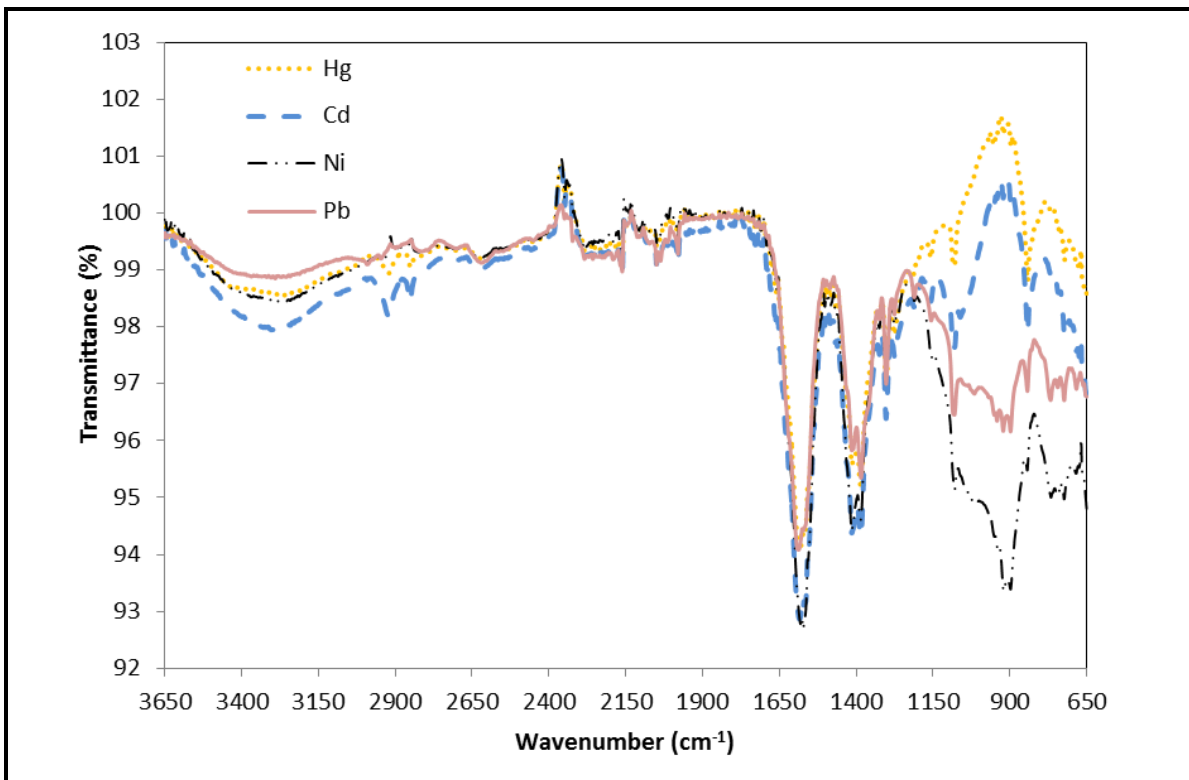


Figure 4-15 ATR-FTIR spectra for the metal ion/AuNP solutions

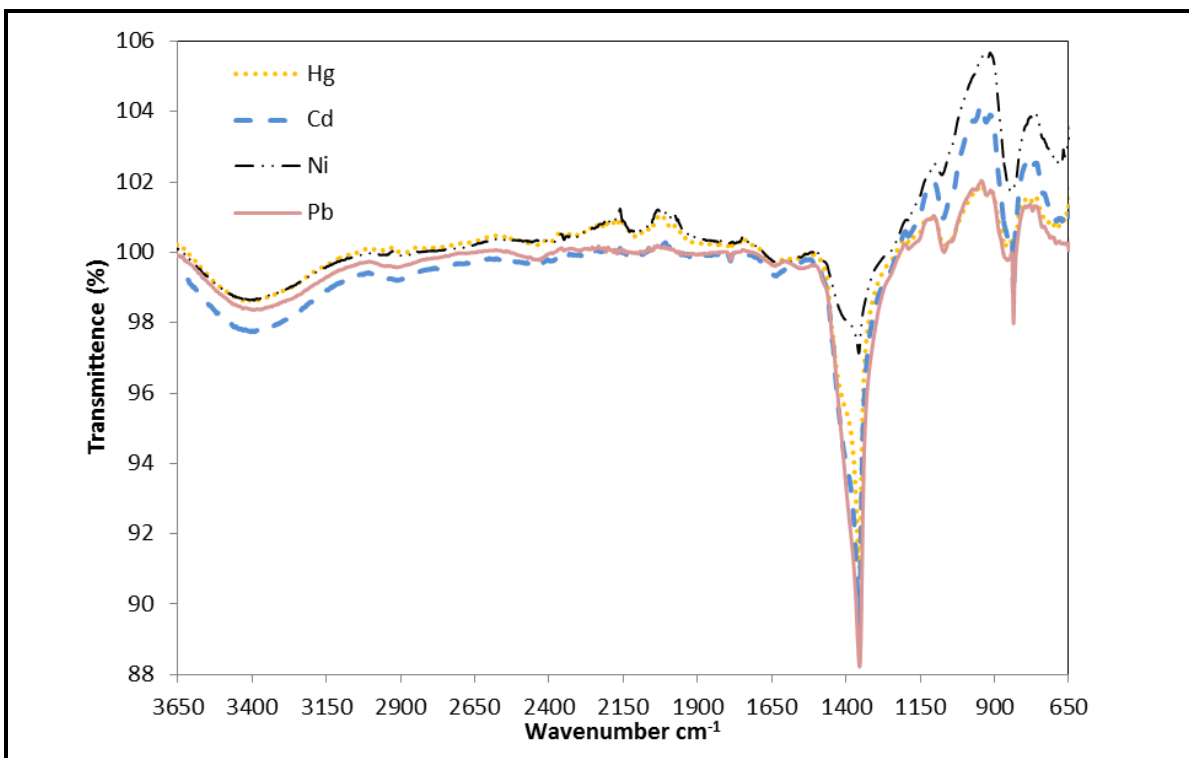
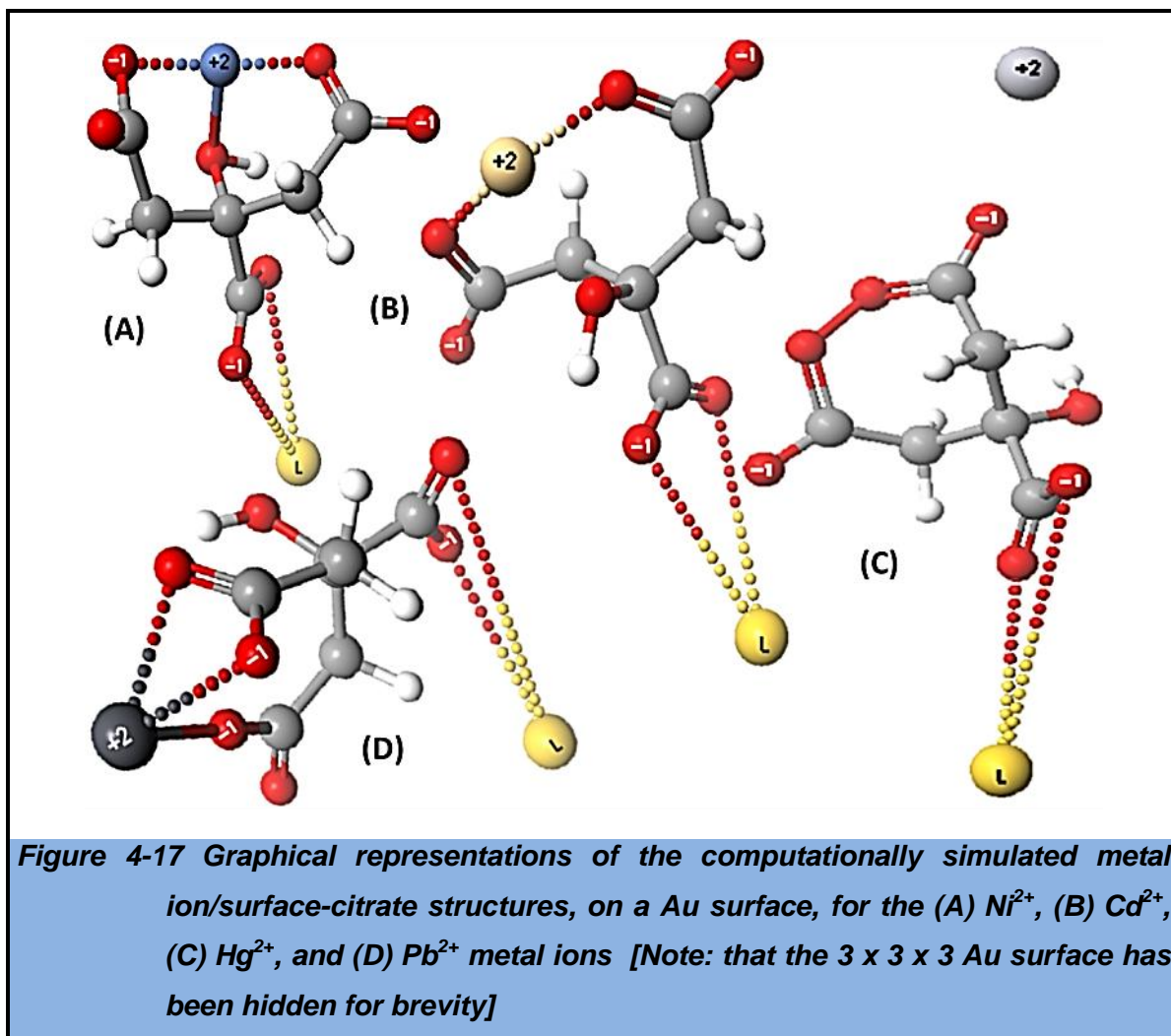


Figure 4-16 ATR-FTIR spectra for the metal ion/AgNP solutions

The symmetric and asymmetric carboxylate stretches are still present for the metal ion/AuNP solutions and the symmetric carboxylate stretches are still present for the metal ion/AgNP solutions. The variances in the intensities of these bands show

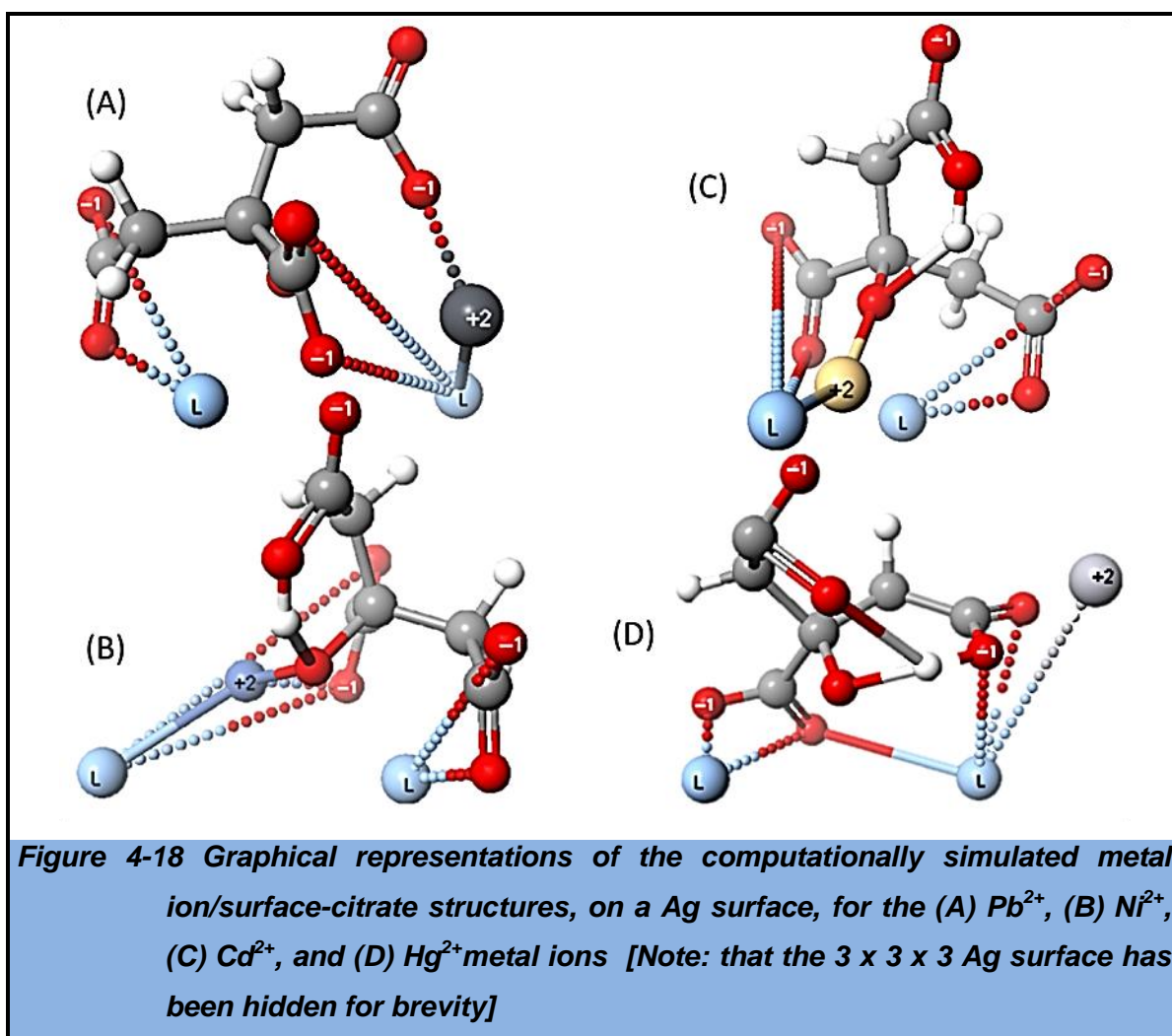
an expected interaction between the metal ions and the carboxylate groups of the bound citrate molecules.

Computational simulations into the potential metal-citrate structures, formed on the surface of the AuNPs, produced unique structures for each metal ion-citrate complex (Figure 4-17).



Using Cd^{2+} , Ni^{2+} and Hg^{2+} ions in the simulation produced structures that retained their negative surface charge, due to at least one negatively charged carboxylate group retaining its negative charge. Cd^{2+} ions were predicted to be weakly bound by the double bond oxygen atoms of the carboxylate groups leaving the two negative charges of the carboxylate groups intact (Figure 4-17B). Ni^{2+} ions were predicted to be weakly bound to a double bond oxygen of one carboxylate group and to a single bond oxygen from the other carboxylate group with a third bond to

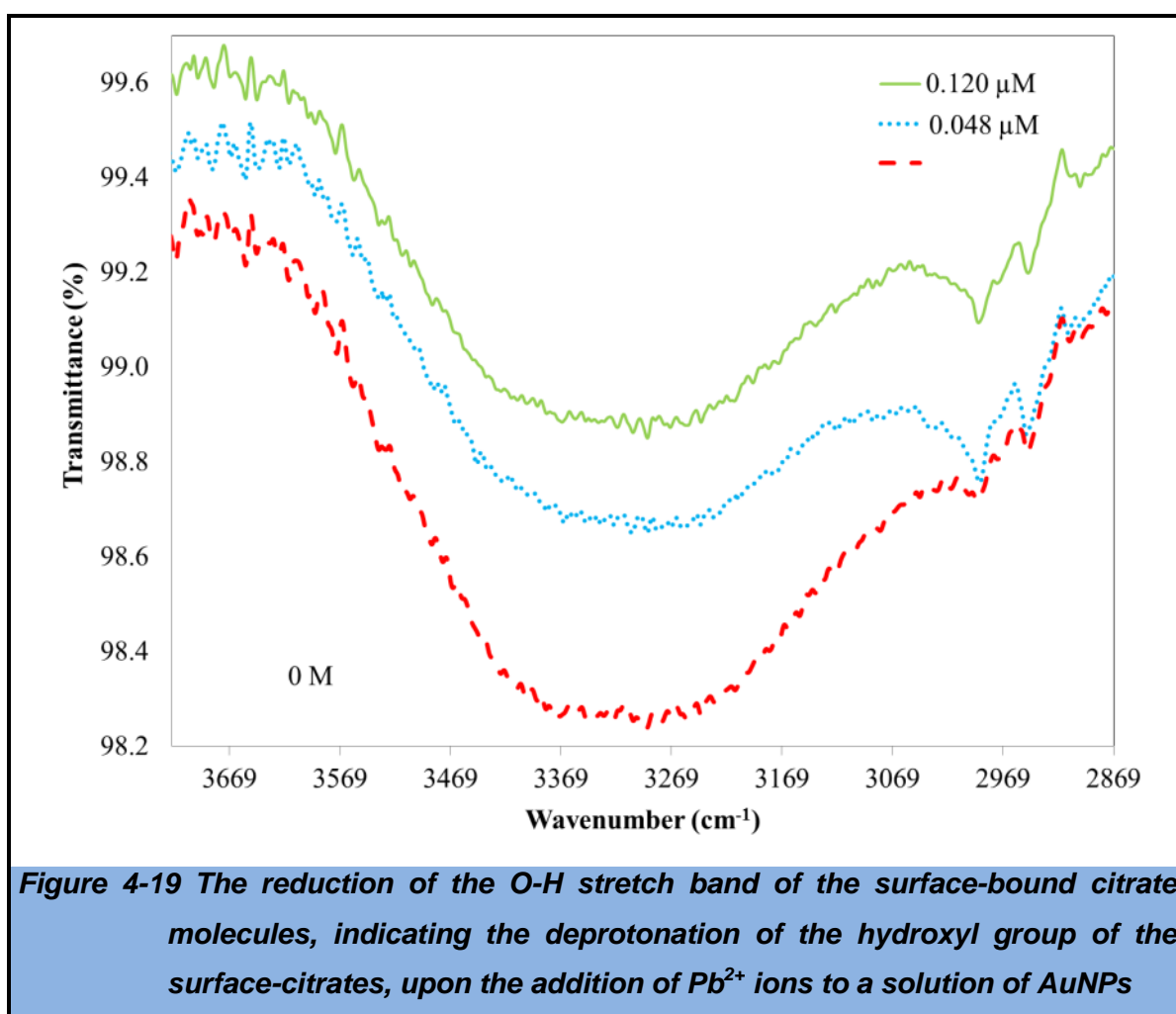
the hydroxyl group oxygen; the surface-bound citrate molecule retained a single negative charge (Figure 4-17A). Surprisingly, Hg^{2+} ions did not bind to the citrate molecules, leaving the original overall charge from the two carboxylate groups of the citrate molecules (Figure 4-17C). The predicted structure for the Pb^{2+} /surface-citrate molecules calculates that all of the unbound carboxylate groups were involved in bonding with the metal ion (Figure 4-17D). This resulted in a cancelling of the negative charges of the simulated surface-citrate molecule. This computational data is strong evidence for the proposed binding of the Pb^{2+} ions, as experimental data shows a large reduction in the surface charge for the Pb^{2+} /AuNP sample. On comparing the simulated metal ion/surface-citrate structures for the AgNP samples, Cd^{2+} , Ni^{2+} and Hg^{2+} ions produced structures that retained their negative surface charge due to their single free carboxylate group retaining a free negative charge (Figure 4-18).



This was achieved by metal ion interactions with the already bound carboxylic groups and the Ag surface. Experimental results are comparable with the

simulated data for Cd^{2+} , Ni^{2+} and Hg^{2+} ions, which show very little change in the surface charge of the AgNPs. In contrast, in simulations the Pb^{2+} ions interacted with the unbound carboxylate group cancelling the negative charge of the surface citrate molecule. This is not shown in the experimental data, in which the surface charge of the Pb^{2+} /AgNPs is comparable to that of the AgNPs.

The intensity for the band associated with the O-H stretch mode was also found to change when comparing the use of different metal ions for the metal ion/NP solutions. Assuming that all of the carboxylic groups are deprotonated, the only other proton source from the surface citrate molecules is from the hydroxyl group. It is then presumed that the large decrease in pH for the Pb^{2+} /AuNP solution is due to the loss of a proton from the hydroxyl group. For the Pb^{2+} /AuNP solution, the intensity of the O-H stretch band diminishes, thus confirming the reduced presence of the O-H stretch.^{111,112} These results are important as they provide evidence for the large decrease in the pH of the Pb^{2+} /AuNP solution, relative to the AuNP solution.



In contrast, the $\text{Pb}^{2+}/\text{AgNP}$ solution shows a relatively small reduction in the pH of the solution. This can be linked to the $\text{Pb}^{2+}/\text{AgNP}$ sample retaining its O-H stretch band, and thus there is little or no deprotonation of the hydroxyl group. Computational simulations into the effect of the different metal ions on the surface citrate molecules showed that the O-H bond of the surface-bound citrate molecule is weakened after the addition of the metal ions. This is probably due to the electron-withdrawing capabilities of the metal ions, which will draw electron density from the molecule and reduce the electron density at the O-H bond; this will weaken the O-H bond. Pb^{2+} is the most electronegative of the metal ions used here. This could be a reason why it was only Pb^{2+} that caused a pH change, by the loss of the hydroxyl proton, for the metal ion/AuNP solutions.

4.6 Using AuNP and AgNP Solutions to Detect Pb^{2+} , Cd^{2+} , Ni^{2+} , or Hg^{2+} Ions at Trace and Ultra-Trace Concentrations by Shifts to the Wavelength of the Plasmon Absorption Band in the UV-Vis Absorption Spectrum

The characterisation of the citrate-functionalised AuNPs and AgNPs has been covered in Sections 3.1 through 3.5. These studies have built-up an understanding of some of the mechanisms involved in the binding between Pb^{2+} , Cd^{2+} , Ni^{2+} , or Hg^{2+} ions with the surface-bound citrate molecules of the Au and Ag NPs. In contrast to all of the metal ion/AuNP combinations that were studied here, it is evident that the combination of Pb^{2+} ions at a concentration of $1.905 \times 10^{-4} \text{ M}$ (39.4716 mg/l) *, with the AuNP solution synthesised here, led distinct spectroscopic features: Visibly, the solution turned from its characteristic red to blue and then clear and ultimately, the LSPR absorption band was found to red-shift, displaying classic plasmon coupling optical effects as the AuNPs underwent aggregation. When reviewing the metal ion/AgNP combinations, with metal ion concentrations of $1.905 \times 10^{-4} \text{ M}$, the $\text{Hg}^{2+}/\text{AgNP}$ solution showed the largest LSPR absorption band shift ($\sim 149 \text{ nm}$) due to the formation of the Ag/Hg

* In previous sections the concentrations of the aqueous metal ions were quoted in the *molar* format, to show that there was an equal number of metal ions present in all of the metal ion/NP samples. The concentrations of the metal ions will now be quoted in weight per litre throughout the rest of this chapter. The reason for this is that the general quotation of the concentrations of metal ions in aqueous samples is regularly quoted in this format; in addition, the concentrations quoted by the WFD and DWD as 'acceptable' are generally in a $\mu\text{g/l}$ format; so for comparative reasons this format will be employed here.

amalgam. Because of the above observations, the choice to use the AuNPs and AgNPs as LSPR absorption based sensors for Pb²⁺ and Hg²⁺ ions respectively was decided.

4.6.1 Citrate Functionalised AuNPs as LSPR Based Nanosensors for Pb²⁺ ions

Solutions of aqueous Pb²⁺ ions were added to the AuNP solutions to make up Pb²⁺ ion concentrations between 30.0 µg/l and 0.0 µg/l. UV-Vis absorption spectroscopy was then carried out to observe any spectral shifts in the LSPR absorption band, as seen at a concentration of 39.9 mg/l. The data unfortunately demonstrates that a LSPR based method, using these citrate functionalised AuNPs, was not suitable to detect Pb²⁺ ions down to the desired concentrations at which the WFD and DWD define as acceptable. The data shows that close to the acceptable levels set by the DWD and WFD (7.2 µg/l and 10 µg/l respectively), there is no shift in the LSPR absorption band wavelength relative to freshly prepared AuNP (0.0 µg/l). These results are listed in Table 4.4.

Table 4.4 A list of the plasmon absorption band positions for the AuNP solutions with Pb²⁺ ion concentrations between 30.0 µg/l and 0.0 µg/l - here * represents the original experiment value noted in Section 3.1, as a comparison

Concentration of Pb ²⁺ Ions in AuNP Solution (µg/l except *)	LSPR Absorption Band Position 1 (nm)	LSPR Absorption Band Position 2 (nm)
* 39.5 (mg/l)	534	630
30.0	522	-
25.0	522	-
10.0	522	-
7.2	522	-
4.0	522	-
1.0	522	-
0.5	522	-
0.0	522	-

4.6.2 Citrate Functionalised AgNPs as LSPR Based Nanosensors for Hg²⁺ Ions

To test the usefulness of the AgNPs as a LSPR based sensor for Hg²⁺ ions, solutions of aqueous Hg²⁺ ions were added to the AgNP solutions to make up Hg²⁺ ion concentrations between 30.0 µg/l and 0.0 µg/l. UV-Vis absorption spectroscopy was then carried out to observe any spectral shifts in the LSPR absorption band, as seen at a concentration of 38.2 mg/l. Unfortunately, the data shows that a LSPR based method, using these citrate functionalised AgNPs, was not useable to detect Hg²⁺ ions down to the desired concentrations at which the WFD and DWD define as acceptable. The data shows that close to the acceptable levels set by the DWD and WFD (0.05 µg/l and 1.0 µg/l respectively) (Table 4.5).

Table 4.5 A table of the plasmon absorption band positions for the AgNP solutions with Hg²⁺ ion concentrations between 30.0 µg/l and 0.0 µg/l - here * represents the original experiment value noted in Section 3.1 as a comparison

Concentration of Hg ²⁺ Ions in a AgNP Solution (µg/l except *)	LSPR Absorption Band Position 1 (nm)
* 38.2 (mg/l)	266
30.0	415
25.0	415
10.0	415
7.2	415
4.0	415
1.0	415
0.5	415
0.0	415

4.7 Evaluating the usefulness of the Citrate Functionalised Gold and Silver Nanoparticles

Through the experiments carried out for the citrate functionalised Au and Ag NPs in solutions of Pb²⁺, Cd²⁺, Ni²⁺, or Hg²⁺ ions it was determined that the Pb²⁺/AuNP sample and Hg²⁺/AgNP sample produced LSPR absorption spectra that were unique when compared to all of the other metal ion/NP solutions.

Unfortunately, these unique optical properties were unsuitable for the detection of these metal ions in the concentration ranges set by the WFD and DWD

To conclude: The LSPR absorption-based analytical technique developed here, using the nanomaterials synthesised for this study, is found to be inadequate for the completion of the aims and objectives set out for this project; therefore, an improved technique was sought in a SERS-based analytical method.

4.8 Summary and conclusion

The $\text{Pb}^{2+}/\text{AuNP}$ and $\text{Hg}^{2+}/\text{AgNP}$ samples produced LSPR absorption spectra that were unique, when compared to all of the other metal ion/NP solutions. Upon the addition of a high concentration of aqueous Pb^{2+} ions there was an exceptional shift in the plasmon absorption band of the AuNPs synthesised here. This has not been published within the literature. Due to this result tests were carried to develop these AuNPs as sensors for aqueous Pb. This technique was found to be unsuitable for an industrial application owing to a lack of sensitivity; but the experimental results were very important for the progression of the project and led to an understanding of the metal-citrate interactions at the surfaces of the Au and Ag NPs. This will provide valuable data to the literature on nanomaterials and their surface interactions with functional molecules and metal ions. This data was also important for the production of a AuNP SERS based analysis technique for the detection of Pb^{2+} ions, as it helped with the identification of the Raman bands which were affected by the introduction of metal ions to the NP sample.

5 Results and Discussion (Part 2): Metal Ion Interaction with Citrate Functionalised Gold Nanoparticles and the Subsequent Raman Signal Enhancement for the Detection of Lead Ions

Continuing from Chapter 3, it was clear that the surface citrate molecules of the AuNPs and AgNPs had a strong interaction with the divalent metal ions Pb^{2+} , Cd^{2+} , Ni^{2+} , and Hg^{2+} in solution. Unfortunately, these interactions and subsequent LSPR absorption band shifts provided unsatisfactory results for practical sensing purposes (practical sensing being described as the ability to detect Pb^{2+} , Cd^{2+} , Ni^{2+} , or Hg^{2+} ions at the concentration levels deemed acceptable by the WFD and DWD (Section 1.3). Although, in addition to LSPR absorption band shifts, the phenomena of LSPR has been further used to great effect for sensing purposes due to the effect known as SERS (Section 2.3). This signal enhancement mechanism has been studied here, using the already shown spectroscopic interaction between the surface citrate molecules on the surface of the AuNPs, and the metal ions in solution, as a base for sensing †

† The signal enhancement for Raman spectroscopy is due to the resonance between the wavelength of the laser used in the Raman spectrometer and the wavelength position of the plasmon band absorbance maximum of the plasmonic nanomaterial (Section 2.5). The result of this is that the closer the spectral overlap between the Raman laser emission and the plasmon absorption band maximum the greater the spectroscopic signal enhancement. Because of this, AuNPs were favoured over AgNPs and the study focussed of the detection of Pb^{2+} ions (see Section 4.1 for a more detailed explanation).

Pb²⁺ ions were singled out as a target ion for detection, because of the unique interactions shown in Chapter 5.

5.1 Characterisation of the Synthesised AuNPs and the Production of the SERS Substrates

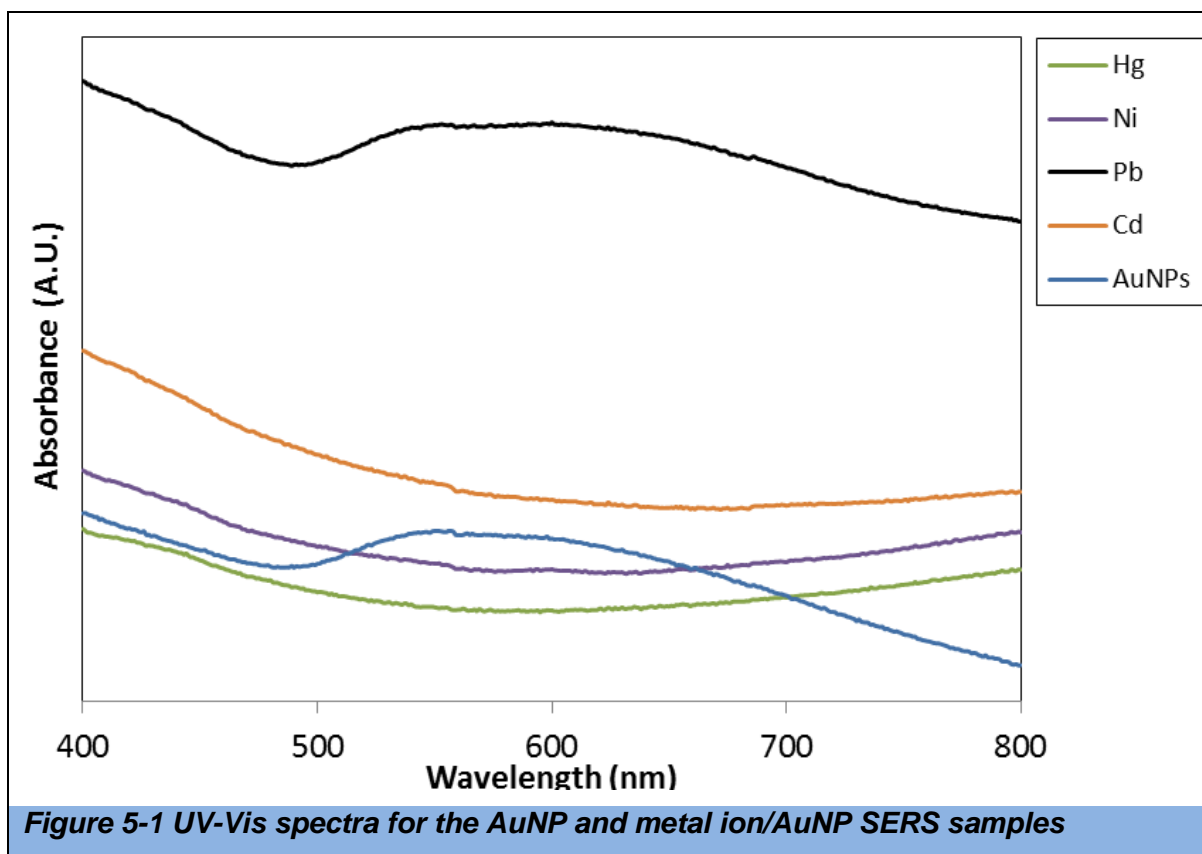
The AuNPs used in Chapter 3 were re-synthesised, so that the two sensing techniques, LSPR plasmon band shifts and SERS could be compared, relative to the same particles. TEM imaging was employed to view the size and shape of the AuNPs. TEM characterisation of the NPs confirmed the synthesis of monodispersed AuNPs, with sizes of ca. 6 nm. This is consistent with the AuNPs used in the previous study (Chapter 4).

Zeta potential readings were also carried out to find the surface charge of the particles. This was undertaken as the surface charge is highly dependent on the surface-bound citrate molecules, and it is these citrate molecules which interact with the heavy metal ions in solution; therefore, the surface charges will change upon the addition of metal ions as they interact with the negative charges of the surface-bound citrate molecules. Zeta potential measurements showed a surface charge of -44.3 mV. This is an exact match with AuNPs used in the study described in Chapter 3. Again, this value of >40 mV indicates a stable colloidal solution, according to DLVO theory.^{113,114} Once more, the AuNPs exhibited LSPR, which was evident from the deep red colour of the suspension and the plasmon absorption band in the UV-Vis absorption spectrum (Figure. 4.2). The wavelength of the plasmon band absorbance maximum was 525 nm. These entire results match the data obtained for the previously synthesised citrate functionalised AuNPs.

In Section 1.4.4 it was stated that plasmonic NPs enhance Raman spectral signals for a Raman spectrometer using a laser wavelength that closely matches the wavelength of the plasmon band absorbance maximum. It was further noted that using a substrate of coagulated AuNPs would further increase the enhancement factor of the boosted Raman signal. Because of this phenomenon, drops of the

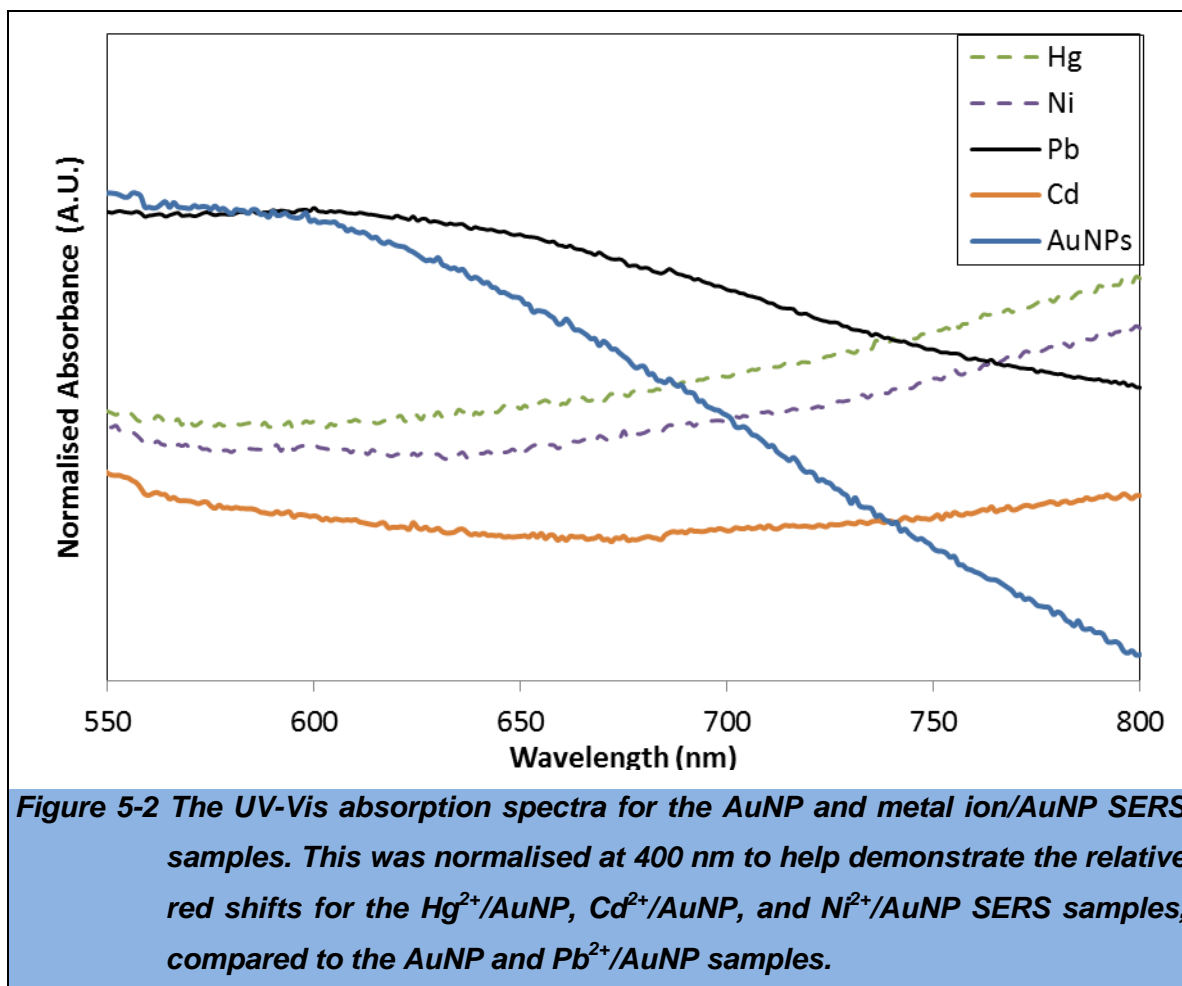
AuNP and metal ion/AuNP solutions were dried onto glass slides to create the SERS samples (Section 3.5.7).

Figure 5-1 is the UV-Vis absorptions spectra obtained for the AuNP SERS samples. It can be noted that there is now no longer any well-defined, intense peak associated with the plasmon band absorption for any of the samples.



The AuNP spectrum shows a broad peak spanning over 200 *nm* from ~510 *nm* to 750 *nm*. This is due to plasmon coupling effects: As the solution dries, the NPs are deposited onto or very close to each other; this leads to an interaction between the plasmon fields for each particle that is in close proximity to another particle causing the plasmon band to shift and broaden (see Section 2.3). In addition to this, there is a small bump at ~540 *nm*. This could tentatively be assigned to the quadrupole mode of the oscillating plasmons, but as this is not noticeable for any other peak aside from the Pb²⁺ ion/AuNP SERS sample, it cannot be confirmed from this data. The maximum absorbance of the band in question is also positioned at a similar wavelength to the AuNP solution, which most likely indicates that it is the plasmon absorption of NPs not experiencing plasmon

coupling *i.e.* NPs that are isolated on the glass slide. All other SERS samples show a large red shift in the plasmon absorption band relative to the AuNP SERS sample, except the $\text{Pb}^{2+}/\text{AuNP}$ sample. This shift is easier to envisage graphically with a normalised UV-Vis absorption spectra (Figure 5-2).



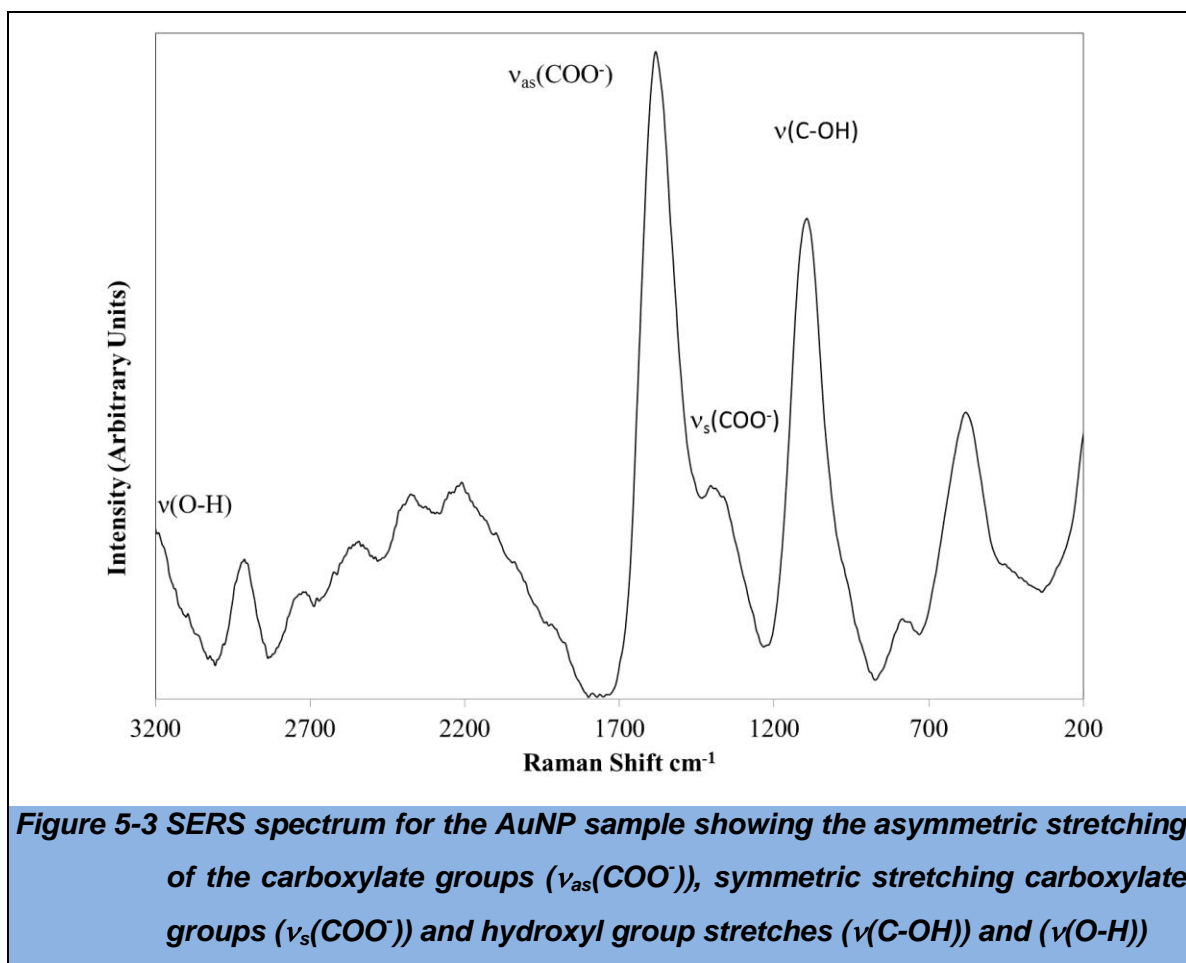
This large red shift can be attributed to the combination of surface interactions between the metal ions and the surface-bound citrate molecules, and plasmon coupling effects between that are AuNPs in close proximity. The $\text{Pb}^{2+}/\text{AuNP}$ SERS sample is unique in several ways: Primarily, the spectra shows a broad peak across 500 nm to 700 nm; secondly, the sample displays increased plasmon absorption relative to all of the other samples tested here (Figure 5-2), and it is this increased absorption that led to the AuNPs being adopted for a Pb^{2+} ion based sensor.

The enhancement of Raman spectroscopic signals via SERS is highly dependent upon the plasmon absorption band wavelength and the intensity of the plasmon

absorption band. This can be seen as, the more intense the plasmon band absorption and plasmon band spectral overlap with the laser emission of the Raman spectrometer, the larger the signal enhancement factor (Section 2.5): Due to the relatively intense absorption band of the $\text{Pb}^{2+}/\text{AuNP}$ SERS sample between 500 nm and 700 nm , this plasmon band covers the emission wavelength of the Raman spectrometer laser (514.5 nm) and will increase the enhancement effects relative to the other metal ion/AuNP SERS samples.

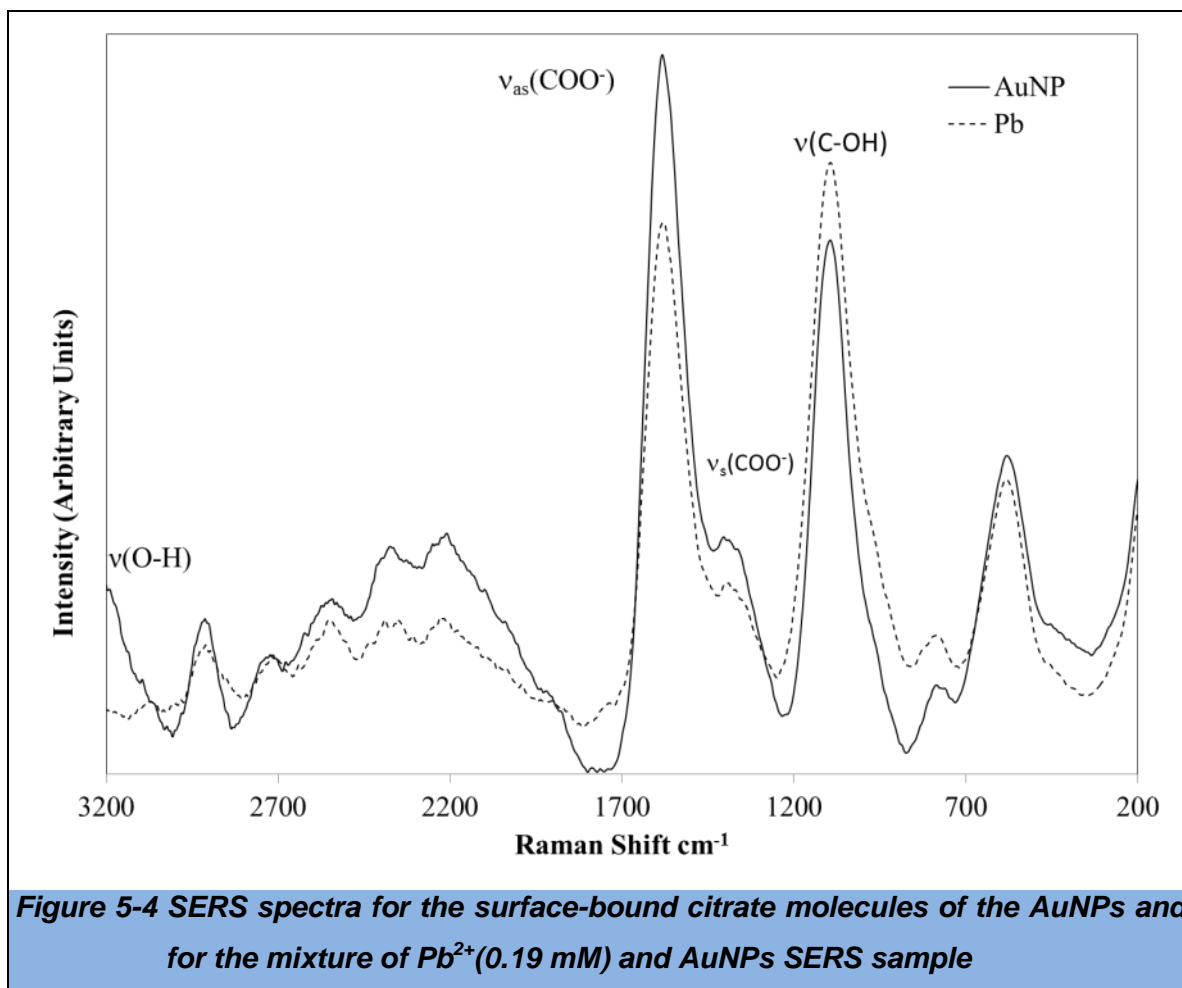
5.2 Monitoring the Effects of Metal Ion Interaction with the Surface-Bound Citrate Molecules with Surface Enhanced Raman Spectroscopy

After the production of the AuNP SERS sample, SERS was carried out as described in Section 3.5.7. This process was used to analyse the spectral properties of the surface-bound citrate molecules of the AuNPs. This was then used as a spectral comparison between the AuNP SERS sample and the metal ion/AuNP SERS samples, containing Hg^{2+} , Cd^{2+} , Ni^{2+} or Pb^{2+} ions. Figure 5-3 shows the SERS spectrum for the AuNP SERS sample.



The band situated at 1578 cm^{-1} represents the asymmetric stretching of the carboxylate groups ($\nu_{\text{as}}(\text{COO}^-)$) of the surface-bound citrate molecules, whereas the symmetric stretching of the carboxylate groups ($\nu_{\text{s}}(\text{COO}^-)$) is shown by the band at 1373 cm^{-1} .^{109,110,112, 115} This peak has shifted from the literature value for free citrate molecules (1417 cm^{-1}) to 1373 cm^{-1} which shows that the citrate molecules are adsorbed on the surfaces of the AuNPs.¹¹⁵ The 1373 cm^{-1} band also shows the presence of two shoulders at approximately 1418 cm^{-1} and 1384 cm^{-1} indicating that the environments of the three carboxylates are non-equivalent. The presence of these two bands, coupled with the ATR-FTIR spectra acquired in Section 4.5.1, indicate that one carboxylate group is bound to the surface of the NP whilst the remaining 2 carboxylate groups remain unbound. In addition to the carboxylate groups of the surface-bound citrate molecules, there are two bands associated with the hydroxyl group, located at 1096 cm^{-1} ($\nu(\text{C-OH})$) and $\sim 3200\text{ cm}^{-1}$ ($\nu(\text{O-H})$).

The surface-bound citrate molecules of the AuNPs underwent binding with Pb^{2+} ions. This was displayed as relative shifts in the peaks assigned to the $\nu_{\text{as}}(\text{COO}^-)$ and $\nu_{\text{s}}(\text{COO}^-)$ bands, and notably, the absence of the $\nu(\text{O-H})$ Raman band (Figure 5-4).



Importantly, the $\nu(O-H)$ band reduced on the addition of Pb^{2+} ions – which was also noted in Chapter 3 when comparing ATR-FTIR spectra for the AuNP and Pb^{2+} /AuNP SERS samples (Figure 4-13). The changes to the O-H stretch band in the ATR-FTIR spectra were directly dependent on the concentration of the Pb^{2+} ions in the AuNP solution. Upon measurement, the pH of the Pb^{2+} /AuNP solutions were much lower than the other metal ion/AuNP solutions. In addition, the pH value was inversely proportional to the concentration of the Pb^{2+} ions, suggesting the loss of the $\nu(O-H)$ band is a result of the de-protonation of the hydroxyl group, upon Pb^{2+} ion binding.

Ni^{2+} , Cd^{2+} , and Hg^{2+} ions also altered the $\nu_{as}(COO^-)$ and $\nu_s(COO^-)$ Raman bands indicating the binding of the ions with the functional molecule's carboxylate groups (Figure 5-5). The SERS spectra obtained for each of the metal ion/AuNP sample was diverse with respects to the $\nu_{as}(COO^-)$ and $\nu_s(COO^-)$ band positions and intensity. Additionally, in comparison to the Pb^{2+} /AuNP sample, all of the other metal ions retained their $\nu(O-H)$ band.

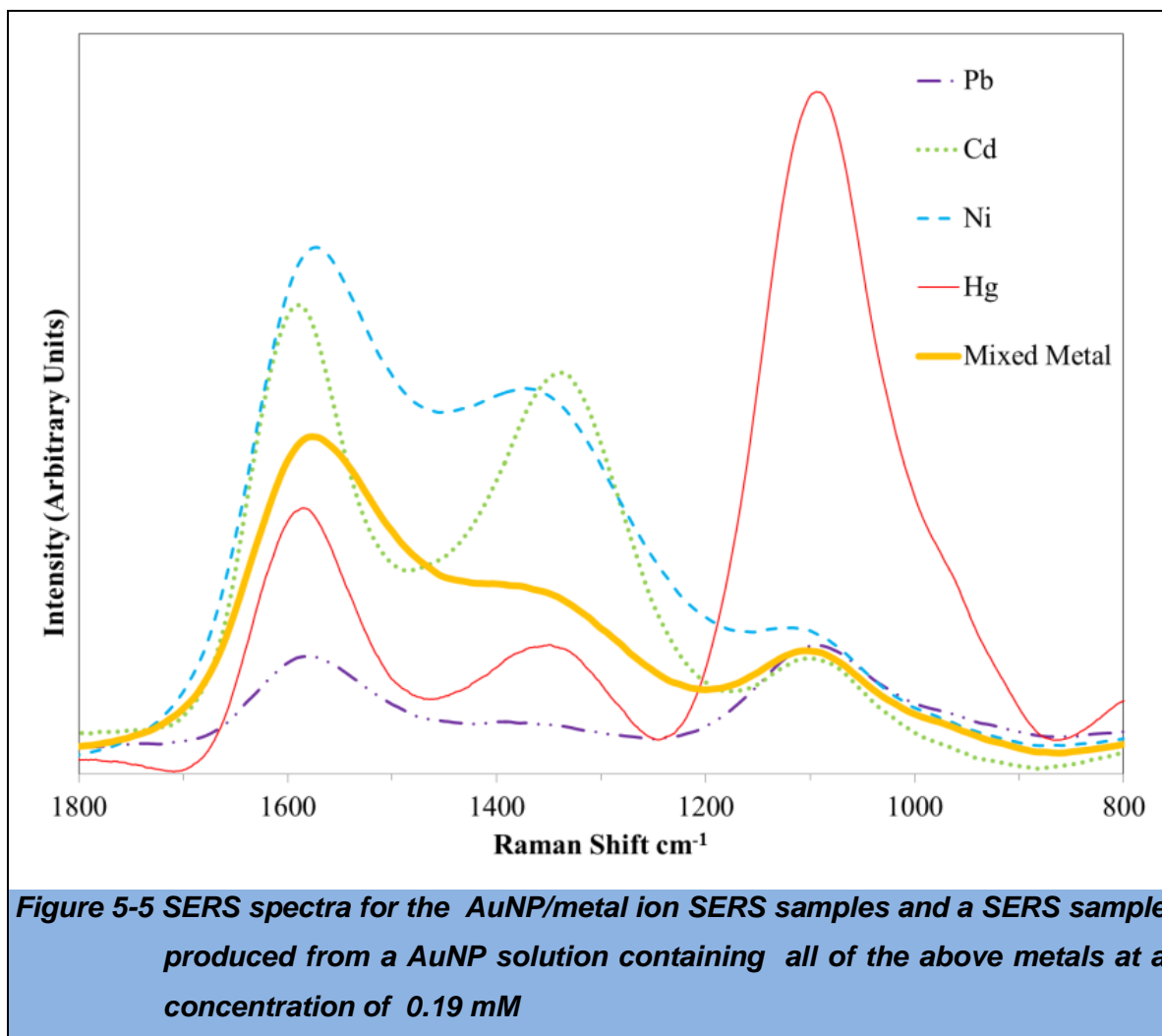


Figure 5-5 also demonstrates that although these spectra were noticeably different, it was impossible to determine a preferred metal-citrate species from a mixed metal ion solution containing 0.19 mM of Ni²⁺, Cd²⁺, Pb²⁺ and Hg²⁺ ions. Therefore, this technique was assigned as a comparison to ion-extraction related analysis techniques. This would be beneficial, as separating out the undesired metals, before the analysis procedure, would mean this technique could then detect Pb²⁺ ions, separated from a mixed-metal solution.

5.3 The Usefulness of AuNP SERS as a Nanosensor at Detecting Pb²⁺ Concentrations at the WFD and DWD Acceptable levels

SERS spectra were taken for Pb²⁺/AuNP solutions which contained varying amounts of Pb²⁺ ions, within the concentration range of 0.025 µg/l to 25 µg/l, using the method described. This concentration range was used as it is a practical working range, which incorporates concentrations of Pb usually found in water

samples (polluted and non-polluted systems), and those classed as ‘acceptable’ by the WFD (7.2 $\mu\text{g/l}$) and DWD (10 $\mu\text{g/l}$).

5.3.1 Detecting Pb^{2+} ions in a Pb^{2+} ion solution using SERS

On decreasing the concentration of the Pb^{2+} ions from 1.000 $\mu\text{g/l}$ to 0.100 $\mu\text{g/l}$ it was observed that the SERS spectra of the $\text{Pb}^{2+}/\text{AuNP}$ samples showed an increased in the intensity for the $\sim 1500\text{ cm}^{-1}$ ($\nu_{\text{as}}(\text{COO}^-)$) peak; whereas the $\sim 1105\text{ cm}^{-1}$ ($\nu(\text{C-OH})$) peak decreases in intensity (Figure 5-6).

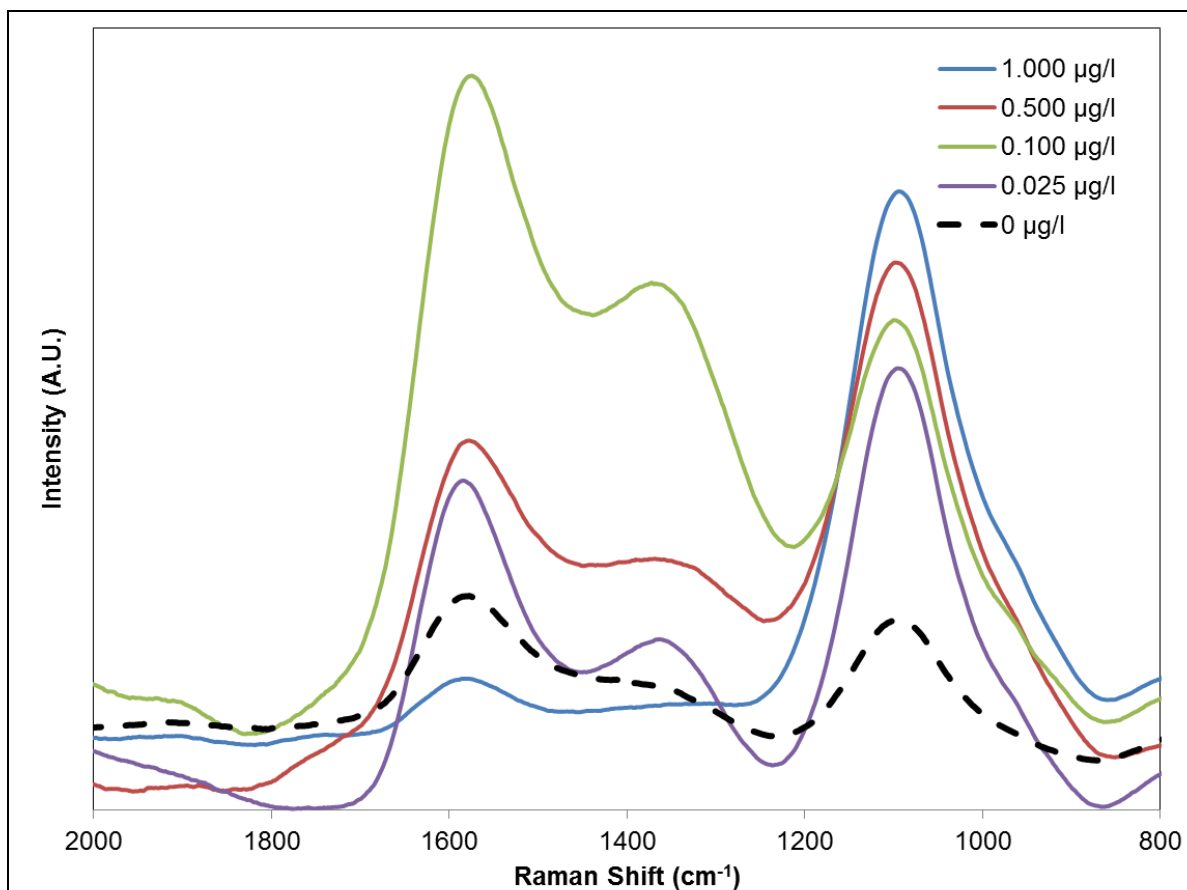


Figure 5-6 The SERS spectral response to concentrations of Pb^{2+} ions within the range of 0 $\mu\text{g/l}$ to 1.000 $\mu\text{g/l}$

Interestingly, at a Pb^{2+} ion concentration of 0.025 $\mu\text{g/l}$, the $\nu_{\text{as}}(\text{COO}^-)$ band does not fit this intensity pattern: The intensity of the $\nu_{\text{as}}(\text{COO}^-)$ band is between the intensities seen for Pb^{2+} ion concentrations of 1.000 $\mu\text{g/l}$ and 0.500 $\mu\text{g/l}$. This shows an inconsistent pattern for the concentration range of 0.025 $\mu\text{g/l}$ to 1.000 $\mu\text{g/l}$ when looking at the $\nu_{\text{as}}(\text{COO}^-)$ band. In contrast, a Pb^{2+} ion concentration of 0.025 $\mu\text{g/l}$ fits the increasing intensity pattern of the $\nu(\text{C-OH})$ band i.e. as the

concentration of Pb^{2+} ions increases, so too does the intensity of the $\nu(\text{C-OH})$ band. Additionally, it was noted that at a Pb^{2+} ion concentration of $0.025 \mu\text{g/l}$, the peak assigned to the $\nu(\text{O-H})$ band becomes present, representing a protonated hydroxyl group of the metal-citrate species. This is of interest, as at higher concentrations this band is not present, thus, this marks a concentration dependent transitional point in the de-protonation of the hydroxyl group of the citrate molecules at the surface of the AuNPs.

The peaks representing the C-OH group linearly decrease with a decreasing concentration range between 100 ng/l and $1 \mu\text{g/l}$ (Figure 5-7).

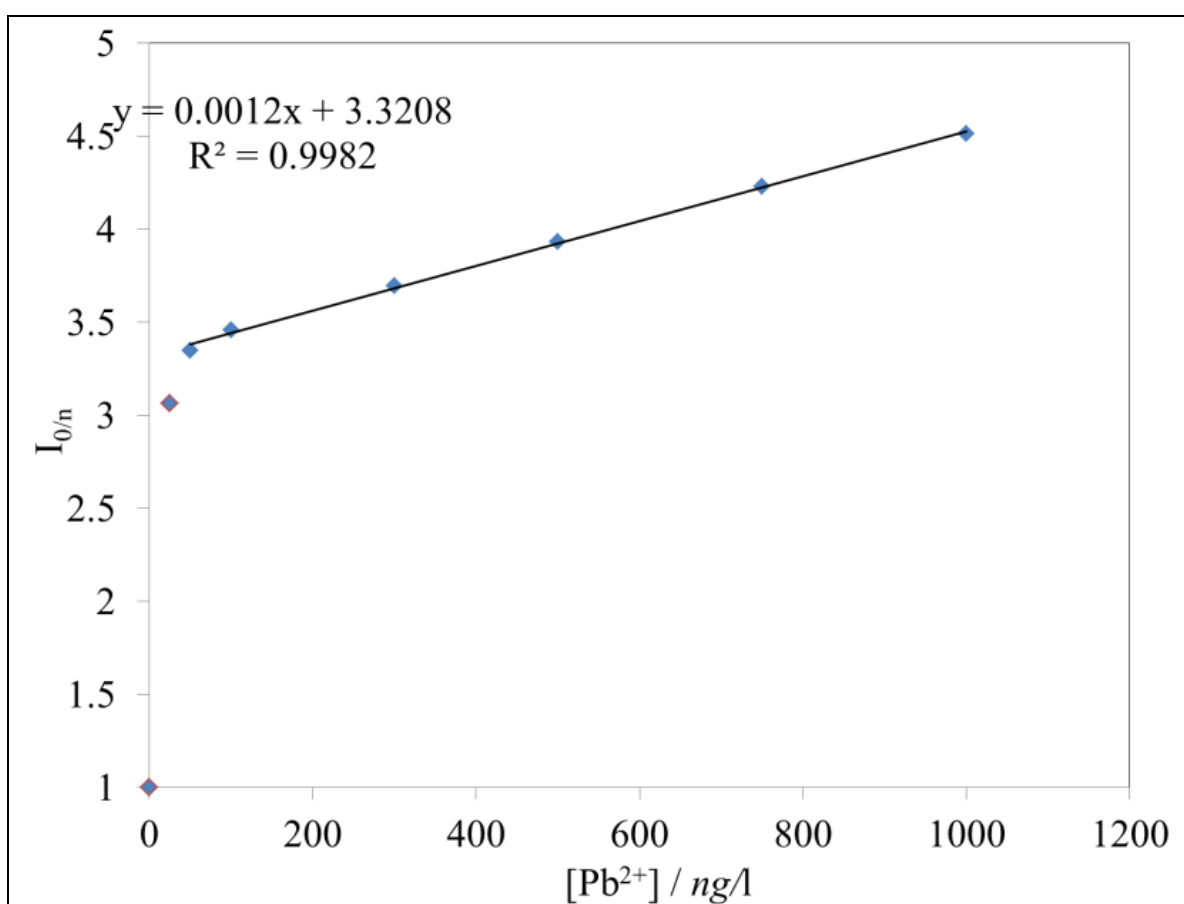


Figure 5-7 A plot of the intensity ratio between the $\nu(\text{C-OH})$ band for the AuNP SERS sample over the $\nu(\text{C-OH})$ band for Pb^{2+} ion/AuNP SERS samples between the concentration range of $1.000 \mu\text{g/l}$ to $0 \mu\text{g/l}$. Error bars have been omitted as the error bar values were too small to be adequately displayed.

For the peak intensity for the $\nu(\text{C-OH})$ band, there was a deviation from linearity when the concentration of Pb^{2+} ions was lowered to 25 ng/l. This would indicate another metal citrate species forming at this concentration of Pb^{2+} ions. This is also backed up by the fact that at 25 ng/l the peak corresponding to the O-H bond appears. This change in metal citrate bonds, though unpredicted, can be expected: As the metal to citrate ratio is an important factor in which metal-citrate species are formed, on changing this ratio, in this case via Pb^{2+} ion concentration, different species with different bonding modes can be formed. Additionally, when the concentration of Pb^{2+} ions was greater than 1.000 $\mu\text{g/l}$, the data did not fit the profile of the calibration plot between 0 $\mu\text{g/l}$ to 1.000 $\mu\text{g/l}$. Therefore it can be assumed that the metal to citrate ratios resulting from >1 $\mu\text{g/l}$ also led to different metal-citrate species to form at the surface of the AuNPs. To combat these nonlinearities data modelling was used to acquire equations relating the concentration of the Pb^{2+} ions and the peak intensity for the $\nu(\text{C-OH})$ band.

5.3.2 Development of a Calibration Curve between 0 $\mu\text{g/l}$ and 1.000 $\mu\text{g/l}$

To improve the accuracy of this technique, the acquisition of the spectra for each SERS sample was carried out at five different areas of the SERS sample. Then the peak intensities for the $\nu(\text{C-OH})$ band were averaged (Table 5.1). This method provided an average standard deviation (SD) of 2.057 and an average relative standard deviation (RSD) of 0.147%.

Table 5.1 A table displaying the $\nu(\text{C-OH})$ band intensity recorded for five measurements for Pb^{2+} ion concentrations between 0 $\mu\text{g/l}$ and 1 $\mu\text{g/l}$

[Pb^{2+}] ($\mu\text{g/l}$)	$\nu(\text{C-OH})$ Band Intensity (A.U.)					Mean Intensity (A.U.)	SD	RSD (%)
	1	2	3	4	5			
0	472	474	474	470	473	473	2	0.3
0.025	1447	1450	1451	1447	1450	1449	2	0.1
0.050	1581	1585	1583	1584	1580	1583	2	0.1
0.100	1635	1636	1634	1638	1633	1635	2	0.1
0.300	1745	1744	1748	1748	1749	1747	2	0.1
0.500	1856	1856	1861	1859	1860	1859	2	0.1
0.750	1998	2001	2002	2001	1998	2000	2	0.1
1.000	2132	2135	2131	2137	2136	2134	2	0.1

Calibration graphs were plotted as the concentration of Pb^{2+} ions over the ratio between the intensity of the $\nu(\text{C-OH})$ peak of the AuNPs, and the $\text{Pb}^{2+}/\text{AuNP}$ samples at different Pb^{2+} concentrations ($[\text{Pb}^{2+}]/I_{0/n}$), versus the Pb^{2+} ion concentration. This produced a more linear response ($R^2 = 0.9903$). Although the data had been displayed in a more linear way, it was found that a polynomial curve ($n = 3$) produced a better fit (Figure 5-8), with a R^2 value of 0.999. Due to this preferable R^2 value, it was the polynomial ($n = 3$) equation which was utilised in calculating the Pb^{2+} ion concentrations of known samples.

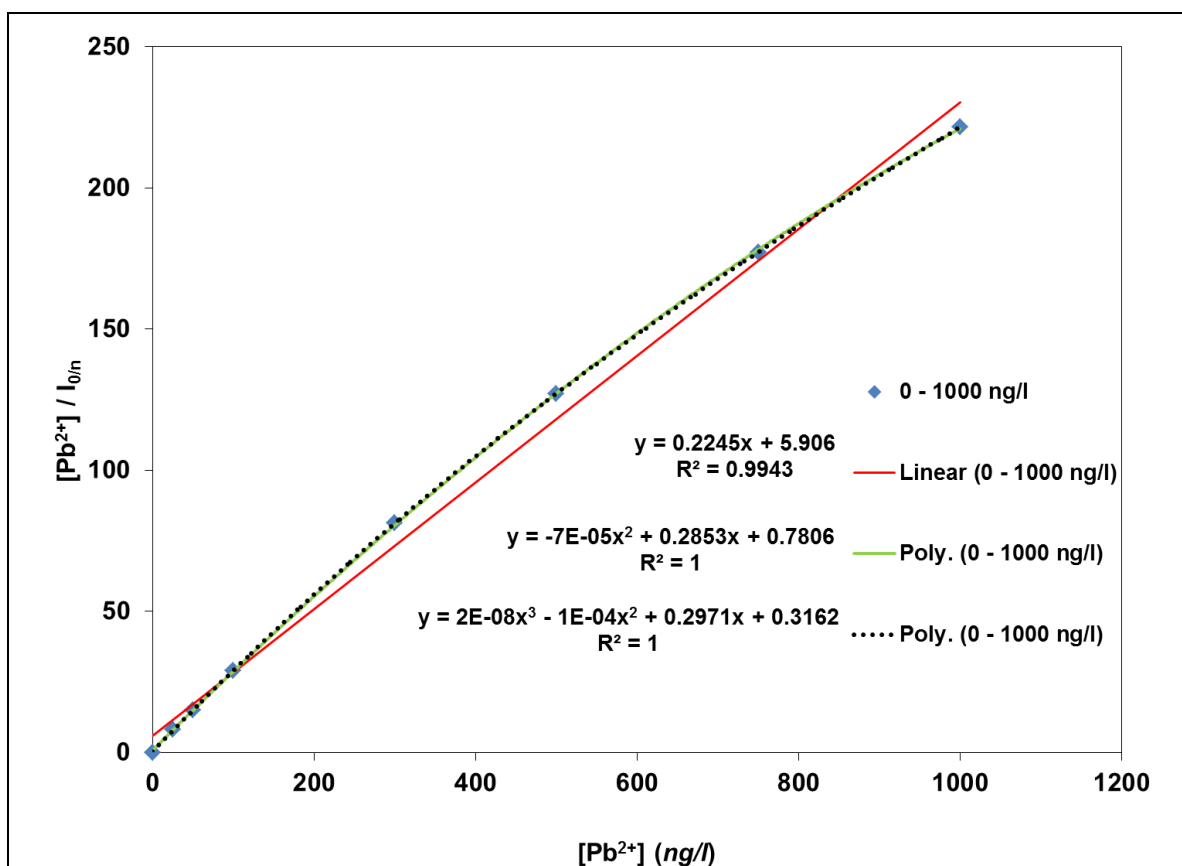


Figure 5-8 A plot of the ratio of the concentration of Pb^{2+} ions over the intensities of the $\nu(\text{C-OH})$ band for the AuNP SERS sample and the $\text{Pb}^{2+}/\text{AuNP}$ SERS samples, for concentrations between 0 ng/l and 1000 ng/l

A plot of the $n = 3$ polynomial equation against the ratio of the intensities of the $\nu(\text{C-OH})$ band for the AuNP SERS sample, and the $\text{Pb}^{2+}/\text{AuNP}$ SERS samples was used to refine the agreement of the line of best fit (Figure 5-9). This plot yielded linear and polynomial fits with R^2 values of 0.9999 and 1 respectively.

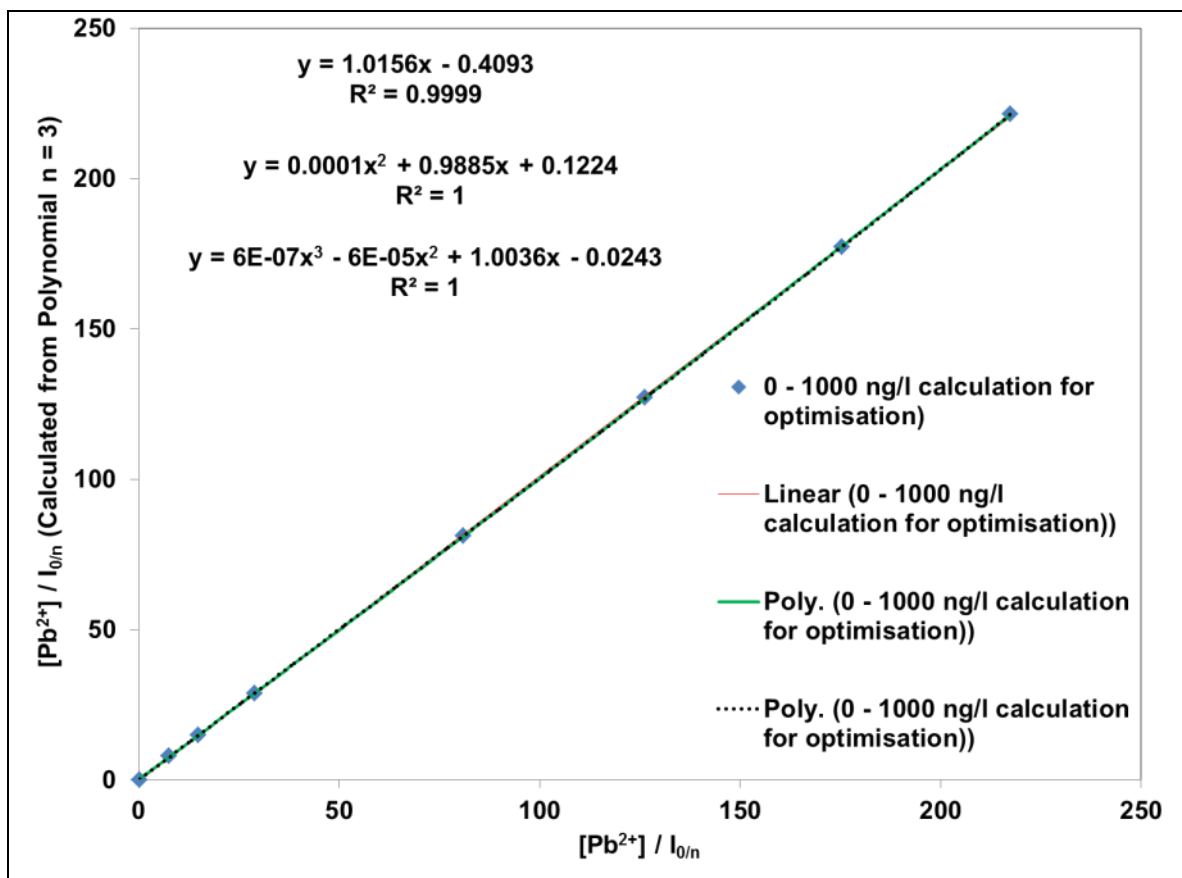
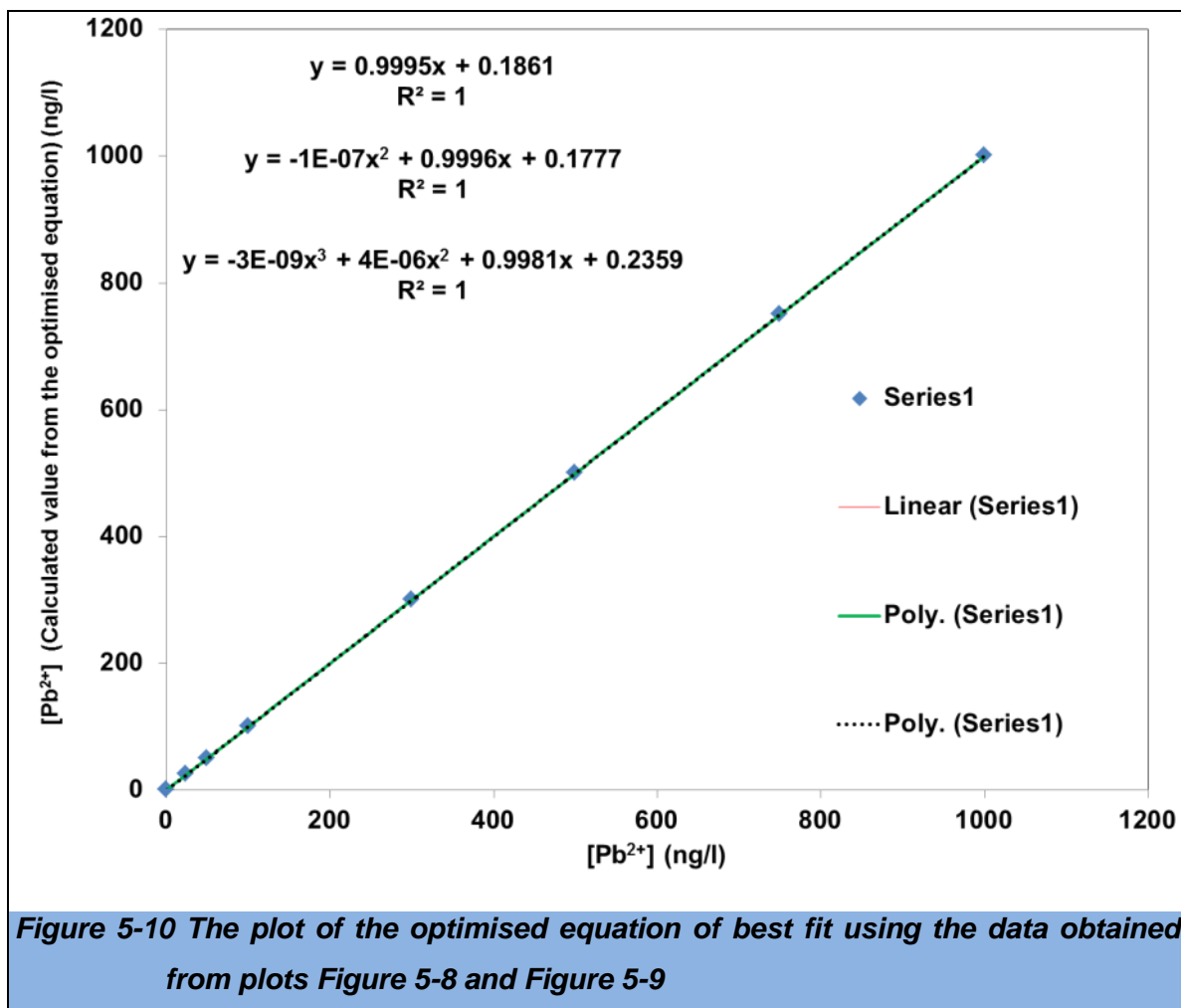


Figure 5-9 The re-plotted calibration plot using the line of best fit obtained from the $n = 3$ polynomial equation from Figure 4.8 ratio of the concentration of Pb^{2+} ions over the intensities of the $\nu(C-OH)$ band for the AuNP SERS sample and the $Pb^{2+}/AuNP$ SERS samples

To obtain an optimised line of best fit, the line equations from Figure 5-9 were used to create a modified version of the polynomial ($n = 3$) from Figure 5-8. This was achieved by rearranging the equations so that the polynomial ($n = 3$) from Figure 5-8 now equalled the intensity ratios of the $\nu(C-OH)$ band of the $Pb^{2+}/AuNP$ SERS samples, for concentrations between 0 *ng/l* and 1000 *ng/l* (the x-axis of Figure 5-9).

After using each equation obtained from Figure 5-9, and using it to optimise the original fit, a new plot of the optimised equation of best fit was obtained (Figure 5-10).

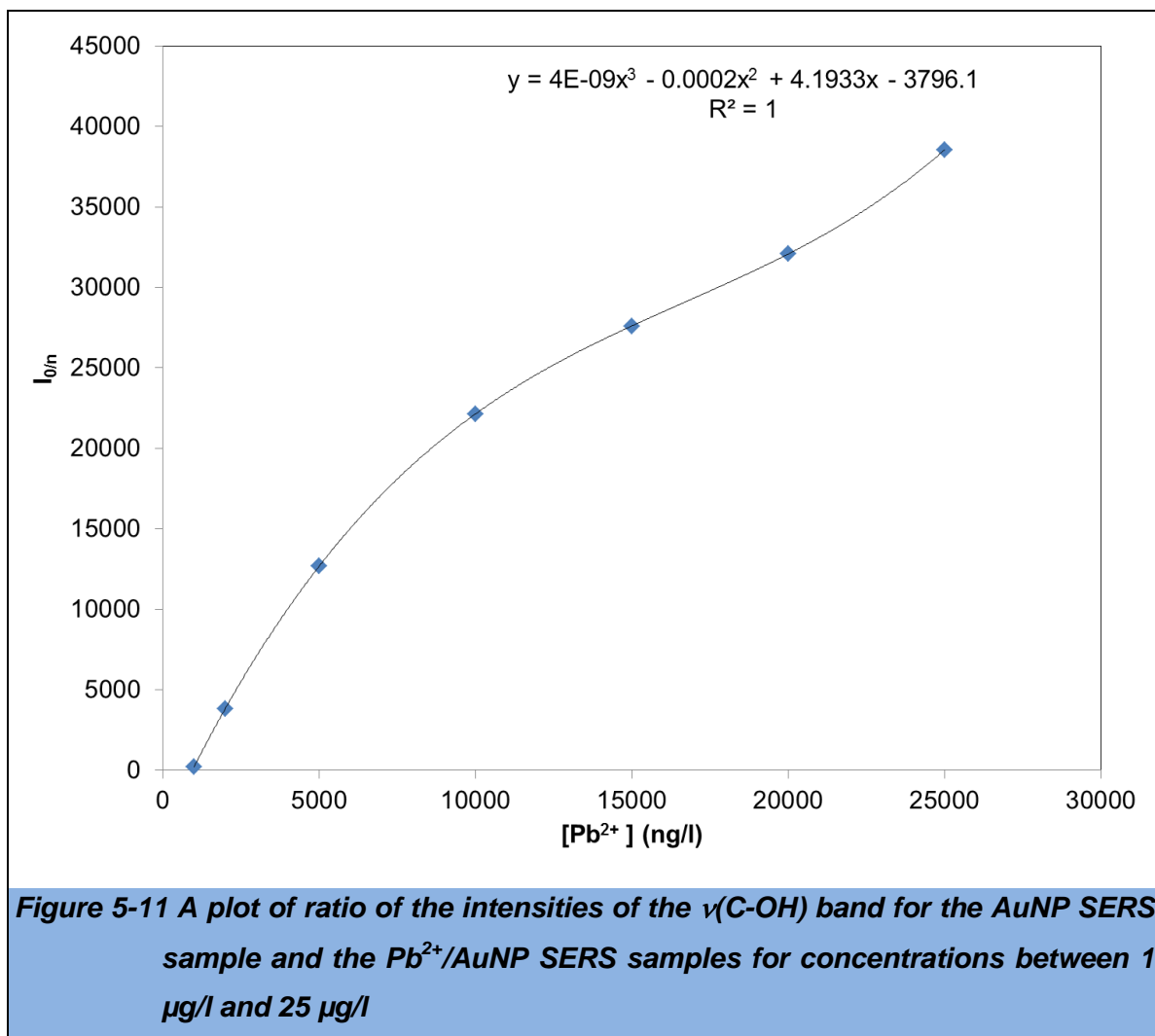


This new optimised equation produced exceptional results within the range of 0 *ng/l* and 1000 *ng/l*, with a correlation coefficient of 1 and an average standard deviation of 0.315 *ng/l*.

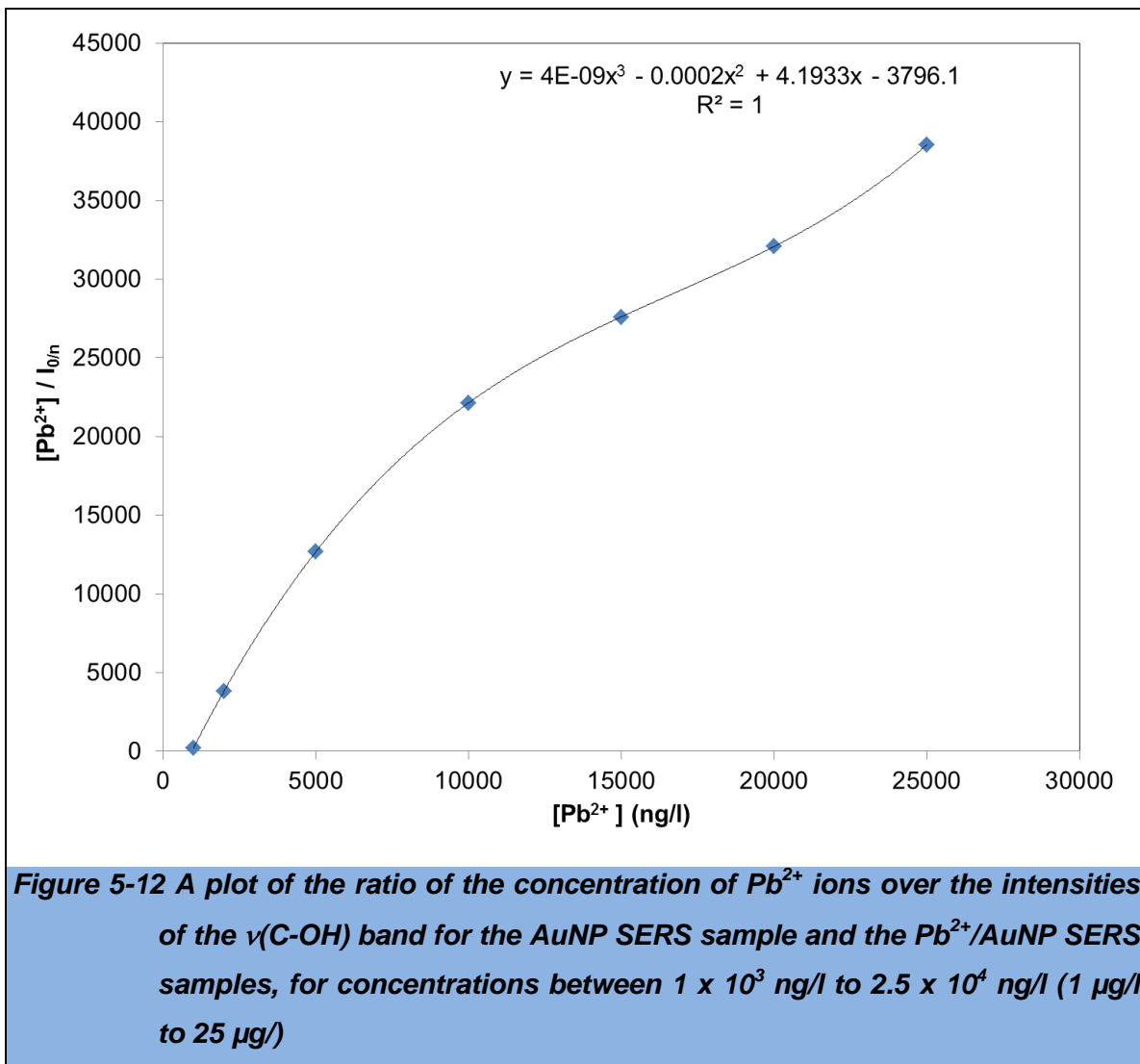
5.3.3 Calibration Curve for 1.000 $\mu\text{g/l}$ to 25.000 $\mu\text{g/l}$

The above technique for acquiring an optimised calibration equation was employed again when extending the concentration range from 1000 *ng/l* to 2.5×10^4 *ng/l* (1 $\mu\text{g/l}$ to 25 $\mu\text{g/l}$) for Pb^{2+} ion solutions. This concentration range was used as it incorporates the concentrations of Pb deemed as 'acceptable' by the WFD and DWD (7.2 $\mu\text{g/l}$ and 10 $\mu\text{g/l}$ respectively).

The intensity ratios were plotted for the $\nu(\text{C-OH})$ band for the AuNP SERS sample and the Pb^{2+} /AuNP SERS samples (Figure 5-11).



Once again, a plot was produced with the concentration of Pb^{2+} ions over the intensity ratios for the AuNP SERS sample and Pb^{2+} /AuNP SERS samples, against the concentration of Pb^{2+} ions (Figure 5-12). This produced a polynomial of order $n = 3$.



The obtained polynomial equation was then plotted against the concentration of Pb²⁺ ions over the intensities of the ν(C-OH) band for the AuNP SERS sample and the Pb²⁺/AuNP SERS samples (Figure 5-13).

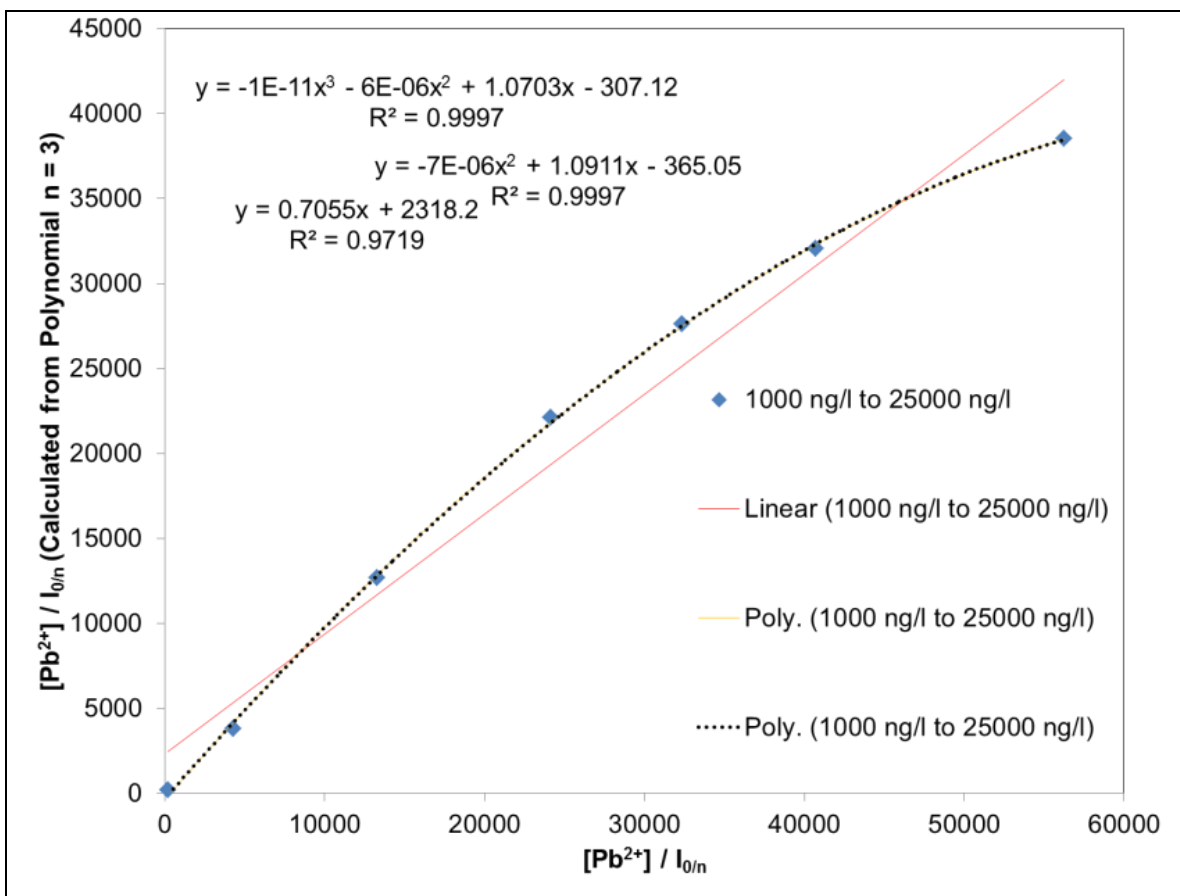


Figure 5-13 The re-plotted calibration plot using the line of best fit obtained from the $n = 3$ polynomial equation from Figure 5-14 versus ratio of the concentration of Pb^{2+} ions over the intensities of the $\nu(C-OH)$ band for the AuNP SERS sample and the $Pb^{2+}/AuNP$ SERS samples

To obtain an optimised line of best fit, the equations from Figure 5-13 were used to create a modified version of the polynomial ($n = 3$) from Figure 5-12. This was achieved by rearranging the equations so that the polynomial ($n = 3$) from Figure 5-12 now equalled the intensity ratios of the $\nu(C-OH)$ band for the AuNP SERS sample and the $Pb^{2+}/AuNP$ SERS samples for concentrations between $1 \times 10^3 \text{ ng/l}$ to $2.5 \times 10^4 \text{ ng/l}$ (the x-axis of Figure 5-13). After using each equation, a new plot of the optimised equation of best fit was obtained (Figure 5-14).

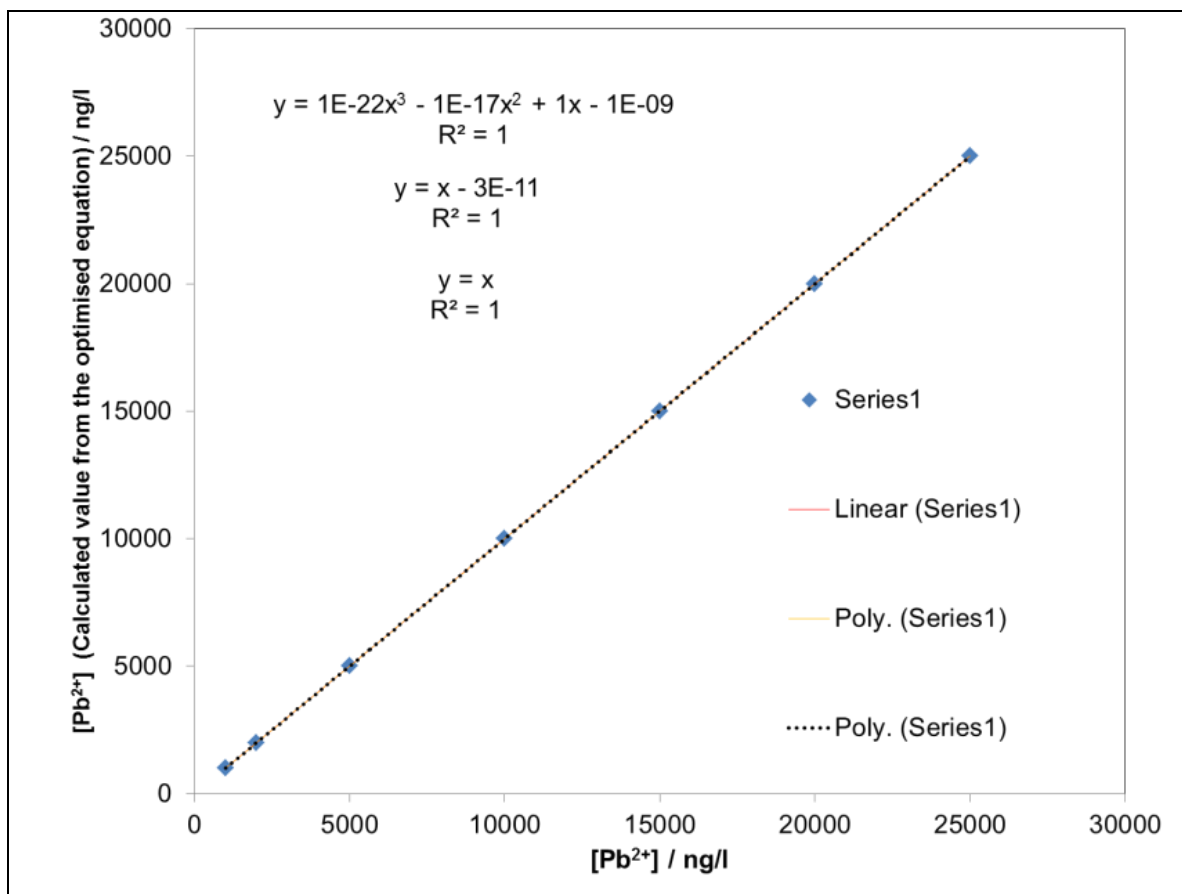


Figure 5-14 A plot of the ratio of the concentration of Pb^{2+} ions over the intensities of the $\nu(C-OH)$ band for the AuNP SERS sample and the $Pb^{2+}/AuNP$ SERS samples, for concentrations between 1×10^3 ng/l to 2.5×10^4 ng/l ($1 \mu\text{g/l}$ to $25 \mu\text{g/l}$)

This new optimised equation produced excellent results within the range of 1×10^3 ng/l to 2.5×10^4 ng/l, with a correlation coefficient of 1 and an average standard deviation of 0 ng/l.

5.3.4 Comparison of this SERS-based technique with standard techniques for the determination of the concentration of Pb in aqueous samples

A solution of Pb^{2+} ions was determined to be $10.08 \mu\text{g/l}$ by ICP-AES. Using the SERS analytical approach developed here, the solution was determined to be $10.00 \mu\text{g/l}$ giving a 99.21 % recovery, with a RSD of 0.2 % ($n = 5$). This shows that this method is competitive with current analytical methods, coupled with preconcentration steps, when looking at just Pb^{2+} ion concentrations (Table 5.2). As this SERS technique is non-ion specific, replacing the spectroscopy component

(GFAAS or FAAS) with this SERS technique and retaining the preconcentration step to obtain selectivity could yield extremely low limits of detection (LOD) but at a much lower cost.

Table 5.2 Standard analytical techniques for the detection Pb	
Method of Analysis	Limit of Detection for concentrations Pb
Flame AAS (ppb, µg/l)	10
GFAAS (ppb, µg/l)	0.04
ICP-AES (Radial) (ppb, µg/l)	14
ICP-AES (Axial) (ppb, µg/l)	1
ICP-MS (Quadrupole) (ppt, ng/l)	0.01-0.1

5.4 Summary and Conclusion

To conclude, in the present work, this work has successfully demonstrated a highly sensitive SERS method for the detection of Pb²⁺ ions in aqueous media. The experimental results showed that Pb²⁺ ions could be detected accurately with a high sensitivity (LOD = 25 ng/l) over a wide linear range (25 ng/l – 1000 ng/l). Although, due to the non-selective nature, this technique would only be highly useful for analysis of solutions after a Pb²⁺ ion-selective preconcentration step has been employed. A major advantage for this technique is that Raman spectrometers are relatively cheaper to purchase and maintain than many standard analytical techniques. Thus, a preconcentration/SERS technique would provide high limits of detection, high sensitivity and a cheaper analysis cost giving this cost-effective and sensitive sensing system great potential for practical application.

It can be seen that the SERS analysis method presented here has a superior LOD to all the listed analysis methods except ICP-MS for the detection of Pb.

It must be noted that this method has only been tested with free metal ions. In natural waters the metal ions can be complexed. These will not be detectable using this method unless the surface-bound citrate molecules have a more favourable solubility constant. For this, the metal ions will have to be removed from their complexes, via preconcentration steps, before this technique is employed. In addition to this disadvantage, the results are conclusive that there is no selective nature of the AuNP solution to Pb^{2+} ions, when in a solution containing other metal ions. This is a disadvantage as in natural waters there are also other ions that may compete with the Pb^{2+} ions. These are two disadvantages that ICP techniques do not suffer from.

In summary, this technique provides good results with a low limit of detection and low standard deviations over a wide range of practical concentrations; These are competitive with current techniques and technologies. This technique has also provided a new contribution to knowledge with the production of new SERS-based nanosensor.

6 Results and Discussion (Part 3): The Synthesis of a CuS Cluster for the Ultra-Sensitive and Selective Detection of Aqueous Hg²⁺ ions using a Cation-Exchange Mechanism

It was shown in Chapters 3 and 4 that the gold nanoparticle-based techniques that were developed during this study were unsuitable for the selective detection and quantification of Pb²⁺, Cd²⁺, Ni²⁺ and Hg²⁺ ions in aqueous media. Chapter 5 concludes this study with the successful synthesis of a cation-exchange CuS cluster that is suitable for the selective determination of Hg²⁺ ion concentrations in a mixed metal aqueous sample.

6.1 Qualitative Analysis of the Synthesised Nanoclusters

6.1.1 Transmission electron microscopy analysis

Transmission electron micrographs were employed to measure the diameters of the clusters synthesised here. For the ZnS clusters, the particle diameters were between 3 nm and 5 nm (Figure 6-1), and for the CuS clusters, TEM imaging displayed cluster sizes of between 4 nm to 5 nm (Figure 6-2). These images confirm that the particles are within the cluster regime.

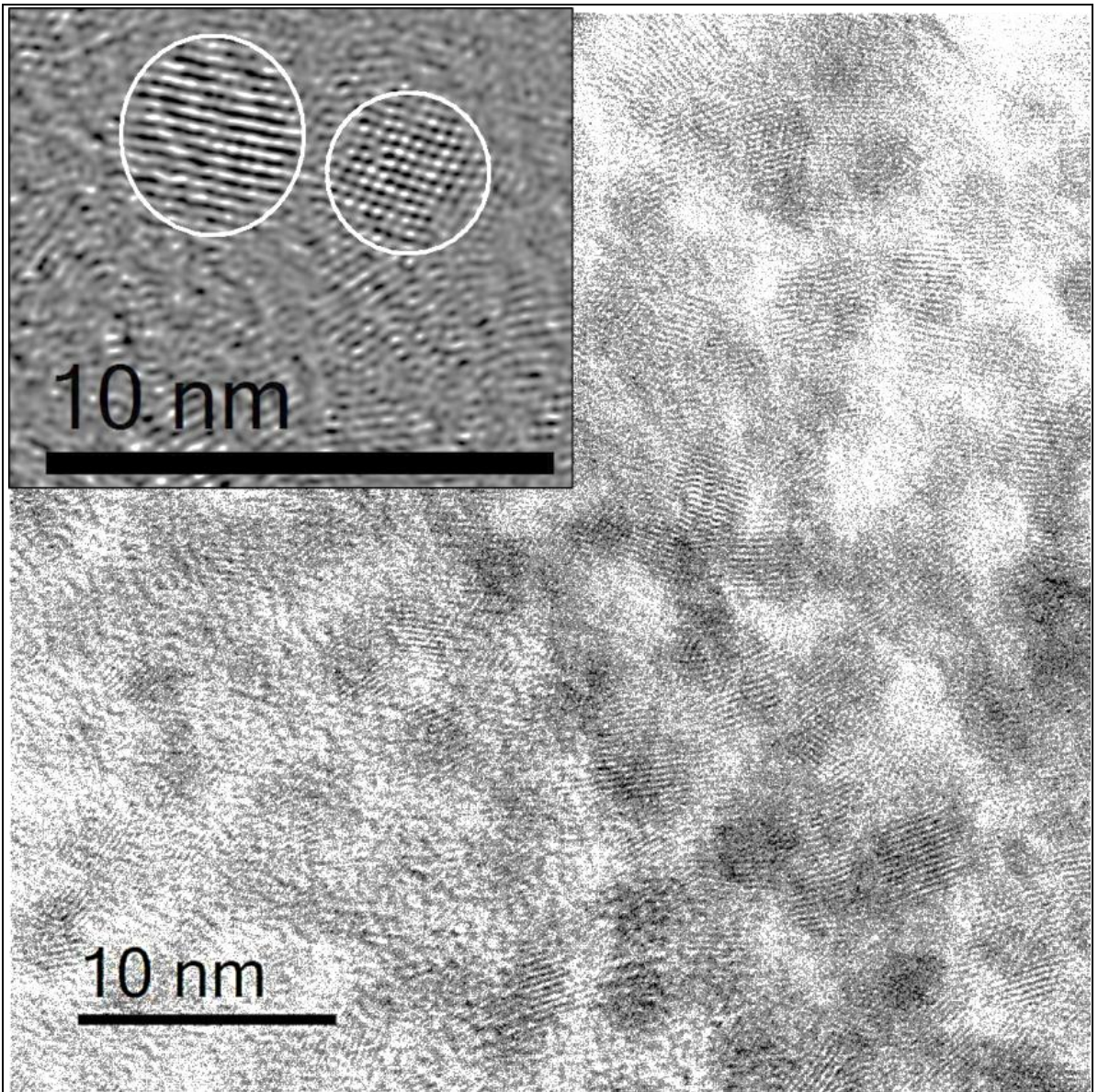


Figure 6-1 TEM micrographs for the ZnS nanoclusters, showing cluster diameters of 3 to 5 nm

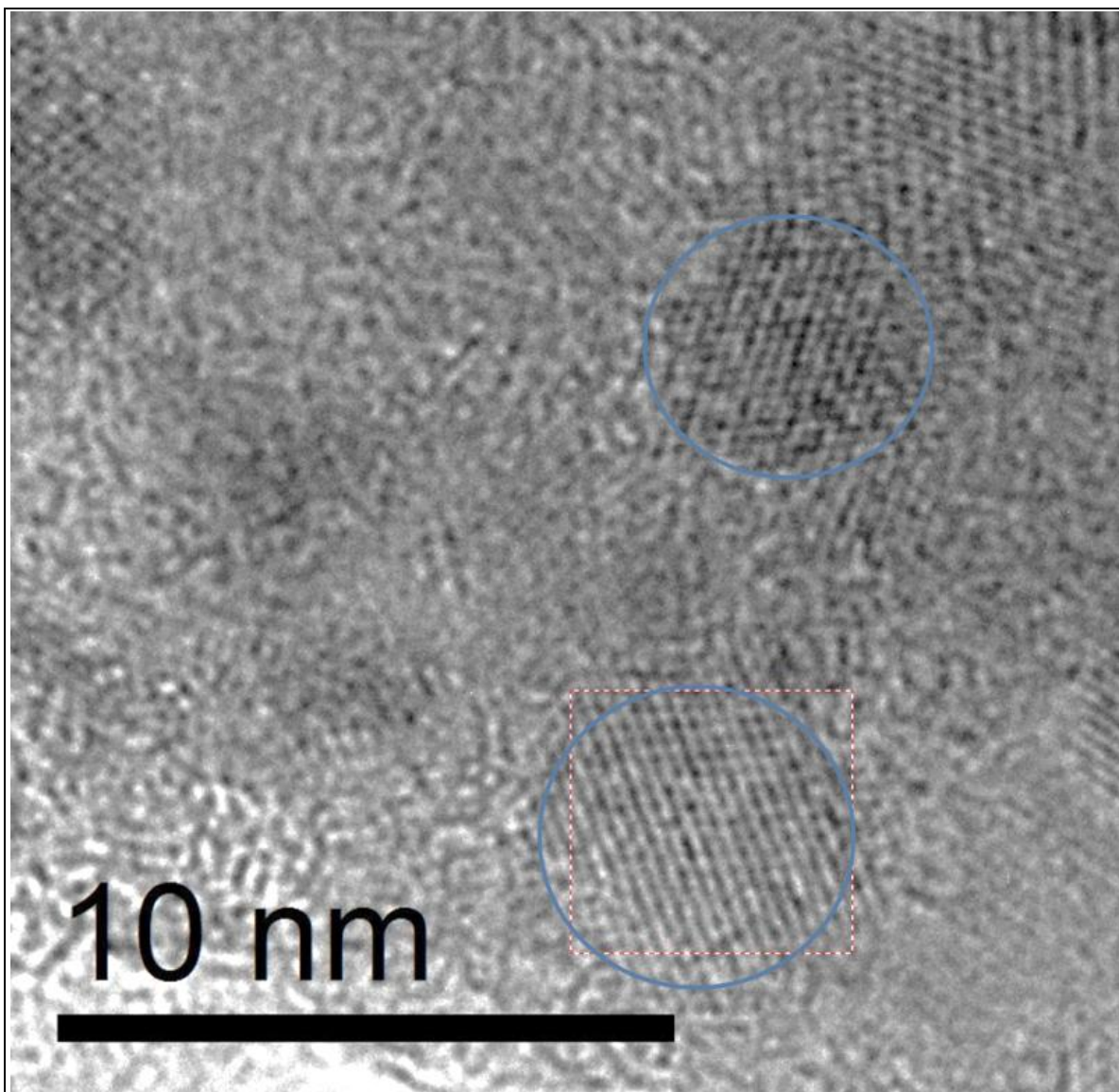
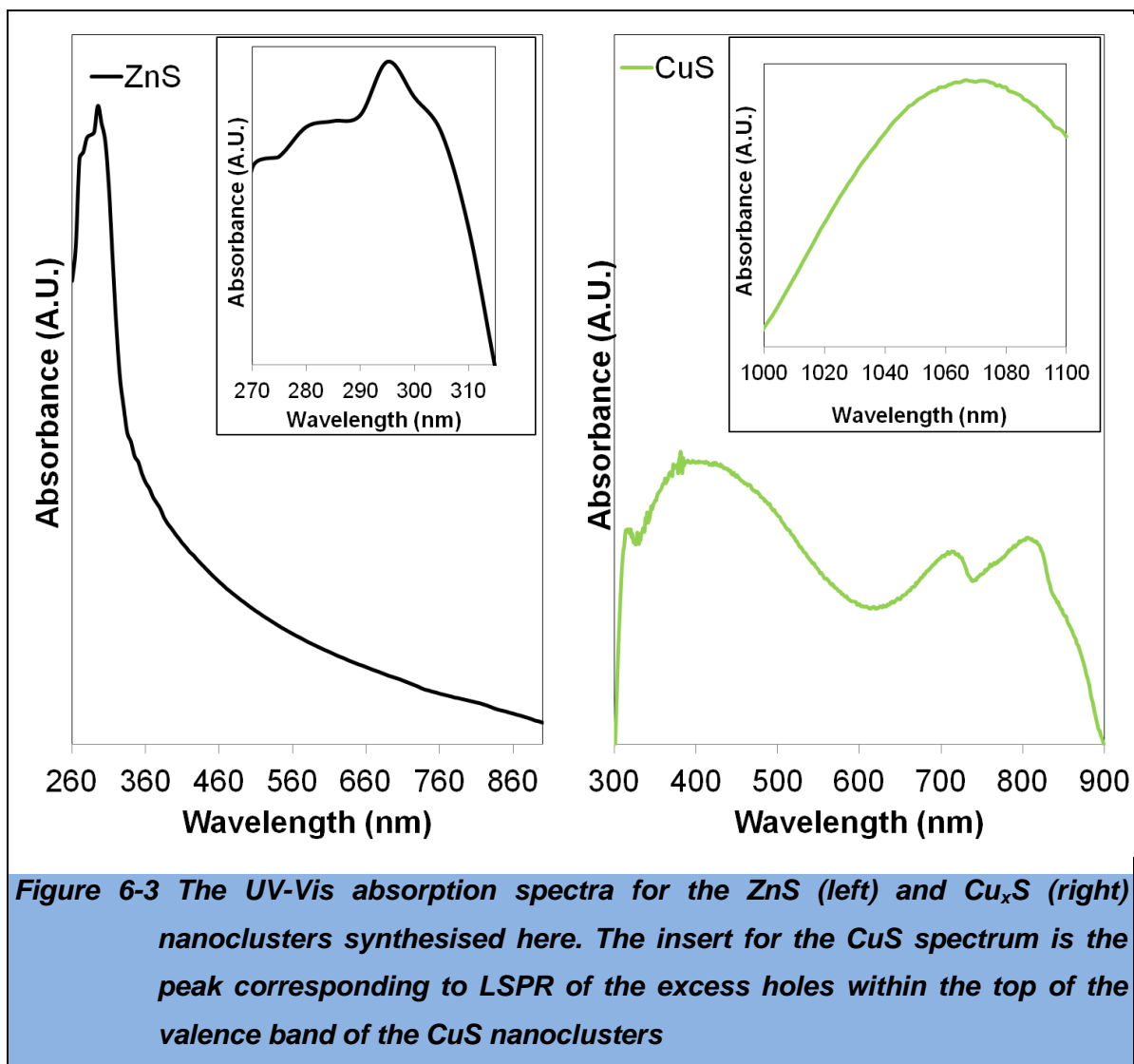


Figure 6-2 TEM micrographs for the CuS nanoclusters, showing cluster diameters of 3 to 5 nm

6.1.2 UV-Vis absorption spectroscopy

UV-Vis absorption spectroscopy was initially used as a qualitative assessment of the nanoclusters synthesised here. The spectral data acquired here shows the characteristic spectra for the original template ZnS clusters and the resulting CuS clusters (Figure 1). The insert of the ZnS spectrum shows a more detailed image of the peaks at the higher absorbance region of the spectrum. The maximum absorption at 295 nm is classified within the literature as the electronic transition between the *valance band* (VB) to the *conduction band* (CB) – the bandgap of the material, E_g . It should be noted that there is a band positioned at 303 nm and a further band present at 322 nm. The band at 322 nm is assigned to interstitial ions

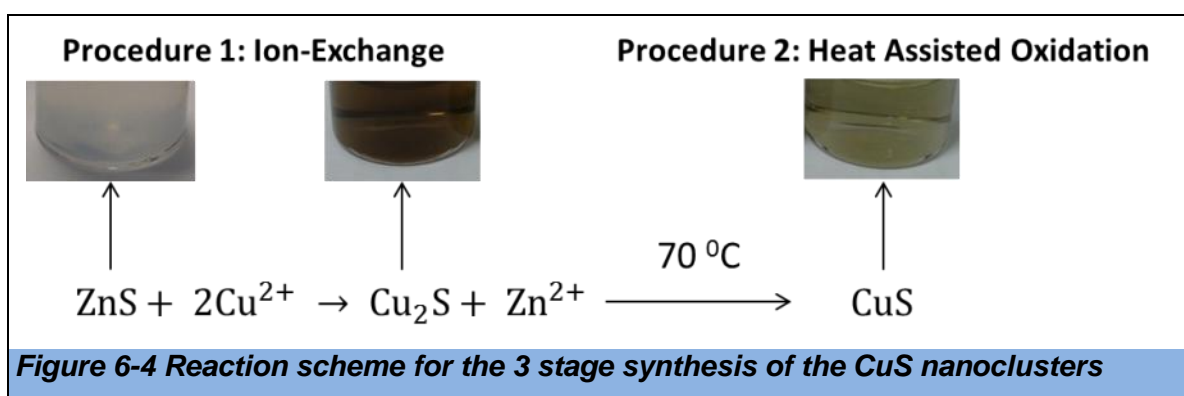
within the crystal structure.^{116,117} The band at 303 nm has not been labelled within the literature but this could also be assigned to interstitial ions. Here the peak at 295 nm corresponds to a bandgap value of 4.2 eV - this value is comparable to literature values for the bandgap of ZnS nanoclusters.¹¹⁷



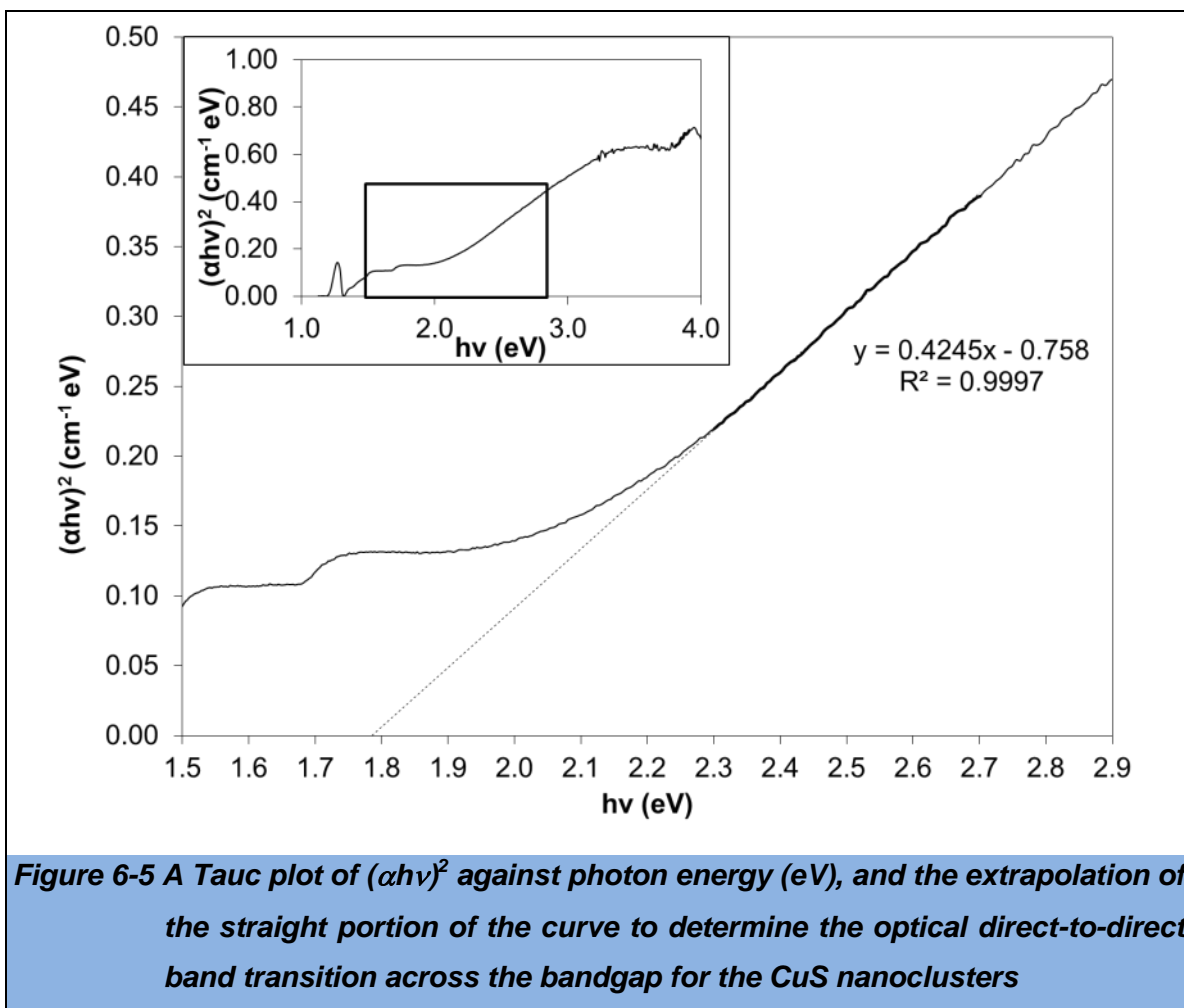
The UV-Vis absorption spectrum for the CuS nanoclusters is analogous to spectra found within the literature (Figure 6-3).¹¹⁹ The peak present at 1070 nm is a clear indication that a Cu_xS nanocluster (where $x < 2$) had been formed. This absorption is due to LSPR: Here, unlike the oscillation of free electrons within the conduction band (as with noble metal nanoparticles), this absorption is a result of the oscillation of excess holes in the top of the valence band.¹¹⁹ The population of these excess holes increase as $x \rightarrow 1$.¹¹⁹ As this localised hole-plasmon absorption is not present for Cu₂S, this peak clearly shows that for this nanocluster sample, $x < 2$. The excess hole population originates from 'self-doping', where

Cu₂S is the original 'undoped' form of the nanocluster, with copper taking on the Cu(I) oxidation state. As x tends towards 1, the oxidation state of the copper becomes Cu(II) leading to a reduction in the electron population *i.e.* an increased concentration of holes.

In addition to the absorption spectra for the CuS nanocluster product, the reaction mixture turned from white to brown during the ion-exchange method, and then to green during the oxidation procedure. The green solution is a known indicator that CuS nanoclusters have been produced; whereas the brown solution confirmed that the initial ion-exchange process between Zn²⁺ ions within the ZnS template and the Cu²⁺ ions in solution had taken place, resulting in the intermediate Cu₂S nanocluster product (Figure 6-4).¹²⁰



The acquired UV-Vis absorption spectrum for CuS nanoclusters was also used to estimate the bandgap energy of the material using 'Tauc plots'. This was carried out to provide a more quantitative analysis of the clusters produced, as the difference in the bandgap values for ZnS and CuS clusters are on the order of several eV. The Tauc plots for allowed direct band transitions (Figure 6-5) and indirect band-to-band transitions (Figure 6-6) were produced for the CuS clusters.



To obtain an estimate for the allowed direct band transition energy across the bandgap the straight portion of a plot of $(\alpha h\nu)^2$, against photon energy (eV), must be extrapolated to $(\alpha h\nu)^2 = 0$. The extrapolation of the straight portion of the absorption curve for the CuS sample produced a direct band transition energy of 1.79 eV. This value matches the literature values for CuS nanoclusters for an allowed direct band transition.¹¹⁸ To obtain an estimate for the indirect optical transition across the bandgap, a plot of $(\alpha h\nu)^{0.5}$ against photon energy is plotted, and the transition energy is taken as the point at which the absorption curve crosses the x-axis. For the CuS nanoclusters, this plot produced an indirect transition energy value of 1.32 eV which does not correspond to the Cu_2S cluster, which has an indirect transition of ~ 1.55 eV, further suggesting that CuS clusters have been formed.

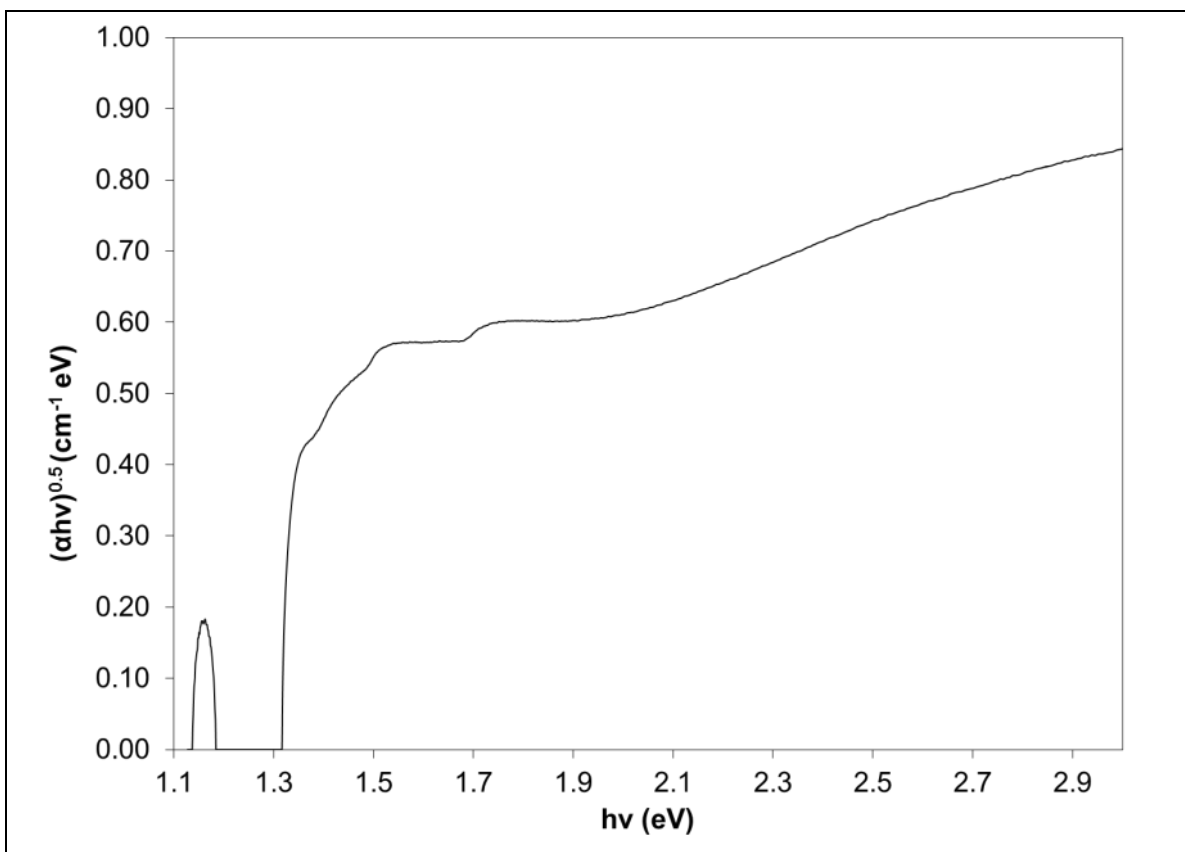


Figure 6-6 A Tauc plot of $(\alpha h\nu)^{0.5}$ against photon energy (eV) and the evolution of the curve to $y = 0$, which determines the indirect optical band transition across the bandgap for the CuS nanoclusters

Both samples also show bandgap values which are much higher than those of the respective bulk bandgap values (ZnS = 3.68 eV, and CuS = 1.4 eV).^{117,121} This increase in the bandgap value from the bulk value is due to quantum confinement effects. This proves that both cluster diameters are comparable or smaller than their respective Bohr exciton radius values (ZnS = 2.5 nm, CuS = 3-5 nm).^{121,122}

6.1.3 X-ray photoelectron spectroscopy

XPS was used here as a qualitative analysis method to record the elemental composition of the clusters. Furthermore, it was an indispensable tool for the determination of the oxidation states of the Cu ions in the CuS based materials. This was important due to the difference in oxidation states for the Cu_xS materials, where $1 \leq x \leq 2$.

The XPS data show that Cu_2S particles were produced after the first procedure of the cluster synthesis. The data then confirms that the CuS clusters were produced in the second step (Figure 6-7).

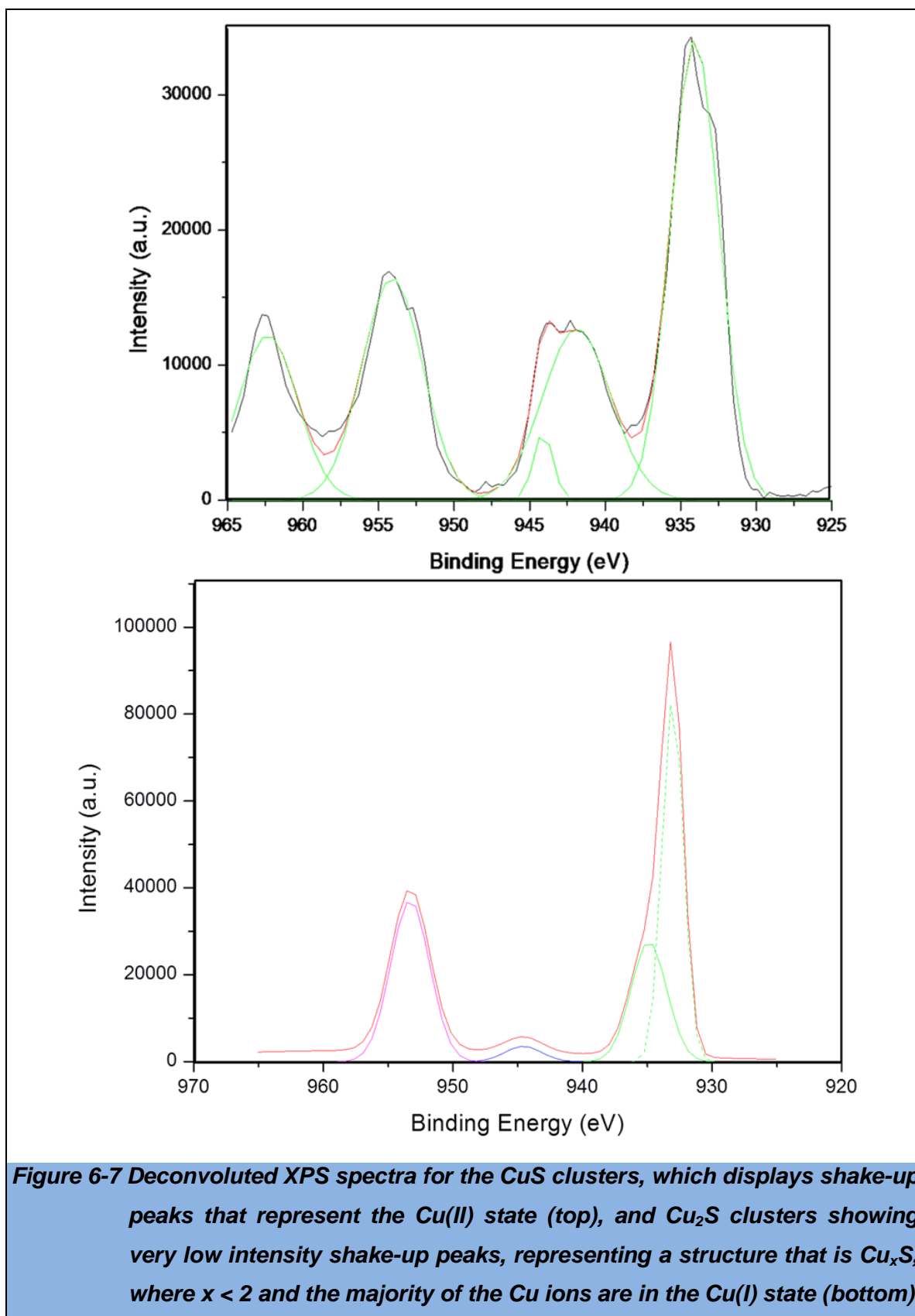


Figure 6-7 Deconvoluted XPS spectra for the CuS clusters, which displays shake-up peaks that represent the Cu(II) state (top), and Cu_2S clusters showing very low intensity shake-up peaks, representing a structure that is Cu_xS , where $x < 2$ and the majority of the Cu ions are in the Cu(I) state (bottom)

The presence of a Cu(II) oxidation state is shown by the presence of 'shake-up' peaks, which are a unique feature of the Cu(II) oxidation states in CuS materials and are only slightly present for Cu(I) oxidation states *i.e.* Cu₂S materials.¹²³ This data is therefore consistent with CuS nanoparticles. The obvious peak splitting of the peaks in Figure 6-7 (left), may be a result of different Cu environments within the cluster and at the surface of the cluster *i.e.* the Cu(II) ions in the centre of the particle will have a slightly different binding energy value than those at the surface; but as these secondary peaks are also seen in the shake-up peaks, it can be said that the Cu components at the surface and interior of the clusters, is mostly of the Cu(II) state. The presence of a Cu(I) oxidation state is confirmed by the XPS spectrum in Figure 5.7, as there is no major display of shake-up peaks, which is consistent with Cu₂S materials. However, there is a small peak consistent with a shake-up satellite indicating that there is a small percentage of Cu(II) present in the sample. The slight presence of shake-up peaks in Figure 6-7 (right) may also be a result of different Cu environments within the cluster and at the surface of the cluster *e.g.* the internal structure of the nanocluster may consist of Cu(II) and the surface Cu(I); but as the surface to volume ratio of the small nanomaterials is so large, the majority of the surface, and thus the particle, can be seen as consisting mostly of the Cu(I) state.

6.2 Characterisation of the CuS Clusters with Increasing Hg Concentration

The synthesised CuS nanoclusters were designed for their theoretical ability to exchange the Cu²⁺ ions of the CuS nanocluster with aqueous Hg²⁺ ions. UV-Vis absorption spectroscopy and TEM techniques were employed to monitor this exchange process: UV-Vis absorption spectroscopy was used to measure optical and electronic changes for the CuS nanoclusters in the presence of increasing amounts of aqueous Hg²⁺ ions, and TEM was employed to monitor particle size and morphology.

6.2.1 The determination of the bandgap energies of the doped nanoclusters and the widths of the band-edge localised states, using 'Tauc plots' and 'Urbach's rule'

The UV-Vis absorption spectra for the CuS nanoclusters, in the presence of different concentrations of Hg^{2+} ions, shows that upon the addition of Hg^{2+} ions, the optical properties of the clusters is affected (Figure 6-8).

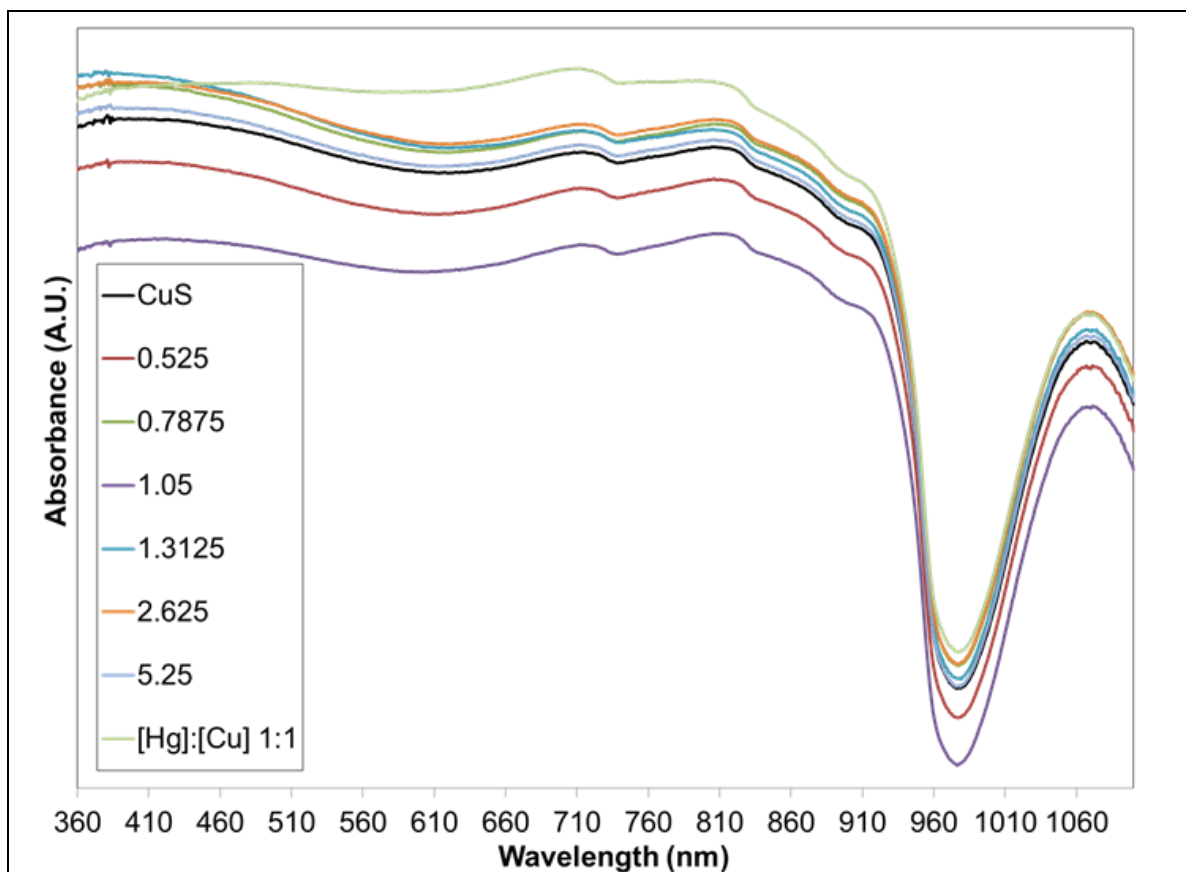


Figure 6-8 The UV-Vis absorption spectra for solutions of CuS nanoclusters, which contain different concentrations of Hg^{2+} ions ranging from 0.0000 $\mu\text{g/l}$ to a 1:1 $[\text{Hg}^{2+}]:[\text{Cu}^{2+}]$ ratio

If ion-exchange had occurred between the aqueous Hg^{2+} ions and the Cu^{2+} ions of the CuS clusters, it would be expected that the electronic properties of the cluster would change *i.e.* the bandgap energy, the potential appearance of localised defect states, the concentration of holes for LSPR etc. Tauc plots were again produced to measure the allowed direct and allowed indirect bandgap transitions of the CuS nanoclusters (Table 6.1).

Table 6.1 Results from Tauc plots taken from UV-Vis absorptions data for solutions of CuS clusters which contain different concentrations of Hg^{2+} ion. The table contains energy values for the allowed direct bandgap transitions (E_d) and allowed indirect bandgap (E_i) transitions, the phonon energy (E_p) associated with the indirect transition ($E_i + E_p = E_g$), the Urbach energy (E_U) and the energy of the LSPR absorption band (E_{LSPR})

[Hg] ($\mu g/l$)	E_d (eV)	E_i (eV)	E_p (eV)	E_U (eV)	E_{LSPR} (eV)
0	1.786	1.318	0.468	0.438	1.209
0.525	1.823	1.321	0.502	0.607	1.204
0.7875	1.811	1.314	0.497	0.798	1.214
1.05	1.871	1.330	0.540	0.316	1.193
1.3125	1.825	1.315	0.510	0.574	1.212
2.625	1.758	1.314	0.444	0.739	1.216
5.25	1.586	1.316	0.270	0.612	1.211

Plotting a graph of the allowed direct bandgap energy (E_g) against the concentration of Hg^{2+} ions in the CuS nanocluster solution, revealed that the evolution of the bandgap energy does not take the shape of a linear or smooth curve (Figure 6-9). The most noticeable features of this plot are the inflection points at 0.7875 $\mu g/l$ and 1.0500 $\mu g/l$.

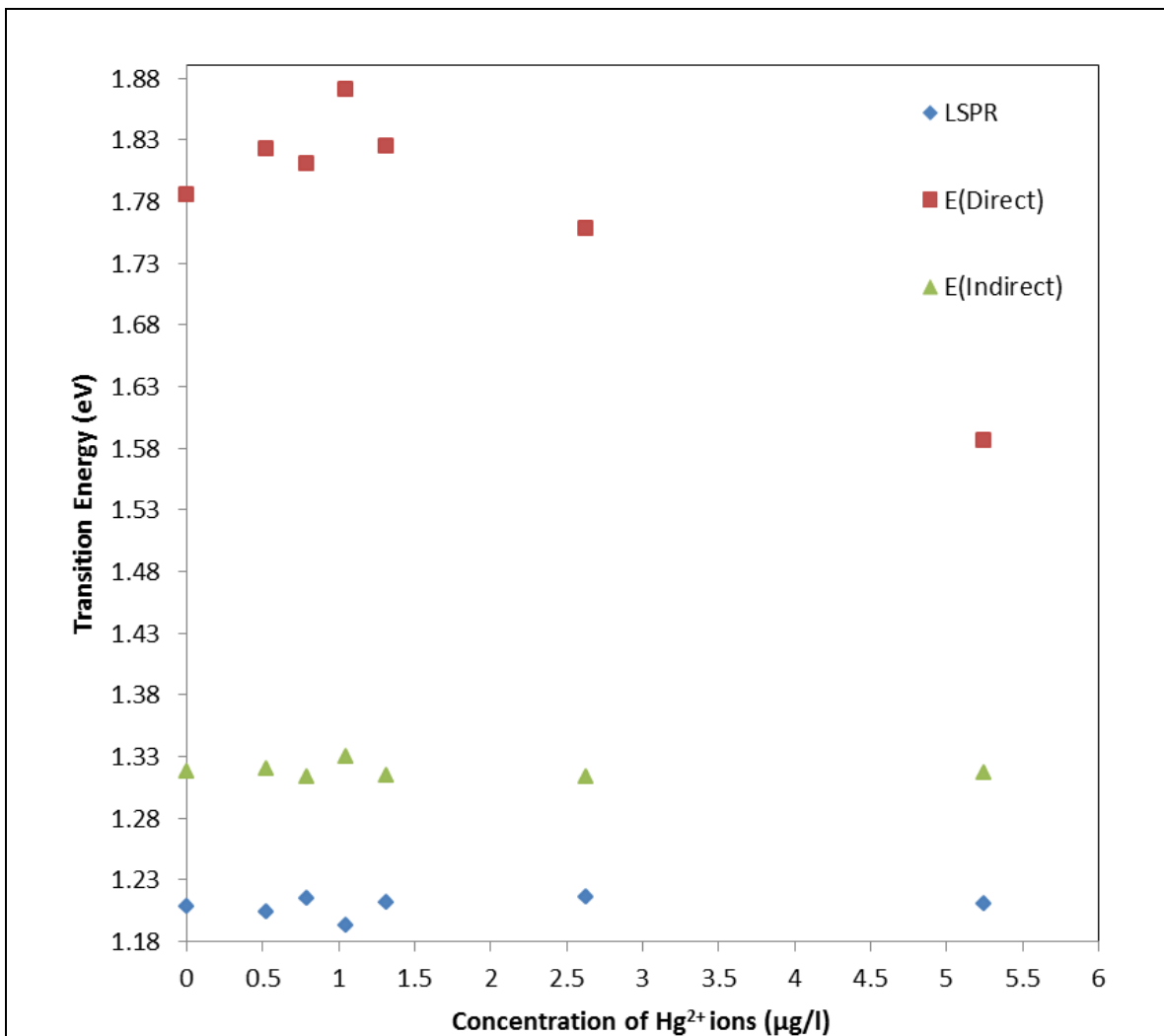


Figure 6-9 A plot of the allowed direct and indirect bandgap energy, and the LSPR absorption band position, vs the concentration of Hg²⁺ ions in the CuS nanocluster solutions

From 0.0000 µg/l to 0.5250 µg/l the direct bandgap energy increases by 0.037 eV. TEM micrographs show that the particles had taken on hollow-shell morphology (Figure 6-10). This is most likely due to the production of interstitial vacancies within the crystals structure, which can be produced by internal strain (Section **Error! Reference source not found.**). This internal strain was most certainly imposed by the larger ionic radius of the Hg²⁺ ions being integrated into the structure of the nanocrystal and the longer Hg-S bonds.

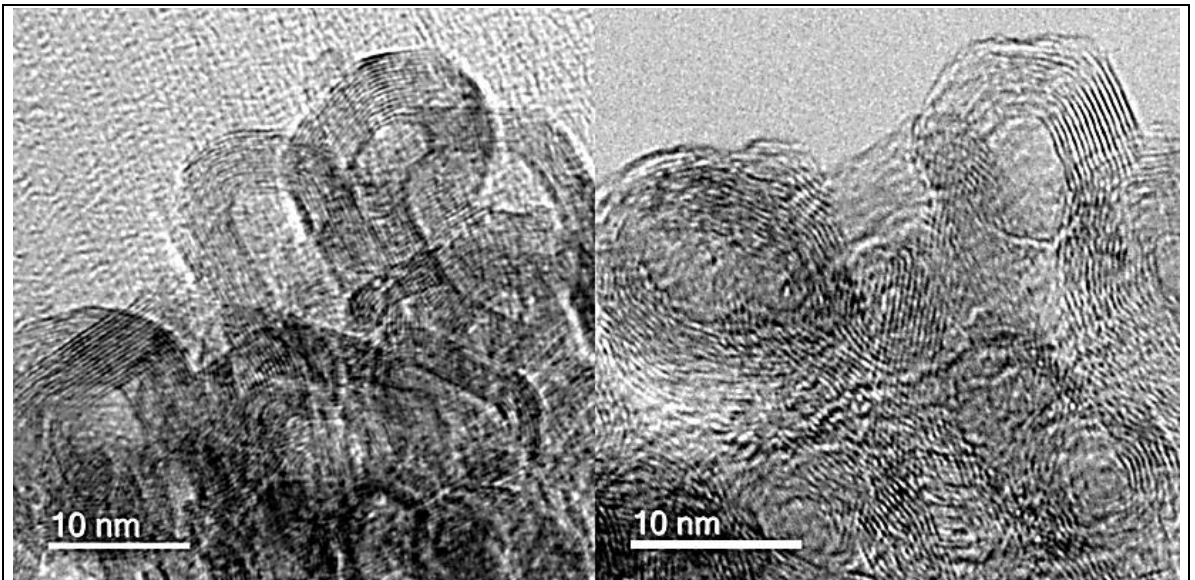
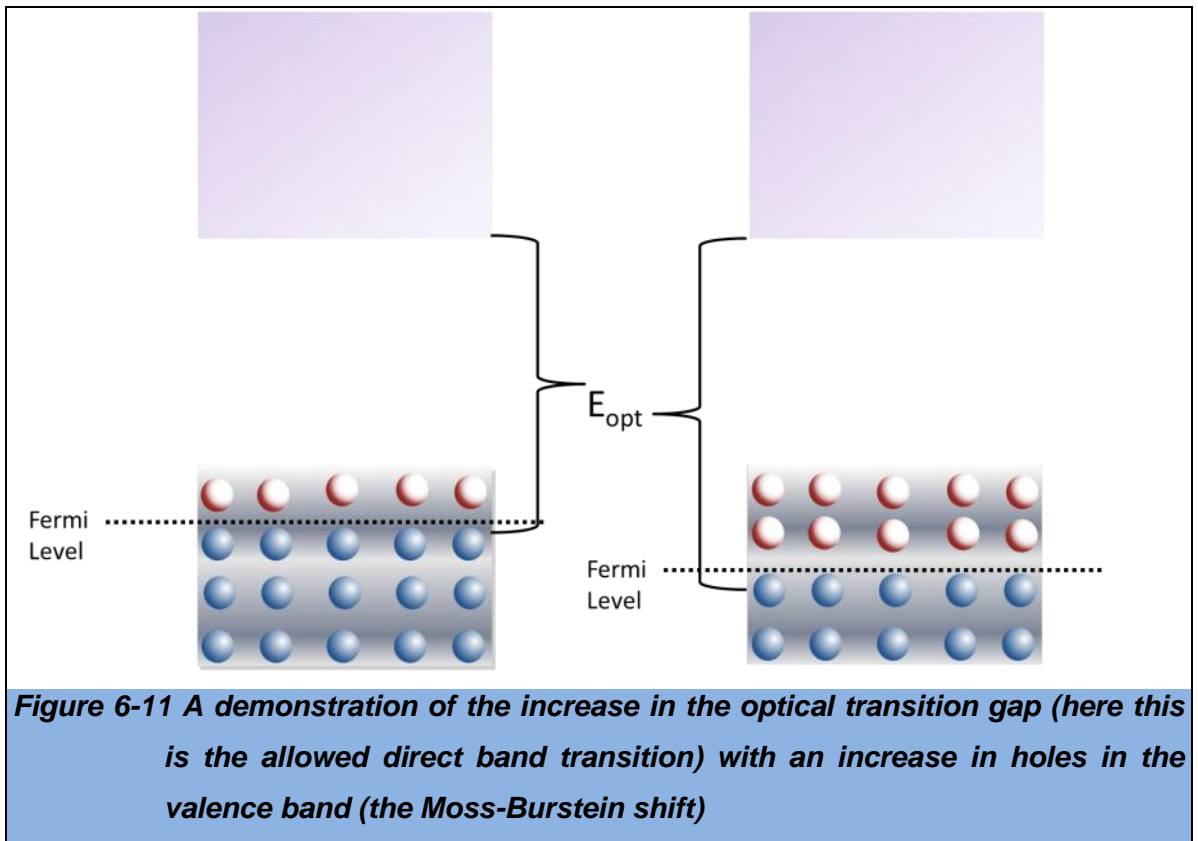
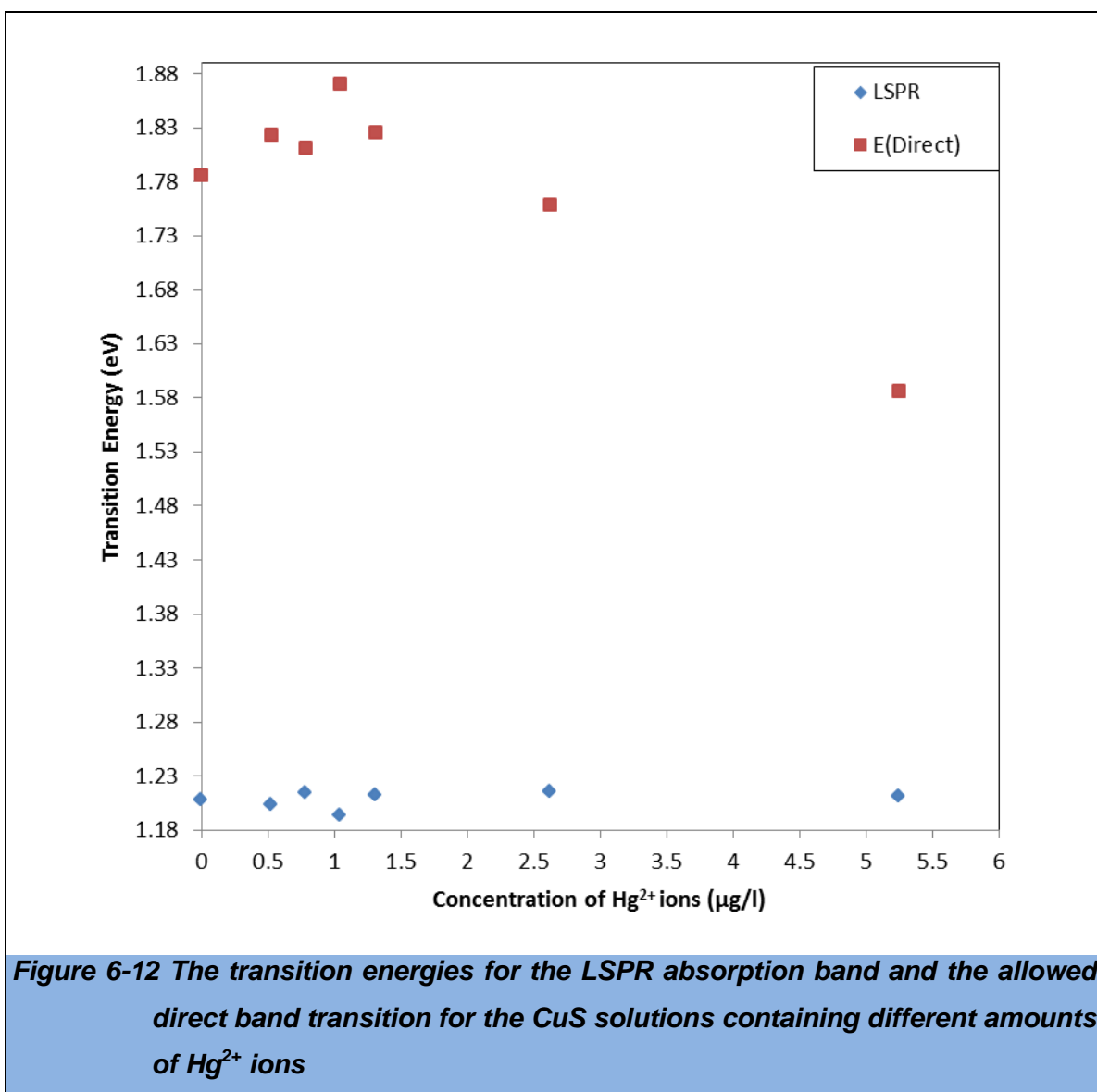


Figure 6-10 TEM micrographs of the hollow core-shell morphology adopted by the CuS/Hg nanoclusters at an aqueous Hg^{2+} ion concentration of 0.5250 $\mu g/l$

It is known that internal strain can increase the bandgap energy of semiconductor crystals. Because of the dramatic change in morphology, and the likely assumption that it is due to internal strain, this provides a good explanation to the rise in bandgap energy (Section **Error! Reference source not found.**). Urbach energy calculations also showed an increase in the number of localised electronic states near the valence and conduction band edges. These states can also be attributed to strain and the increased concentration of impurity ions in the crystal structure *i.e.* Hg^{2+} ions. TEM results also show that there is an increase in the dimensions of the material for this concentration range - In this case, this is the width of the shell, relative to the diameter of the CuS nanoclusters. Therefore the increase in the bandgap energy cannot be due to the increased size of the material, as the bandgap is inversely proportional to the width of the material *i.e.* the shell. It has been predicted that the initial bandgap increase, when going from Cu_2S to CuS, is a consequence of the Moss-Burstein shift.¹¹⁹ The Moss-Burstein shift is attributed to an increase or decrease in electrons in a semiconductor material. The increase in the concentration of holes (decrease in the concentration of the electrons) in the valence band of the CuS material lowers the Fermi energy level and widens the transition energy between the filled electron levels in the valence band and the conduction band. This increases the optical bandgap value (Figure 6-11).



This is not an acceptable reason for the change in the bandgap value here: As the LSPR absorption band energy is proportional to the number of holes present in the valence band, any shift in the LSPR band can be attributed to the changes in concentration of the valence band holes (this does not take into account any surface related effects such as the concentration of metal ions on the surface or size of the particle).¹²¹ It was found that as the bandgap value increased, the energy position of the LSPR band decreased (Figure 6-12). The increase in the bandgap potentially displays a reduction in the concentration of electrons in the valence band *i.e.* an increase in the concentration of holes in the valence band; but this is contradicted by the decrease in the energy position of the LSPR peak, which indicates a decrease in the concentration of holes in the valence band *i.e.* according to the Moss-Burstein shift, if the bandgap energy increases the LSPR peak can be expected to shift to a higher energy position. Now, the increase in Urbach energy can be considered: As strain and distortion increases, the bandgap value is expected to change, but this would not necessarily change the concentration of holes in the valence band – and thus energy position of the LSPR peak. Therefore it is reasonable to assume that the increase in the bandgap value is a consequence of strain instead of an increase in the concentration of holes in the valence band.



It was then found that the direct bandgap energy decreased at a concentration of 0.7875 µg/l and the hollow particles became whole again, with the solution containing cluster sizes ranging from 3 nm to 7 nm (Figure 6-13).

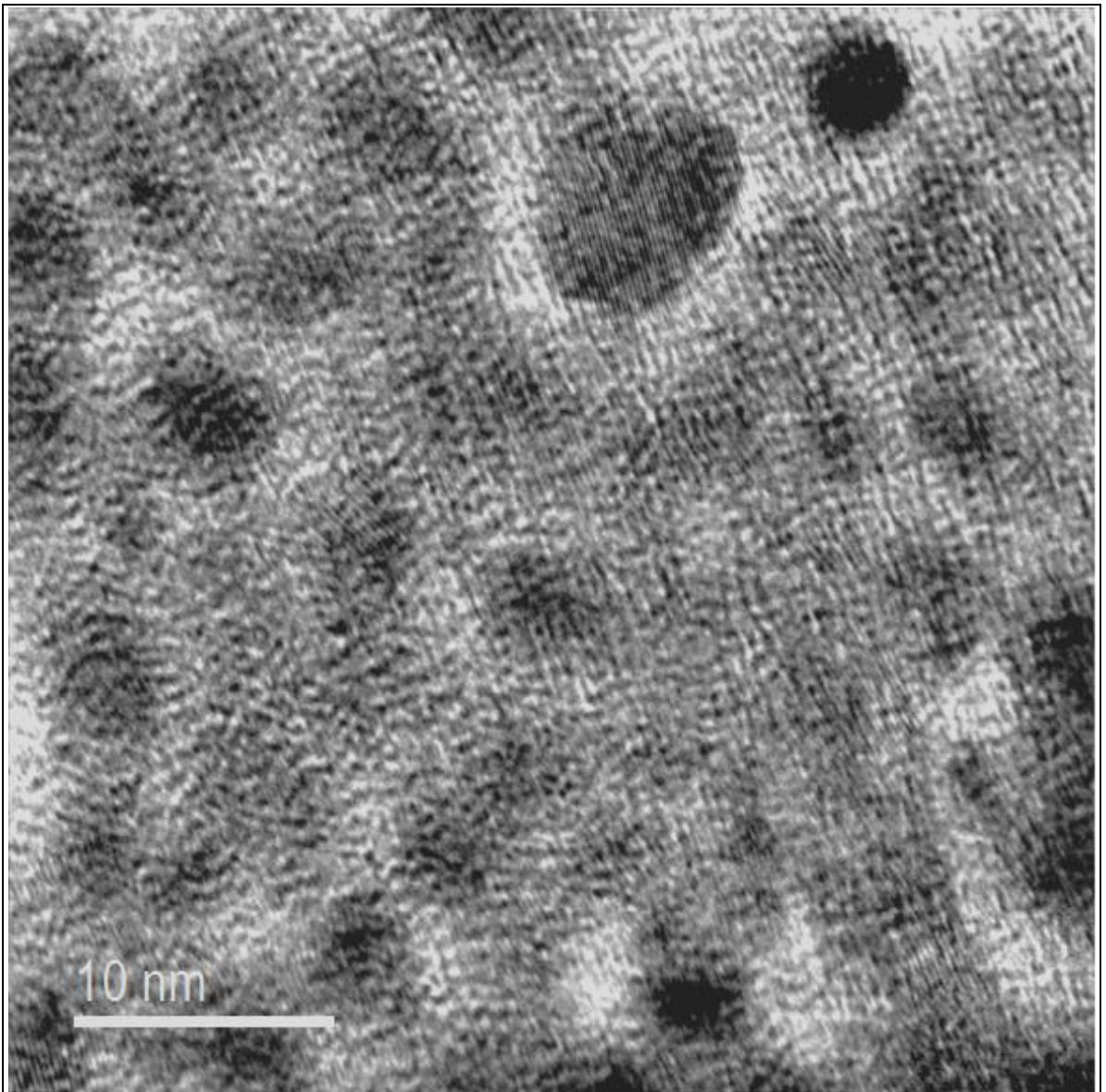


Figure 6-13 At a Hg^{2+} ion concentration of $0.7875 \mu\text{g/l}$, the hollow particles became whole with many different sizes ranging from 3 nm to 7 nm

This change in morphology and size distribution could indicate the breaking-up of the particles to form different sized particles which had a more stable crystal structure. There was a further increase in the Urbach energy, most likely due to an increasing concentration of Hg^{2+} ions being incorporated into the CuS nanocrystals. What is interesting in this data is that after increasing the Hg^{2+} ion concentration to $1.0500 \mu\text{g/l}$, the Urbach energy drops significantly, and the bandgap energy increases considerably. TEM images show that at a Hg^{2+} ion concentration of $1.0500 \mu\text{g/l}$, the particle diameter reduced down to sizes comparable to (and smaller than) the original CuS nanoclusters (c.a. 1 nm to 2 nm) (Figure 6-14).

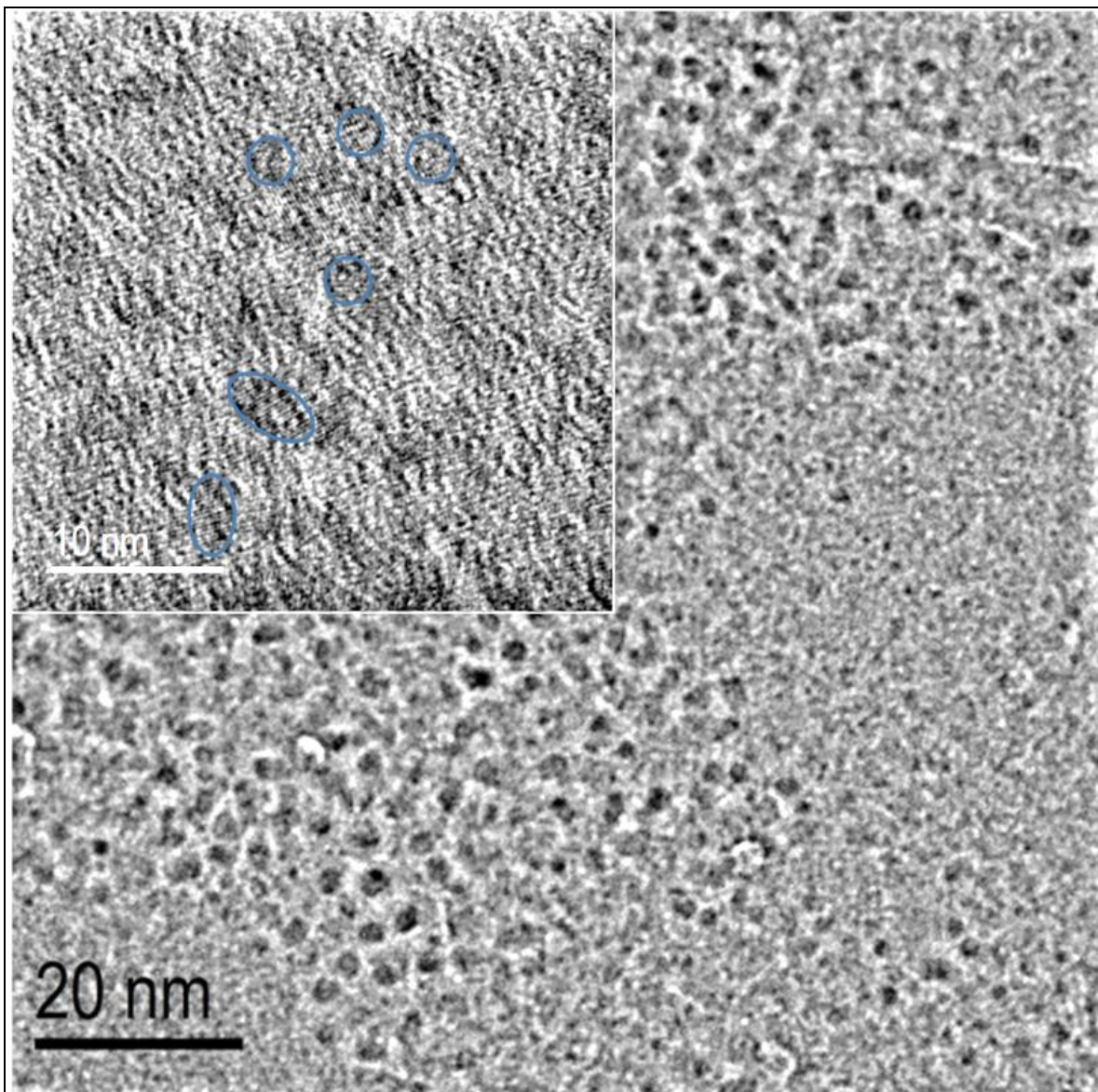


Figure 6-14 TEM micrographs showing the morphology of the CuS/Hg nanoclusters at an aqueous Hg^{2+} ion concentration of 1.0500 $\mu g/l$

This increase in the direct bandgap energy is most likely a result of strong quantum confinement as the Bohr exciton radius for CuS has been estimated to be between 3 *nm* to 5 *nm*, with strong quantum confinement effects becoming apparent <10 *nm*.¹²⁴ Therefore a CuS nanocluster size of 1 *nm* to 2 *nm* would display very strong quantum confinement effects, i.e. a large increase in the bandgap energy of the material, relative to the larger particle samples.

A further increase in the Hg^{2+} ion concentration produced more hollow-shell structures. Interestingly, at $5.2500 \mu\text{g/l}$, the particles were relatively large in diameter ($\sim 14 \text{ nm}$) and they appeared to be composed of concentric shells going towards the centre of the particle (Figure 6-15).

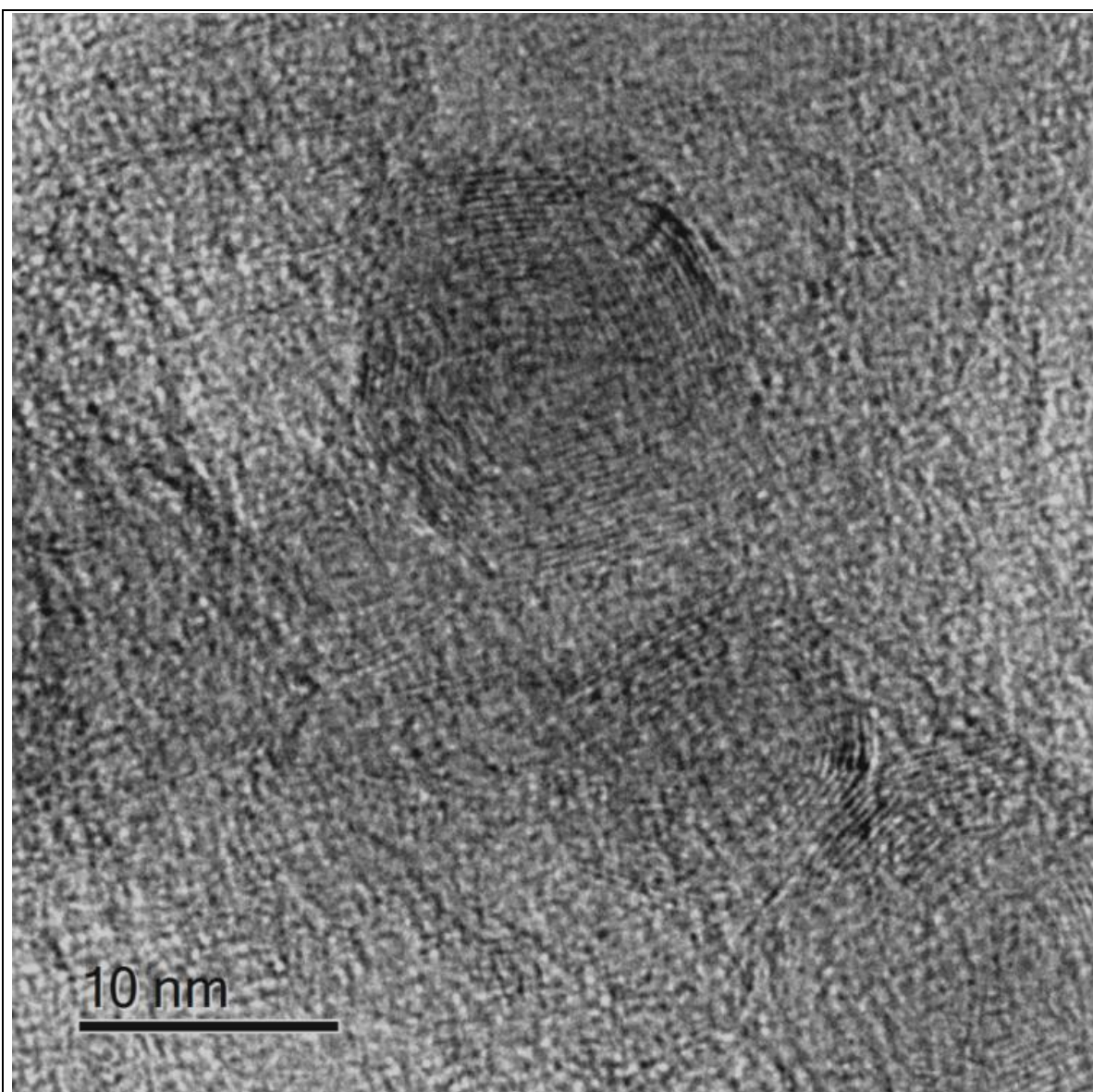
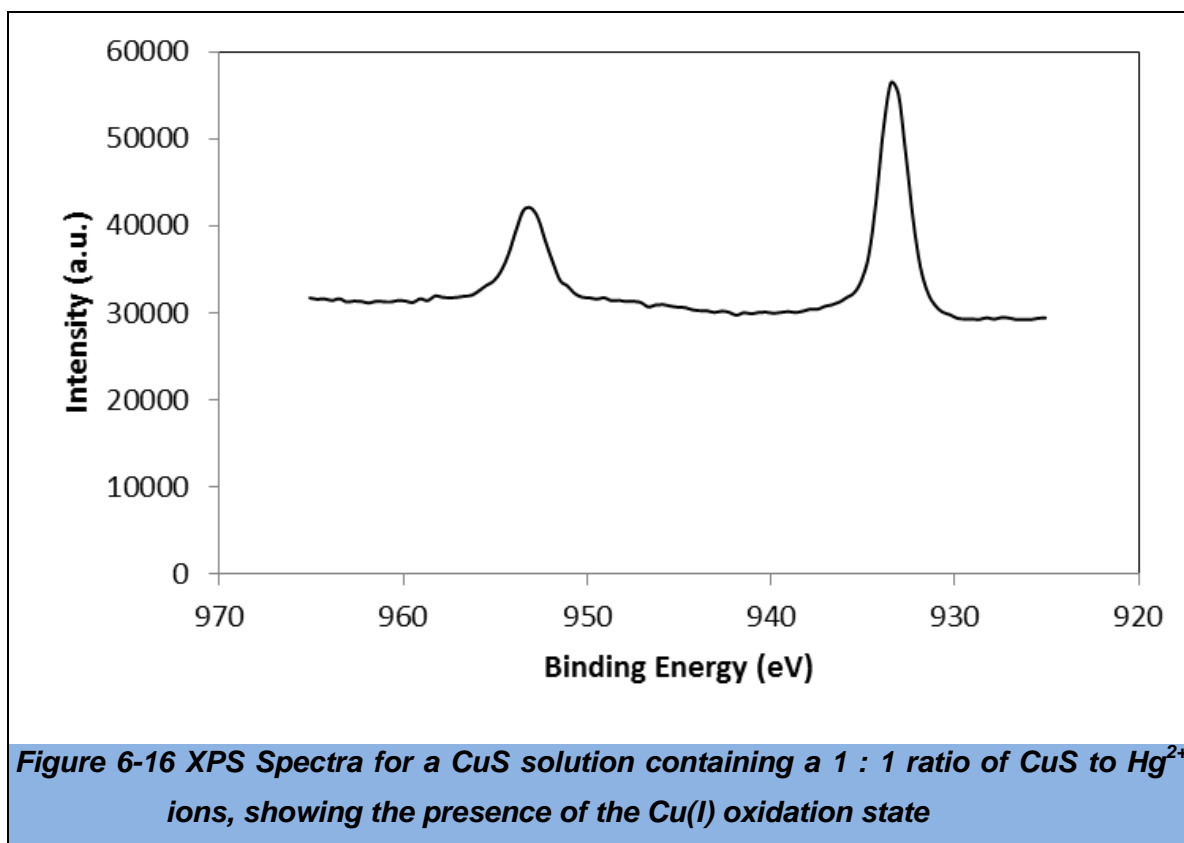


Figure 6-15 TEM micrograph of CuS/Hg nanoclusters at an aqueous Hg^{2+} ion concentration of $5.2500 \mu\text{g/l}$

The size of the structure could be a reason for the reduced bandgap value, as the increased size would reduce the effects of quantum confinement and cause the bandgap to shrink towards the bulk bandgap value of the material; but additionally, as the concentration increases, the nanocrystals should start to take on the form of HgS, which can have a relatively lower bandgap value in the β -HgS form ($\sim 0 \text{ eV}$).

To attempt to get a full ion-exchange conversion and synthesise HgS nanoclusters, a 1:1 [Cu²⁺]:[Hg²⁺] concentration of Hg²⁺ ions was added to a solution of CuS nanoclusters. This resulted in the greatest relative reduction in the direct bandgap energy. TEM micrographs of this sample showed that there were small large particles present, comparable to 5.25 $\mu\text{g/l}$. However, XPS data does show the presence of Cu(II) (Figure 6-16).



This is possibly the creation of a hybrid Cu₂S/HgS material or a material with the Cu²⁺ ions reducing to Cu¹⁺, on the incorporation of the Hg²⁺ ions to the crystal structure. This cannot be a definitive answer as the LSPR peak is still present for this sample. This indicates the continued presence of free-carrier resonance, which is usually attributed to the valence band holes of the CuS species. As the LSPR peak is in the same region as the LSPR absorption peak for CuS, it can be assumed that there is still a considerable amount of CuS presence in the particle, contrary to the XPS data. Although, it must be noted that as the particles increase in size, XPS analysis will be less likely to probe the entire depth of the nanoparticle (penetration depth is usually ~ 10 nm), thus a considerable concentration of CuS may be inaccessible. Alternatively, the lack of any shake-up peaks also suggests a potential Cu(0) component to the nanomaterial. Cu NPs also display LSPR, but at

~520 nm. This could still be the cause of the LSPR peak to appearing in a similar position as the LSPR peak for CuS as plasmonic heterostructures are known to cause large shifts in the LSPR wavelength of the individual plasmonic components.

6.3 Evaluating the CuS Ion-Exchange Sensor for the Selective Detection of Aqueous Hg²⁺ Ions

The UV-Vis characterisation data given in Section 6.2 was used as a calibration plot for the detection of Hg²⁺ ions in a solution of mixed metal ions. The metal ion concentrations were chosen from a report on current metal concentrations in ground water samples, from different areas of the UK.[‡] The mixed metal ion solution contained Pb²⁺ (2.32 µg/l), Cd²⁺ (0.18 µg/l), Ni²⁺ (15.49 µg/l), Zn²⁺ (60.64 µg/l), Fe²⁺ (2.15.24 µg/l) and Cu²⁺ (9.27 µg/l) ions. The Hg²⁺ ion concentration was varied within each mixed metal solution. The average value for five readings were taken (RSD = 0.02%) and Tauc plots were then produced to estimate the allowed direct bandgap value for the CuS nanoclusters in the mixed metal ion solutions, and in the solutions containing only Hg²⁺ ions (Figure 6-17). The results show an excellent fit between the two data sets, with a correlation coefficient of 0.9985.

[‡] These values were provided by United Utilities plc and cannot be referenced as they do not exist in a public domain.

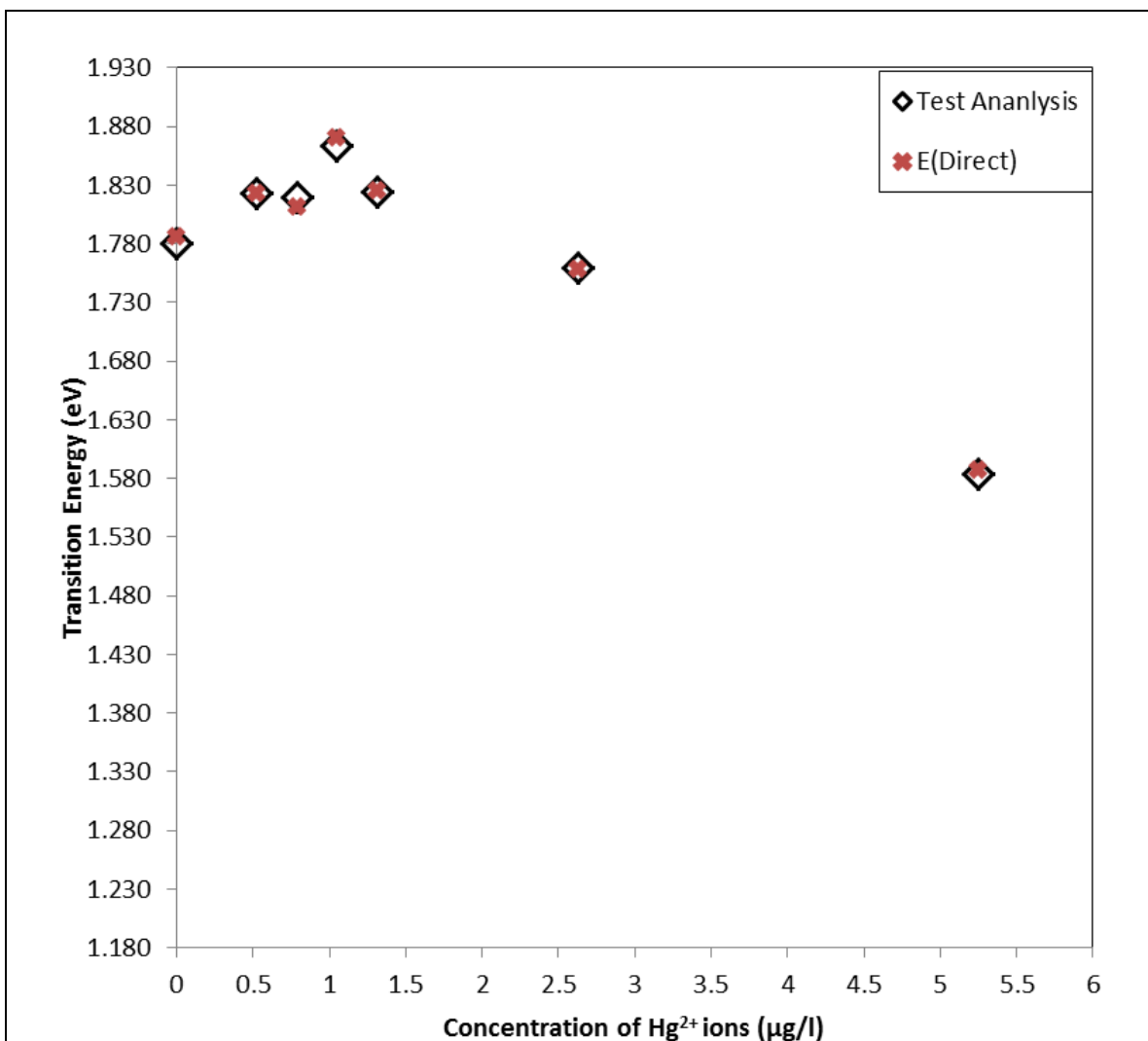


Figure 6-17 A plot of the allowed direct band transition energy for different CuS/Hg²⁺ solutions and the corresponding test solutions containing the same amounts of Hg²⁺ ions in a mixed metal ion solution

The extremely good fit between the data obtained for the CuS nanoclusters in the Hg²⁺ ion solutions and in the mixed metal ion solutions, confirms that the main process here is the cation-exchange between the Hg²⁺ ions in the solution and the Cu²⁺ ions in the CuS nanocluster. This was as expected as the K_{sp} values for the MS materials (M = Pb, Cd, Ni, Fe and Zn) are much higher than that of the CuS and HgS materials. Therefore, the only metal cations that should exchange with the CuS cluster will be the Hg²⁺ ions.

6.4 Summary and Conclusion

The data provided within this chapter clearly demonstrates that this CuS cation-exchange nanosensor is extremely useful for the selective detection and accurate quantification of Hg^{2+} ions in a solution containing a mixture of different metal ions. This method is also suitable for the detection of Hg^{2+} ions down to very low concentrations, including those set by the DWD as 'acceptable'.

In conclusion, respective of the DWD, this method fully accomplishes the aims and objectives set for this research project. This method has also produced a highly original method with several contributions to knowledge; including: A new synthetic route to obtain CuS NCs via an ion exchange route; and a new highly selective and highly sensitive nanosensor for the detection of Hg^{2+} ions.

7 Future Work

7.1 Preliminary Results for a ZnS Nanocluster Chromatography-Style Sensor

It was shown in Chapter 6 that Hg^{2+} ions can be detected down to concentrations as low as 500 ng/l, using a solution of CuS clusters. This idea was based on the fact that in the prepared solutions of Hg^{2+} ions and CuS clusters, HgS has a lower solubility product constant, K_{sp} , and is therefore less soluble than CuS. This has the effect of Hg^{2+} ions exchanging with the Cu^{2+} ions of the CuS clusters to form the less soluble HgS. It was therefore proposed that using a material with a relatively higher K_{sp} value than other metal sulfides, could be used to detect the concentrations of several different metal ions - by the same cation-exchange principle, as was described in Chapter 6.

This penultimate chapter of the thesis presents the preliminary results for the development of a multi-metal ion detection method which utilises ZnS cation-exchange clusters.

7.2 Justification for using Zinc Sulfide Clusters for the detection of Lead, Cadmium, Copper and Mercury Ions

On inspection of the K_{sp} value for ZnS, it is found that there are several metal sulfides which have lower K_{sp} values (Figure 7-1). These include PbS, CdS, Cu_2S and CuS, and HgS, whose metal-cation components are commonly found in aquatic systems. Of these metal components, Pb, Cd and Hg are additionally classified as *priority substances* by the WFD and DWD and are thus target pollutants. These metals should take part in a cation-exchange process with the ZnS clusters to produce their respective metal sulfides.

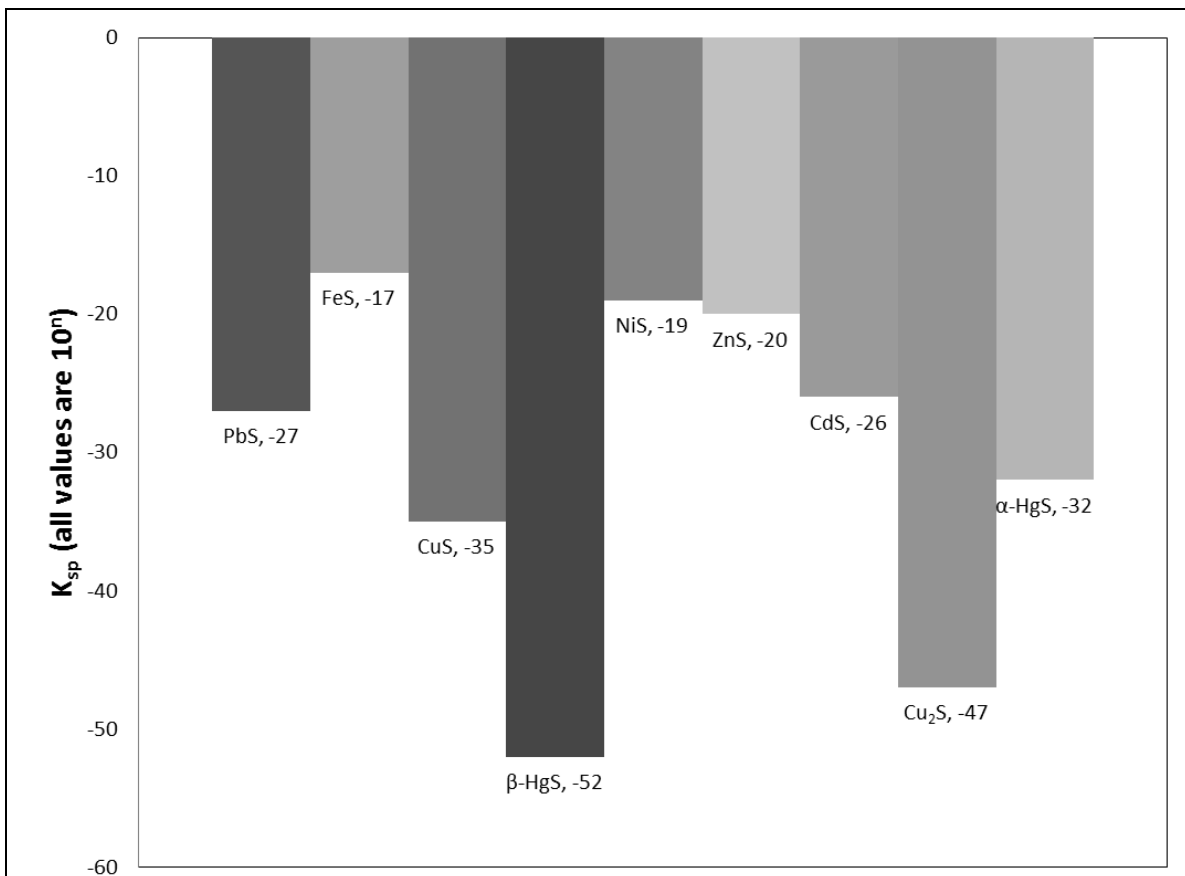


Figure 7-1 The K_{sp} values for several metal sulfide materials (shown as 10^n) containing metals commonly found in aquatic systems

To observe any changes in the visual properties of the ZnS clusters in solution, the metal ions were introduced to the ZnS solution to give a concentration which was slightly higher than the Zn^{2+} ion composition of the cluster; this technique was used to help the formation of the counterpart metal sulfides. Cu^{2+} , Pb^{2+} , Hg^{2+} , Ni^{2+} , and Cd^{2+} ions were used in this study due to the classification of these metals as *priority substances* by the WFD and DWD.

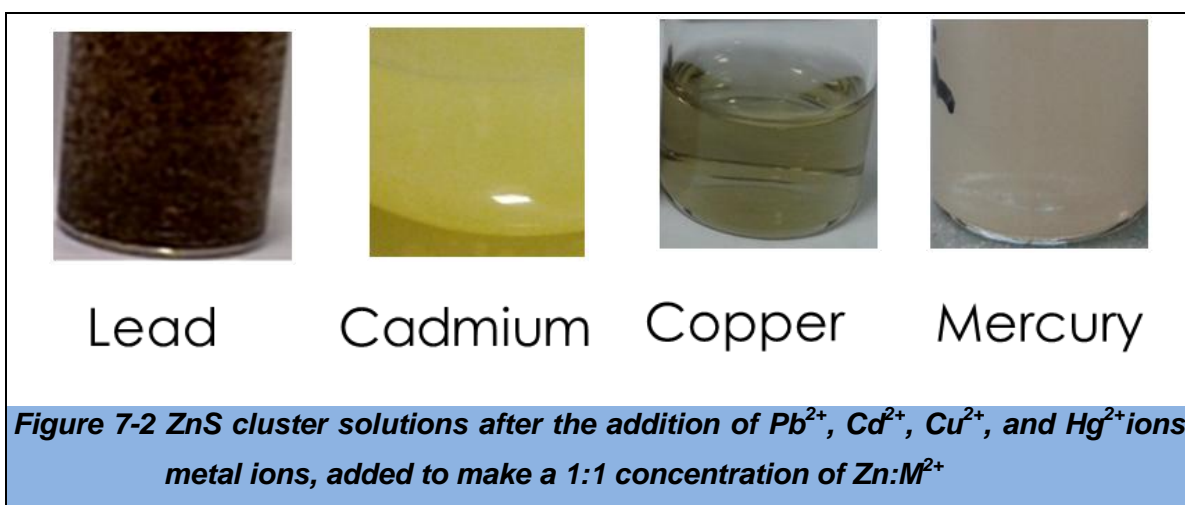


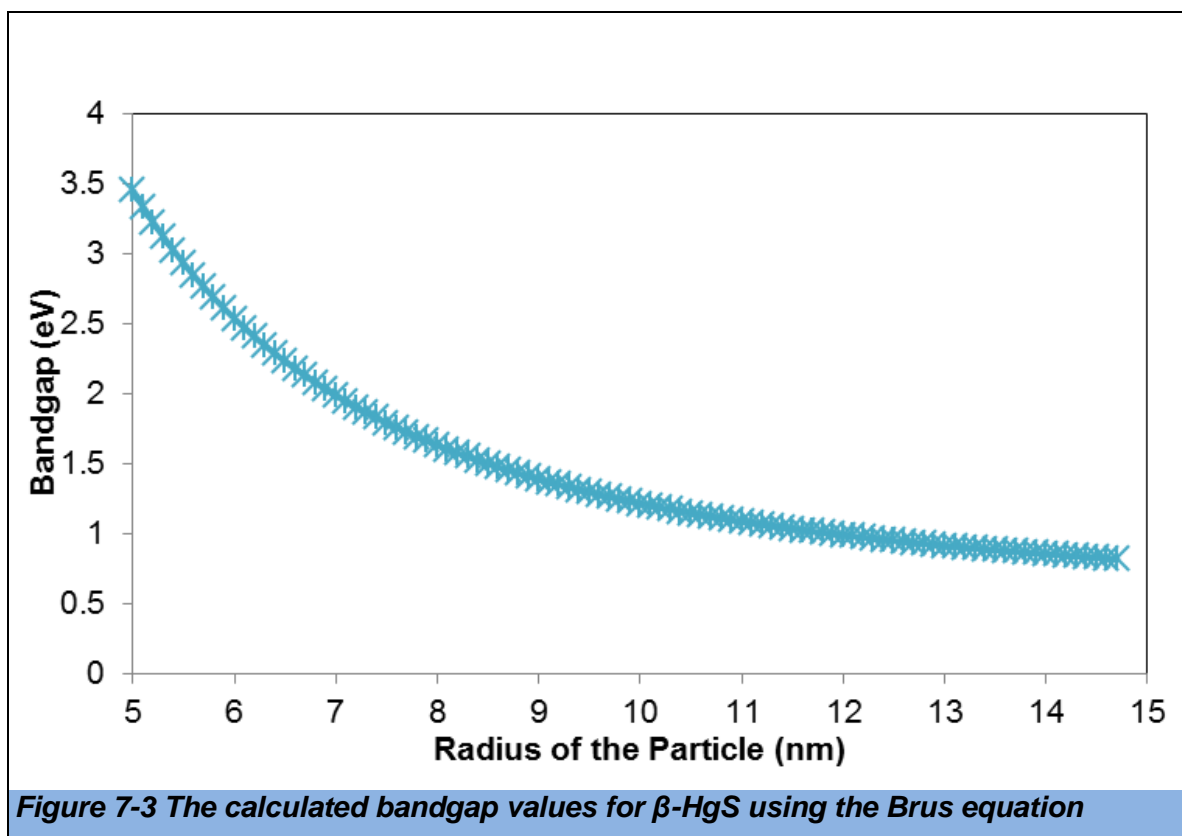
Figure 7-2 ZnS cluster solutions after the addition of Pb^{2+} , Cd^{2+} , Cu^{2+} , and Hg^{2+} ions metal ions, added to make a 1:1 concentration of $\text{Zn}:\text{M}^{2+}$

As noted in Chapter 6 (Section 6.1.2), at a cation concentration, which was slightly higher than the Zn component of the clusters, the white ZnS cluster solution became brown on the addition of Cu^{2+} ions. This change was a result of the cation-exchange between the Zn^{2+} ions of the ZnS clusters and the aqueous Cu^{2+} ions; these Cu^{2+} ions then reduce to form Cu_2S clusters. The reason for the production of the Cu_2S form is related to the K_{sp} values for the CuS and Cu_2S clusters. As Cu_2S has a lower K_{sp} value than CuS it will preferentially form via the cation-exchange reaction between ZnS and Cu^{2+} ions. As discussed in Chapter 6, the formation of Cu_2S , instead of CuS, is further shown by the absence of shake-up peaks in the Cu 2p XPS spectrum (Section 6.1.3) and the absence of the plasmon absorbance peak at $\sim 1000 \text{ nm}$.

On the introduction of Pb^{2+} ions, the ZnS solution became black and contained large aggregated particles which precipitated out of solution within a few seconds. Firstly, the black solution is an expected result of the production of PbS nanomaterials. This is due to the relatively small bandgap of PbS (0.41 eV), which corresponds to the infrared region of the electromagnetic spectrum and leads to infrared optical transitions.¹²⁵ Because humans cannot see infrared radiation the solution appears black. Secondly, the production of the large aggregates is a consequence of PbS clusters being highly unstable with respect to particle-particle repulsion.¹²⁵ This leads to mass aggregation.

Interestingly, on the addition of Hg^{2+} ions to the ZnS cluster solution, the colour initially became yellow. The solution remained yellow for several minutes before becoming white again. HgS clusters are commonly found as the zinc-blend phase crystal structure (known as β -HgS), or the hexagonal phase crystal structure (known as α -HgS). Each of these phases has a unique bandgap value: Bulk α -HgS has a bandgap value of 2.0 eV and is a red semiconductor material; bulk β -HgS is a black material with a bandgap value of $\sim 0.5 \text{ eV}$, thus bulk β -HgS is categorised as a semi-metal.^{126,127} Because of these bulk bandgap values it can be said that the final colour of the solution is due to the formation of α -HgS but, on applying the Brus equation to the optical values for β -HgS, it can be seen that

the bandgap of the material rises sharply in the radius range corresponding to clusters. At a radius of $<7 \text{ nm}$ the bandgap is being increased to the region of UV optical transitions. Although the Brus equation cannot be used accurately for clusters, it does provide evidence that $\beta\text{-HgS}$ clusters are capable of having large bandgaps with UV transitions.



Interestingly, Cd^{2+} ions did not cause a rapid change in colour. The solution became yellow over a matter of weeks. On inspection of the K_{sp} values for ZnS and CdS , it is expected that a rapid reaction will occur, as it did for Pb^{2+} ions. This could be caused by several things including a low ion mobility speed through the ZnS lattice. On viewing the thermodynamic data for the formation of CdS from ZnS (Table 7.1), it can be shown that the process is less spontaneous than that for the other metal ions discussed so far (Figure 7-4).

Table 7.1 Thermodynamic data for the cation-exchange for the reaction $ZnS + M_{ion} \rightarrow MS + Zn^{2+}$ using the formula $\Delta G^{\circ}_{TOTAL} = \sum \Delta G^{\circ}(\text{products}) - \sum \Delta G^{\circ}(\text{reagents})$

ΔG° (kJ/mol) ¹²⁸				ΔG°_{TOTAL} (kJ/mol)
Cd²⁺	-77.7	CdS	-156.5	-24.71
Fe²⁺	-84.9	FeS	-100.4	38.59
Hg²⁺	164.38	α-HgS	-50.6	-160.89
Ni²⁺	-46.4	NiS	-79.5	20.99
Pb²⁺	24.3	PbS	-98.7	-68.91
Zn²⁺	-147.2	ZnS	-201.29	0
Cu²⁺	64.98	CuS	-53.6	-64.49
Cu¹⁺	50.2	Cu₂S	-86.2	-132.51
Hg²⁺	164.38	β-HgS	-47	-157.29

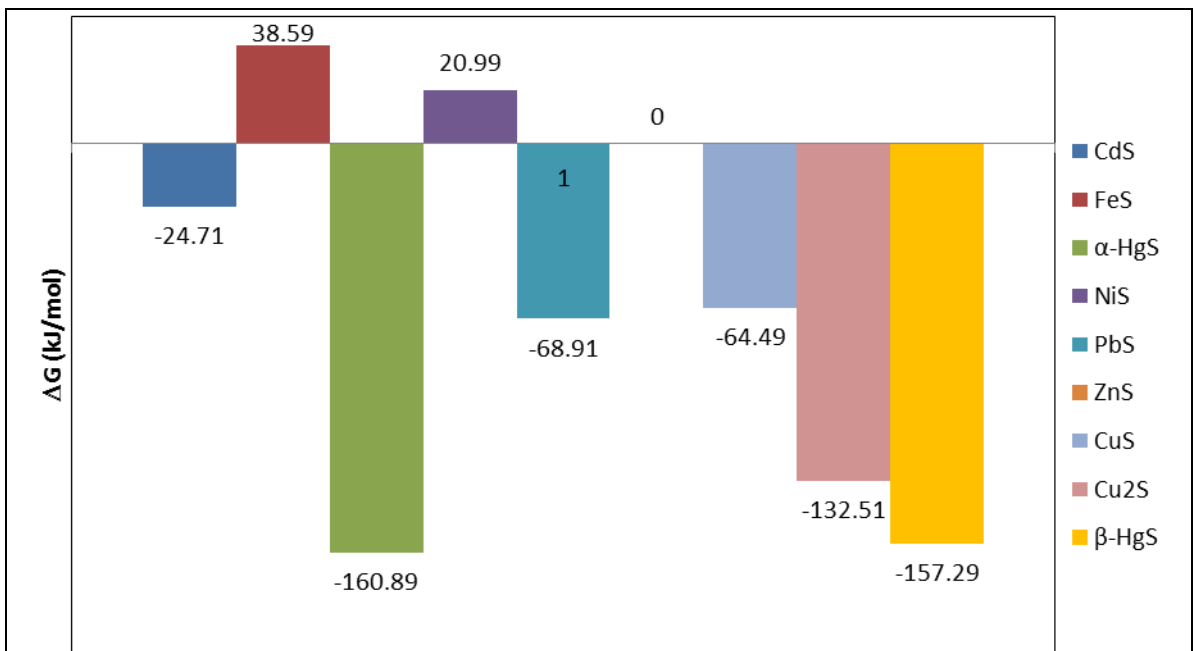


Figure 7-4 The Gibbs energy of formation for the cation-exchange reaction between ZnS and the respective divalent metal ions

Further inspection of Figure 7-4 shows that all of the other reactions discussed so far are thermodynamically favourable and more spontaneous than in the synthesis of CdS (a more negative value represents a more preferred, spontaneous reaction). In addition, the thermodynamic data points to the reactions for the

cation-exchange synthesis of FeS and NiS were unfavourable - this was also suggested by the relatively high K_{sp} values. This data explains the results obtained experimentally, as on the addition of Fe^{2+} and Ni^{2+} ions to solutions of ZnS clusters, there was no change in colour of the solution.

7.3 The Production of a Chromatography-Style ZnS Cation-Exchange Sensor for the Quantitative determination of Several Metal Ions in a Mixture of Aqueous Metal Ions

The above section showed the first preliminary stage for the production of a metal ion sensor that could detect multiple metal ions in a single solution of several other metal ions. The next procedure was the creation of a chromatography-style ZnS cation exchange system which would be able to separate out the metal ions according to their solubility and thermodynamic values *i.e.* the most reactive will react with the ZnS clusters first and then the next most reactive *etc.* To achieve this, normal laboratory filter paper was soaked in a solution of ZnS clusters (Figure 7-5). The paper was then allowed to dry in air at room temperature.



Figure 7-5 The production of a chromatography-style absorbent paper

A sample of metal ions was then added to these strips of absorbent ZnS cation-exchange sheets via a pipette and the colour change was noted (Figure 7-6).

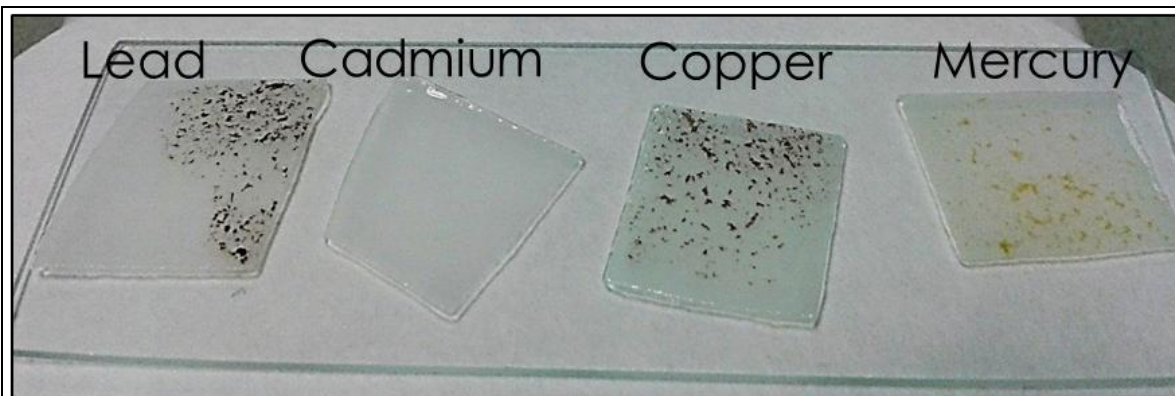


Figure 7-6 The chromatography-style ZnS cation-exchange sheets after the addition of different metal ion solutions

It was clearly visible that the ZnS clusters had reacted with the Hg^{2+} , Cu^{2+} , and Pb^{2+} metal ion solutions to produce their respective metal sulfide clusters. As expected, the Cd^{2+} ion solution did not result in an instantaneous colour change.

The next step was to add a drop of a mixed metal ion solution to the bottom of a strip of the ZnS cluster absorbent paper.



Figure 7-7 The ZnS cluster cation-exchange sheets after the addition of one drop of (left to right) Hg^{2+} , Pb^{2+} , Cu^{2+} , and Hg^{2+} and Cu^{2+} solutions (each metal ion solution contains a respective equal concentration)

Figure 7.7 clearly shows that as the solution moves up the absorbent material it reacts with the ZnS clusters. When these metals are mixed together they form bands which can be ascribed to the respective metal ions present in solution. Table 7.2 shows the width of these bands.

Table 7.2 The band widths for the coloured bands in Figure 7-7	
Metal Ions Tested	Band Width
Hg ²⁺	20 mm
Pb ²⁺	21 mm
Cu ²⁺	11 mm
Hg ²⁺	10 mm
Cu ²⁺	4 mm

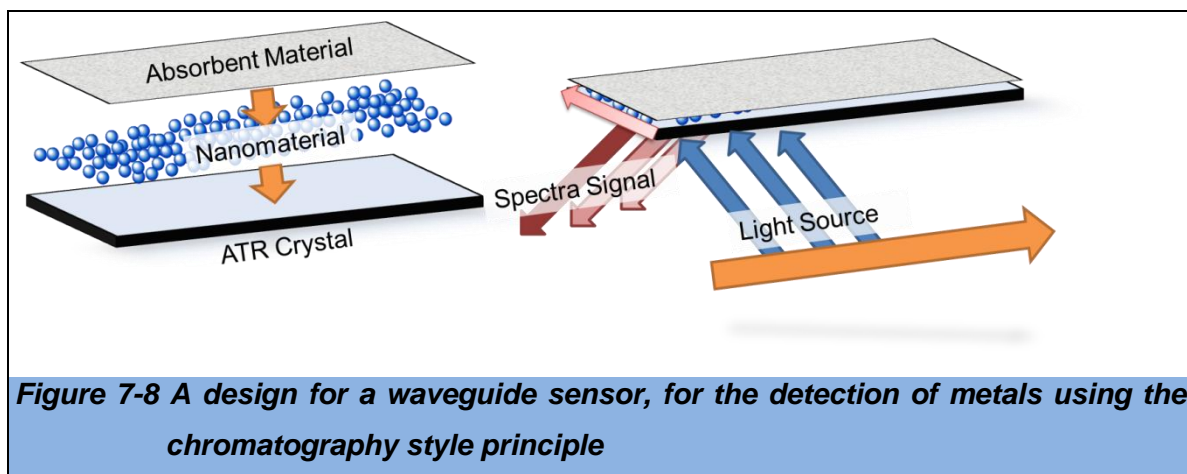
As the concentration of each metal ion solution is equal, it is interesting that the band widths for Cu²⁺ solutions are approximately half the width of the Pb²⁺ and Hg²⁺ bands. This is due to the fact that the preferable metal sulfide for Cu is the Cu₂S, which contains twice as much Cu than S. Therefore, the Cu²⁺ ions in the solution will be consumed in twice the distance compared to the other metal ions, assuming a spontaneous reaction.

These preliminary results show that the ideas developed throughout this project can further lead to a multifunctional detection system for different metal ions. Furthermore, this idea can be applied to other nanosensor designs, for the detection of aqueous metal ions.

**7.3.1 Potential Designs for Further Nanosensor Technologies:
Chromatography-Style LSPR based sensor for the detection of
aqueous metals**

The chromatography–style detection material, explored in this chapter, could be adapted to make a SERS sensor for the detection of aqueous metals. This method would use functionalised plasmonic NPs, instead of the ZnS ion exchange NCs. As the solution moves up the chromatography strip, the most reactive metals will

be separated out until they have been extinguished, leaving separated areas of different metal/NP combinations. This could be achieved with a waveguide sensor (Figure 7-8).



Here, a light source provides an evanescent wave, as with the ATR-FTIR spectrometer. This method has been used extensively to excite plasmons for sensing purposes.¹³⁰ As the light interacts with the plasmonic NPs an evanescent wave forms, interacting with the NPs along the short length of the strip. When the strip has been applied to a sample and the metal ions have been separated, leaving areas of varying local refractive indexes, the light source will be moved up the strip. This will excite the plasmons of the NPs. As the dominant metals on the surface of the NP change, with the progression of the light source, the spectral signal will start to shift to another value, as with normal LSPR sensing.

One of the main advantages this will provide will be the simplification of the UV-Vis spectra for the chromatography strip: The plasmonic NPs will display the typical single LSPR absorption band. The advantage of this is that, to monitor the concentrations of the particular metals along the metal/NP segments, the shifting of the single LSPR band only needs to be considered. This is a relative advantage to the more complicated spectra of the SC NC chromatography strips, which will have a much more complex spectrum. For computerised monitoring software, this will also be an advantage, as the position of the single peak will be easy to distinguish within a spectrum. In contrast, the absorption spectrum for the SC-based strips may have several peaks, assigned to dopants, defects etc.

This method would require timed studies to be conducted into the reaction speed of the various metals and the surface bound molecules. As this technique requires rapid reaction times to allow the formations of the metal/NP bands, slow reactions would result in the various metals being inseparable. This method should also be studied using various functional molecules with a high affinity for metals to try and find a functional molecule which has a rapid binding mechanism for the target metals, with a wide range of compatible metals.

8 Conclusion

This thesis has investigated 3 spectroscopic techniques for the detection of aqueous metals, incorporating citrate functionalised Au and Ag NPs, citrate functionalised AuNPs, and CuS NCs: LSPR absorption spectroscopy, SERS and UV-vis absorption spectroscopy, respectively.

This project was undertaken to design a functional nanomaterial capable of detecting low level concentrations ($20 \mu\text{g/l}$ to $0.05 \mu\text{g/l}$) of a metal identified as a pollutant in the *Water Framework Directive (WFD)*, and the *Drinking water Directive (DWD)*; and evaluate its potential for determining the concentration of an aqueous metal in a mixed-metal solution.

The conclusions for each individual nanosensor technique are provided below.

8.1 Citrate Functionalised Gold and Silver Nanoparticle LSPR Absorption-Based sensor

Through the experiments carried out here, it was determined that the $\text{Pb}^{2+}/\text{AuNP}$ and $\text{Hg}^{2+}/\text{AgNP}$ samples produced unique LSPR absorption spectra, compared to all of the other metal ion/NP solutions. Although, using these particular materials, this technique was unsuitable for the detection of these metal ions in the concentration ranges set out in the aims of the project ($20 \mu\text{g/l}$ to $0.05 \mu\text{g/l}$). This was due to a lack of sensitivity and selectivity, under the experimental conditions used. However, the present study makes several noteworthy contributions to the general field of nanomaterials: Firstly, no reports were present in the literature, at the time of this project, which compared the chemical states of the surface-bound citrate molecules on AuNPs and AgNPs; Secondly, at the time of this project, there were no reports into the subsequent metal-citrate speciation at the surface of the functionalised Au and Ag NPs; thirdly, no one has ever noted the resultant change in pH, upon the addition of metal ions to citrate functionalised NPs.

Though these results demonstrate unsuitability for the aims of this project, there is much scope for the development of these sensors, which could not be studied due

to time restrictions. Citrate molecules are sensitive to the pH of the surrounding solution, alteration of this parameter may lead to a strong selectivity towards a certain metal ion. The concentration of the NPs could also be reduced and confined to a small area, possibly by attaching the particles to a surface or embedding them in a surface matrix. This would increase the citrate to metal ratio and the amount of metal ions available to the surfaces of the NPs; this in turn will cause LSPR absorbance band shifts at much lower metal concentrations. A further nanosensor could possibly be developed using the Pb^{2+} ion induced pH change, when using the AuNPs used here, as this was found to be concentration dependent. As very different responses were obtained when using AuNPs or AgNPs, a study into the effects of other citrate functionalised plasmonic NPs would be useful. These may yield selectivity towards a certain metal due to different surface-citrate responses to metal ions induced by changing the material of the NP.

8.2 AuNP SERS Sensing Method

As the Au and Ag NP LSPR-based sensing technique did not fulfil the aims of the project, a SERS based nanosensor was developed using the same citrate functionalised AuNPs synthesised for the LSPR sensor. This method was designed to detect aqueous Pb^{2+} ions. As these metal ions had such a unique effect on the speciation of the surface citrate molecules, *i.e.* the deprotonation of the citrate hydroxyl group, it was predicted that this may provide a useful SERS substrate. The citrate functionalised AuNP SERS technique provided results that completed the aim of the project, by detecting one of the priority metals from the WFD and DWD, between the concentrations of $20 \mu\text{g/l}$ to $0.05 \mu\text{g/l}$. It was found to have a low limit of detection of $0.025 \mu\text{g/l}$, with low standard deviations over a wide range of practical concentrations ($\sim 25 \text{ ng/l}$ to 25000 ng/l).

The current findings add to a growing body of literature on SERS based nanosensors by providing a new SERS material. From an industrial perspective, this technique requires a preconcentration step due to its lack of selectivity, resulting in this sensor needing further post-sample processing. Even though this is a common procedure for the analysis of water samples, it means that this technique will still incur the usual time and transport steps as standard analytical procedures. This leads to this developed technique being comparable to standard

analytical techniques, with respect to sample processing and transport cost. Although, a Raman spectrometer is far cheaper than an ICP based instrument; this would result in a reduction in general maintenance and running costs. Therefore, developing this technique to incorporate more types of metals would be an economic benefit to the water industry – such as for UU.

Further studies into the response of this sensor, for different concentrations of the other metal named in the WFD and DWD would be needed to develop this technique into a standard analytical technique. If this technique is used as a post-preconcentration analytical technique, an aqueous sample containing a mixture of metals can be easily analysed for any of the present metals; this would be achieved by utilising a selective preconcentration step for the desired metal. Once the metal is separated, it can be analysed using this SERS method, potentially, with very low LOD and sensitivity – as with the Pb^{2+} ions studied here.

A further technique could be adapted from Chapter 7, to make a SERS sensor based on a chromatography-style substrate. This method would use functionalised AuNPs instead of the ZnS ion exchange NCs. As the solution moves up the chromatography strip, the most reactive metals will be separated out until they have been extinguished, leaving separated areas of different metal/AuNP combinations. This would require timed studies to be conducted into the reaction speed of the various metals and the surface bound molecules. As this technique requires rapid reaction times to allow the formations of the metal/NP bands, slow reactions would result in the various metals being inseparable. This method should be studied using various other functional molecules with a high affinity for metals.

8.3 Hg^{2+} Selective Ion-Exchange CuS Nanocluster Sensor

The most impressive results, for any of the nanomaterial based chemical sensors produced in this study, were those obtained for the CuS cation-exchange nanosensor. The material was found to not only be sensitive to the concentration of aqueous Hg^{2+} ions, but also be selective to the Hg^{2+} ions in a solution containing several different metal ions commonly found in water samples. The data provided clearly demonstrates that this CuS cation-exchange nanosensor can be extremely useful for the selective detection and accurate quantification of Hg^{2+} ions at concentrations between $0.525 \mu\text{g/l}$ to $5.25 \mu\text{g/l}$. This makes the method

suitable for the detection of Hg^{2+} ions at levels set by the DWD ($1 \mu\text{g/l}$) as 'acceptable'.

This method has the potential for applications in mobile-sensing, where the water sample can be tested on-site. Due to its selectivity towards Hg^{2+} , no processing of the sample may be required. Additionally, with a portable handheld UV-Vis spectrometer this method reduces the time-scale for an analytical result, and a reduction in costs incurred through sample transport, post-processing and analysis by expensive instruments, such as ICP. Therefore, it is clear that this technique has industrial application for the detection of Hg^{2+} . It would be particularly useful for the rapid determination of the source of a suspected Hg contamination, by analysing several sites in relatively quick succession, as opposed to waiting for an analytical result to be obtained by standard methods in industry.

The results obtained for the ion-exchange CuS NC also provide several contributions to knowledge: The exact synthesis routes taken to produce the CuS NCs have not been described within the literature; nor have observations been documented into the optical effects of Hg^{2+} ion-exchange doping in CuS NCs.

Finally, a number of important limitations need to be considered. First, the mixed metal ion solution only contained metal ions. In real water samples, taken from a test site, there will be further chemical factors that will need to be considered: The sample will possibly contain organic and inorganic components that could preferably form metal complexes, relative to the CuS/Hg clusters. This would reduce the incorporation of the Hg^{2+} ions into the cluster and provide a misleading result for the concentration of Hg in the sample. Second, Cu complexes, that are preferable to CuS, would remove the Cu from the NCs, possibly leading to NCs comprising of other metals than Cu and Hg. Therefore, further experimental investigations are needed to estimate the implications of these effects on the reliability of the spectroscopic signal obtained for Hg detection in a real water sample.

It is recommended that further research be undertaken on increase the sensitivity of the NC sensor: The sensitivity of this method can be greatly improved by reducing the NC concentration. This leads to a higher Hg^{2+} to CuS NC ratio and

thus an increased interaction of Hg^{2+} ions per NC. This will result in a more responsive optical spectrum, as less Hg^{2+} ions are required to cause a comparable change in the E_g value of the NC. This would be the easiest adaptation to reach the level required to detect Hg at the level set by the WFD ($0.05 \mu\text{g/l}$). It is further recommended that research be carried out on the effects of other contaminants found in real water samples, especially those pertaining to possible Cu and Hg complexing agents.

9 References

- [1] J. E. McLean and B. B. E, "Behavior of Metals in Soils EPA/540/S-92/018," Environmental Protection Agency, 1992. [Online]. Available: <http://www.epa.gov/superfund/remedytech/tsp/download/issue14.pdf>.
- [2] World Health Organisation, "WHO Air quality guidelines for particulate matter, ozone, nitrogen dioxide and sulfur dioxide," 2006.
- [3] Agency Environment Protection Agency, "Air Pollution [Online] Available at: www.epa.gov/airtrends/2010/report/airpollution.pdf".
- [4] World Health Organisation, "Ambient (outdoor) air quality and health (Fact sheet N°313)," 2014.
- [5] W. Dr Yasmin von Schirnding, "Health in Sustainable Development Planning: The role of indicators," World Health Organisation, 2002.
- [6] X. Qiao, A. H. Schmidt, Y. Tang, Y. Xu and C. Zhang, "Demonstrating urban pollution using toxic metals of road dust and roadside soil in Chengdu, southwestern China," *Stochastic Environmental Research and Risk Assessment*, vol. 4, no. 28, pp. 911-919, 2014.
- [7] American Cancer Society, "Arsenic," 2014. [Online]. Available: <http://www.cancer.org/cancer/cancercauses/othercarcinogens/intheworkplace/arsenic>.
- [8] L. Järup, "Hazards of heavy metal contamination.," vol. 68, no. 1 167-182, 2003.
- [9] Environment Protection Agency, "Arsenic in the Environment," Environment Protection Agency, [Online]. Available: www.epa.gov/ogwdw/arsenic/.../abernathy.arsenic_in_environment.pdf.
- [10] B. P. Lanphear, K. Dietrich, P. Auinger and C. Cox, "Cognitive deficits associated with blood lead concentrations <10 microg/dL in US children and adolescents," *Public health reports*, vol. 115, no. 6, pp. 521-529, 2000.
- [11] EPA, Office of Water, "Controlling Nonpoint Source Runoff Pollution from Roads, Highways and Bridges," EPA, 1995.

- [12] Safe Drinking Water Foundation, "Water Pollution [Online] Available at: <http://www.safewater.org/PDFS/resourcesknowthefacts/WaterPollution.pdf>".
- [13] P. J. L. P. Grandjean, "Developmental neurotoxicity of industrial chemicals," vol. 368, no. 9553 pp. 2167-78, 2006.
- [14] P. J. Landrigan, "Lessons from the past and prospects for the future," vol. 48, no. (5), pp 1319-1330, 2001.
- [15] EPA, "Ground Water Issues [Online] Available at: <http://www.epa.gov/tio/tsp/download/issue14.pdf>," 1992.
- [16] J. M. VanBriesen, M. Small, C. Weber and W. Wilson, "Modelling Chemical Speciation: Thermodynamics, Kinetics and Uncertainty," *Modeling Pollutants in Complex Environmental Systems*, vol. 2, p. 135, 2010.
- [17] European Commission, "Water Framework Directive (2000/60/EC)," J. Eur. Commun, 2000 pp 1-73.
- [18] European Commission, "L 327 Water Framework Directive," 2000.
- [19] European Commission, "Drinking Water Directive, Council Directive 98/83/EC," 1998.
- [20] K. Fytianos, "Speciation analysis of heavy metals in natural waters: A review," *Journal of AOAC International*, vol. 84, no. 6, pp. 1763-1769, 2001.
- [21] R. J. Brown and M. J. Milton, "Analytical techniques for trace element analysis: an overview," *TrAC Trends in Analytical Chemistry*, vol. 24, no. 3, pp. 266-274, 2005.
- [22] F. Rouessac and A. Rouessac, *Chemical analysis: modern instrumentation methods and techniques*, John Wiley & Sons, 2013.
- [23] Hydrology Project, "Potentiometric Analysis of Water Quality [Online] Available at: <http://cwc.gov.in/main/HP/download/32%20Potentiometric%20Analysis%20of%20Water%20Quality.pdf>".
- [24] S. P. Kounaves, "Voltammetric Techniques [Online] Available at: <http://www.prenhall.com/settle/chapters/ch37.pdf>".
- [25] Thermo Scientific, "AAS, GFAAS, ICP or ICP-MS? Which technique should I use?" Thermo Scientific, [Online]. Available: www.thermo.com/eThermo/CMA/PDFs/Articles/articlesFile_18407.pdf.

- [26] J. S. DietzeBecker and H. J. Dietze, "Inorganic trace analysis by mass spectrometry," *Spectrochimica Acta Part B: Atomic Spectroscopy*, vol. 53, no. 11, pp. 1475-1506, 1998.
- [27] ALS Environmental, "New Limits and Procedures for Elemental Impurities in Pharmaceuticals and Dietary Supplements [Online] Available at: <http://www.caslab.com/News/heavy-metals-testing-usp-revisions.html>," ALS Environmental, 2011.
- [28] DelAgua, "Lead (LeadTrak), Colorimeter II Test Kit [Online] Available at: <http://www.delagua.org/products/details/10089-Lead-LeadTrak-Colorimeter-II-Test-Kit>".
- [29] DelAgua, "Heavy Metal Analyser Portable PDV6000plus [Online] Available at:<http://www.delagua.org/products/details/10103-Heavy-Metal-Analyser-Portable-PDV6000plus>".
- [30] J. Riu, A. Maroto and F. X. Rius, "Nanosensors in environmental analysis," *Talanta*, vol. 69, no. 2, pp. 288-301, 2006.
- [31] O. Lupan, G. Chai and L. Chow, "Novel hydrogen gas sensor based on single ZnO nanorod," *Microelectronic Engineering*, vol. 85, no. 11, pp. 2220-2225, 2008.
- [32] R. A. Sperling and W. J. Parak, "Surface modification, functionalization and bioconjugation of colloidal inorganic nanoparticles," *Philosophical Transactions of the Royal Society A: Mathematical, Physical and Engineering Sciences*, vol. 368, pp. 1333-1383, 2010.
- [33] M. Frigoli, K. Ouadahi and C. Larpent, "A Cascade FRET-Mediated Ratiometric Sensor for Cu²⁺ Ions Based on Dual Fluorescent Ligand-Coated Polymer Nanoparticles," *Chemistry-A European Journal*, vol. 15, no. 33, pp. 8319-8330, 2009.
- [34] E. Sharpe and S. Andreescu, "Portable Nanoparticle Based Sensors for Antioxidant Analysis In Advanced Protocols in Oxidative Stress III," New York, Springer, 2015, pp. 221-231.
- [35] L. Wang, W. Ma, L. Xu, W. Chen, Y. Zhu, C. Xu and N. A. Kotov, "Nanoparticle-based environmental sensors," *Materials Science and Engineering R Reports*, vol. 70, no. 3, pp. 265-274, 2010.

- [36] L. Mu, W. Shi, J. C. Chang and S. T. Lee, "Silicon nanowires-based fluorescence sensor for Cu (II)," *Nano letters*, vol. 8, no. 1, pp. 104-109, 2008.
- [37] H. Li, Y. Li and J. Cheng, "Molecularly imprinted silica nanospheres embedded CdSe quantum dots for highly selective and sensitive optosensing of pyrethroids," vol. 22, no. 8 2451-2457., 2010.
- [38] D. V. Talapin, A. L. Rogach, I. Mekis, S. Haubold, A. Kornowski, M. Haase and H. Weller, " Synthesis and surface modification of amino-stabilized CdSe, CdTe and InP nanocrystals," *Colloids and Surfaces A: Physicochemical and Engineering Aspects*, vol. 202, no. 2, pp. 145-154, 2002.
- [39] W. Chen, Z. Wang, Z. Lin and L. Lin, "Absorption and luminescence of the surface states in ZnS nanoparticles," *Journal of applied physics*, vol. 82, no. 6, pp. 3111-3115, 1997.
- [40] S. K. Ghosh and T. Pal, "Interparticle Coupling Effect on the Surface Plasmon Resonance of Gold Nanoparticles: From Theory to Applications," *Chemical Reviews*, vol. 107, no. 11, pp. 4797-4862, 2007.
- [41] Y. Sun and Y. Xia, "Shape-controlled synthesis of gold and silver nanoparticles," *Science*, vol. 298, no. 5601, pp. 2176-2179, 2002.
- [42] G. McNay, D. Eustace, W. E. Smith, K. Faulds and D. Graham, "Surface-enhanced Raman scattering (SERS) and surface-enhanced resonance Raman scattering (SERRS): a review of applications," *Applied spectroscopy*, vol. 65, no. 8, pp. 825-837, 2011.
- [43] Y. Chen and H. Ming, "Review of surface plasmon resonance and localized surface plasmon resonance sensor," *Photonic Sensors*, vol. 2, no. 1, pp. 37-49, 2012.
- [44] X. Hu, G. Li and J. C. Yu, "Design, fabrication, and modification of nanostructured semiconductor materials for environmental and energy applications," *Langmuir*, vol. 26, no. 5, pp. 3031-3039, 2009.
- [45] X. Zhao, L. Lv, B. Pan, W. Zhang, S. Zhang and Q. Zhang, "Polymer-supported nanocomposites for environmental application: a review," *Chemical Engineering Journal*, vol. 170, no. 2, pp. 381-394, 2011.

- [46] B. J. Sanghavi, O. S. Wolfbeis, T. Hirsch and N. S. Swami, "Nanomaterial-based electrochemical sensing of neurological drugs and neurotransmitters," *Microchimica Acta*, vol. 182, no. 1-2, pp. 1-41, 2015.
- [47] J. H. J. Wilson, *Optoelectronics An Introduction (3rd Edition)*, Prentice Hall Europe, First Printed 1998.
- [48] N. Green, *Quantum Mechanics 1: Foundations*, Oxford: Oxford University Press, 1997.
- [49] M. G. Bawendi, M. L. Steigerwald and L. E. Brus, "The quantum-mechanics of larger semiconductor clusters (quantum dots)," *Annual Review of Physical Chemistry*, vol. 41, no. 1, pp. 477-496, 1990.
- [50] T. Trindade, P. O'Brien and N. L. Pickett, "Nanocrystalline semiconductors: synthesis, properties, and perspectives," *Chemistry of Materials*, vol. 13, no. 11, pp. 3843-3858, 2013.
- [51] L. Brus, "Electronic wave functions in semiconductor clusters: experiment and theory," no. 12 pp. 2555-2560., 1986.
- [52] E. Goldburt, "Nanocrystals of Widegap II-VIs and Their Bandgaps," in *Properties of Wide Broad Band II-VI Semiconductors*, INSPEC, 1996.
- [53] A. S. de Dios and M. E. D. García, "Multifunctional nanoparticles: Analytical prospects," no. 666, 2010.
- [54] S. Ilıcan, M. Caglar and Y. Caglar, "Sn doping effects on the electro-optical properties of sol gel derived transparent ZnO films," *Applied Surface Science*, vol. 256, no. 23, pp. 7204-7210, 2010.
- [55] J. Tauc, R. Grigorovici and A. Vancu, "Optical properties and electronic structure of amorphous germanium," *Physica status solidi (b)*, vol. 15, no. 2, pp. 627-637, 1966.
- [56] P. Blood, "Material issues in AlGaInP red-emitting laser diodes," *Materials Science and Engineering: B*, vol. 66, no. 1, pp. 174-180, 1999.
- [57] A. Arakawa, Y. YarivArakawa and A. Yariv, "Quantum Well Lasers-Gain, Spectra, Dynamics," *IEEE journal of quantum electronics*, vol. 22, no. 9, pp. 1889-1899, 1986.

- [58] C. Skierbiszewski, H. Turski, G. Muziol, M. Siekacz, M. Sawicka, G. Cywiński and S. Porowski, "Nitride-based laser diodes grown by plasma-assisted molecular beam epitaxy," *Journal of Physics D: Applied Physics*, vol. 47, no. 7, 2014.
- [59] T. Trindade, "Nanocrystalline Semiconductors: Synthesis, Properties, and Perspectives," no. 13, pp. 3843-3858, 2001.
- [60] H. J. Choi, J. C. Johnson, R. He, S. K. Lee, F. Kim, P. Pauzauskie and P. Yang, "Self-Organized GaN Quantum Wire UV Lasers," *The Journal of Physical Chemistry B*, vol. 107, no. 34, pp. 8721-8725, 2003.
- [61] A. J. Nozik, "Spectroscopy and hot electron relaxation dynamics in semiconductor quantum wells and quantum dots," *Annual Review of Physical Chemistry*, vol. 52, no. 1, pp. 193-231, 2001.
- [62] A. V. Subashiev, O. Semyonov, Z. Chen and S. Luryi, "Urbach tail studies by luminescence filtering in moderately doped bulk InP," *Applied Physics Letters*, vol. 97, no. 18, 2010.
- [63] A. M. Smith and S. Nie, "Semiconductor nanocrystals: structure, properties, and band gap engineering," *Accounts of chemical research*, vol. 43, no. 3, pp. 190-200, 2009.
- [64] H. S. Zhou, H. Sasahara, I. Honma, H. Komiyama and J. W. Haus, "Coated semiconductor nanoparticles: the CdS/PbS system's photoluminescence properties," *Chemistry of materials*, vol. 6, no. 9, pp. 1534-1541, 1994.
- [65] J. Yu, J. Zhang and S. Liu, "Ion-exchange synthesis and enhanced visible-light photoactivity of CuS/ZnS nanocomposite hollow spheres," *The Journal of Physical Chemistry C*, vol. 114, no. 32, pp. 13642-13649, 2010.
- [66] P. K. Jain, L. Amirav, S. Aloni and A. P. Alivisatos, "Nanoheterostructure cation exchange: Anionic framework conservation," *Journal of the American Chemical Society*, vol. 132, no. 29, pp. 9997-9999, 2010.
- [67] M. Ethayaraja and R. Bandyopadhyaya, "Model for Core-Shell Nanoparticle Formation by Ion-Exchange Mechanism," *Industrial & Engineering Chemistry Research*, vol. 47, no. 16, pp. 5982-5985, 2008.
- [68] D. H. Son, S. M. Hughes, Y. Yin and A. P. Alivisatos, "Cation exchange reactions in ionic nanocrystals," *Science*, vol. 306, no. 5698, pp. 1009-1012, 2004.

- [69] K. L. Kelly, E. Coronado, L. L. Zhao and G. C. Schatz, "The Optical Properties of Metal Nanoparticles: The Influence of Size, Shape, and Dielectric Environment," *The Journal of Physical Chemistry B*, vol. 107, no. 3, pp. 668-677, 2003.
- [70] J. Zheng, P. R. Nicovich and R. M. Dickson, "Highly Fluorescent Noble Metal Quantum Dots," *Annual review of physical chemistry*, vol. 58, pp. 409-431, 2007.
- [71] K. M. Mayer and J. H. Hafner, "Localized surface plasmon resonance sensors," *Chemical reviews*, vol. 111, no. 6, p. 3828–3857, 2011.
- [72] M. E. Stewart, C. R. Anderton, L. B. Thompson, J. Maria, S. K. Gray, J. A. Rogers and R. G. Nuzzo, "Nanostructured plasmonic sensors," *Chemical reviews*, vol. 108, no. 2, pp. 494-521, 2008.
- [73] A. Moores and F. Goettmann, "The plasmon band in noble metal nanoparticles: an introduction to theory and applications," *New Journal of Chemistry*, vol. 30, no. 8, pp. 1121-1132, 2006.
- [74] J. T. Krug, G. D. Wang, S. R. Emory and S. Nie, "Efficient Raman Enhancement and Intermittent Light Emission Observed in Single Gold Nanocrystals," *Journal of the American Chemical Society*, vol. 121, no. 39, pp. 9208-9214, 1999.
- [75] S. J. Lee, Z. Guan, H. Xu and M. Moskovits, "Surface-enhanced Raman spectroscopy and nanogeometry: The plasmonic origin of SERS," *The Journal of Physical Chemistry C*, vol. 111, no. 49, pp. 17985-17988, 2007.
- [76] L. S. Jung, C. T. Campbell, T. M. Chinowsky, M. N. Mar and S. S. Yee, "Quantitative interpretation of the response of surface plasmon resonance sensors to adsorbed films," *Langmuir*, vol. 14, no. 19, pp. 5636-5648, 1998.
- [77] T. Kiatkumjorn, P. Rattanarat, W. Siangproh, O. Chailapakul and N. Praphairaksit, "Glutathione and l-cysteine modified silver nanoplates-based colorimetric assay for a simple, fast, sensitive and selective determination of nickel," *Talanta*, vol. 128, pp. 215-220, 2014.
- [78] J. P. Chaudhary, A. Kumar, P. Paul and R. Meena, "Carboxymethylagarose-AuNPs generated through green route for selective detection of Hg 2+ in aqueous medium with a blue shift," *Carbohydrate polymers*, vol. 117, pp. 537-542, 2015.

- [79] Y. Liu, Y. Zhao, Y. Wang and C. M. Li, "Polyamine-capped gold nanorod as a localized surface Plasmon resonance probe for rapid and sensitive copper (II) ion detection," *Journal of colloid and interface science*, vol. 439, pp. 7-11, 2015.
- [80] S. Nie and S. R. Emory, "Probing single molecules and single nanoparticles by surface-enhanced Raman scattering," *science*, vol. 275, no. 5303, pp. 1102-1106, 1997.
- [81] E. C. Le Ru, P. G. Etchegoin "Single-Molecule Surface-Enhanced Raman Spectroscopy," vol. 103, no. p. 9846, 1999.
- [82] P. L. Stiles, J. A. Dieringer, N. C. Shah and R. P. Van Duyne, "Surface-enhanced Raman spectroscopy," *Annu. Rev. Anal. Chem*, vol. 1, pp. 601-626, 2008.
- [83] F. Li, F. Li, J. Wang, Y. Lai, C. Wu, S. Sun, Y. He and H. Ma, "Ultrasensitive and selective detection of copper (II) and mercury (II) ions by dye-coded silver nanoparticle-based SERS probes," *Biosensors and Bioelectronics*, vol. 39, no. 1, pp. 82-87, 2013.
- [84] D. Grasseschi, V. M. Zamarion, K. Araki and H. E. Toma, "Surface enhanced Raman scattering spot tests: a new insight on Feigl's analysis using gold nanoparticles," *Analytical chemistry*, vol. 82, no. 22, p. 9146-9149, 2010.
- [85] L. Zhang and M. Fang, "Nanomaterials in pollution trace detection and environmental improvement," *Nano Today*, vol. 5, no. 2, pp. 128-142, 2010.
- [86] G. a. Pal, vol. 107, no. 11, 2007.
- [87] M. Liu, Z. Wang, S. Zong, H. Chen, D. Zhu, L. Wu and Y. Cui, "SERS Detection and Removal of Mercury (II)/Silver (I) using Oligonucleotide-Functionalized Core/Shell Magnetic Silica Sphere@ Au Nanoparticles.," *ACS applied materials & interfaces*, vol. 6, no. 10, pp. 7371-7379, 2014.
- [88] L. Xu, H. Yin, W. Ma, H. Kuang, L. Wang and C. Xu, "Ultrasensitive SERS detection of mercury based on the assembled gold nanochain," *Biosensors and Bioelectronics*, vol. 67, pp. 472-476, 2015.
- [89] M. Koneswaran and R. Narayanaswamy, "l-Cysteine-capped ZnS quantum dots based fluorescence sensor for Cu²⁺ ion," *Sensors and Actuators B: Chemical*, vol. 139, no. 1, pp. 104-109, 2009.

- [90] J. Wang, N. Li, F. Shao and H. Han, "Microwave-assisted synthesis of high-quality CdTe/CdS@ ZnS–SiO₂ near-infrared-emitting quantum dots and their applications in Hg²⁺ sensing and imaging," *Sensors and Actuators B*, vol. 207, pp. 74-82, 2015.
- [91] C. Chu, K. Darling, R. Netusil, R. P. Doyle and J. Zubieta, "Synthesis and structure of a lead (II)–citrate:{Na(H₂O)₃}[Pb₅(C₆H₅O₇)₃(C₆H₆O₇)(H₂O)₃· 9.5 H₂O," *Inorganica Chimica Acta*, vol. 378, no. 1, pp. 186-193, 2011.
- [92] R. W. Parry and F. W. Dubois, "Citrate complexes of copper in acid solutions," *Journal of the American Chemical Society*, vol. 74, no. 15, pp. 3749-3753, 1952.
- [93] S. Robertson, "Transmission Electron microscope for JEOL TEM [Online] Available at: <http://nanonet.rice.edu/manuals/tem.htm>".
- [94] Sheffield Hallem University, "UV-Vis Absorption Spectroscopy: Instrumentation [Online] Available at: <http://teaching.shu.ac.uk/hwb/chemistry/tutorials/molspec/uvvisab3.htm>".
- [95] Princeton Instruments , "Raman Spectroscopy Basics [Online] Available at: http://content.piacton.com/Uploads/Princeton/Documents/Library/UpdatedLibrary/Raman_Spectroscopy_Basics.pdf".
- [96] K. Kneipp, H. Kneipp, I. Itzkan, R. R. Dasari and M. S. Feld, "Ultrasensitive chemical analysis by Raman spectroscopy," *Chemical reviews*, vol. 99, no. 10 , pp. 2957-2975, 1999.
- [97] Malvern Instruments Ltd, "Zetasizer Nano Series User Manual [Online] Available at: <http://www.nbtc.cornell.edu/facilities/downloads/Zetasizer%20Manual.pdf>," 2004.
- [98] S. Link and M. A. El-Sayed, "Size and temperature dependence of the plasmon absorption of colloidal gold nanoparticles," *The Journal of Physical Chemistry B*, vol. 103, pp. 4212-4217, 1999.
- [99] P. C. Lee and D. Meisel, "Adsorption and surface-enhanced Raman of dyes on silver and gold sols," *The Journal of Physical Chemistry*, vol. 86, pp. 3391-3395, 1982.

- [100] Guan, J., Jiang, L., Zhao, L., Li, J., and Yang, W. (2008). pH-dependent response of citrate capped Au nanoparticle to Pb²⁺ ion. *Colloids and Surfaces A: Physicochemical and Engineering Aspects*, 2008, 325, pp.194-197.
- [101] J. J. P. Stewart, "Optimization of parameters for semiempirical methods V: Modification of NDDO approximations and application to 70 elements," *Journal of Molecular Modelling*, vol. 13, pp. 1173-1213, 2007.
- [102] F. Limited, "MO-G Version 1.1," 2008.
- [103] A. Henglein, "Colloidal silver nanoparticles: photochemical preparation and interaction with O₂, CCl₄, and some metal ions," *Chemistry of Materials*, vol. 10, no. 1, pp. 444-450, 1998.
- [104] A. Henglein and C. Brancewicz, "Absorption spectra and reactions of colloidal bimetallic nanoparticles containing mercury," *Chemistry of materials*, vol. 9, no. 10, pp. 2164-2167, 1997.
- [105] P. C. Hidber, T. J. Graule and L. J. Gauckler, "Citric acid—a dispersant for aqueous alumina suspensions," *Journal of the American Ceramic Society*, vol. 79, pp. 1857-1867, 2005.
- [106] H. E. Toma, V. M. Zamarion, S. H. Toma and K. Araki, "The Coordination Chemistry at Gold Nanoparticles," *Journal of the Brazilian Chemical Society*, vol. 21, no. 7, pp. 1158-1176, 2010.
- [107] I. A. Mudunkotuwa and V. H. Grassian, "Citric acid adsorption on TiO₂ nanoparticles in aqueous suspensions at acidic and circumneutral pH: surface coverage, surface speciation, and its impact on nanoparticle–nanoparticle interactions," *Journal of the American Chemical Society*, vol. 132, no. 42, pp. 14986-14994, 2010.
- [108] R. W. Parry and F. W. Dubois, " Citrate Complexes of Copper in Acid Solutions," *J. Am. Chem Soc*, vol. 74, pp. 3749-3753, 1952.
- [109] S. Floate, M. Hosseini, M. R. Arshadi, D. Ritson, K. L. Young and R. J. Nichols, "An in-situ infrared spectroscopic study of the adsorption of citrate on Au (111) electrodes," *Journal of Electroanalytical Chemistry*, vol. 542, pp. 67-74, 2003.

- [110] R. J. Nichols, I. Burgess, K. L. Young, V. Zamlynny and J. Lipkowski, "A quantitative evaluation of the adsorption of citrate on Au (111) using SNIFTIRS," *Journal of Electroanalytical Chemistry*, vol. 563, pp. 33-39, 2004.
- [111] M. Lindegren, J. S. Loring and P. Persson, "Molecular structures of citrate and tricarballylate adsorbed on α -FeOOH particles in aqueous suspensions," *Langmuir*, vol. 25, pp. 10639-10647, 2009.
- [112] J. D. Kubicki, L. M. Schroeter, M. J. Itoh, B. N. Nguyen and S. E. Apitz, "Attenuated total reflectance Fourier-transform infrared spectroscopy of carboxylic acids adsorbed onto mineral surfaces," *Geochimica et Cosmochimica Acta*, vol. 63, pp. 2709-2725, 1999.
- [113] P. C. Hidber, T. J. Graule and L. J. Gauckler, "Influence of the dispersant structure on properties of electrostatically stabilized aqueous alumina suspensions," *Journal of the European Ceramic Society*, vol. 17, no. 2, pp. 239-249, 1997.
- [114] Y. Kim, R. C. Johnson and J. T. Hupp, "Gold nanoparticle-based sensing of "spectroscopically silent" heavy metal ions," *Nano Letters*, vol. 1, no. 4, pp. 165-167, 2001.
- [115] C. H. Munro, W. E. Smith, M. Garner, J. W. P. C. Clarkson and P. C. White, "Characterization of the surface of a citrate-reduced colloid optimized for use as a substrate for surface-enhanced resonance Raman scattering," *Langmuir*, vol. 11, no. 10, pp. 3712-372, 1995.
- [116] Y. Li, Y. Ding, Y. Zhang and Y. Qian, "Photophysical properties of ZnS quantum dots," *Journal of Physics and Chemistry of Solids*, vol. 60, no. 1, pp. 13-15, 1999.
- [117] S. Wageh, Z. S. Ling and X. Xu-Rong, "Growth and optical properties of colloidal ZnS nanoparticles," *Journal of Crystal Growth*, vol. 255, no. 3, pp. 332-337, 2003.
- [118] T. Kuzuya, K. Itoh and K. Sumiyama, "Low polydispersed copper-sulfide nanocrystals derived from various Cu-alkyl amine complexes," *Journal of Colloid and interface Science*, vol. 319, no. 2, pp. 565-571, 2008.

- [119] P. Lukashev, W. R. Lambrecht, T. Kotani and M. van Schilfgaarde, "Electronic and crystal structure of Cu_{2-x}S : Full-potential electronic structure calculations," *Physical Review B*, vol. 76, no. 19, p. 195202, 2007.
- [120] K. V. Yumashev, P. V. Prokoshin, A. M. Malyarevich, V. P. Mikhailov, M. V. Artemyev and V. S. Gurin, "Optical transient bleaching and induced absorption of surface-modified copper sulfide nanocrystals," *Applied Physics B*, vol. 64, no. 1, pp. 73-78, 1996.
- [121] J. M. Luther, P. K. Jain, T. Ewers and A. P. Alivisatos, "Localized surface plasmon resonances arising from free carriers in doped quantum dots," *Nature materials*, vol. 10, no. 5, pp. 361-366, 2011.
- [122] N. Kumbhojkar, V. V. Nikesh, A. Kshirsagar and S. Mahamuni, "Photophysical properties of ZnS nanoclusters," *Journal of Applied Physics*, vol. 88, no. 11, pp. 6260-6264, 2000.
- [123] J. F. Watts and W. J. An Introduction to Surface Analysis by XPS and AES, Chichester: Wiley, 2003.
- [124] Y. Zhao, H. Pan, Y. Lou, X. Qiu, J. Zhu and C. Burda, "Plasmonic Cu_{2-x}S Nanocrystals: Optical and Structural Properties of Copper-Deficient Copper (I) Sulfides," *Journal of the American Chemical Society*, vol. 131, no. 12, pp. 4253-4261, 2009.
- [125] M. A. Hines and G. D. Scholes, "Colloidal PbS nanocrystals with size-tuneable near-infrared emission: observation of post-synthesis self-narrowing of the particle size distribution," *Advanced Materials*, vol. 15, no. 21, pp. 1844-1849, 2003.
- [126] H. Wang and J. J. Zhu, "A sonochemical method for the selective synthesis of α -HgS and β -HgS nanoparticles," *Ultrasonics sonochemistry*, vol. 11, no. 5, pp. 293-300, 2004.
- [127] B. K. Patel, S. Rath, S. N. Sarangi and S. N. Sahu, "HgS nanoparticles: structure and optical properties," *Applied Physics A*, vol. 86, no. 4, pp. 447-450, 2007.
- [128] CRC Press, CRC Handbook of Chemistry and Physics 59th ed. R. Weast, Ed.
- [129] Guan, J., Jiang, L., Zhao, L., Li, J., and Yang, W. (2008). pH-dependent response of citrate capped Au nanoparticle to Pb^{2+} ion. *Colloids and*

Surfaces A: Physicochemical and Engineering Aspects, 2008, 325, pp.194

- [130] Borah, S. B., Bora, T., Baruah, S., & Dutta, J. Heavy metal ion sensing in water using surface plasmon resonance of metallic nanostructures. *Groundwater for Sustainable Development*, 2015, 1, pp. 1-11.